

# Impact of compositional gradients on the dynamics of solid-liquid-vapor contact lines

Dissertation  
FOR THE AWARD OF THE DEGREE  
*'Doctor rerum naturalium'*  
at the Georg-August-Universität Göttingen

within the doctoral program  
Göttingen Graduate Center for Neurosciences,  
Biophysics, and Molecular Biosciences (GGNB),  
Physics of Biological and Complex Systems (PBCS)

submitted by  
**Olinka Johani Ramírez Soto**  
from Taxco de Alarcón, México

Göttingen, 2022

## **Thesis advisory committee**

Dr. Stefan Karpitschka  
Research Group Interfaces of Complex Fluids  
Max Planck Institute for Dynamics and Self-Organization

Prof. Dr. Marcus Müller  
Institute for Theoretical Physics  
Georg-August-Universität Göttingen

Prof. Dr. Karen Alim  
Research Group Biological Physics and Morphogenesis  
Center for Functional Protein Assemblies

## **Members of the examination board:**

*Referee:* Dr. Stefan Karpitschka  
Research Group Interfaces of Complex Fluids  
Max Planck Institute for Dynamics and Self-Organization

*Co-referee:* Prof. Dr. Marcus Müller  
Institute for Theoretical Physics  
Georg-August-Universität Göttingen

## **Other members of the Examination Board:**

Prof. Dr. Karen Alim  
Research Group Biological Physics and Morphogenesis  
Center for Functional Protein Assemblies

Prof. Dr. Peter Sollich  
Institute for Theoretical Physics  
Georg-August-Universität Göttingen

Prof. Dr. Stefan Klumpp,  
Institute for the Dynamics of Complex Systems,  
Georg-August-Universität Göttingen

Prof. Dr. Joerg Enderlein  
III. Physical Institute Biophysics,  
Georg-August-Universität Göttingen

Date of oral examination: 2022-02-24

# Abstract

The motion of a liquid over a solid surface is a process that happens in natural phenomena and everyday life situations, therefore its understanding is of great importance. The motion of the liquid is limited by the dynamics of the solid-liquid-vapor contact line. In this thesis, the effect that the liquid composition has over moving contact lines is studied, in particular when surface tension gradients, driven by compositional gradients, are present. The objective is to get insights of the governing mechanisms. The model system is Marangoni-contracted drops. The wetting behavior is investigated by experiments that allow for a control of the ambient conditions, macroscopic observations, and micro-PIV, simultaneously. A quantitative description of the shape and the internal flows of the drops is obtained and used to build a theoretical understanding of the governing mechanisms. First, a system where two wetting mechanisms compete is presented. These mechanisms are: Marangoni contraction and autophobing. The regimes where the mechanisms dominate are presented. Then, it is shown that Taylor-Aris dispersion dominates the evolution of the compositional field of Marangoni-contracted drops. The theoretical model, based on thin film theory and accounts for Taylor-Aris dispersion, is proposed. Then, it is shown that in systems where liquid-liquid phase separation is induced, Marangoni-contraction is lost. The responsible of this are surface forces causing an earlier phase separation in the precursor film. The previous studies were done on smooth high energy surfaces. In the last part of this thesis, the behavior of Marangoni contracted drops on porous substrates is explored and preliminary results are given.

# Contents

<b>1</b>	<b>Introduction</b>	<b>8</b>
1.1	Motivation . . . . .	8
1.2	Objectives and approach . . . . .	9
1.3	Outline of the thesis . . . . .	10
<b>2</b>	<b>Overview: Wetting</b>	<b>12</b>
2.1	Static contact lines . . . . .	13
2.2	Dynamic contact lines . . . . .	16
	Molecular-kinetic theory. . . . .	18
	Hydrodynamic theory. . . . .	19
2.3	Dynamics of evaporating drops . . . . .	26
2.4	Multicomponent droplets . . . . .	30
<b>3</b>	<b>Droplet shape and internal flow quantification method</b>	<b>38</b>
3.1	Overview . . . . .	38
3.2	Materials . . . . .	39
	Chemicals. . . . .	39
	Liquid mixtures. . . . .	39
	Tracer particles. . . . .	40
	Smooth hydrophilic substrates. . . . .	40
	Porous hydrophilic substrates. . . . .	42
	Syringe and needle cleaning. . . . .	42
3.3	Experimental setup . . . . .	43
	3.3.1 Ambient humidity control . . . . .	43
	3.3.2 Contact angle measurements . . . . .	45
	3.3.3 Micro-Particle Image Velocimetry data acquisition . . . . .	46
3.4	Micro Particle Image Velocimetry data analysis . . . . .	47
	3.4.1 Adaptive interrogation window size method . . . . .	47

## CONTENTS

---

3.4.2	Velocity profiles . . . . .	47
3.4.3	Correction to the $\mathbf{z}$ location of the velocity . . . . .	48
3.4.4	Surface tension gradients . . . . .	49
<b>4</b>	<b>Marangoni contraction versus autophobing</b>	<b>51</b>
	Citation and credit: . . . . .	51
	Title: . . . . .	51
	Authors: . . . . .	51
	Contribution: . . . . .	51
4.1	Abstract . . . . .	52
4.2	Introduction . . . . .	52
4.3	Results and Discussion . . . . .	53
4.3.1	Marangoni contraction . . . . .	53
4.3.2	Autophobing . . . . .	56
4.3.3	Effect of the molecular structure . . . . .	59
4.4	Conclusion . . . . .	61
4.5	Experimental methods . . . . .	62
4.5.1	Contact angle measurements . . . . .	62
4.5.2	Surface tension measurements . . . . .	63
4.5.3	Micro-particle image velocimetry measurements . . . . .	63
4.5.4	Ellipsometry measurements . . . . .	64
4.6	Acknowledgement . . . . .	65
4.7	Supporting Information . . . . .	65
4.7.1	Contact angle measurements . . . . .	65
4.7.2	Micro-particle image velocimetry measurements . . . . .	66
4.7.3	Ellipsometry measurements . . . . .	66
4.7.4	Marangoni contraction scaling law . . . . .	66
4.7.5	Estimate of molecular size . . . . .	68
<b>5</b>	<b>Compositional Evolution of Marangoni-contracted drops</b>	<b>70</b>
	Citation and credit: . . . . .	70
	Title: . . . . .	70
	Authors . . . . .	70
	Contribution: . . . . .	70
5.1	Abstract . . . . .	70
5.2	Introduction . . . . .	71
5.3	Experiments . . . . .	73
5.4	Lubrication theory . . . . .	75

5.5	Numerical simulations . . . . .	80
5.6	Conclusion . . . . .	81
5.7	Acknowledgements . . . . .	82
5.8	Supplementary materials . . . . .	82
5.8.1	Experimental method . . . . .	82
5.8.2	Contact angle measurements . . . . .	85
5.8.3	Micro particle image velocimetry analysis . . . . .	85
5.8.4	Velocities and surface tension gradients . . . . .	86
5.8.5	Lubrication theory with bulk solutes . . . . .	88
	Problem formulation. . . . .	88
	Hydrodynamic fluxes and height evolution . . . . .	90
	Compositional evolution . . . . .	91
	Limit I — $\epsilon_\phi \ll \epsilon_h$ . . . . .	93
	Limit II — $\epsilon_\phi \sim \epsilon_h$ . . . . .	94
	Limit III — $\epsilon_\phi \gg \epsilon_h$ . . . . .	96
<b>6</b>	<b>Liquid-Liquid phase separation</b>	<b>101</b>
	Citation and credit: . . . . .	101
	Title: . . . . .	101
	Authors: . . . . .	101
	Contribution: . . . . .	101
6.1	Abstract . . . . .	101
6.2	Introduction . . . . .	102
6.3	Experimental setup and system . . . . .	103
6.4	Abrupt spreading . . . . .	105
6.5	Impact of phase separation on spreading . . . . .	106
6.6	Impact of surface forces on phase separation . . . . .	109
6.7	Preferential wetting in the two-phase region . . . . .	111
6.8	Discussion and conclusions . . . . .	113
6.9	Acknowledgements . . . . .	114
6.10	Materials and Methods . . . . .	114
	6.10.1 Preparation of the substrate . . . . .	114
	6.10.2 Preparation of the binary mixture . . . . .	115
	6.10.3 Preparation of two mutually saturated phases . . . . .	115
	6.10.4 Measurements of liquid viscosity, surface tension and contact angle . . . . .	116
	6.10.5 Observation of the main droplet . . . . .	116
	6.10.6 On-site ellipsometric measurements of the precursor film	117

## CONTENTS

---

6.11	Supplementary Information . . . . .	117
6.11.1	Supplementary Videos . . . . .	117
6.11.2	Supplementary Figures and Table . . . . .	118
<b>7</b>	<b>Dynamics of spreading and imbibition of Marangoni-contracted drops on porous substrates</b>	<b>125</b>
	Citation and credit: . . . . .	125
	Title: . . . . .	125
	Authors: . . . . .	125
	Contribution: . . . . .	125
7.1	Introduction . . . . .	125
7.2	Experimental methods . . . . .	128
7.3	Results and Discussion . . . . .	131
7.3.1	Dynamics of the drop . . . . .	132
7.3.2	Dynamics of the imbibition front. . . . .	136
7.3.3	Internal flow. . . . .	140
7.3.4	Drop motion in inhomogeneous atmospheres. . . . .	142
7.4	Conclusion. . . . .	143
<b>8</b>	<b>Conclusion and perspectives</b>	<b>145</b>
8.1	Main results . . . . .	145
8.1.1	Marangoni contraction and autophobic wetting regimes	145
8.1.2	Taylor dispersion in thin liquid films . . . . .	146
8.1.3	Liquid-liquid phase separation and wetting dynamics .	147
8.1.4	Marangoni contraction over porous substrates . . . . .	147
8.2	General conclusions and perspectives . . . . .	148
	<b>Bibliography</b>	<b>150</b>

# Chapter 1

## Introduction

### 1.1 Motivation

The motion of a liquid over a solid surface is a process that takes place in every day life situations. A wide variety of examples are found from natural phenomena to technological applications. For example in biological fluids as nectar plants, rain, and blood (Bohn et al., 2004; Snoeijer et al., 2013; Brutin et al., 2010), in beverages like coffee and wine (Deegan et al., 1997; Venerus et al., 2015), in materials for artistic techniques as paints, inks, resins, and coatings (Baglioni et al., 2013; Abdulsalam et al., 2015; Zenit, 2019), in engineering applications such as coating, semiconductor fabrication, and irrigation (Overdiep, 1986; Leenaars et al., 1990; March et al., 2016).

In such systems, inducing or preventing modifications to the solid surface due to the liquid motion is important. Examples of these are found in pattern collapse on microelectronics and in lubrication (Tanaka et al., 1993; Reynolds, 1886). Likewise, motion manipulation of such liquids is of interest. For instance, in microfluidics (Squires et al., 2005).

Liquids wet, dewet, pin or unpin over solid surfaces. Thus, the motion is limited by the solid-liquid-vapor contact line. The dynamics of the contact line is determined by molecular interactions and hydrodynamics, making it a multi-scale problem (Blake, 2006; Snoeijer et al., 2013). The contact line motion is affected by the liquid composition, the solid surface topography and chemical composition, the liquid and surface temperatures, the atmospheric conditions, and by external forces such as gravitational and electric.

Generally, liquids consists of mixtures of multiple components with differ-

ent physical and chemical properties (Lohse et al., 2020). In these systems, complex phenomena arises, for instance the formation of ‘tears’ in a glass full of wine (Venerus et al., 2015). The responsible of these phenomena are compositional or thermal gradients that form when the system is out of equilibrium. At the same time, these gradients induce flows that advect the compositional field. Due to the complexity, the coupling of wetting with this mechanisms is not fully understood.

In this work, we study the influence of compositional gradients on moving contact lines. Marangoni contracted drops, which are important in technological applications, serve as the model system. These are evaporating drops composed of two miscible liquids that dewet surfaces that the pure liquids individually would completely wet. The focus is in the coupling of the macroscopic shape of the drop, the drop evaporation in ambient atmospheres, the flow and the compositional field inside the drop.

## 1.2 Objectives and approach

This work focuses on the study of fundamental aspects of the motion of solid-liquid-vapor contact lines when compositional gradients in the liquid phase are present. We study the wetting mechanisms of Marangoni-contracted drops, as a model system. The droplet behavior is investigated by experiments that allow for a control of the ambient conditions, simultaneous macroscopic observations, and micro-PIV. Quantification of the relations between the macroscopic drop shape, the velocity of the internal flows, the liquid composition, and the atmospheric conditions provide a better understanding of the wetting mechanism and the mass transport.

The main objectives, with the corresponding approach, of this thesis are:

- Objective 1: Understand which is the mechanism or mechanisms responsible of the wetting behavior of flows with compositional gradients.

Approach: Systematic experimental study of Marangoni contracted drops on high energy surfaces. The drop shape and the internal flows are measured for different liquid compositions and atmospheric conditions.

- Objective 2: Understand how the compositional field affects the wetting dynamics.

Approach: Calculation of the surface tension gradients from the velocity fields obtained experimentally in drops of different liquid composition on different atmospheric conditions, for comparison with theoretical models.

- Objective 3: Determine the impact of liquid-liquid phase separation on moving contact lines.

Approach: Systematic experimental study of drops of binary liquid mixtures that present phase separation at critical temperatures, over heated surfaces.

- Objective 4: Determine how compositional gradients drive contact lines over heterogeneous solid surfaces.

Approach: Systematic experimental study of the spreading of Marangoni contracted drops over porous surfaces. The drop shape and the imbibition length were measured for different atmospheric conditions.

### 1.3 Outline of the thesis

This thesis has 8 chapters, including the present one.

In Chapter 2, the fundamental theories of wetting phenomena are presented, as well as many relevant studies on the field are mentioned.

In Chapter 3 the experimental method used in this work (setup, data acquisition, and data analysis) is described.

In Chapter 4 two wetting regimes are studied. Experimental observations of water - 1,2-Hexanediol drops over smooth high energy surfaces for different concentrations and ambient humidities are presented. Measurements with  $\mu$ PIV technique and with ellipsometry reveal two distinct wetting regimes governed by different mechanisms.

In Chapter 5, the coupling between drop shape, internal flows, compositional field, and evaporation of Marangoni contracted drops is explored. Experiments of water-diol drops over smooth high energy surfaces for different diols, concentrations, and ambient humidities are presented. The agreement between measurements of velocity fields of the internal flows and surface tension gradients of water-diol mixtures to simulations shows the mechanism

### 1.3. OUTLINE OF THE THESIS

---

responsible of the evolution of the compositional field, and thus of the overall drop evolution.

In Chapter 6, the interplay between phase separation and wetting on Marangoni contracted drops is studied. Systematic experimental observation on the shape of water-glycol ether drops over heated and smooth high energy surfaces show that liquid-liquid phase separation changes the wetting behavior. Ellipsometric measurements show the mechanism that initiates the earlier the phase separation in the precursor film around the main drop.

In Chapter 7, the dynamics of spreading of Marangoni contracted drops over porous medium is studied. Experiments of water drops on atmospheres with 2-Propanol vapor content are presented. Observations on the drop shape and the imbibition film show a difference of wetting behavior from pure liquid drops on porous surfaces.

In Chapter 8, a general conclusion of the thesis is provided and an outlook is given.

# Chapter 2

## Overview: Wetting

When a liquid is placed on a solid surface surrounded by a gas, the transition line that divides the wet and the dry regions on the solid is called the three-phase contact line (Figure 2.1(a)). The behavior of this line is determined, at first, by surface and interfacial interactions (Gennes et al., 2004; Snoeijer et al., 2013). For example, by surface tensions. The surface tension originates, from a molecular point of view, from the attraction forces between the molecules in each phase. At the interface, the molecules experience an anisotropic cohesive force in the normal direction to the surface (Figure 2.1(b)), compared to the ones in the bulk, resulting in an excess of stress at the surface (Gennes et al., 2004). Thus, the surface tension is defined as the force acting across the interface per unit length, parallel to the surface. Or, it can also be defined as the Gibbs energy per area at the surface, when considering the thermodynamic work needed to increase the surface area.

In the presence of wet and dry regions on a solid surface, there is a surface tension for each interface separating two phases:  $\gamma_{SG}$  for solid-gas,  $\gamma_{SL}$  for solid-liquid, and  $\gamma$  for liquid-gas interfaces. Instead of the gas phase, it can also be a vapor phase. With this, the spreading parameter, defined as  $S = \gamma_{SG} - (\gamma_{SL} + \gamma)$ , compares the surface energy per unit area of the substrate when it is wet and dry (Gennes et al., 2004). The spreading parameter  $S$  allows to distinguish between two different wetting behaviors (Figure 2.1(c)). When  $S < 0$ , the solid surface is partially wet. In this regime, the liquid does not spread but adopts a static equilibrium shape on the solid. Contrary for  $S > 0$ . The liquid completely wets the solid surface. Mostly, under this regime, the equilibrium is reached in a long period of time. At the end, the

## 2.1. STATIC CONTACT LINES

---

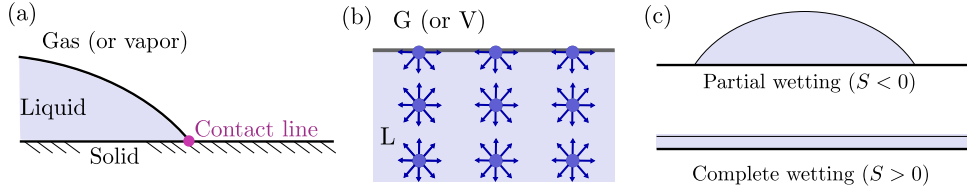


Figure 2.1: (a) Cross-sectional sketch of the region near a solid-liquid-gas (or vapor) contact line. (b) Schematic representation of the attractive interactions between liquid molecules near a liquid-gas (or vapor) interface. (c) Sketch of the two different wetting behaviors, characterized by the spreading parameter  $S$ .

liquid forms a thin film. During this period, a dynamic process takes place. To describe the contact line behavior, this chapter I divided it in static and dynamic cases. It has been shown that dynamic contact lines are also affected by other processes, besides molecular interactions, taken on the liquid and the vapor phase, these are also presented here in this chapter.

## 2.1 Static contact lines

Placing the liquid on a solid surface, the liquid-vapor interface forms a macroscopic contact angle  $\theta_{\text{app}}$  with respect to the solid-liquid interface at the contact line, measured inside the liquid phase (Figure 2.2(a)). According to Young's law (Young, 1805), there is a static equilibrium resulting from the balance of the components of the surface tensions parallel to the substrate acting on the contact line:

$$\gamma \cos \theta_{\text{eq}} = \gamma_{SV} - \gamma_{SL}, \quad (2.1)$$

with  $\theta_{\text{eq}}$  as the value of the contact angle at equilibrium, and the surface tensions as constant properties of the interfaces. Even though it is a well accepted model, it is not practical from an experimental point of view (Dusan V., 1979; Gennes, 1985; Bonn et al., 2009; Brutin et al., 2018). The first problem encountered is that there are not direct methods to determine  $\gamma_{SV}$  and  $\gamma_{SL}$ . Secondly, the static contact angle has shown not to have a unique value, even under exact same material configurations, which is commonly known as contact angle hysteresis. There have been several attempts to justify and understand these experimental observations. The most common

ones referred to the equilibrium conditions of the liquid and vapor phases, the roughness and chemical inhomogeneities of the solid surface, and the presence of solutes in the liquid phase as contaminants. Thus, the main aspect to consider is that Eq. 2.1 is derived for pure liquids in thermodynamic equilibrium with its own vapor on a smooth and rigid surface.

In most experimental situations, the liquid and vapor phases are out of equilibrium. This can be deduced (Sharma, 1998; Brutin et al., 2018) by considering the chemical equilibrium between the molecules in both phases, which follows Kelvins equation (Thomson, 1871; Barnes et al., 2011):

$$\ln\left(\frac{p_s}{p_e}\right) = \frac{V_m}{RT}(\Delta p) \quad (2.2)$$

where  $p_s$  is the pressure of saturated vapor at temperature  $T$ ,  $p_e$  is the equilibrium pressure of the vapor with the liquid,  $V_m$  is the molar volume of the liquid,  $R$  is the gas constant, and  $\Delta p$  is the pressure change in the liquid due to interfacial forces. Considering that the pressure difference is higher inside the liquid than outside when the interface is concave towards the liquid,  $\Delta p < 0$ . Thus, the condition for equilibrium is  $p_e > p_s$ . According to Laplace equation (Genies et al., 2004; Barnes et al., 2011), which defines the equilibrium, the pressure difference  $\Delta p$  balances the pressure exerted by the surface tension  $\gamma$ , known as the capillary pressure,

$$\Delta p = \gamma\kappa, \quad (2.3)$$

where  $\kappa$  is the mean curvature of the interface. Hence, the curvature of the liquid interface, which affects the apparent contact angle (Churaev, 1995), reaches equilibrium at oversaturated vapor conditions. Note that when a liquid film is present, like in complete wetting or when vapor molecules adsorbed at a high energy solid surface, the pressure change  $\Delta p$  includes a term that accounts for the molecular interactions between the solid and vapor, known as the disjoining pressure  $\Pi$  (Derjaguin et al., 1978; Wayner, 1991). Together with the capillary pressure, both define the equilibrium condition. The derived condition is not fulfilled within most experimental frames, thus the system is out of equilibrium.

Another aspect affecting the system is that most of the solid surfaces are not completely flat and have roughness in the nano and micrometer scales (Dussan V., 1979). Also chemical inhomogeneities might be present (Quéré, 2008). Over these defects, contact lines tend to pin and do not move

## 2.1. STATIC CONTACT LINES

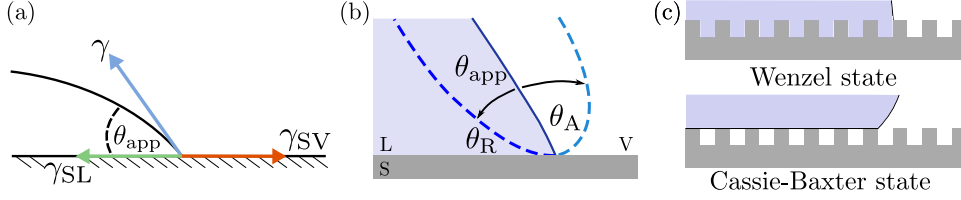


Figure 2.2: (a) Schematic representation of the surface tensions (arrows) at the three-phase contact line and the apparent contact angle  $\theta_{app}$  that the free interface makes with the solid surface. (b) Sketch of the advancing angle  $\theta_A$ , which is the angle formed when the contact line moves towards the vapor phase, and the receding angle  $\theta_R$ , when it moves towards the liquid phase.  $\theta_{app}$  lies between  $\theta_A$  and  $\theta_R$ . (c) Sketches of a liquid over a textured solid surface, showing two different configurations: the Wenzel state, when the liquid fills the grooves on the solid, and the Cassie-Baxter state, when vapor is trapped below the liquid.

further. This leads to a contact angle hysteresis, where the static contact angle is not unique. When depositing the liquid on the solid surface,  $\theta_{app}$  lies in an interval between a maximum and a minimum defined by an advancing or receding contact line, respectively (Figure 2.2(b)). A contact line is considered to advance when it moves towards the vapor phase. Just before it moves,  $\theta_{app}$  reaches a value called the advancing contact angle  $\theta_A$ . In the same way, the receding angle  $\theta_R$  is defined just before the contact line moves towards the liquid phase. That is to say, the static contact angle highly depends on the way the liquid is deposited. The difference between these two angles is the contact angle hysteresis,  $\Delta\theta = \theta_A - \theta_R$ . The apparent contact angle  $\theta_{app}$ , and thus  $\Delta\theta$ , are affected by the surface roughness in accordance with Wenzel (1936) model (Figure 2.2(c))

$$\cos \theta_{app} = r \cos \theta_{eq}, \quad (2.4)$$

with  $r$  as the roughness factor given by the ratio between the area of the actual solid-liquid interface and the area of the solid surface if it was flat (Gennes et al., 2004). If  $r < 1$ ,  $\theta_{eq} < 90^\circ$ , ie. the system will be in partial wetting, whereas  $r > 1$ ,  $\theta_{eq} > 90^\circ$ , the liquid wets less. In Wenzel model, it is assumed that the solid below the liquid is in complete contact with the liquid but there are cases when vapor is trapped between the defects (Figure 2.2(c)). These two situations are known as Wenzel and Cassie-Baxter states, respectively.

When the liquid is in Cassie-Baxter state (Cassie et al., 1944; Cassie, 1948), some fraction of the solid under the droplet is still in contact with vapor,  $\theta_{\text{app}}$  is given by

$$\cos \theta_{\text{app}} = -1 + f(\cos \theta_{\text{eq}} + 1), \quad (2.5)$$

where  $f$  is the fraction of the solid in contact with the liquid (Gennes et al., 2004). Microscopically, the Cassie-Baxter state involves many contact lines on the asperities of the surface. Because Cassie-Baxter state is a metastable state and it is less energetically favorable than Wenzel state (Quéré, 2008), the transition between Wenzel to Cassie-Baxter can be induced with small perturbations, for instance with vibrations, evaporation, air diffusion, and impact (Lv et al., 2014; Brutin et al., 2018). For chemical heterogeneous surfaces (Gennes et al., 2004), Cassie-Baxter equation gives a relation in a similar way for  $\theta_{\text{app}}$  when the solid has a fractional coverage of one material,  $f_1$ , and a second material,  $f_2$ ,

$$\cos \theta_{\text{app}} = f_1 \cos \theta_1 + f_2 \cos \theta_2. \quad (2.6)$$

As shown, defects modify the wetting properties of solid surfaces. In material and wetting science, this is used to tailor surface wettability (Hao et al., 2016).

## 2.2 Dynamic contact lines

There are two ways of inducing contact line motion. One is by applying an external force to the three-phase contact line system (forced wetting). The other way is when a liquid is spreading on a solid surface, driven by pure capillary forces. In both cases, the system is out of equilibrium and Young's equation (Eq. 2.1) no longer applies (Gennes et al., 2004). Instead, different physical aspects are involved at different scales, and the angle that the free interface makes with the substrate is locally dependent.

To describe the wetting dynamics out of equilibrium, the macroscopic angle that the free interface makes with the solid surface, is generally used. It is known as dynamic or apparent contact angle,  $\theta_{\text{app}}$ , and there is no general equation that determines it. For forced wetting,  $\theta_{\text{app}}$  depends monotonically on the velocity (direction and speed) of the contact line,  $\vec{U}$ , as shown qualitatively in Figure 2.3(a). For spreading, a liquid volume is deposited on a solid surface forming a drop with  $\theta_{\text{app}}$  decreasing, while the drop's foot print

## 2.2. DYNAMIC CONTACT LINES

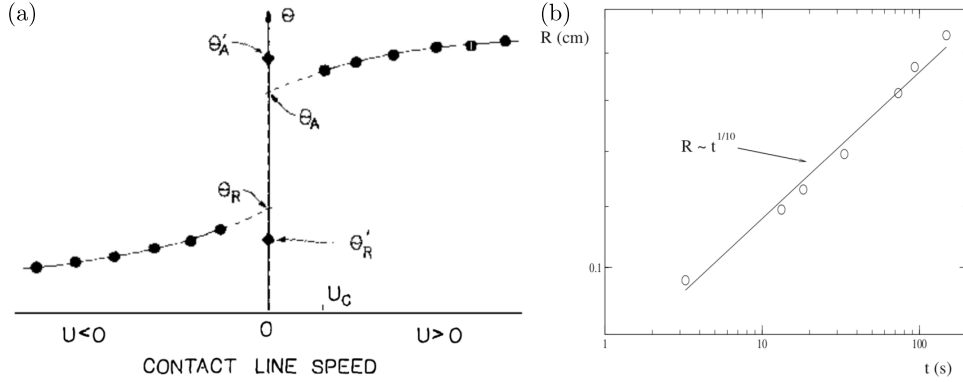


Figure 2.3: (a) Representation of typical experimental measurements of the apparent contact angle  $\theta$  with respect to the velocity of the contact line  $U$  in partial wetting systems (Taken from Dussan V., 1979).  $U < 0$  corresponds to a receding contact line and  $U > 0$  for an advancing contact line.  $\theta_R$  and  $\theta_A$  are the receding and the advancing angles, respectively. (b) The temporal evolution of the radius  $R$  of a spreading drop for a complete wetting system (Taken from Bonn et al., 2009). The radius follows tanners law  $R \sim t^{1/10}$ .

increases, until reaching equilibrium, characterized by  $\theta_{\text{eq}}$ . For complete wetting this implies  $\theta_{\text{eq}} = 0$ . If the drops are small, ie.  $R \ll \ell_\gamma$ , with  $R$  as the radius of the drop base,  $\ell_\gamma = \sqrt{\gamma/g\rho}$  as the capillary number,  $\rho$  as the liquid density, and  $g$  as the acceleration of gravity, the drop shape is determined only by surface tension, and the contributions from gravity are negligible. In this regime, the drop shape can be approximated to a spherical cap. For small drops in complete wetting of non-volatile viscous liquids, the rate of spreading follows the power law

$$\theta_{\text{app}} \sim t^{-3/10}, \quad (2.7a)$$

$$R \sim t^{1/10} \quad (2.7b)$$

known as Tanner's law after L. Tanner's (1979) experimental work on silicone oils (Figure 2.3(b)). Its theoretical derivation can be found in Gennes et al. (2004), Gennes (1985), and Bonn et al. (2009). Tanner's law showed that the spreading rate is independent of the spreading parameter  $S$ , ie. it is independent of the available surface energy.

The origin of  $\theta_{\text{app}}$  and the source of energy dissipation for a moving contact line is debated between two theories (Gennes et al., 2004, Chap-

ter 6; Snoeijer et al., 2013; Blake, 2006; Gennes, 1985; Bonn et al., 2009); the molecular-kinetic theory (MKT) and the hydrodynamic theory.

**Molecular-kinetic theory.** MKT was developed by Blake and Haynes (1969), and it is based on chemical reaction rate theory for condensed phases (Hänggi et al., 1990; Wynne-Jones et al., 1935). In MKT it is assumed that the solid surface has adsorption sites that can be occupied by liquid molecules (Figure 2.4). When a liquid is in contact with a solid surface, a large number of adsorption sites are occupied by the liquid molecules and others not, the three-phase contact line defines the transition between the two adsorption conditions. Liquid molecules displace over the solid in the region near the contact line either by surface migration or from the bulk. The frequency of molecular displacement parallel to the surface is  $K = K_0 \exp(-\Delta G^*/Nk_B T)$ , where  $K_0 = k_B T/h \sim 10^{13}$  Hz is the thermal frequency for molecular motion,  $k_B = 1.3 \times 10^{-23}$  J · K<sup>-1</sup> is the Boltzmann constant,  $T$  is the absolute temperature,  $h = 6.6 \times 10^{-34}$  J · s is the Planck constant,  $\Delta G^*$  is the activation free energy, and  $N = 6.022 \times 10^{23}$  mol<sup>-1</sup> is the Avogadro number. At equilibrium, the net rate of molecular displacements is zero. Out-of-equilibrium, it is determined by the rate of displacements in forward and reverse directions  $K_{\pm}$ . The total displacement of the contact line results from the favored direction, with a speed  $U = \lambda(K_+ - K_-)$ , where  $\lambda$  is the average distance between centers of adsorption sites. To induce contact line motion, a driving force is needed to provide energy in the form of work. This force increases and reduces the activation free energy in the forward and reverse directions by the same amount,  $K_{\pm} = K_0 \exp(-\Delta G^*/Nk_B T \pm w/2nk_B T)$ , where  $w$  is the work per unit area of the driving force, and  $n$  is the number of sites per unit area on the solid at which the work is dissipated. The amount of work done by the driving force is equal to the unbalanced surface tension force acting at the contact line,  $w = \gamma(\cos \theta_{\text{eq}} - \cos \theta)$ . From this, it is obtained that the contact line moves with an average speed

$$U = 2K\lambda \sinh \left[ \frac{\gamma(\cos \theta_{\text{eq}} - \cos \theta)}{2nk_B T} \right]. \quad (2.8)$$

Eq. 2.8 is applicable for flat surfaces. A similar analysis is done for heterogeneous surfaces, obtaining a modified equation (Rolley et al., 2007).

According to MKT, the energy dissipation occurs at this level due to the adsorption of the liquid molecules on the solid surface at the moving contact

## 2.2. DYNAMIC CONTACT LINES

---

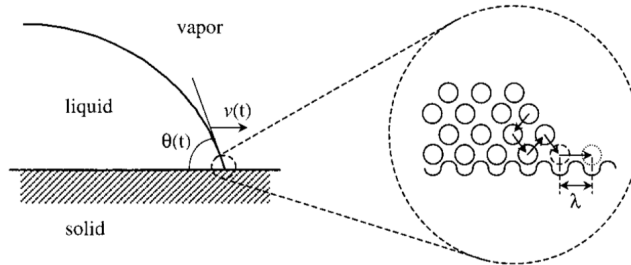


Figure 2.4: Schematic representation of a moving contact line according to the molecular-kinetic theory (MKT, taken from Ruijter et al., 1999).

line (Ruijter et al., 1999; Blake, 2006). From a first approximation of Eq. 2.8, it is obtained

$$U = \gamma(\cos \theta_{\text{app}} - \cos \theta) / \xi, \quad (2.9)$$

with  $\xi = nk_B T / K \lambda$  as a friction coefficient per length of the contact line. This result considers that the dissipation happens only in the zone close to the contact line. Moreover, it establishes that the contact angle is determined by capillary forces and dissipation from a friction with the solid surface.

MKT has received several critiques. While it has shown to be consistent for some experimental observations in terms of the contact angle-velocity dependence, for others it does not apply (Blake, 2006; Petrov et al., 2003; Rolley et al., 2007). It is commonly accepted that the MKT works for small capillary numbers (Petrov et al., 2003; Snoeijer et al., 2013). At the same time, it is not clear if the model should consider the dynamic contact angle  $\theta$  in Eq. 2.9 as a microscopic angle. Even, it is not clear which is the mechanism of the displacement of the molecules at the contact line. A gradient of the chemical potential in the liquid at the solid-liquid interface has been proposed as the origin (Ruckenstein et al., 1977). Also, the model ignores the dissipation due to the flow. Although a relation between  $K$  and the viscosity has been proposed, MKT lacks a connection to the hydrodynamics of the system.

**Hydrodynamic theory.** To describe the hydrodynamics of the three-phase contact line motion, two approximations are considered (Huh et al., 1971). One is the Stokes or creeping flow approximation (Huh et al., 1971; Dussan V. et al., 1974; Snoeijer et al., 2014). And the other where in addition the lubrication approximation is applied (Oron et al., 1997). The latter

is generally used for describing the dynamics of thin films and drops with small contact angles. For the interest of this work, the focus will be on this. In the lubrication, or long-wave approximation, an asymptotic analysis is done by considering the dynamical and geometrical aspects of the system. This method was proposed by Reynolds in his theoretical work in 1886, motivated by previous experiments on lubrication of bearings. It is applied to incompressible flows. First, it is considered that the inertial force can be neglected when comparing it with the viscous force, ie. for  $Re \ll 1$ , with  $Re = \rho U_o D / \mu$  as the Reynolds number,  $\rho$  the density of the fluid,  $U_o$  the characteristic velocity of the system,  $D$  the characteristic length, and  $\mu$  the viscosity of the fluid. Secondly, the length of the flow is much larger than its thickness. Thus, the flow is mainly parallel to the major axes. By considering the above aspects, the Stokes and the continuity equations,

$$\mu \nabla^2 \vec{u} - \vec{\nabla} p = 0, \quad (2.10a)$$

$$\partial_t \rho + \vec{\nabla} \cdot (\rho \vec{u}) = 0, \quad (2.10b)$$

respectively, reduce to a simpler system of equations (Kundu et al., 2012, Subchapter 8.3; Oron et al., 1997). In two dimensions and with no external force, these are:

$$\mu \partial_z^2 u_x - \partial_x p = 0, \quad (2.11a)$$

$$-\partial_z p = 0, \quad (2.11b)$$

$$\partial_x u_x + \partial_z u_z = 0, \quad (2.11c)$$

where  $u_x$ ,  $u_z$ ,  $p$  are the velocity components in the horizontal and vertical directions, and the pressure in the fluid, respectively. The system 2.11 can be integrated in the perpendicular direction of the flow given the pressure and velocity boundary conditions.

For a fluid bounded with a solid surface from one side and a vapor from the other (Figure 2.5), no-slip and no-flux boundary conditions applied at the solid-liquid interface ( $u_x|_{z=0} = 0$ ,  $u_z|_{z=0} = 0$ ), but the shape of the free interface,  $h(x, t)$ , should be determined as part of the problem. From conservation of mass, an evolution equation for the thickness of the film is obtained by considering that a change on the film height on a domain corresponds to the net inflow:

$$\partial_t h + \partial_x Q = 0, \quad (2.12)$$

## 2.2. DYNAMIC CONTACT LINES

---

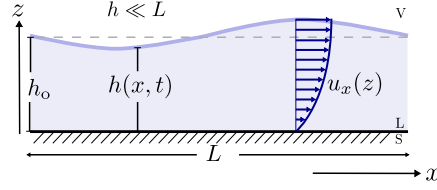


Figure 2.5: Cross-sectional sketch of a thin liquid film between a solid and a vapor. The lubrication approximation is applied when the characteristic length in the perpendicular direction to the flow motion is smaller than the characteristic length in the direction of the flow motion.

where  $Q = \int_0^h u_x(z) dz$  is the flux. Eq. 2.12 together with 2.11a result in the general lubrication equation, which shows the coupling of the interface shape with the flow in the film.

Eq. 2.11b implies that the pressure is uniform along the  $z$  direction and it just depends on  $x$ . Thus,  $p$  is imposed by the condition at the free interface. Assuming the capillary pressure as the boundary condition for the pressure at the interface,  $p = \gamma \partial_x^2 h$ . Integrating 2.11a two times with respect to  $z$ , using the no-slip ( $u_x|_{z=0} = 0$ ) and the Marangoni (shear stress,  $\partial_x \gamma = \mu \partial_z u_x|_{z=h}$ ) boundary conditions, and replacing the obtained expression for  $u_x$  in the flux, Eq. 2.12 becomes

$$\partial_t h + \frac{1}{\mu} \partial_x \left[ -\frac{h^3}{3} \partial_x (\gamma \partial_x^2 h) + \frac{h^2}{2} \partial_x \gamma \right] = 0. \quad (2.13)$$

When surface tension gradients are neglected, 2.13 simplifies to

$$\partial_t h - \frac{\gamma}{3\mu} \partial_x (h^3 \partial_x^3 h) = 0. \quad (2.14)$$

In the case of a film or a drop with a moving contact line, a problem arises when finding the solution. When considering the no-slip condition, a discontinuous velocity field is obtained at the contact line. The theoretical proof can be found in the work of Dussan V. and Davis (1974). A mathematical, but not realistic, implication of the discontinuous field is that the force exerted by the fluid on the solid surface diverges logarithmically near the contact line, ie., an infinite force would be required for the contact line to move. To remove this singularity, several approaches have been proposed. One is to solve the problem up to a limiting small scale, where the hydrodynamics work (Voinov, 1976). In a different approach, a Navier slip (Lauga

et al., 2008) condition is allowed near the contact line, where it is assumed that the slip is proportional to the shear stress,  $u_x|_{z=0} = \beta \partial_z u_x|_{z=0}$ , (Huh et al., 1971; Dussan V., 1976; Hocking, 1976). Details on these or other methods can be found in Dussan V. (1979), Oron et al. (1997), Blake (2006), Bonn et al. (2009), and Snoeijer et al. (2013). In any case, a full solution that covers all relevant length scales is not obtained, instead, the solutions at the different scales are coupled.

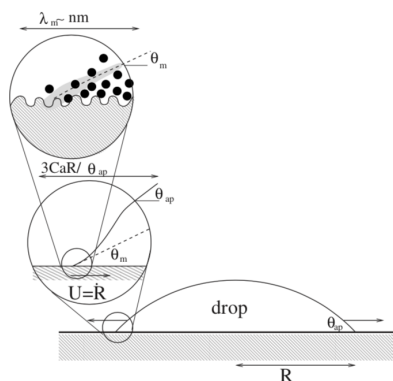


Figure 2.6: Schematic representation of a moving contact line according to the hydrodynamic model (Taken from Bonn et al., 2009). The interface in the intermediate region between the microscopic and macroscopic regions is highly curved due to the viscous bending.

To solve Eq. 2.17 one can assume a traveling wave with a constant speed  $V$  at the free interface. The shape of the interface can be expressed as  $H(Vt - x)$  from the co-moving frame. By defining  $\xi = Vt - x$  and using Eq. 2.17 in the co-moving frame, the evolution equation for the film height is

$$\partial_t H(\xi) - \frac{\gamma}{3\mu} \partial_x [[H(\xi)]^3 \partial_x^3 H(\xi)] = 0. \quad (2.15)$$

After applying the chain rule for the partial derivatives of  $H(\xi)$ , Eq. 2.15 becomes

$$V \partial_\xi H(\xi) + \frac{\gamma}{3\mu} \partial_\xi [[H(\xi)]^3 \partial_\xi^3 H(\xi)] = 0. \quad (2.16)$$

Considering that the total flux is zero in the co-moving frame, the integration of Eq. 2.16 over  $\xi$ , and dividing the result with  $[H(\xi)]^3$ , leads to

$$\frac{V}{[H(\xi)]^2} - \frac{\gamma}{3\mu} \partial_\xi \partial_\xi^3 H(\xi) = 0. \quad (2.17)$$

## 2.2. DYNAMIC CONTACT LINES

---

Rearranging terms, and using  $h$  as the notation for the film height in the co-moving frame, the governing equation for the film height reduces to

$$\partial_x^3 h - \frac{3Ca}{h^2} = 0. \quad (2.18)$$

$Ca = \mu V/\gamma$  is the capillary number, which compares the viscous forces with the surface tension forces. The derivation of the similarity solution, Eq. 2.18, can be found in Oron et al. (1997) and Bonn et al. (2009). Eq. 2.18 is independent of time, and it represents the balance between the capillarity (first term) and the viscous stresses (second term). From this, it is possible to see that even though the velocity field does not appear, the viscous stresses diverge in the limit when  $h \rightarrow 0$ . The details on the solution of Eq. 2.18 differ between systems and the approach followed to remove the singularity.

An illustrative solution is the one obtained by Voinov (1976) and Cox (1986). Given the ansatz for Eq. 2.18 in an asymptotic expansion in the outer region, which corresponds to the hydrodynamic regime, the solution has the form

$$\partial_x h(x) \approx \theta(x) \simeq [9Ca \ln(x)]^{1/3}. \quad (2.19)$$

This equation shows the viscous bending of the interface, ie. the logarithmic dependence of the interface shape with the distance to the contact line (Figure 2.6). Thus, for the hydrodynamic model the energy dissipation (per unit time and unit length) happens at this level, due to the viscous bending (Gennes et al., 2004, Chapter 6; Bonn et al., 2009), and it is given by

$$D_{\text{visc}} \sim \iint \mu \partial_z u_x dx dz \sim \frac{\mu U_0^2}{\theta_{\text{app}}} \int \frac{dx}{x}. \quad (2.20)$$

At the microscopic region, the solution to Eq. 2.18 should result in the microscopic contact angle  $\theta_m$  at the contact line. Doing an asymptotic expansion for the interface shape for the inner region, which is the region close to the contact line, when  $h \rightarrow 0$ , up to the limiting small scale  $h_m$ , the solution obtained is

$$\theta(x) \sim \theta_m + \left[ 9Ca \ln \left( \frac{x}{h_m} \right) \right]^{1/3}. \quad (2.21)$$

Matching the solutions of the outer and the inner regions gives the solution for the entire interface shape, thus for the apparent contact angle, known as Cox-Voinov law,

$$\theta_{\text{app}} = \left[ \theta_m^3 + 9Ca \ln \left( \frac{h_o}{h_m} \right) \right]^{1/3}, \quad (2.22)$$

where  $h_o$  is the macroscopic length scale. Eq. 2.22 shows that the dynamic contact angle depends on the viscous bending of the free interface close to the contact line. This result was experimentally shown by Dussan V. et al. (1991) in a system with a different configuration but with a similar solution. Similar analysis have been extended for solid surfaces with roughness (Hocking, 1976) and for interfaces with large contact angles (Snoeijer, 2006).

The hydrodynamic model has been questioned by some aspects, most of them related to the methods used to solve the break down at the microscopic scale. At this level, microscopic models are required to introduce a length where the model fails and also to introduce the interaction with the solid surface. Some of these microscopic models lack of experimental evidence. Although good agreement with experimental observations of the free interface profile in the mesoscopic and macroscopic scales have been obtained, deviations for distances of few micrometers close to the contact line have been observed (Shen et al., 1998).

The discrepancies and successes of the hydrodynamic model and MKT have made considered a combined model, with questioned remarks, specially because they differ on the fundamental physics.

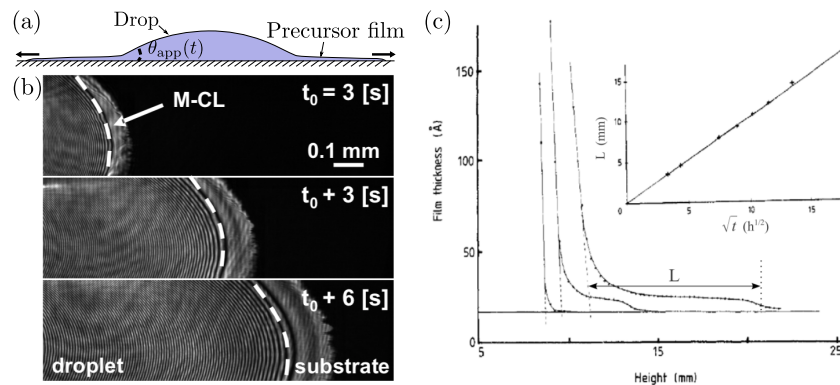


Figure 2.7: (a) Cross-sectional sketch of a spreading drop with a precursor film forming ahead of the drop. (b) Example of a precursor film developing ahead of a spreading drop (Taken from Hashimoto et al., 2012). Time-lapse images taken with a Brewster angle microscope. (c) Examples of the thickness profile ( $y$ -axes) of films developing ahead of a bulk fluid, placed on a vertical solid surface, with respect to the vertical distance to a referential point in the bulk fluid ( $x$ -axes) (Taken from Popescu et al., 2012).

A spatial case in dynamic contact lines is found in perfectly wetting liquid-

## 2.2. DYNAMIC CONTACT LINES

---

surface combinations. In these systems, precursor films are observed. These are microscopic films formed ahead of the spreading liquid which expand further than the bulk fluid (Popescu et al., 2012; Bonn et al., 2009) (Figure 2.7(a)). Their thickness varies from 10 to 100 nm, and at the edge form a zero angle with the solid surface. The precursor films can have two origins: i) through deposition of liquid from the vapor phase on the surface ahead of the drop of volatile liquids (Anderson et al., 1995; Ajaev, 2005), or ii) through a flow from the drop of nonvolatile liquids (Bangham et al., 1938; Cazabat et al., 1997). The first evidence of the film formation was given by Hardy et al. (1919), who measured the change in static friction caused by the film, by quantifying the resistance to slip of a watch-glass before and after depositing a drop on a clean glass surface. Afterwards, multiple experimental works confirmed the formation of the film by using different techniques, as interference microscopy (Bascom et al., 1964), Brewster angle microscopy (Hashimoto et al., 2012) (Figure 2.7(b)), ellipsometry (Bascom et al., 1964; Beaglehole, 1989; Feslot et al., 1989) (Figure 2.7(c)), electron microscopy (Radigan et al., 1974), electrical resistance measurements (Ghiradella et al., 1975), polarized reflection microscopy (Ausserré et al., 1986), phase-modulated interference microscopy (Kavehpour et al., 2003), atomic force microscopy (Xu et al., 2004), and epifluorescence inverted microscopy (Hoang et al., 2011).

Spreading of complete wetting systems are of particular interest from a fundamental point of view for the following reasons. Due to the formation of the precursor film, the spreading shows a behavior independent of the liquid-solid system, represented in Eq. 2.7. Mathematically, its presence removes the problems that appear in the hydrodynamic model at the contact line, ie. no singularity appears at the contact line. First, the microscopic contact angle is well known,  $\theta_m = 0$ . And second, the singularity at the edge of the bulk fluid can be removed by introducing a disjoining pressure  $\Pi(h)$  (Derjaguin et al., 1978). Again, by assuming a traveling wave with constant velocity  $V$  and solving Eq. 2.17, the governing equation reduces to a similarity form

$$\partial_x^3 h(x, t) - \frac{3Ca}{h^2} - \frac{3a^2}{h^4} \partial_x h = 0, \quad (2.23)$$

where  $a = A/6\pi\gamma$  is the microscopic length scale and  $A$  is the Hamaker constant (Bonn et al., 2009; Popescu et al., 2012; Snoeijer et al., 2013). The disjoining pressure is defined as  $\Pi(h) = \frac{d\omega}{dh}$ , such that  $\omega(h)$  is an effective potential that accounts for the molecular interactions between the solid-liquid and liquid-vapor interfaces due to the thickness of the film, and it contributes

to the interfacial free-energy. It is also required that  $\frac{d\omega}{dh}|_{h=l} = 0$ , with  $l$  as the thickness of the precursor film. Since the free interface has a nonzero thickness everywhere, there is no divergence on Eq. 2.23. A direct comparison between the experiments and theory on the precursor film profile in the full scale range has not been possible due to the limit of the resolution of the experimental techniques.

## 2.3 Dynamics of evaporating drops

Far below the boiling point, evaporation of liquids may occur in two distinct conditions: i) evaporation into vacuum or pure vapor, in absence of an inert atmosphere, or ii) into an ambient atmosphere. Since the early works of Maxwell (1877), Langmuir (1918), Hertz (1882), and Knudsen (1915), it is well known that the process limiting the interfacial transport of liquid molecules is different in each case. In pure vapor ambient, it is determined by a kinetic process (Cazabat et al., 2010; Lu et al., 2019), whereas in an ambient atmosphere, it is controlled by a diffusion process and, in a limit, by a buoyant convection in the gas phase (Langmuir, 1918; Carle et al., 2013; Lu et al., 2017). For the interest of this work, the focus will be on the case of evaporation in an ambient atmosphere without atmospheric convection. During evaporation, an exchange of molecules between the liquid interface and the gas phase occurs. Since the rate of exchange ( $\sim 10^{-10}$  s order of magnitude) is faster than the rate of diffusion ( $\sim 1$  s) (Popov, 2005), the region near the liquid interface saturates with vapor molecules. This creates a vapor density gradient from the interface to the far field (Figure 2.8(a)). The gradient induces a vapor mass flux, normal to the interface, governed by Fick's law of diffusion:

$$\vec{j} = -D_v \vec{\nabla} \rho_v. \quad (2.24)$$

$D_v$  is the diffusion coefficient of the vapor molecules in the ambient atmosphere and  $\rho_v$  is the vapor density.

The density profile follows the diffusion equation  $\nabla^2 \rho_v = D_v \partial_t \rho_v$ . On a quasi-stationary diffusion process, and in an isothermal limit, the time derivative is negligible, thus the diffusion equation reduces to the Laplace equation

$$\nabla^2 \rho_v \simeq 0. \quad (2.25)$$

The total evaporation rate (the evaporative mass loss per unit area per unit time) depends on the rate of diffusion, and it is derived by evaluating Eq. 2.24

### 2.3. DYNAMICS OF EVAPORATING DROPS

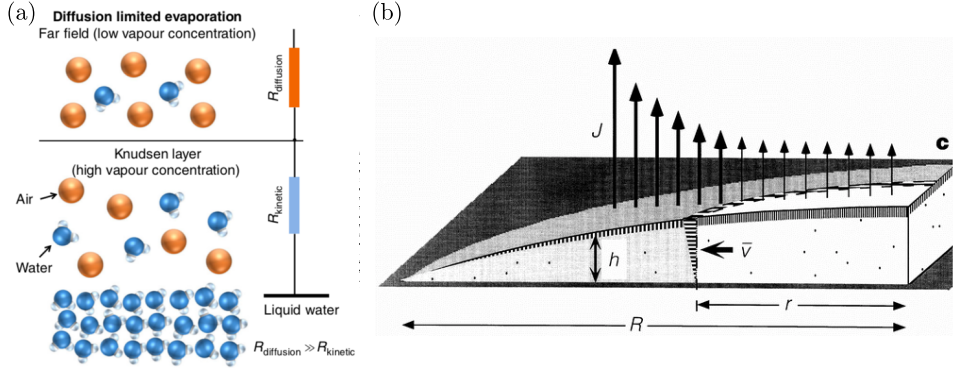


Figure 2.8: (a) Schematic representation of evaporation in air (Taken from Lu et al., 2019). The evaporation is limited by the diffusion of liquid molecules near the liquid-air interface to the surroundings. (b) Sketch of an evaporating sessile drop with  $\theta_{\text{app}} < \pi$  (Taken from Deegan et al., 1997). The evaporating flux  $J$  (arrows) increases from the center of the drop towards the contact line. The height  $h$  of the free interface, the evaporation flux, and the internal flow  $\vec{v}$  are strongly coupled.

together with Eq. 2.25 over the entire liquid surface. The evaporation rate depends on the geometrical aspects of the liquid configuration.

For sessile drops, ie. drops resting on a solid surface, with small capillary numbers, the drop shape can be approximated to a spherical cap. The boundary conditions for an evaporating sessile droplet are the following: i) along the drop interface,  $\rho_v = \rho_s$ , where  $\rho_s$  is the constant density of saturated vapor, ii) far from the drop,  $\rho_v = \rho_\infty$ , where  $\rho_\infty$  is the constant ambient vapor density, and iii) there is no vapor penetration at the solid surface outside the drop footprint,  $\partial_z \rho_v = 0$ . Solving Eq. 2.25 together with the boundary conditions, and replacing this in Eq. 2.24, it results in an equation for the local evaporation flux  $\vec{j}$ . Picknett et al. (1977) and Deegan et al. (1997) followed Maxwell's approach (Maxwell, 2011b) of solving this problem through a mathematical analogy with the problem of finding an electric field  $\vec{E} = -\vec{\nabla} \phi_E$ , with an electrostatic potential  $\phi_E$ . In this case  $\phi_E$  satisfies Laplace equation, and is originated from a charged conductor at constant potential and with its shape as the drop shape with its reflection. The details for deriving the solution can be found in Picknett et al. (1977), Deegan et al. (2000), Lebedev (1965), Hu et al. (2002), Popov (2005), and

### 2.3. DYNAMICS OF EVAPORATING DROPS

Cazabat et al. (2010). Near the contact line, the evaporation flux becomes

$$j(r, t) \sim (R - r)^{-\lambda}, \quad (2.26)$$

with  $r \leq R$  as the radial coordinate, in a cylindrical coordinate system, along the solid surface,  $\lambda = (\pi - 2\theta_c)/(2\pi - 2\theta_c)$  as a fitting parameter, and  $\theta_c = \theta_c(r)$  as the angle that the free interface makes with the solid surface.

Eq. 2.26 together with  $\lambda$ , show the nonuniformity of the evaporation flux along the free interface. For drops with contact angles  $\theta_{\text{app}} < \frac{\pi}{2}$ , the evaporative flux increases towards the contact line and diverges at it (Figure 2.8(b)). Physically, the singularity of the evaporation rate at the contact line is not possible. Various methods have been proposed to regularize it, these include introducing a cut-off length where the evaporation rate saturates (Poulard et al., 2005; Morris, 2014), or introducing a disjoining pressure that competes with the evaporation (Eggers et al., 2010).

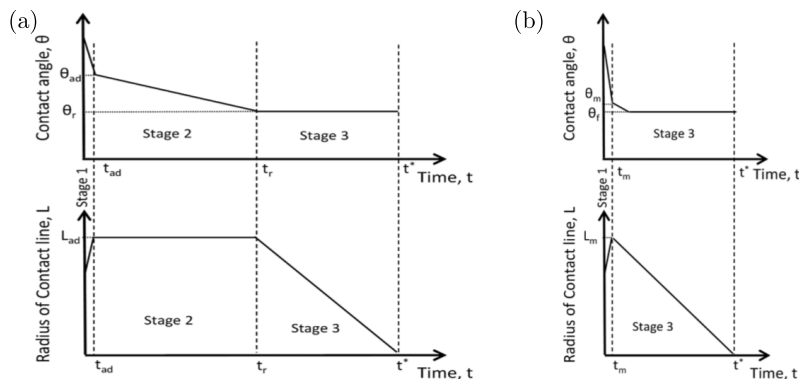


Figure 2.9: Representation of the time-evolution of the apparent contact angle  $\theta$  and the drop radius  $L$  of evaporating drops with pinned contact lines, panel (a), and with unpinned contact lines, panel (b) (Taken from Arjmandi-Tash et al., 2017 for describing the evolution of  $\theta$  and  $L$  of drops spreading on porous surfaces, which is similar to the evolution of evaporating drops, Brutin et al., 2018).

Due to evaporation, capillary flows are induced inside the drop. These flows tend to replenish the liquid that has been removed during the evaporation process with the liquid remaining on the drop. The origin of the capillary flows is the change of the interface curvature, ie. the internal flows and the drop shape are coupled.

### 2.3. DYNAMICS OF EVAPORATING DROPS

---

In partial wetting, the drop shape evolves following two modes (Figure 2.9). When deposited on the solid surface, the drop first spreads in a fast way, reaching the equilibrium contact angle. Then, if the contact line is pinned, the drop radius remains constant but the contact angle decreases (Figure 2.9(a)). If the contact line is unpinned it recedes, while the drop radius decreases and the contact angle remains constant (Figure 2.9(b)). At the end of the drop's life the radius decreases to zero and the contact angle remains constant, for both pinned and unpinned contact lines. In a stick-slip behavior, the contact line pins and then unpins repeatedly due to physical or chemical heterogeneities on the solid surface, and the radius and contact angle decrease. Examples of these can be found in the reviews from Bonn et al. (2009), Cazabat et al. (2010), Sefiane (2014), and Brutin et al. (2018) (also for complete wetting).

In partial wetting, the hydrodynamic flows and the drop shape are considered to be nearly independent (Popov et al., 2003; Deegan et al., 2000). This is because the flow velocities observed on these systems are lower than the characteristic velocity of the system  $u_0 \sim \gamma/\eta$ , ie. viscous stresses are negligible. This allows for a first approximation where the internal flows at a given time are derived using the equilibrium shape of the interface at that same time.

In complete wetting, the internal flows and drop shape are strongly coupled and have to be derived simultaneously. This is a dynamic situation where the contact line moves during the entire drop life. After deposition, the drop spreads fast, driven by capillarity. At the same time, the drop evaporates, and it will have disappeared before spreading to a vanishing contact angle. Due to the coupling of the shape and the internal flow, the contact line recedes despite complete wetting, leading to the observation of an evaporative contact angle.

For perfectly wetting pure liquids it is observed that the drop radius reaches a maximum and then decreases following a power law. For non-volatile liquids, ie. when the evaporation is weak,  $\theta_{\text{app}}$  follows Tanner's law which is a power law with an exponent 1/10, Eq. 2.7, where  $\theta_{\text{app}} \rightarrow 0$  during the receding stage. This has been proven in various experiments (Voinov, 1976; Tanner, 1979; Cazabat et al., 1986; Levinson et al., 1988; Chen et al., 1989). But for volatile liquids, experiments show different exponents, specific to the liquid (Lelah et al., 1981; Deegan, 2000; Cachile et al., 2002; Poulard et al., 2003; Shahidzadeh-Bonn et al., 2006). Moreover, it has also been observed that the evaporation can lead to a nonzero dynamic contact

angle in the final evaporation stages (Elbaum et al., 1994; Bourgès-Monnier et al., 1995; Cachile et al., 2002; Jambon-Puillet et al., 2018). Therefore, for describing the system that is close to equilibrium a theoretical model that accounts for the evaporation has to be considered.

In the context of the hydrodynamic model this involves solving the problem of the liquid flow and the interface profile coupled to the vapor flow (Figure 2.8(b)). This translates into solving a modified version of the lubrication equation, Eq. 2.12, that includes the evaporative flux, Eq. 2.24,

$$\partial_t h + \frac{1}{3\mu} \nabla [h^3 \nabla p] + j = 0, \quad (2.27)$$

where  $p$  accounts for the Laplace pressure and the disjoining pressure. The resolution of the hydrodynamic equation is an ongoing debate. Several theoretical and numerical approaches have been proposed (Cachile et al., 2002; Poulard et al., 2003; Poulard et al., 2005; Sultan et al., 2005; Eggers et al., 2010; Morris, 2014; Jambon-Puillet et al., 2018). The problem of finding a solution becomes more complex when additional effects are considered. For instance, thermal effects from the substrate can play a role (Anderson et al., 1995; Kim et al., 1996; Morris, 2001; Ristenpart et al., 2007; Tam et al., 2009; Sadafi et al., 2019). Ambient convection can also affect the dynamics (Kelly-Zion et al., 2013; Carle et al., 2013). And in multicomponent liquids, evaporation might induce compositional gradients that have to be included in the models.

## 2.4 Multicomponent droplets

Multicomponent systems are formed by solvent-mixtures of two or more domains with different physical and chemical properties. These are present in different settings, for example, drops embedded in a different liquid, either in a bulk fluid or a bigger drop (Squires et al., 2005; Shimizu et al., 2015; Tan et al., 2016; Sheth et al., 2020), coalescence of fluids of different liquid composition (Aarts et al., 2005; Karpitschka et al., 2010), or thin films of mixtures on solid or liquid surfaces (Quééré, 1999; Sefiane, 2014; Keiser et al., 2017). When this systems are out of equilibrium, processes like evaporation, adsorption, phase change or dissolution happen (Larson, 2014; Lohse et al., 2020). In multicomponent systems, compositional fields are present and induce diffusive fluxes and fluid flows that, at the same time, advect

## 2.4. MULTICOMPONENT DROPLETS

---

the compositional field (Cates et al., 2018). For describing these systems, the governing equation for the free interface is used, but also the evolution equation for the compositional field  $\phi$  (or temperature). The latter is given by the advection-diffusion equation

$$\partial_t \phi - \vec{\nabla} \cdot (D \vec{\nabla} \phi - \vec{u} \phi) = 0, \quad (2.28)$$

where  $D$  is the diffusion coefficient and  $\vec{u}$  the velocity field of the fluid flow. In most of the studies where the lubrication approximation is applied, it is assumed that the diffusion is strongly fast that the concentration in the perpendicular direction to the flow is uniform (Doumenc et al., 2010). This assumption has been questioned. The coupling of the aforementioned mechanisms will determine the dynamics of the system.

Different types of additives have been of interest for fundamental and technological applications. The most common additives are inert particles and liquids, which influence the fluid flow in different ways.

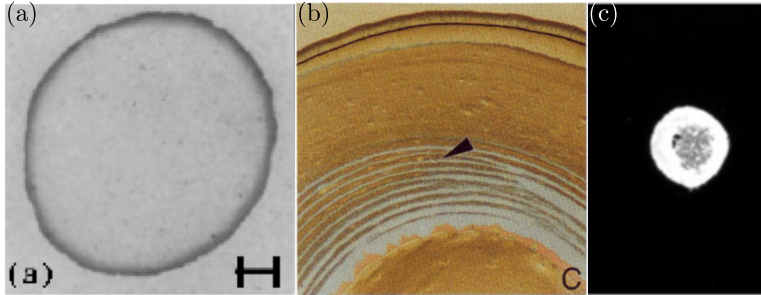


Figure 2.10: (a) Picture of a coffee stain. Typical pattern formed for pinned contact lines. The scale bar corresponds to 1 cm (Taken from Deegan et al., 2000). (b) Snapshot of a typical set of ring patterns left by a contact line with a stick-slip behavior. The pattern is formed using PS particles of 144 nm size. The size of the image is 0.5 mm (Taken from Adachi et al., 1995). (c) Snapshot of a drying pattern with particles distributed almost uniformly, for an unpinned contact line. The suspension contained glass beads of  $\sim 10 \mu\text{m}$  size (Taken from Choi et al., 2011).

Inert solid particles are considered to have no influence in the surface tension or the viscosity of the liquid. These particles are advected in the presence of flows. In an evaporating drop, the particles are advected and are

deposited in the solid surface. The patterned left on the surface after complete evaporation depends on the particle size and concentration, liquid, solid surface, and ambient humidity (Trybala et al., 2013; Sefiane, 2014; Brutin et al., 2018; Tarafdar et al., 2018). But also, it will depend on the contact line dynamics. On pinned contact lines, the fluid flows radially outwards, from the drop center to the contact line where they are deposited (Deegan et al., 2000; Deegan, 2000; Kajiya et al., 2008). This is known as the ‘coffee-ring’ effect, as a reference to the ring stain observed after drying of a coffee drop (Figure 2.10(a)), which origin is the capillary flow (Deegan et al., 1997). But, if the contact line shows a stick-slip behavior, a set of ring stains is formed instead (Figure 2.10(b)), each ring corresponding to a pinning stage (Adachi et al., 1995; Shmuylovich et al., 2002; Askounis et al., 2014). For unpinned contact lines, the particles form a layer almost uniform at the center of the drop upon complete evaporation (Figure 2.10(c), Choi et al., 2011), as well in complete wetting systems (Brutin et al., 2018).

At the same time, the particles affect the wetting dynamics. It has been observed that these can induce self-pinning of the contact line (Deegan, 2000; Rio et al., 2006). Additionally, the particles can also enhance the evaporation rate of the drop (Conway et al., 1997).

In case there is a second liquid present in the mixture the situation changes as compared to inert particles. Marangoni flows are generally present. These are induced by compositional gradients at the interface. In a mixture of two miscible liquids, Marangoni flows originate from the difference in volatility and surface tension between the liquids. For evaporating sessile drops, the difference in volatility between the liquids and the difference in the rate of evaporation along the drop deplete one of the components, forming local concentration gradients on the interface and within the drop. Because the liquids have a different surface tension and the surface tension changes with composition, the concentration gradient creates a surface tension gradient at the free interface. The Marangoni stresses induce an interfacial flow that drives convective transport inside the drop. The direction of the flow is determined by the interplay between the distribution of the evaporation rate along the surface and the volatility and surface tension of both liquids.

A radially outward flow, which goes from the center of the drop to the contact line, is obtained when the liquid with the highest surface tension enriches near the contact line. This flow is the origin of the ‘tears of wine’ effect (Figure 2.11(a)), observed in wine and spirits when the alcohol evaporates from the liquid surface near the glass wall (Thomson, 1855; Marangoni, 1871;

## 2.4. MULTICOMPONENT DROPLETS

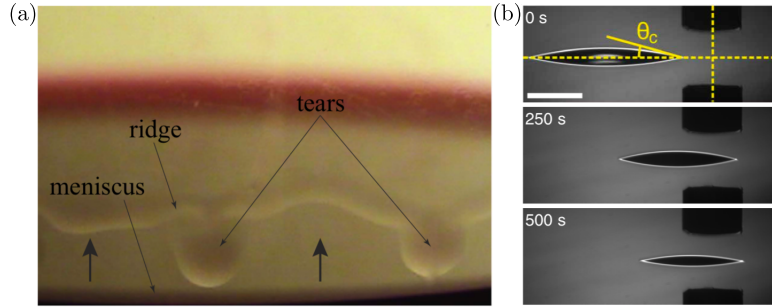


Figure 2.11: (a) Picture of typical ‘tears of wine’. The width of the image is 30 mm (Taken from Venerus et al., 2015). (b) Time-lapse images of a Marangoni contracted drop (elliptical shadow) moving due to a vapor gradient that goes from the needle tip (squared shadow) to the surroundings. Drop of water-PG mixture. The scale bar corresponds to 1 mm (Taken from Malinowski et al., 2020).

Venerus et al., 2015). For sessile drops, it has been shown that the dynamic contact angle depends on the evolution of the concentration, and the initial contact angle decreases with the initial concentration of the most volatile component (Rowan et al., 2000; Sefiane et al., 2003; Cheng et al., 2006; Diddens et al., 2017; Williams et al., 2021). ie. the drop shape and compositional field are coupled. Moreover, the evolution of the drop shape changes for different wetting scenarios. On unpinned contact lines, the drop shape goes through three main stages. One is determined by high concentrations of the most volatile component, where the evolution is comparable to that of the same liquid. A second stage, for intermediate concentrations, where the drop shape is distorted and instabilities can appear. And a third stage where it is similar to that of the residual component. Later studies revealed a coupling with the internal drop flows by using particle image velocimetry (PIV) technique (Christy et al., 2011). It was shown that the flow evolution follows also three stages, with multiple vortices in the first stage, an outward radial flow that was associated to Marangoni convection, in the second stage, and an outward radial flow characteristic of pure liquids in the third stage. Additionally, the drop shape is affected by the ambient humidity (Sefiane et al., 2008). All this phenomena show the interplay between evaporation, compositional field, Marangoni flows, and drop interface profile.

Inward flows, in contrast to outward Marangoni flows, form when the liquid with the lowest surface tension enriches near the contact line. Marangoni

flows are the origin of Marangoni contracted drops. These are drops that exhibit a non zero apparent contact angle on surfaces where the pure liquids that compose the mixture completely wet the surface. In such case, a flow going from the center of the drop to the contact line and then to the drop apex is observed. Even though the drop does not completely spread in the contracted stage, a precursor film is present. Marangoni contracted drops move freely with no contact line pinning (Benusiglio et al., 2018) and respond to vapor gradients (Figure 2.11(b), Malinowski et al., 2020). It was also observed that the drop shape is sensitive to ambient humidities, where the initial contact angle highly depends on the relative humidity. Two models predict a power law dependency but with different exponents (Karpitschka et al., 2017; Benusiglio et al., 2018). The models proposed different contraction mechanism. One of the models (Benusiglio et al., 2018) proposes a surface tension balance along the contact line between the surface tensions on the bulk fluid and on the precursor film. The other model (Karpitschka et al., 2017) establishes a flux balance between the capillary and the Marangoni flows. Inward Marangoni flows can also be present in systems where the ambient is saturated with a compound with lower surface tension than the liquid on the solid (Leenaars et al., 1990). Through vapor absorption at the free interface, a surface tension gradient is induced, and with it inward Marangoni flows and retraction of the contact line.

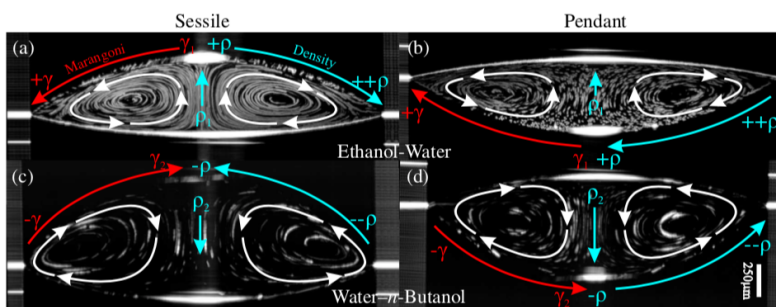


Figure 2.12: Cross-sectional view of sessile and pendant binary liquid drops. The streak images of seeded particles were taken with optical coherence tomography. The red arrows show the direction of the surface tension gradient, the blue ones of the density gradient, and the white ones of the flow. (Taken from Edwards et al., 2018).

Buoyancy-driven flows also play a role in the hydrodynamics of two com-

## 2.4. MULTICOMPONENT DROPLETS

---

ponent drops. Buoyancy-driven flows can appear in mixtures of two miscible liquids due to the difference on the density of both liquids. In evaporating sessile drops, the surface tension and density gradients might have the same direction, making difficult to distinguish between Marangoni and buoyancy-driven flows. Cross sectional views, with optical coherence tomography (Figure 2.12, Edwards et al., 2018), and bottom views, with  $\mu$ PIV method (Li et al., 2019), of such drops with tracer particles show a reversal in the flow pattern with respect to the solid surface when changing the drop from sessile to pendant. In pendant drops, both gradients oppose each other, so the resulting convective flow makes evident that gravitational forces, promoted by density gradients, dominate over surface tension forces. Buoyancy-driven flows were observed to dominate over Marangoni flows on drops with large contact angles.

When a mixture contains surfactants, the dynamics change as compared to ideal mixtures and liquid mixtures with some degree of surface activity. Surfactants are molecules that tend to adsorb at a liquid interface (Manikantan et al., 2020; Matar et al., 2009; He et al., 2015). These are surface active agents, which lower the surface tension of the liquid (Smit et al., 1990; Gennes et al., 2004). Most of the surfactants have an amphiphilic molecular structure, containing a hydrophilic part and a hydrophobic part. Two types of surfactants can be found, soluble and insoluble. Soluble surfactants dissolve in the bulk solution in contrast to insoluble ones.

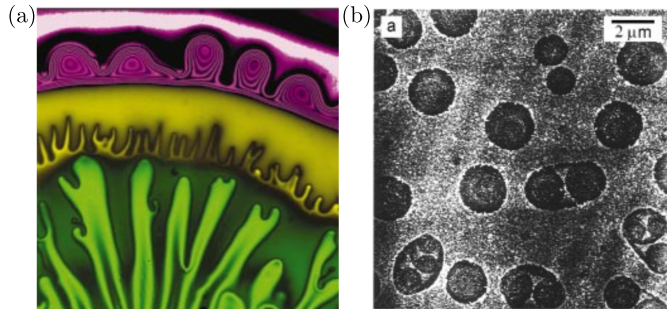


Figure 2.13: (a) Snapshot of the pattern formed by a spreading drop (green) of glycerol with a surfactant (sodium dodecyl sulfate) on a pure glycerol film (gray). The height of the image is 1 cm (Taken from Darhuber et al., 2003). (b) Snapshot of a thin liquid layer of a surfactant solution (octadecylphosphonic acid) on mica. The liquid layer dewets forming holes on the film (Taken from Woodward et al., 1997).

Soluble surfactants show micellization, ie. they can aggregate to form micelles (Degiorgio, 1985; Hajji et al., 1989; Gennes et al., 2004). The formation of micelles happens when the micelle concentration reaches a critical value (CMC) for which the formation of aggregates is energetically favorable. When this stage is reached, the increase of surfactant concentration leads to an increase of the amount of micelles but not of adsorbed molecules at the interface. Accordingly, surface tension does not reduce further upon increasing the bulk concentration of surfactant above the CMC (Smit et al., 1990). In the presence of surfactant concentration gradients at the interface, surface tension gradients rise. The surface stresses associated to this gradient, Marangoni stresses, induce an interfacial flow. In turn, this flow can deform the interface (Schwartz et al., 1995) and also induce diffusion and advection at the interface and within the bulk fluid (Jensen et al., 1993). Besides, surfactants can also alter substrate wettability (Afsar-Siddiqui et al., 2003). When a surfactant solution is placed on a solid surface, the attraction forces between the molecules and the surface can cause adsorption of the molecules onto the surface ahead of the contact line (Rupprecht et al., 1991). The transport of the molecules occurs through the same liquid phase (Yaminsky et al., 1997) or through the vapor phase. Whether the attraction is with the hydrophilic or hydrophobic part of the molecule, the other part, exposed to the air, changes the surface energy, promoting spreading (Zhu et al., 1994; Karapetsas et al., 2011), autophobing (Birch et al., 1994) or intermediate states (Frank et al., 1995a). Surfactants gives rise to phenomena like higher spreading rates (Stoebe et al., 1996), fingering (Figure 2.13(a), Marmur et al., 1981; Darhuber et al., 2003; Hamraoui et al., 2004), and dewetting (Figure 2.13(b), Woodward et al., 1997; Takenaka et al., 2014).

Multicomponent liquids can go through liquid-liquid phase separation. This is observed, for example, in two-component bulk mixtures, when the system reaches a critical solution temperature and the liquids are not longer miscible (Lai et al., 1999). Or in ternary systems when the concentrations, relative to each other, reach a critical value (Kahlweit et al., 1985; Alany et al., 2000). Liquid-liquid phase separation is also present in wetting systems, for example, when selective evaporation occurs. In this process, accumulation of one of the components along the contact line induces segregation (Kim et al., 2016; Dietrich et al., 2017; Karpitschka, 2018; Li et al., 2020), In such systems, drop nucleation and grow can occur (Figure 2.14, Tan et al., 2016; Li et al., 2018). It has been observed that phase separation modifies the evaporation process, the internal flows, and the general evolution of the

## 2.4. MULTICOMPONENT DROPLETS

---

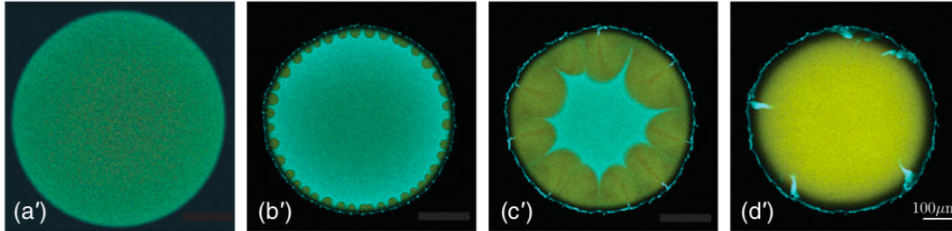


Figure 2.14: Time-lapse images of a drop composed of a water (blue) and 1,2-Hexanediol (yellow) mixture, taken with a confocal microscope, from bottom view. It shows the nucleation and grow of 1,2-Hexanediol droplets at the contact line, in the first 65 s after drop deposition (Taken from Li et al., 2018).

liquid.

In general for multicomponent systems, a model to describe the coupling between hydrodynamic flows, phase separation, interaction between the components, wetting, compositional evolution, and phase changes, is not yet available. Despite the huge amount of studies on multicomponent liquids, and the amount of findings of different mechanisms, an agreement of a general model that accounts for all the possible contributions, and distinguishes between them or the dominant mechanism is still lacking. This is not just from the theoretical differences but also from a qualitative agreement with experiments. At the same time, there are experimental challenges that when solved allow to direct comparisons with the models.

# Chapter 3

## Droplet shape and internal flow quantification method

### 3.1 Overview

The effect of compositional gradients in the dynamics of contact lines was studied from an experimental approach. Marangoni contracted drops were used as the model system. Drop shape and internal flows were measured. During experiments, a drop was deposited gently over a solid substrate, in-

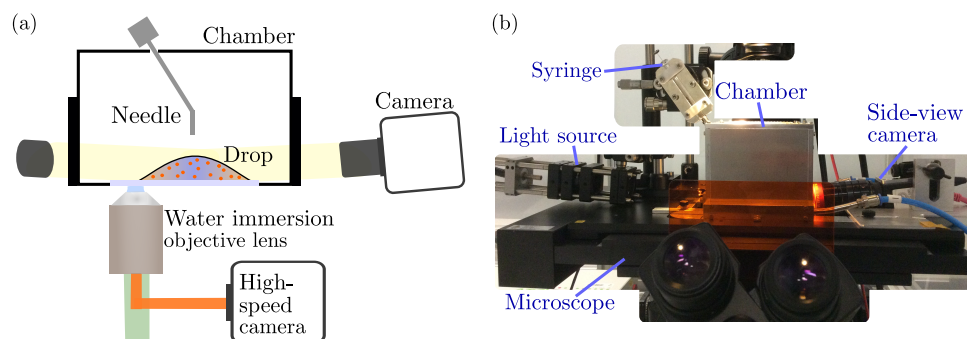


Figure 3.1: Experimental setup. (a) Sketch of the experimental setup from side view. (b) Picture of the setup taken from the side.

side a controlled atmosphere chamber (Figure 3.1). The chamber is placed on the sample stage of an inverted fluorescence microscope, coupled to a camera for side view imaging. Before starting an experiment, a new substrate was placed in the sample holder inside the chamber, the chamber was closed,

## 3.2. MATERIALS

---

and the vapor conditions were set. We then waited for equilibration of the atmospheric conditions for 1 – 5 min. Then, a droplet with controlled volume was deposited onto the substrate with a syringe and a needle that was introduced to the chamber through a small hole. Side and bottom view images were recorded simultaneously during and after injection of the droplet, for measuring drop shape and internal flow, respectively. Different drop compositions, ambient conditions, and type of substrates were explored. Below follows a description for each of these parts and their preparation. Additionally, in each chapter it is stated which materials were used specifically.

### 3.2 Materials

**Chemicals.** The chemicals used for drop and atmospheric compositions are: water (“Milli-Q”, resistivity  $18 \text{ M}\Omega \cdot \text{cm}$ ), Ethylene Glycol (1,2-EG, Sigma Aldrich, purity  $\geq 99.5\%$ ), 1,2-Propanediol (1,2-PD, Sigma Aldrich, purity  $\geq 99.5\%$ ), 1,2-Butanediol (1,2-BD, Sigma Aldrich, purity  $\geq 98\%$ ), 1,2-Hexanediol (1,2-HD, Sigma Aldrich, purity  $98\%$ ), and 2-Propanol (IPA, Carl Roth, purity  $\geq 99.9\%$ ). Polystyrene microspheres (Thermo Fisher Scientific F8809,  $0.2 \mu\text{m}$  diameter, stock solution concentration  $2\%$  w/v, excitation/emission maxima =  $540/560 \text{ nm}$ ) were added as tracers into the liquid mixtures or pure liquids for flow visualization. The chemicals were used as received.

**Liquid mixtures.** Binary mixtures were prepared of water and one of the following carbon diols: Ethylene Glycol, 1,2-Propanediol, 1,2-Butanediol, and 1,2-Hexanediol. The mixtures were prepared and stored in piranha cleaned borosilicate glass vials (VWR, capacity  $4 \text{ mL}$ ). An analytical balance (Thermo Fischer Scientific Analytical Series, readability  $0.1 \text{ mg}$ ) was used to prepare mixtures of desired mass fraction  $0 < \phi < 1$ , by pipetting the chemicals into the vials on the balance. Tracer particles were added into the mixtures for flow visualization technique. The mixtures were sonicated in an ultrasonic bath (VWR Ultrasonic Cleaner USC-TH) for  $\sim 2 \text{ min}$ . The mixtures were stored in a low temperature environment ( $\sim 5^\circ\text{C}$ ) to avoid changes in concentration due to evaporation. The mixtures were used within the first two days after preparation and were replaced by fresh ones afterwards.

**Tracer particles.** The mass fraction of the particle stock solution in the total liquid mass was  $7.8 \times 10^{-5}$ . The used particle concentration was  $\sim 1.7 \times 10^{10}$  particles/mL. After adding the tracer particles into the liquids, the liquids were sonicated in an ultrasonic bath for  $\sim 2$  min. The liquids were stored in a low temperature environment ( $\sim 5^\circ\text{C}$ ) to avoid evaporation and were protected from light with aluminum foil. Before experiments, the liquids were sonicated for  $\sim 2$  min to ensure good dispersal of the tracer particles.

Common particle properties considered in flow visualization techniques are non corrosive, chemical inert, and their size has to be small enough to truly follow the flow and large enough to scatter light (Dabiri, 2007). A way to determine that the particles are good tracers is that the particle relaxation time ( $\sim 3.7 \times 10^{-6}$  s for the aforementioned particles) has to be smaller than the time scale of the fluid ( $\sim 0.7$  s for Marangoni-contracted drops). Additionally, faithful tracers should have a size ( $0.2 \mu\text{m}$  for the aforementioned particles) smaller than the length scale of the shear stress ( $\sim 1 \mu\text{m}$  for Marangoni-contracted drops), so the particle's velocity is solely due to advection of the flow (Melling, 1997; Saffman, 1965; McLaughlin, 1991). In particular, in our case we choose particle size and concentration considering also two main criteria. One is that the particle density close to the contact line has to be large enough to get good image correlations for micro particle image velocimetry technique ( $\mu\text{PIV}$ ). However, the image of individual particles in the focal plane should still be distinguishable (Dabiri, 2007; Lindken et al., 2009). Densities for which on average three particles were found in an interrogation window of  $12 \text{ px} \times 12 \text{ px}$  gave good results. In our setup the particle image diameter is of  $\sim 1 \text{ px}$ . The second criteria is that the particles must not induce self-pinning of the drop. It was observed that high particle concentrations induce contact line pinning. Also, bigger particles, for example with  $1 \mu\text{m}$  of diameter, tend to be deposited on the solid surface in greater quantity than those of  $0.2 \mu\text{m}$  diameter, inducing pinning.  $1 \mu\text{m}$  size particles are of the same order of magnitude as the length scale of the shear, not being good tracers for the system here studied.

**Smooth hydrophilic substrates.** Microscope glass coverslips (VWR cover glass class 1,  $24 \text{ mm} \times 24 \text{ mm}$  size,  $170 \mu\text{m}$  thick) were cleaned with piranha solution (hydrogen peroxide 30%, VWR Chemicals, and sulfuric acid 95%, VWR Chemicals, mixture, volume fraction 1 : 3, respectively) for 20 min in

### 3.2. MATERIALS

---

a soda-lime glass staining jar (DWK Life Sciences). Afterwards, the substrates were rinsed five times with fresh water (“Milli-Q” water, resistivity  $18 \text{ M}\Omega \cdot \text{cm}$ ) and were sonicated for 10 min in hot water at  $\sim 80 \text{ }^\circ\text{C}$ , to ensure complete removal of residues from the piranha solution (Lessel et al., 2015; Karpitschka et al., 2010). The substrates were stored in fresh water and used on the day of preparation. The substrates were dried with a nitrogen drying gun immediately before the experiment under a laminar flow hood. The nitrogen was blown parallel to the substrate from the corner opposite of the tweezers (PTFE or metallic PTFE coated) that were used to hold the slide. The substrate was kept protected from dust with a glass petri dish during its transfer from the laminar flow hood to the humidity control chamber where the experiment was done.

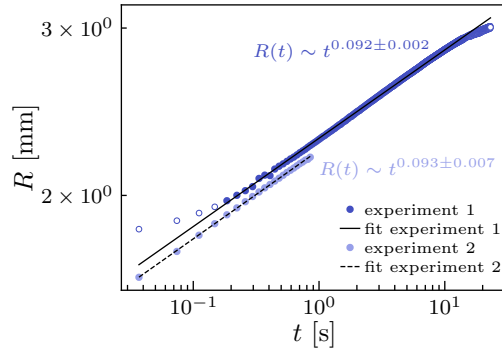


Figure 3.2: Evolution of the radius of a water drop over a glass coverslip treated with piranha for two experiments with same conditions: measurements (circles), power law fit (lines). The equations of the fitted lines are in agreement with Tanner’s law. The unfilled circles of experiment 1 were excluded from the fit. In experiment 1, the drop was pulled with the needle when removing it after depositing the drop, causing the deviations from the power law in the start of the spreading. The deviations at the end show the limit where the drop shape no longer follows Tanner’s law, which corresponds to  $\theta_{\text{app}} \sim 5^\circ$ .

Piranha solution is usually used for removing organic contaminants (Mak, 2010) and for increasing hydrophilicity (Paredes et al., 2017; Lessel et al., 2015), making it a good method for substrate preparation. The spreading rate of a  $\sim 0.5 \mu\text{L}$  water drop over the glass coverslipes piranha cleaned

followed a power law  $R(t) \sim t^{0.09}$ , in agreement with Tanner’s law, confirming a highly hydrophilic surface and a surface free of pinning sites. The contact angle down to which this behavior was confirmed is  $\sim 5^\circ$ .

**Porous hydrophilic substrates.** Quartz microscope cover slips (Thermo Fisher Scientific cover slip, 25.4 mm  $\times$  25.4 mm size, 0.15–0.25 mm thick) were coated with a layer of candle soot as a template for a porous medium. The candle soot layer consists of a porous network of  $\sim 50$  nm size carbon nanobeads (Deng et al., 2012). We used the following preparation protocol to fabricate hydrophilic porous substrates, inspired by the method reported previously by Paven et al. (2013) and Paven et al. (2014) and used in Ramírez-Soto et al. (2020). The slides were sonicated for cleaning with a series of solvents (ethanol, Carl Roth, purity  $\geq 99.5$  acetone, Sigma Aldrich, purity  $\geq 99.5$ , and toluene (Sigma Aldrich, purity  $\geq 99.9\%$ ) and water) for  $\sim 3$  min in each solvent. Afterward, the slides were dried in an oven at  $70^\circ\text{C}$ . When coating the slides with candle soot, the glass slides were held above the candle flame, with constant oscillatory motion in the horizontal plane, perpendicular to the flame, to form a uniform layer of soot particles. The coated slides were placed on a desiccator and stored for 24 h with an open borosilicate glass vial containing 3 ml of ammonium and a second vial with 3 ml of tetraethoxysilane. By this, a chemical vapor deposition of tetraethyl orthosilicate catalyzed by ammonia takes place. A 30 – 40 nm silica thick layer is deposited over the porous nanostructures (Paven et al., 2013). The substrates were annealed in an oven (Carbolite Gero 30-3000  $^\circ\text{C}$ ) at  $990^\circ\text{C}$  for 3 h inside ceramic cases for dust protection. At this annealing temperatures, the silica particles increase stiffness, becoming closer to that of fused silica (Zhang et al., 2010). The substrates were kept dry and protected from dust until use. The main difference with Paven et al. (2013) and Paven et al. (2014) is that we skipped the step where oxygen plasma is applied and the silanization step.

**Syringe and needle cleaning.** Borosilicate glass syringes (Hamilton Gastight Series 1700, PTFE plunger tip, volume 10  $\mu\text{L}$ ) with stainless steel needles (Hamilton Removable Needle, small PTFE hub, gauge 22s, tip type 3) were used for drop volume control and deposition. Syringes and needles of other materials, like plastic and cooper, were not used to avoid any possible contamination from the material itself. The syringes and needles were

### 3.3. EXPERIMENTAL SETUP

---

cleaned with a series of solvents (ethanol and acetone, and water).

## 3.3 Experimental setup

### 3.3.1 Ambient humidity control

Experiments were done inside an atmospheric control chamber (aluminum walls, size  $\sim 10\text{ cm} \times 10\text{ cm} \times 10\text{ cm}$ , Figure 3.3). During the experiments,

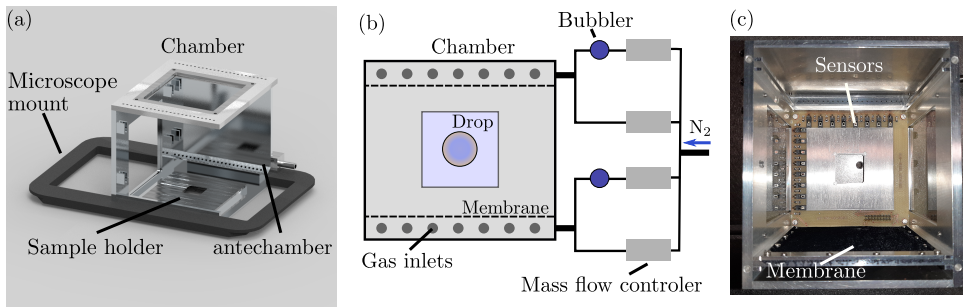


Figure 3.3: Atmospheric control system. (a) 3D image of the humidity chamber from the inside, together with the microscope mounting system and the sample holder. (b) Sketch of the chamber and the humidity control system from top view. (c) Picture of the inside of the chamber and the humidity sensors, taken from the top.

a gas mixture of controlled vapor was continuously injected to membrane-separated antechambers in the main chamber. The membranes connecting the antechambers to the main chamber were made of interwoven fabric (Wilox Hosiery GmbH tight VITAL 40, 88% polyamide, 12% elastane). They spanned almost the entire area of two opposing side walls, minimizing convection in the main chamber while ensuring quick diffusive exchange with the feed gas. Each antechamber is connected to an independent gas line (Figure 3.3(b)). This configuration allows to generate not just homogeneous atmospheres but also atmospheres with vapor gradients across the main chamber. To achieve arbitrary vapor conditions, fluxes of dry nitrogen and nitrogen saturated with water or IPA were regulated with mass flow controllers (MKS Instruments Type MF1) to the desired proportion, with a constant total flux of 500 sccm. Water vapor or IPA vapor were produced by injecting nitrogen into gas bubblers (VWR borosilicate glass gas washing

bottle, head with sintered glass disc porosity 2) filled with the desired liquid. The bubblers are connected to the gas lines for mixing the vapor with dry nitrogen. Several humidity sensors (Honeywell HIH-4000 Series, Figure 3.3(c)) distributed in the chamber provided a measurement of the humidity distribution. These sensor just work for water vapor measurements but not for IPA vapor.

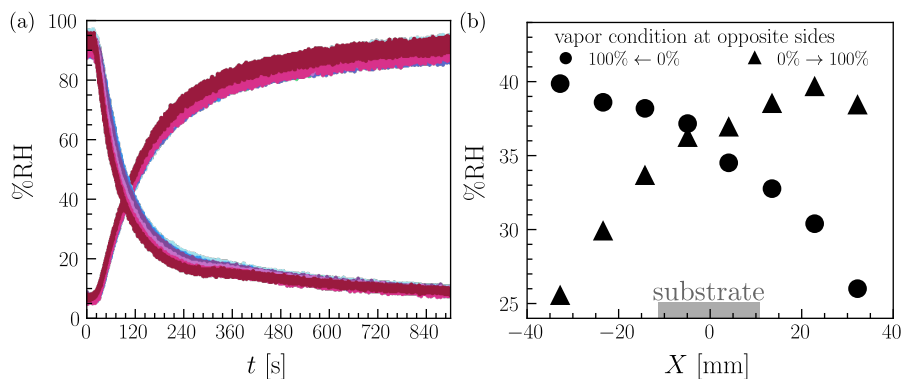


Figure 3.4: Humidity distribution in the chamber. (a) Humidity transients, from  $\sim 0\%RH$  to  $\sim 100\%RH$  and from  $\sim 100\%$  to  $\sim 0\%RH$ : each color represents the measurement of a single humidity sensor located in the perpendicular direction to the membranes. (b) Humidity distribution in atmospheres with vapor gradients: when setting 100% water vapor on the left side of the chamber and 0% on the right side (circles), and when inverting the vapor conditions (triangles).

Figure 3.4(a) shows measurements of the chamber humidity under transient conditions, from dry atmosphere ( $\sim 0\%RH$ ) to  $\sim 100\%RH$ , and from  $\sim 100\%$  to  $\sim 0\%RH$ , for the humidity sensors located in the perpendicular direction to the membranes. The color of the data represents the reading of a single sensor. The time that takes to the gas to travel from the gas mixing system to the chamber is  $\sim 3$  s. The fact that the measurements taken by all the sensors follow the same trends shows the homogeneous distribution of the humidity across the chamber. It takes  $\sim 10$  min to reach 90%RH or 10%RH. Based on these measurements, whenever changing the atmospheric conditions to extreme conditions, we waited around 10 min for equilibration, before starting an experiment, otherwise we waited 1- 5 min. Figure 3.4(b) shows the humidity distribution across the chamber 10 min after setting 100% water vapor in one side of the chamber and 0% in the other side. A gradient

### 3.3. EXPERIMENTAL SETUP

---

with a difference of  $\Delta RH \sim 15\%$  between the opposite sides.

#### 3.3.2 Contact angle measurements

Side-view shadowgraph imaging was performed with a camera (Point Grey Grasshopper2, imaging speed at 27 FPS), equipped with a telecentric macro lens (Thorlabs Bi-Telecentric lens, 1.0X, W.D. 62.2 mm) and a collimated-light source on the opposite side, both attached to the sample stage of the microscope (Figure 3.1(b)). The droplets were observed from an angle of

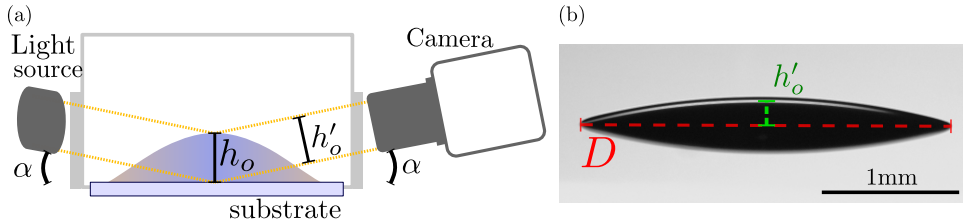


Figure 3.5: Side-view shadowgraph imaging. (a) Drop illuminated with a collimated light from a source tilted with an angle  $\alpha$  with respect to the substrate. The light (yellow lines) is reflected on the substrate and on the drop apex to the camera, also tilted with the same angle  $\alpha$  with respect to the substrate. (b) Side aspect of the drop.

$\alpha = 6^\circ$  with respect to the substrate (Figure 3.5(a)). The advantage of this arrangement is the possibility of observing the entire three phase contact line around the droplet as shown in Figure 3.5(b). This allows for a precise measurement of the footprint diameter  $D$  of the droplet. The top surface of the drop reflects light directly from the light source to the camera, which allows a precise detection of the drop apex, thus of the contact angle.

For each frame from the side-view camera, the droplet's radius  $R$  and the apical height  $h_o$  were extracted from the images. By assuming that the drop shape is close to a spherical cap, the apparent contact angle was calculated as  $\theta_{app} = 2h_o/R$ . The images were analyzed with an in-house-developed code. The major axes length of the drop image is obtained either by fitting an ellipse to the drop image and measuring its major axes or by detecting the two extremes of the drop in the image frame in the horizontal direction and measuring the distance between them. The maximum intensity on the axis perpendicular to the major axis corresponds to the top of the drop. For finding the apex position with subpixel resolution, a second order polynomial is

fitted to the intensity peak. To calculate  $h_o$ , the shorter distance  $h'_o$  from the drop base to the apex is measured. The finite observation angle is corrected according to  $h_o = h'_o/\cos(\alpha)$ .  $R$  is defined as half of the major axis length  $D$ .

### 3.3.3 Micro-Particle Image Velocimetry data acquisition

To measure the flow inside the drop, micro particle image velocimetry method ( $\mu$ PIV) was used (Wereley et al., 2010). The atmospheric control chamber was mounted on top of an inverted epi-fluorescence microscope (Nikon Eclipse Ti2E) with large field of view (diameter 25 mm in the image plane), see Figure 3.1. A high power white light source (Lumencor SOLA Light Engine) was used for illumination of the fluorescent particles. The excitation/emission wavelength range of the fluorescent particles was selected with a custom fluorescence filter cube (AHF Analysentechnik, transition wavelength 542 nm). The microscope was equipped with a water immersion objective lens (Nikon CFI APO LWD 20X WI) with a numerical aperture of 0.95. The immersion medium of the objective was selected such that it matches with that of the drop, to achieve diffraction-limited imaging even in the bulk of the working medium (Botcherby et al., 2012). This is important for a good  $z$ -plane selectivity (Agard, 1984). The focal plane, parallel to the substrate, was moved with the microscope focusing stage in vertical direction to scan the drop at different  $z$ -planes in an automated procedure. The time for switching between focal planes was  $\sim 100$  ms. The full  $z$ -scan was on the order of 10 s, shorter than the time scale on which the flow velocities change for a quasi-stationary drop. Successive upward and downward scans were done to check this. A sequence of hundreds of frames was recorded for each plane with a high-speed camera (Phantom VEO 4K-L, imaging speed at 600 to 1000 FPS).

Since the experiments were recorded with the side view camera immediately before the drop's deposition until the end of the PIV recording, synchronization was performed through the shutter of the epifluorescence excitation light, which was faintly visible in the side view due to scattering.

## 3.4 Micro Particle Image Velocimetry data analysis

### 3.4.1 Adaptive interrogation window size method

To quantify the flow, the images captured from the  $\mu$ PIV measurements were analyzed with an in-house Python developed code. The data is evaluated through cross-correlation with correlation-averaging (Meinhart et al., 2000) over  $\sim 100$  frames. Here we propose to include in the algorithm an adaptive interrogation window size method. First, single-pixel correlations (Westerweel et al., 2004) are calculated for the entire image and all displacements within a pre-defined search range. Instead of correlating intensity values directly, we used the dot product of the gradient (first order differences). Then, correlations are integrated over interrogation windows of various sizes by convolution with a square kernel of the desired size. We used five different interrogation window sizes of 4, 8, 16, 32, and 64 px side-length. The final correlation maps are then evaluated by a weighted average between the different window sizes, using the mean square of the intensity gradient values in the interrogation window and a size-dependent bias as weight. This method allows for a high resolution in regions of strong velocity gradients, while preventing artifacts from false correlations where particle densities are low. The method was implemented through the Python API of Tensor Flow, to enable fast computation on graphics processing units.

### 3.4.2 Velocity profiles

2D velocity fields in each  $z$ -plane are obtained from the method described above. From this velocities, the radial velocity and the velocity profile in the cross section of the drop are obtained.

Figure 3.6 shows examples of the measured velocities. Panel (a) shows an example of the velocity field in a plane close to the contact line. The radial dependence of the velocity was calculated by azimuthally averaging over  $\sim 100 \mu\text{m}$  in each of these horizontal planes. Panel (b) shows examples of the radial velocity for different  $z$  planes as a function to the distance to the contact line  $d$ , for a single experiment. The uncertainties of the velocities are estimated using the standard deviation over the weighted interrogation windows. Velocity profiles are obtained with parabolic fits of the radial velocities in each  $z$  plane at a certain distance to the contact line, as shown in

### 3.4. MICRO PARTICLE IMAGE VELOCIMETRY DATA ANALYSIS

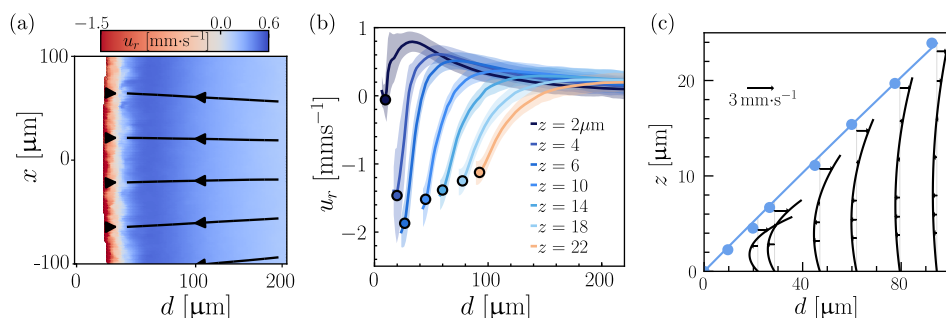


Figure 3.6: Flow velocity in a Marangoni contracted drop. (a) Example of a velocity field in a  $z$ -plane close to the substrate: the radial component of the velocity (color code) and streamlines (black arrows). The white area corresponds to the region outside the drop. (b) Example of radial velocities vs. distance to the contact line  $d$ , for a single experiment. Each plot has the radial velocity measured at each  $z$  plane above the substrate (solid lines), the associated errors (shaded bands), and the velocities at the interface (circles). (c) Drop cross-sectional view: free surface (blue discs and fit line), horizontal velocity (black arrows) and velocity profiles (black lines), for data taken from panel (b).

panel (c).

#### 3.4.3 Correction to the $z$ location of the velocity

Whenever the focal plane comes close to the free surface, correlations are picked up preferentially from below the focal plane because there are no particles outside the drop. This leads to a shift in the correlation plane relative to the focal plane. Thus, a correction to the  $z$  location of the velocity signal relative to the distance from the free surface is applied. The correction is obtained by estimating the point spread function and the correlation sensitivity as a function of distance to the focal plane. This sensitivity is convolved with a unit-step function in  $z$  for the particle density. We modeled the depth of correlation as a Gaussian with  $1.5 \mu\text{m}$  standard deviation.

The substrate level was determined at the contact line of the droplet, by focusing onto particles at the substrate. To account for possible substrate tilt and non-planarity, we extracted the expected substrate location from parabolic fits to the velocity profile with a no-slip condition at an offset  $z_0$  in the  $z$ -coordinate. Then we obtained  $0 > z_0 \gtrsim 3 \mu\text{m}$  for  $0 < d < 500 \mu\text{m}$ . Then

### 3.4. MICRO PARTICLE IMAGE VELOCIMETRY DATA ANALYSIS

---

we approximated  $z_0(d)$  over the full range of  $d$  by a third order polynomial with  $z_0(d = 0) = 0$ , and used it to correct the vertical substrate location as a function of  $d$ . The offset obtained is within the range of the substrate deformation measured by profilometry on a sample of six glass slides.

The velocity profiles in Figure 3.6(c) were obtained after the correction.

#### 3.4.4 Surface tension gradients

The surface tension gradient was obtained from the first derivative of the velocity profiles in the cross section evaluated at the interface, and multiplied by the viscosity.

Parabolic fits for the velocity profiles in the cross section,  $u_r(z)$ , were done for all the data along the radial axis. The first derivative of these fits is used to evaluate the surface tension.

The location of the drop interface in each focal plane was obtained manually, by observing the location where particles moving from lower planes to the focal plane become well focused. The drop interface profile (half of the drop to be more precise) was obtained from the interface locations at each  $z$  plane and with the apical height  $h_o$  measured from the side view images, by fitting a third order polynomial to these data. This polynomial  $f(d)$  had to satisfy  $f(d = 0) = 0$ ,  $f(d = R) = h_o$ , and  $f'(d = R) = 0$ .

The viscosities with respect to the liquid composition were interpolated from the data in Moosavi et al., 2017; George et al., 2003; Jarosiewicz et al., 2004. The fitting curves follow the form  $\mu(\phi) = e^{(c_1\phi^3+c_2\phi^2+c_3\phi+c_4)}$ , based on the relation presented in Moosavi et al., 2017, where  $c_1$ ,  $c_2$ ,  $c_3$  and  $c_4$  are fitting parameters.

Panel (a) in Figure 3.7 shows the radial velocity at the interface  $u_r(z = h)$  vs. the distance to the contact line  $d$ , for the entire data along the radial axis, for the example in Figure 3.6. The green plot shows the data without the correction to the  $z$  location, and the black plot shows the data with the correction. Panel (b) shows the surface tension gradient vs.  $d$ , for the same example, with and without correction. In both panels (a) and (b), the green curves are not smooth close to the contact line, having peaks at the intersections between the drop interface and the focal plane. This highlights the importance of doing the correction.

### 3.4. MICRO PARTICLE IMAGE VELOCIMETRY DATA ANALYSIS

---

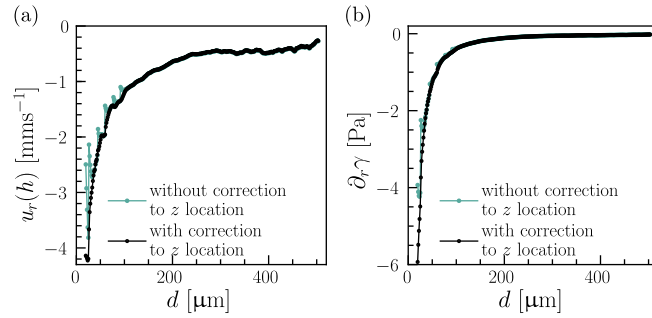


Figure 3.7: (a) Radial velocity evaluated at the interface vs. distance to the contact line with correction of the  $z$  location of the velocity (black line) and without correction (green line). (b) Surface tension gradient vs. distance to the contact line, with and without correction. The data corresponds to the example in Figure 3.6.

# Chapter 4

## Marangoni contraction versus autophobing

**Citation and credit:** Reprinted with permission from Langmuir, volume 37, pp. 3605–3611, 18th March 2021, DOI: 10.1021/acs.langmuir.0c03571. Copyright 2021, American Chemical Society.

**Title:** “*Wetting of Two-Component Drops: Marangoni Contraction Versus Autophobing*”

**Authors:** Michiel A. Hack<sup>1</sup>, Wojciech Kwieciński<sup>2</sup>, Olinka Ramírez-Soto<sup>3</sup>, Tim Segers<sup>1</sup>, Stefan Karpitschka<sup>3</sup>, E. Stefan Kooij<sup>2</sup>, and Jacco H. Snoeijer<sup>1</sup>  
<sup>1</sup>Physics of Fluids Group, Max Planck Center for Complex Fluid Dynamics, Faculty of Science and Technology, University of Twente, P.O. Box 217, 7500 AE Enschede, The Netherlands

<sup>2</sup>Physics of Interfaces and Nanomaterials Group, MESA+ Institute for Nanotechnology, University of Twente, P.O. Box 217, 7500 AE Enschede, The Netherlands

<sup>3</sup>Max Planck Institute for Dynamics and Self-Organization, Am Faßberg 17, 37077 Göttingen, Germany

**Contribution:** I designed and built the  $\mu$ PIV experimental setup, performed the  $\mu$ PIV experiments, analyzed the  $\mu$ PIV experimental data, made the corresponding figures (which are the plots with the data of the flows

inside the droplets), and wrote the corresponding descriptions for these experiments, and edited manuscript.

---

## 4.1 Abstract

The wetting properties of multi-component liquids are crucial to numerous industrial applications. The mechanisms that determine the contact angles for such liquids remain poorly understood, with many intricacies arising due to complex physical phenomena, for example due to the presence of surfactants. Here, we consider two-component drops that consist of mixtures of vicinal alkanediols and water. These diols behave surfactant-like in water. However, the contact angles of such mixtures on solid substrates are surprisingly large. We experimentally reveal that the contact angle is determined by two separate mechanisms of completely different nature, namely Marangoni contraction (hydrodynamic) and autophobing (molecular). The competition between these effects can even inhibit Marangoni contraction, highlighting the importance of molecular structures in physico-chemical hydrodynamics.

## 4.2 Introduction

Many industrial processes require a fundamental understanding of the wetting properties of liquids on solid surfaces (Starov et al., 2018). Examples are inkjet printing (Wijshoff, 2010), oil recovery (Haagh et al., 2019), and lithography (Winkels et al., 2011). A key concept in the description of wetting is the contact angle  $\theta$ , as defined in Figure 4.1. Properties of the liquid together with the surface chemistry of the solid determine the value of  $\theta$  (Young, 1805; Bonn et al., 2009). The wetting properties and contact angles of single-component liquids have been extensively studied (Gennes et al., 2004; Drelich et al., 2020). However, a large number of industrial applications require mixtures of liquids (Leenaars et al., 1990) or the addition of surfactant to enhance the spreading properties of a liquid (Matar et al., 2009). For complex drops consisting of two or more components, the wetting properties are far from understood. The components may phase separate (Tan et al., 2016; Li et al., 2018), selectively evaporate (Sefiane et al., 2008), emulsify (Keiser et al., 2017), adsorb at interfaces (Kim et al., 2016), and even

gravity can play a role (Edwards et al., 2018; Li et al., 2019), leading to intricate wetting properties on solid surfaces.

Here, we study the contact angle  $\theta$  of multi-component drops, where the less volatile component acts as a surfactant on OH-terminated substrates that are fully wetted by water. Figure 4.1 shows the contact angle of drops consisting of water–1,2-hexanediol (1,2-HD) mixtures on a piranha solution-cleaned hydrophilic glass substrate (microscope coverslips, Menzel-Gläser) with minimal pinning. The reported angle is attained within seconds after deposition of the drop (see Supporting Information 4.7). The key result of Figure 4.1 is that  $\theta$  continually increases with the 1,2-HD mass fraction  $\phi$ . This is surprising for two reasons. First, 1,2-HD has been shown to exhibit surfactant-like properties when mixed with water due to its amphiphilic molecular structure (Hajji et al., 1989; Frindi et al., 1991; Székely et al., 2007; Tan et al., 2018). Increasing the mass fraction  $\phi$  of 1,2-HD lowers the surface tension  $\gamma_{LV}$  (see the inset of Figure 4.1), which normally would lead to enhanced spreading. However, the opposite trend is found:  $\theta$  increases with  $\phi$ . A second surprise is that this increase continues above the critical micelle concentration (CMC)  $\phi_{\text{CMC}} \approx 0.1$ , even though  $\gamma_{LV}$  is constant in this range (Romero et al., 2007). Here we show that these unexpected features are the result of two mechanisms of different origins – one of hydrodynamic nature: Marangoni contraction, and the other of molecular nature: autophobing. This resolves the relation between two controversial models for Marangoni contraction (Cira et al., 2015; Karpitschka et al., 2017; Benusiglio et al., 2018) and, for the first time, describes quantitative limitations of the contracted state and its sensitivity to the molecular structure of the surface active component.

## 4.3 Results and Discussion

### 4.3.1 Marangoni contraction

We first turn to the hydrodynamic mechanism, which is known as ‘Marangoni contraction’ (Karpitschka et al., 2017). Some multi-component drops (for example water–1,2-propanediol mixtures) can form non-zero contact angles on high-energy surfaces, even though the individual liquids themselves perfectly wet the surface at equilibrium (i.e.  $\theta = 0^\circ$ ) (Leenaars et al., 1990; Marra et al., 1991; Cira et al., 2015; Karpitschka et al., 2017; Benusiglio et al., 2018).

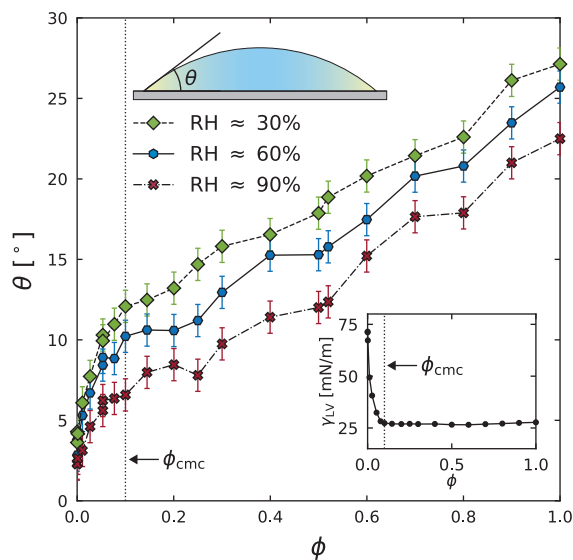


Figure 4.1: Contact angle ( $\theta$ ) of water–1,2-hexanediol (1,2-HD) mixtures as a function of the mass fraction ( $\phi$ ) of 1,2-HD, for various relative humidities (RH). The vertical dotted line indicates the critical micelle concentration ( $\phi_{\text{CMC}} \approx 0.1$ ). The filled areas indicate the measurement error. Schematic: Definition of  $\theta$ . The mass fraction of 1,2-HD (yellow) is higher near the contact line due to selective evaporation. Inset: Surface tension ( $\gamma_{\text{LV}}$ ) of water–1,2-HD mixtures, measured using the pendant drop method.

There are two requirements that need to be satisfied for Marangoni contraction to occur: i) one of the two liquids must be significantly more volatile than the other, and ii) the least volatile liquid should have the lowest surface tension of the two liquids. Selective evaporation at the contact line (where the evaporative flux is highest (Deegan et al., 1997)) of the volatile component (typically water), then leads to a composition gradient in the drop and a surface tension gradient across the drop’s interface. This in turn drives a Marangoni flow towards the center of the drop, which opposes the spreading of the drop, such that the drop is ‘contracted’. The presence of Marangoni contraction invalidates Young’s law, which only holds at equilibrium, i.e. in the absence of flow (Young, 1805; Gennes et al., 2004), and its effect is opposite to Marangoni spreading (Mouat et al., 2020).

Water–1,2-HD mixtures are expected to contract, since 1,2-HD is con-

### 4.3. RESULTS AND DISCUSSION

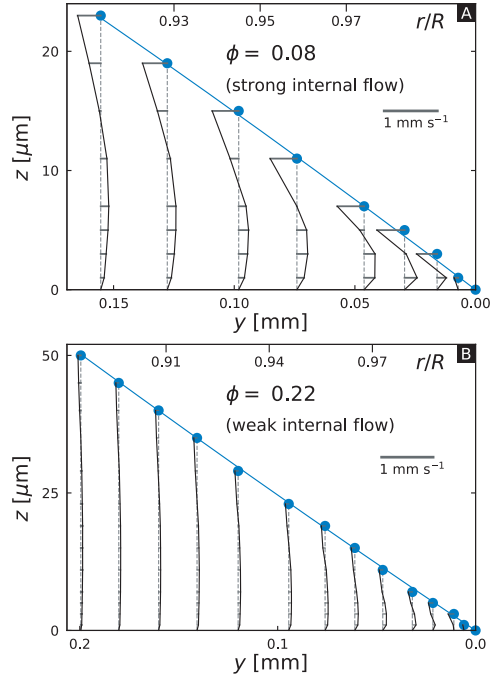


Figure 4.2: Horizontal velocity component in the drops measured using high resolution micro-particle image velocimetry. The blue line indicates the outer surface of the drop. The horizontal lines indicate the velocity, where the direction is indicated by the location with respect to the vertical dashed line. (a) Velocity field for  $\phi = 0.08$  and  $\text{RH} = 71\%$  ( $\theta = 9^\circ$ ). (b) Velocity field for  $\phi = 0.22$  and  $\text{RH} = 40\%$  ( $\theta = 14^\circ$ ), which is significantly weaker than that in (a).

siderably less volatile than water (Li et al., 2018), and has a surface tension lower than that of water (see the inset of Figure 4.1). Figure 4.2(a) shows the flow field inside a  $\phi = 0.08$  drop, as measured using high resolution micro-particle image velocimetry. The blue line indicates the outer surface of the drop, and the contact line is located at  $y = 0$ . A strong inward flow exists near the surface of the drop, while an outward flow towards the contact line is observed in the bulk of the drop. This flow field is typical for Marangoni contracted drops (Karpitschka et al., 2017). To further test the hypothesis that the increase of  $\theta$  is due to Marangoni contraction, we varied the relative humidity (RH). A low RH enhances the evaporation that drives the

flow inside the drop (Semenov et al., 2014). Indeed, Figure 4.1 shows that with a lower RH the raise of  $\theta$  is significantly enhanced, and for small  $\phi$  our data follows the Marangoni contraction scaling law (see Supporting Information 4.7) (Karpitschka et al., 2017). Therefore, we conclude that Marangoni contraction is responsible for the enhanced contact angle of water-1,2-HD drops at small  $\phi$ .

Marangoni contraction alone, however, cannot explain the full range of data in Figure 4.1. At  $\phi = 1$  all surface tension gradients are removed, but nevertheless a large (non-zero)  $\theta$  is observed. Furthermore, a monotonic increase of  $\theta$  with  $\phi$  is observed in Figure 4.1, even though a decrease in  $\theta$  is expected for  $\phi \gtrsim 0.6$ , as is the case for 1,2-propanediol which has been shown to contract, due to smaller surface tension gradients and weaker internal flow (Karpitschka et al., 2017; Benusiglio et al., 2018). Figure 4.2(b) shows the velocity field in a drop at  $\phi = 0.22$ , which is almost one order of magnitude smaller than the velocity in the  $\phi = 0.08$  drop, which is too weak to sustain a contracted drop.

### 4.3.2 Autophobing

Another mechanism must be responsible for the large  $\theta$  measured for large  $\phi$ . We recall the surfactant-like nature of 1,2-HD molecules. Some surfactant-containing liquids are known to autophobe on selected substrates, a phenomenon where  $\theta$  increases due to modification of the solid surface energy by a precursor of adsorbed surfactant molecules (Scales et al., 1986; Zhu et al., 1991; Rupprecht et al., 1991; Birch et al., 1994; Birch et al., 1995; Thiele et al., 2018). This layer of adsorbed molecules, which is of (quasi)monolayer thickness, is of different origin than the liquid precursor that is observed in ‘regular’ wetting (Bonn et al., 2009). The surface energy of a precursor depends on RH, the composition of the drop, and the molecular nature of the adsorbing molecules (Afsar-Siddiqui et al., 2004; Matar et al., 2009; Thiele et al., 2013). To the best of our knowledge, autophobing and Marangoni contraction have never been reported to compete in a single multi-component system. Importantly, the apparent shapes of the drops is indistinguishable between the two states, but their dynamic behavior, especially their mobility and internal flows, are very different (Benusiglio et al., 2018).

To induce autophobing, surfactant molecules have to adsorb on the solid-liquid interface (inside the drop) or on the solid-vapor interface (the precursor outside the drop), resulting in an overall decrease of  $\gamma_{SV} - \gamma_{SL}$ , where  $\gamma_{SV}$  is

### 4.3. RESULTS AND DISCUSSION

the surface tension of the solid-vapor interface, and  $\gamma_{\text{SL}}$  is the surface tension of the solid-liquid interface. In Figure 4.3(a) we report the adsorption properties of water–1,2-HD mixtures on the solid-vapor interface under ambient conditions, measured using ellipsometry (Novotny et al., 1991). Here,  $\Gamma$  is the number density of adsorbed 1,2-HD molecules, which we normalize by  $\Gamma_{\infty}$ , the number density of adsorbed molecules corresponding to saturated coverage (measured in a closed chamber with saturated 1,2-HD vapor). All values of  $\Gamma/\Gamma_{\infty}$  were obtained after equilibrium was reached, as determined by measuring the temporal evolution of the adsorbed layer (Figure 4.3(b)), typically within a few minutes after deposition of the liquid. Complete desorption of the precursor upon removal of the drop typically takes an order of magnitude longer than the time it takes for the precursor to form (see Supporting Information 4.7).

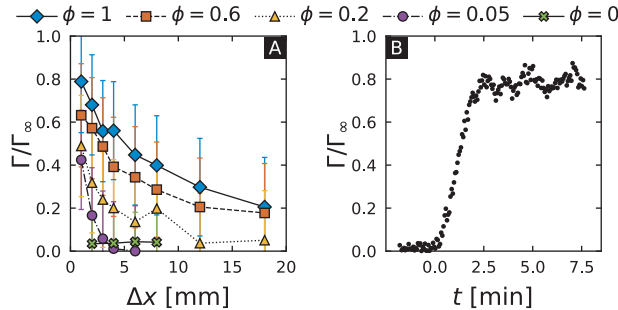


Figure 4.3: (a) Normalized adsorption density ( $\Gamma/\Gamma_{\infty}$ ) as a function of distance to the contact line ( $\Delta x$ ) for several water–1,2-HD mixtures. (b) Temporal adsorption dynamics of pure 1,2-HD at  $\Delta x \approx 5$  mm. The liquid is deposited at  $t = 0$ .

Figure 4.3(a) shows clear evidence of the adsorption of 1,2-HD molecules on the substrate. Additionally, it shows that  $\Gamma/\Gamma_{\infty}$  decreases both with the distance to the contact line  $\Delta x$  and with  $\phi$ . This indicates that the concentration of 1,2-HD in the vapor surrounding the drop is of key importance to the equilibrium surface concentration of molecules adsorbed on the substrate. As we increase  $\Delta x$  or decrease  $\phi$ , the concentration of 1,2-HD molecules in the vapor decreases. Hence, a lower amount of 1,2-HD molecules is available in the vapor to adsorb on the substrate, while water becomes more abundant. Therefore, water coverage increases with increasing  $\Delta x$  and decreasing

$\phi$ , resulting in a lower  $\Gamma/\Gamma_\infty$ .

This indeed offers a direct explanation of the result in Figure 4.1, even when  $\phi > \phi_{\text{CMC}}$ , where  $\theta$  increases with  $\phi$  and decreases with RH. An increase in RH leads to a lower  $\Gamma/\Gamma_\infty$ , due to the increased water coverage. Conversely, the 1,2-HD coverage increases by increasing  $\phi$ . Adsorbed molecules change the surface energy of the substrate, making it more hydrophobic (Bera et al., 2016). This offers clear and direct evidence that the contact angles of autophobed drops depend on the RH of the close surrounding of the contact line. We remind that the internal flow is very weak at large  $\phi$  (Figure 4.2(b)), for which we thus expect to recover the true equilibrium contact angle. In Young’s law, which remains valid at equilibrium in the presence of surfactants (Thiele et al., 2018), the increased hydrophobicity of the substrate is reflected in the  $\gamma_{\text{SV}} - \gamma_{\text{SL}}$  term, which becomes smaller with increasing  $\Gamma/\Gamma_\infty$ . Consequently,  $\theta$  must increase, even though  $\gamma_{\text{LV}}$  remains constant above the CMC. This mechanism is reminiscent of the “modified Young’s law” modeling approach used for multi-component drops in Cira et al. (2015) and Benusiglio et al. (2018). Molecules may also adsorb on the solid-liquid interface, which we are unable to measure using our experimental setup (Bera et al., 2018). Such adsorption, if dominant, could lower  $\gamma_{\text{SL}}$ , increase  $\gamma_{\text{SV}} - \gamma_{\text{SL}}$ , and thus lead to a decrease in  $\theta$ . The increase of  $\theta$  and strong dependence of  $\theta$  on RH (Figure 4.1) indicate that adsorption on the solid-vapor interface is dominant over adsorption on the solid-liquid interface, leading to a decrease in  $\gamma_{\text{SV}} - \gamma_{\text{SL}}$  and an increase in  $\theta$  at large  $\phi$ .

Contrary to many previous works on autophobing (Marmur et al., 1981; Frank et al., 1996; Takenaka et al., 2014; Bera et al., 2016; Zhong et al., 2016; Bera et al., 2018; Tadmor et al., 2019), we do not see an initial spreading phase followed by a retraction to the quasi-steady  $\theta$  (see Supporting Information 4.7). This is likely due to the relatively high diffusion coefficient of 1,2-HD, which is a result of its small molecular size in comparison to other more common surfactants (Kirkwood et al., 1948). The region of the substrate that is sampled by the liquid in determining the stationary  $\theta$  is no larger than  $10 \mu\text{m}$  (Decker et al., 1999). The timescale associated with forming the equilibrium adsorption layer within this region is smaller than the spreading timescale (Frank et al., 1995b), which is relatively long due to the high viscosity of 1,2-HD ( $\eta \approx 82 \text{ mPa}\cdot\text{s}$  (Jarosiewicz et al., 2004)).

### 4.3.3 Effect of the molecular structure

Our experiments show that water–1,2-HD mixtures exhibit a competition between Marangoni contraction and autophobing. How generic is the observed competition between Marangoni contraction and autophobing and what is the influence of the surface activity  $d\gamma_{LV}/d\phi$ ? Here, we address these questions by considering three shorter vicinal alkanediols: 1,2-propanediol (1,2-PrD), 1,2-butanediol (1,2-BD), and 1,2-pentanediol (1,2-PeD), which have three, four, and five carbon atoms in their chain, respectively. These diols are non-volatile and have a low  $\gamma_{LV}$  (Karpitschka et al., 2010). The surfactant-like behavior (i.e. the surface activity  $d\gamma_{LV}/d\phi$ ) depends on the length of the aliphatic chain. Short chain alkanediols show weaker surfactant-like behavior (smaller  $d\gamma_{LV}/d\phi$ ) due to the decreased hydrophobicity of the molecule (Karpitschka et al., 2010; Smit et al., 1990).

We study the properties of these diols using the same procedure as we used for 1,2-HD. Figure 4.4(a) shows  $\theta$  as a function of  $\phi$  at RH  $\approx$  60%. Starting at small  $\phi$ , we see that all diols follow a universal curve. This is perfectly consistent with Marangoni contraction, as long as  $d\gamma_{LV}/d\phi$  is sufficiently smaller than zero, and water remains more volatile in the mixture, the hydrodynamic mechanism remains insensitive to molecular details, while absolute flow velocities depend on the material parameters. Mixtures of other liquids are also expected to contract as long as their volatility and surface tension contrasts are in the same regime as those of water and carbon diols (Cira et al., 2015). By contrast, the curves start to diverge and the length of the aliphatic chain matters for larger  $\phi$  – consistent with autophobing. The longest diol studied here, 1,2-HD, exhibits strong autophobing behavior. As we move to short chain diols, the autophobing strength becomes smaller, indicated by smaller values of  $\theta$  at  $\phi = 1$ . Additionally, Figure 4.4(a) shows that Marangoni contraction is the dominant mechanism up to a larger  $\phi$  for shorter diols. While for 1,2-HD, autophobing is dominant starting from  $\phi \approx 0.3$ , for 1,2-PrD, by contrast, the full range of  $\phi$  is consistent with Marangoni contraction – there is no autophobing at all. Hence, a higher surface activity does not necessarily lead to stronger Marangoni contraction. In fact, the surface activity of the molecules may inhibit contraction, leading to autophobed drops. For example, at large  $\phi$ , 1,2-HD (highest  $d\gamma_{LV}/d\phi$ ) shows the strongest autophobing, whereas 1,2-PrD (lowest  $d\gamma_{LV}/d\phi$ ) drops are contracted. Thus, our results show that, in addition to the two requirements listed above, there is a third requirement that needs to be satisfied for drops to contract: the

contact angle achievable by Marangoni contraction needs to be larger than the microscopic contact angle as governed by molecular forces. However, the microscopic angle may be larger than zero.

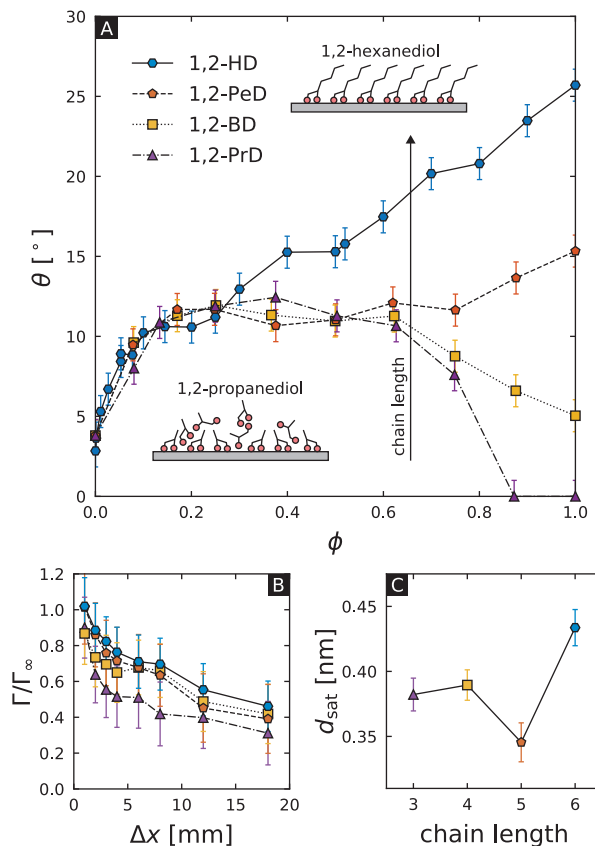


Figure 4.4: (a) Contact angle ( $\theta$ ) as a function of mass fraction ( $\phi$ ) for several mixtures of water and vicinal alkanediols (RH = 60%). The schematics show the structure of adsorbed 1,2-propanediol molecules and 1,2-hexanediol molecules. (b) Normalized adsorption density ( $\Gamma/\Gamma_\infty$ ) as a function of distance to the contact line ( $\Delta x$ ). (c) Thickness of the saturated film ( $d_{\text{sat}}$ ) for several vicinal alkanediols.

All four molecules adsorb on the substrate, as seen from the ellipsometry measurements presented in Figure 4.4(b). The reduced autophobing strength of the shorter diols is caused by the shorter hydrophobic chain in these molecules. The distance between the hydrophilic and hydrophobic parts

of the molecule is smaller in shorter chain molecules, meaning that the polar nature of the hydroxyl groups becomes more relevant for the surface energy of an adsorbed layer of a short chain molecule such as 1,2-PrD. The result is a more hydrophilic surface and therefore a smaller  $\theta$ . Figure 4.4(b) shows that all diols studied here adsorb onto the substrate with similar  $\Gamma/\Gamma_\infty$ . However, as shown in Figure 4.4(c), not all adsorb in the same way as 1,2-HD. Despite their smaller size, the saturated thickness  $d_{\text{sat}}$  of 1,2-PrD and 1,2-BD is larger than that of 1,2-PeD, and only slightly smaller than that of 1,2-HD, suggesting that they do not form monolayers (an estimate of the size of each molecule is given in the Supporting Information 4.7), since a monotonic increase in  $d_{\text{sat}}$  with the chain length is expected if monolayers are formed. Their hydroxyl groups remain partially exposed, allowing them to form disordered multi-layered structures (see the schematic in Figure 4.4(a)) similar to layers of adsorbed water molecules (Hu et al., 1995), hence they do not strongly affect the surface energy. By contrast, 1,2-PeD and 1,2-HD likely adsorb in a monolayer structure (see the schematic in Figure 4.4(a)), indicated by the increasing  $d_{\text{sat}}$  between 1,2-PeD and 1,2-HD in Figure 4.4(c), and the decrease in  $d_{\text{sat}}$  between 1,2-PrD and 1,2-PeD. This means that their long aliphatic chains are exposed, increasing the hydrophobicity of the surface. Therefore, autophobing occurs at large  $\phi$  for molecules with a long aliphatic chain, due to the strong effect of the adsorbed molecules on the surface energy of the solid. By contrast, adsorbed molecules with a short aliphatic chain have little effect on the surface energy of the solid and Marangoni contraction dominates over the full range of  $\phi$ . One can thus tune  $\theta$  over a large range by selecting the correct diol and a particular combination of  $\phi$  and RH.

## 4.4 Conclusion

Our results reveal that Marangoni contraction and autophobing both provide valid descriptions for the wetting of two-component drops, albeit in different regimes. A minute change in one of the control parameters is sufficient to change the dominant wetting mechanism. While the visual appearance of drops in either of the two wetting states is indistinguishable, Figure 4.2 demonstrates a strong difference in their internal flows. We have shown (Figure 4.1 and 4.4(a)) that Marangoni contraction is possible only if the microscopic contact angle, as governed by molecular forces, is smaller than the angle achievable by contraction. Additionally, we show (Figure 4.2) that

the internal flows should be used to determine the state of a drop rather than the contact angle or apparent drop shape. By systematically changing the molecular structure of the volatile liquid, we show that a higher surface activity  $d\gamma_{LV}/d\phi$  does not necessarily lead to stronger Marangoni contraction. In fact, excessive surface activity may inhibit contraction, and lead to drops whose contact angle is governed by molecular forces. Hence, the chemical structure of the liquid needs to be taken into account when designing multi-component drop systems with specific properties. Importantly, these mechanisms are generic and expected to be present in most mixtures containing (volatile) surfactant-like liquids (for example single alcohols).

Marangoni contracted drops are attractive for technological applications due to their high mobility (Cira et al., 2015; Huethorst et al., 1991; Benusiglio et al., 2018), which is suppressed for drops in the autophobing or partial wetting states. Our result may also be of interest to applications that require high contact angles of drops consisting of low surface tension liquids, such as inkjet printing (Wijshoff, 2018) or semiconductor processing (Leenaars et al., 1990).

## 4.5 Experimental methods

### 4.5.1 Contact angle measurements

The contact angle  $\theta$  was determined from side-view images (obtained using a Ximea XiQ MQ013MG-ON camera with Zeiss Makro-Planar 1:2.8 f=60 mm lens with Olympus ILP-2 light source). We determined  $\theta$  by fitting a circle to the drop interface and a straight line to the substrate. The height  $H$  and base radius  $R$  of the drop are extracted from the circle fit, and used to calculate the contact angle using  $\theta = 2 \tan^{-1}(H/R)$ . The uncertainty in the contact angle, which originates from the pixel error and small variations in time (see Figure S1), is estimated to be  $\pm 1^\circ$ . The relative humidity RH was controlled using a home-built apparatus (for details see Bruning et al., 2018), and was constantly monitored along with temperature  $T$  during the measurement using a sensor (Honeywell HIH6130) in the setup. Example measurements of the time evolution of  $\theta$  for  $\phi = 0.08$  and  $\phi = 1$  are shown in the Supporting Information 4.7.

### 4.5.2 Surface tension measurements

The surface tension measurements were performed using the pendant drop method (Hansen et al., 1991). For each aqueous solution of 1,2-hexanediol, the surface tension of ten drops of 2.5  $\mu\text{L}$  was measured ( $T = 20\text{ }^\circ\text{C}$ ,  $\text{RH} = 45\%$ ), with ten images collected for each drop over a period of 1 s. The surface tensions  $\gamma_{\text{LV}}$  reported in the inset of Figure 1 are an average of these measurements (i.e. 100 images per datapoint), with an average error of 0.57 mN/m.

### 4.5.3 Micro-particle image velocimetry measurements

The flow velocities within evaporating binary drops of 1,2-hexanediol and water were quantified by micro-particle image velocimetry ( $\mu\text{PIV}$ ). We used fluorescent polystyrene microspheres (Thermo Fisher Scientific F8809, 0.2  $\mu\text{m}$  diameter, stock solution concentration 2% w/v) as tracers, with a mass fraction of  $7.8 \cdot 10^{-5}$  of the particle stock solution in the final mixture. The particles within the drops were visualized with an inverted epifluorescence microscope (Nikon Eclipse Ti2), equipped with a water immersion objective (Nikon CFI APO LWD 20 $\times$  WI) with a numerical aperture of 0.95. Thin correlation depths (i.e., high plane selectivity) require diffraction-limited imaging. To achieve this not only close to the substrate but also in the bulk fluid, the refractive index of the immersion medium has to be close to that of the working medium, for which water immersion objectives are ideally suited. The focal plane was parallel to the substrate and moved in vertical direction with the closed-loop focusing stage of the microscope. The time required to switch between planes was less than 100 ms. For each  $z$ -plane, a sequence of approximately 500 frames was recorded with a high speed camera (Phantom VEO 4K 990L, imaging speed at 900 to 1000 fps). Thus, the time required for a full  $z$ -scan was on the order of approximately 10 s, much shorter than the time scale on which the flow velocities change for a quasi-stationary drop. This was checked by comparing data from successive upward and downward scans. To evaluate the flow velocities, the images were analyzed with an in-house developed cross-correlation based algorithm with adaptive interrogation window sizes and correlation averaging over approximately 100 frames. The analysis was implemented through the Python API of Tensor Flow, to enable fast computation on graphics processing units. Example velocity fields in the  $z$ -plane are shown in the Supporting Informa-

tion 4.7. The velocities presented in Figure 4.2 were obtained by azimuthally averaging over approximately 100  $\mu\text{m}$ . Additionally, simultaneous shadowgraphy of the drop contour was performed to record the contact angle with a second camera (Point Grey Grasshopper2, imaging speed at 27 fps) through a macro lens (Thorlabs Bi-Telecentric lens, 1.0 $\times$ , working distance 62.2 mm). Experiments were conducted in a humidity-controlled chamber mounted on top of the microscope. As substrates we used piranha-cleaned microscope coverslips (Menzel Gläser).

#### 4.5.4 Ellipsometry measurements

The ellipsometry measurements (J. A. Woolam Co. VB-400-VASE ellipsometer with WVASE32 software) were performed on  $2 \times 2 \text{ cm}^2$  piranha solution-cleaned silicon (100) substrates (Okmetic) in ambient conditions ( $T = 21 \text{ }^\circ\text{C}$ ,  $\text{RH} = 40 \pm 5\%$ ). The thickness  $d$  of the layer of adsorbed molecules was obtained by fitting the obtained ellipsometric spectrum to a model of a surface composed of a silicon substrate with a native oxide layer and the Cauchy layer on top. The thickness of the native oxide layer (typically 1.8 nm for these substrates) was determined for each substrate separately before performing the adsorption experiments. The Cauchy layer is an empirical model for the dependence of the refractive index on the wavelength of a dielectric layer:

$$n(\lambda) = A + B/\lambda^2 + C/\lambda^4 + \dots, \quad (4.1)$$

where  $n$  is the refractive index,  $\lambda$  is the wavelength of the light that is used, and  $A$ ,  $B$ ,  $C$  are the material-dependent empirical coefficients (Fujiwara, 2007). Here, we used the values  $A = 1.45$ ,  $B = 0.1$ ,  $C = 0$ , and all other higher order terms were set to zero.

During the measurement, the substrate is vertically placed above a Teflon container, a sketch of this configuration is available in the Supporting Information 4.7. A dynamic scan (3.5 eV,  $75^\circ$ ) is used to resolve the adsorption of molecules over time. The measurement spot is located at a distance  $\Delta x = 1 \text{ mm}$  from the liquid interface, and has a diameter of approximately 1 mm. The obtained thickness is an average over the area of the measurement spot. To obtain the thickness of the adsorbed layer we perform a measurement of the ellipsometric spectrum (1.2 - 4.5 eV,  $75^\circ$ ), once the dynamic measurement indicates that the adsorption has reached equilibrium. The

## 4.6. ACKNOWLEDGEMENT

---

normalized adsorption density  $\Gamma/\Gamma_\infty$  is calculated from the thickness using  $\Gamma/\Gamma_\infty = d/d_{\text{sat}}$ . The value of  $d_{\text{sat}}$ , the thickness of the adsorbed film under saturated vapor conditions, is measured in a separate experiment in a closed chamber. The uncertainty in the ellipsometry measurements originates from the uncertainty in the native oxide layer thickness and the uncertainty in the Cauchy layer fit which is used to determine the adsorbed layer thickness.

The substrate on which the adsorption is measured is never in direct contact with the liquid. A similar technique was used by Novotny et al., 1991. This means that all measurements only take into account the molecules that are transported across the vapor phase separating the substrate and liquid. We compare a measurement with gap (i.e. the case where no direct contact between the substrate and the liquid exists) to one without gap (i.e. the case where direct contact between the substrate and liquid exists; the drop was placed directly on the substrate) in the Supporting Information 4.7. Within the error margin there is no significant difference between the two measurements, indicating that the bulk of molecules adsorbed on the solid are transported across the vapor, and not, for instance, by fluid flow in a precursor film on the substrate.

## 4.6 Acknowledgement

M. A. H., W. K. and O. R.-S. contributed equally to this manuscript. We thank M. Flapper, W. Tewes and H. Wijshoff for stimulating discussions. Financial support from an Industrial Partnership Programme of the Netherlands Organisation for Scientific Research (NWO), cofinanced by Canon Production Printing Netherlands B.V., University of Twente, and Eindhoven University of Technology, and from the University of Twente–Max Planck Center “Complex fluid dynamics–Fluid dynamics of Complexity” is acknowledged.

## 4.7 Supporting Information

### 4.7.1 Contact angle measurements

See Figure 4.5.

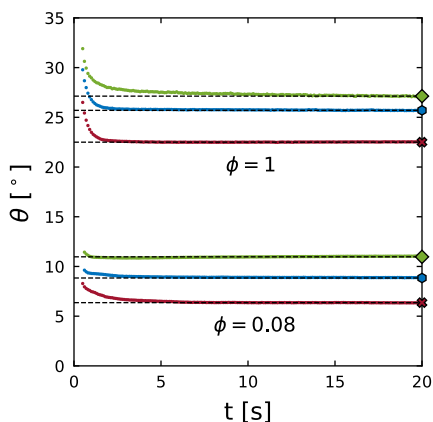


Figure 4.5: Evolution of the contact angle ( $\theta$ ) over time ( $t$ ) for  $\phi = 0.08$  (bottom three lines) and  $\phi = 1$  (top three lines) for RH = 30% (green lines), RH = 60% (blue lines) and RH = 90% (red lines). The drops are gently placed at  $t = 0$ , after which a rapid decrease of  $\theta$  to a quasi-steady value is observed. The horizontal black dashed lines and large markers (at  $t = 20$  s) indicate averages of all values in the quasi-steady regions (from approximately  $t = 10$  s onwards) and correspond to the datapoints in Figure 1 of the main text.

#### 4.7.2 Micro-particle image velocimetry measurements

See Figure 4.6.

#### 4.7.3 Ellipsometry measurements

See Figure 4.7.

#### 4.7.4 Marangoni contraction scaling law

Figure 4.8(a) shows all data from Figure 1 and Figure 4(a) of the main text. This data is scaled according to the scaling law  $\theta(\phi) \propto (\text{RH}_{\text{eq}}(\phi) - \text{RH})^{1/3}$  (i.e. Eq. 1 from Karpitschka et al., 2017) in Figure 4.8(b). Figure 4.8(c) shows  $\text{RH}_{\text{eq}}$ , the relative humidity at which a drop spreads completely (i.e.  $\theta = 0^\circ$ ), as determined by a model equation (Eq. 7 from Karpitschka et al., 2017), which is used in Figure 4.8(b). All data points below the red line in Figure 4.8(d) indicate experiments where the contact angle should be zero if

## 4.7. SUPPORTING INFORMATION

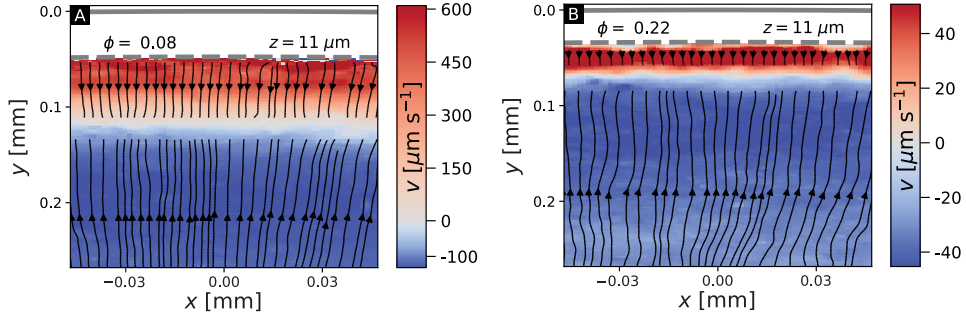


Figure 4.6: Example velocity fields in the  $z$ -plane for (A)  $\phi = 0.08$ , RH = 71% and (B)  $\phi = 0.22$ , RH = 40%. The thick grey line denotes the three-phase contact line at the substrate ( $z = 0$ ). The dashed line indicates the interface of the drop at  $z = 11 \mu\text{m}$ .

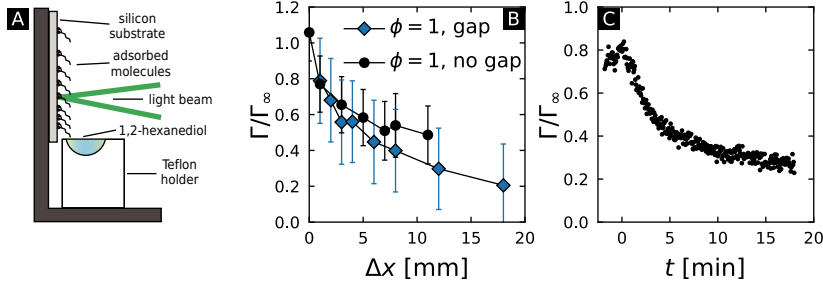


Figure 4.7: (A) Ellipsometry setup. The substrate is mounted vertically, and is not in direct contact with the liquid (here: 1,2-hexanediol). The adsorption of molecules is measured at a small distance from the liquid's interface. (B) Adsorption close to pure 1,2-hexanediol drops. A 'gap' means that the substrate on which the ellipsometry measurement is performed is not in direct contact with the liquid (as sketched in Figure 4.7A). Conversely, 'no gap' means that there is direct contact between the liquid and the substrate. (C) Temporal desorption dynamics of pure 1,2-HD at  $\Delta x = 5 \text{ mm}$ . The container with liquid is removed at  $t = 0$ , after which an immediate change in  $\Gamma/\Gamma_\infty$  is visible. Complete desorption of the adsorbed molecules takes an approximately an order of magnitude longer than adsorption (the adsorption dynamics are shown in Figure 3B of the main text).

the contact angle is determined by Marangoni contraction, yet, for most of these experiments, the contact angle is larger than zero due to autophobing (c.f. Figure 4.8(a)). This prevents us from experimentally determining  $\text{RH}_{\text{eq}}$ . The key point of Figure 4.8 is the excellent collapse of the data for  $\phi \lesssim 0.2$ , indicating that Marangoni contraction is the dominant mechanism for these mass fractions.

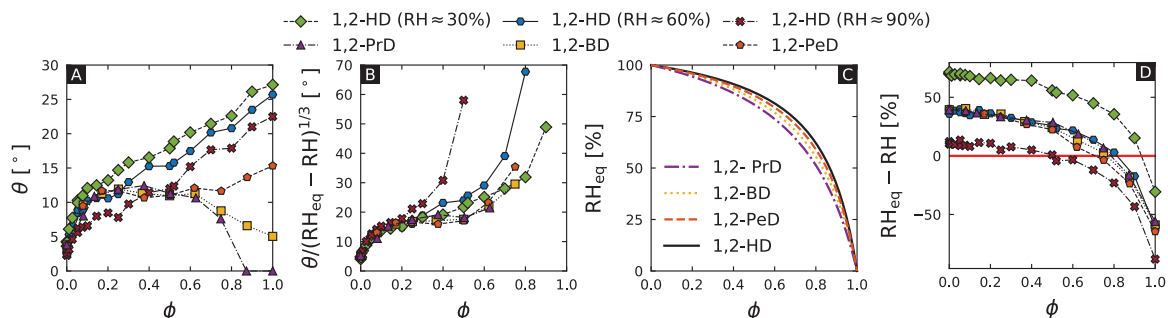


Figure 4.8: (a) Contact angle ( $\theta$ ) as a function of mass fraction ( $\phi$ ) of the diol. This is the data that is shown in Figure 1 and Figure 4(a) of the main text. (b) Marangoni contraction scaling law (Eq. 1 from Karpitschka et al., 2017) applied to the data in (a). Note the excellent collapse for small  $\phi$ . (c) The relative humidity at which the drop spreads completely ( $\text{RH}_{\text{eq}}$ ) as a function of mass fraction as determined by the model (Eq. 7 from Karpitschka et al., 2017). (d) Difference between  $\text{RH}_{\text{eq}}$  and RH as a function of mass fraction. Any data point below the red line should spread completely ( $\theta = 0^\circ$ ), but autophobing prevents this (c.f. (a)).

#### 4.7.5 Estimate of molecular size

The length of a molecule can be estimated using

$$l = \left( \frac{M}{\rho N_A} \right)^{\frac{1}{3}} \quad (4.2)$$

where  $M$  and  $\rho$  are the molar mass and density of the molecule, and  $N_A = 6.022\,140\,76 \times 10^{23}$  is the Avogadro constant. An overview of the properties and resulting molecular lengths is shown in Table 4.1. Note that these

## 4.7. SUPPORTING INFORMATION

---

lengths are approximations; the molecular length depends strongly on the confirmation of the molecule, which is influenced by the surroundings of the molecule, which is not accounted for in Eq. 4.2.

molecule	$M$ [g/mol]	$\rho$ [kg/m <sup>3</sup> ]	$l$ [Å]
1,2-propanediol	76.09	1036	4.96
1,2-butanediol	90.12	1006	5.30
1,2-pentanediol	104.15	971	5.63
1,2-hexanediol	118.17	951	5.91

Table 4.1: Properties of several alkane diols and the resulting estimated molecule lengths obtained using Eq. 4.2.

# Chapter 5

## Compositional Evolution of Marangoni-contracted drops

**Citation and credit:** Reprinted from O. Ramírez-Soto and S. Karpitschka, 7th February 2022, Taylor dispersion in thin liquid films of volatile mixtures: A quantitative model for Marangoni contraction, *Physical Review Fluids*, volume 7: L022001. DOI: 10.1103/PhysRevFluids.7.L022001.

**Title:** *“Taylor Dispersion in Thin Liquid Films of Volatile Mixtures: A Quantitative Model for Marangoni Contraction”*

**Authors** Olinka Ramírez-Soto<sup>1</sup> and Stefan Karpitschka<sup>1</sup>

<sup>1</sup>Max Planck Institute for Dynamics and Self-Organization (MPI-DS), Am Fassberg 17, 37077 Göttingen

**Contribution:** I designed and built the experimental setup, performed the experiments, analyzed the experimental data, made all figures, and edited manuscript.

---

### 5.1 Abstract

Marangoni contraction of sessile droplets occurs when a binary mixture of volatile liquids is placed on a high-energy surface. Although the surface is wetted completely by the mixture and its components, a quasi-stationary non-vanishing contact angle is observed. This seeming contradiction is caused

by Marangoni flows that are driven by evaporative depletion of the volatile component near the edge of the droplet. Here we show that the composition of such droplets is governed by Taylor dispersion, a consequence of diffusion and strong internal shear flow. We demonstrate that Taylor dispersion naturally arises in a self-consistent long wave expansion for volatile liquid mixtures. Coupled to diffusion limited evaporation, this model quantitatively reproduces not only the apparent shape of Marangoni-contracted droplets, but also their internal flows.

## 5.2 Introduction

Wetting and dewetting of volatile liquid mixtures on solid surfaces is abundant in natural phenomena and technological applications (Lohse et al., 2020; Brutin et al., 2018; Snoeijer et al., 2013; Bonn et al., 2009; Smith et al., 2018). Many examples are found in everyday life situations, for instance, biological fluids like blood (Brutin et al., 2010) and tears (Traipe-Castro et al., 2014), inks for inkjet printing (Gans et al., 2004; Park et al., 2006), and paints for artistic techniques (Zenit, 2019; Giorgiutti-Dauphiné et al., 2016). Marangoni contraction is a prime example that gained significant attention recently, not least motivated by its applications in printing and semiconductor processing (Cira et al., 2015; Karpitschka et al., 2017; Benusiglio et al., 2018; Sadafi et al., 2019; Malinowski et al., 2020; Williams et al., 2021; Hack et al., 2021; Shiri et al., 2021): Volatile liquids seemingly dewet from high energy surfaces over which they spread if evaporation was suppressed, see Figure 5.1(a, c). Evaporation causes compositional (Cira et al., 2015; Karpitschka et al., 2017; Benusiglio et al., 2018; Williams et al., 2021; Hack et al., 2021) or thermal (Shiri et al., 2021) gradients, inducing an inward Marangoni flow which contracts the droplet. The opposite case may lead to Marangoni spreading and contact-line instabilities (Darhuber et al., 2003; Gotkis et al., 2006; Wodlei et al., 2018). The dynamics of contact lines is a multi-scale problem which involves both macroscopic hydrodynamics and molecular interactions (Bonn et al., 2009; Oron et al., 1997). Thus, while multi-component liquids with pinned contact lines are understood quite well (Zhang et al., 2011; Christy et al., 2011; Soulie et al., 2015; Marin et al., 2019; Rossi et al., 2019; Karapetsas et al., 2016; Diddens, 2017; Diddens et al., 2017; Li et al., 2019; Gaalen et al., 2021; Pahlavan et al., 2021a), moving contact lines challenge both experimentalists and theoreticians.

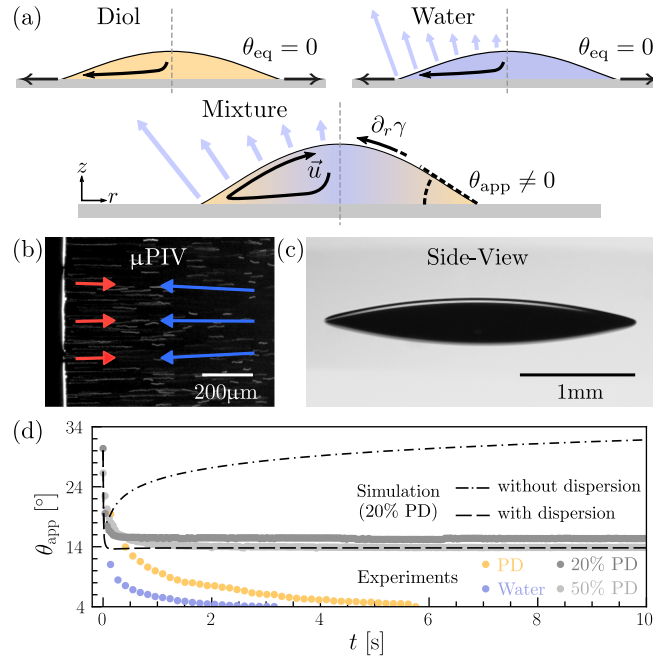


Figure 5.1: (a) Pure droplets of water or diols spread on hydrophilic glass, but their mixtures display Marangoni contraction: Evaporative enrichment drives a Marangoni flow which compensates the capillarity-driven spreading flow. (b) Streak image of fluorescent particles inside a drop, in a plane parallel to the substrate. Close to the contact line, the flow is directed into the droplet. (c) Side aspect of the same drop. (d) Apparent contact angle vs. time for a relative humidity  $\sim 35\%$ : experiments (symbols) with pure liquids (blue & yellow) and mixtures (gray), compared to long-wave simulations of a mixture with 20%PD, with and without Taylor dispersion (dashed and dash-dotted lines, respectively). Simulations are in close agreement with experimental data only when dispersion is taken into account.

Dimensional reduction in the limit of long waves is a powerful tool to analyze moving contact lines (Oron et al., 1997; Craster et al., 2009; Gaalen et al., 2021; Thiele et al., 2012; Thiele et al., 2016; Xu et al., 2015; Gaalen et al., 2021): The evolution of the local liquid height is derived from the net flux, treating the short (vertical) axis fully implicitly. For mixtures, however, vertical compositional gradients are unavoidably generated by shearing any horizontal gradients. This impedes the use of dimensional reduction, unless taking the limit of infinitely fast diffusion along the short axis. All existing

### 5.3. EXPERIMENTS

---

lubrication models are formulated in this limit (Moshinskii, 2004; Ajdari et al., 2006; Mukahal et al., 2017; Vilquin et al., 2020). Commonly, however, the time scale of diffusion is finite and, in combination with shear flow, leads to strong dispersion. This so-called Taylor-Aris dispersion (Taylor, 1953; Aris, 1956) has important consequences in many natural (Chakrabarti et al., 2020) and technological scenarios (Ottino et al., 2004). To date it remains unclear whether shear dispersion is consistent with a long-wave expansion, so no expression for the effective dispersion in general thin-film flows is available in literature.

Here we show that small vertical compositional gradients are in agreement with the usual assumptions in a long-wave expansion. We provide a general expression for the effect of shear dispersion in thin liquid films, thus enabling lubrication theory for the first time to be consistently applied to bulk liquid mixtures. Our model is in quantitative agreement with experimental observations of Marangoni-contracted droplets. We expect our analysis to be relevant well beyond droplet studies, as it offers a general route for implementing the effect of advected bulk fields in dimensional reduction problems.

## 5.3 Experiments

We measured the apparent shape and the internal flows of Marangoni-contracted droplets inside an atmospheric control chamber (size  $\sim 10\text{ cm} \times 10\text{ cm} \times 10\text{ cm}$ ), at room temperature. The droplets were composed of mixtures of water (“Milli-Q”, resistivity  $18\text{ M}\Omega \cdot \text{cm}$ ) and a carbon diol (Sigma Aldrich,  $\geq 98\%$ ). Piranha cleaned microscopy glass coverslips ( $170\text{ }\mu\text{m}$  thick) were used as substrates (see supplement 5.8 for details). The humidity was set by continuously injecting a well-defined mixture of dry and moist nitrogen behind gas-permeable membranes at the side-walls of the chamber. Droplets had initial volumes of  $0.5$  to  $1\text{ }\mu\text{L}$ . Micro particle image velocimetry ( $\mu\text{PIV}$ , Figure 5.1(b)) was performed with an inverted fluorescence microscope and a high-aperture water-immersion objective (20x, NA 0.95) to allow for diffraction limited imaging in the bulk droplet. Polystyrene microspheres (Thermo Fisher Scientific F8809, diameter  $200\text{ nm}$ ) were used as flow tracers, with a mass fraction of  $7.8 \times 10^{-5}$  of the particle stock solution in the binary mixture. Images of the particles were captured with a high-speed camera at 600 to 1000 FPS, quickly switching between  $z$ -planes by automating the focus system of the microscope. Simultaneous side-view imaging of the drop was

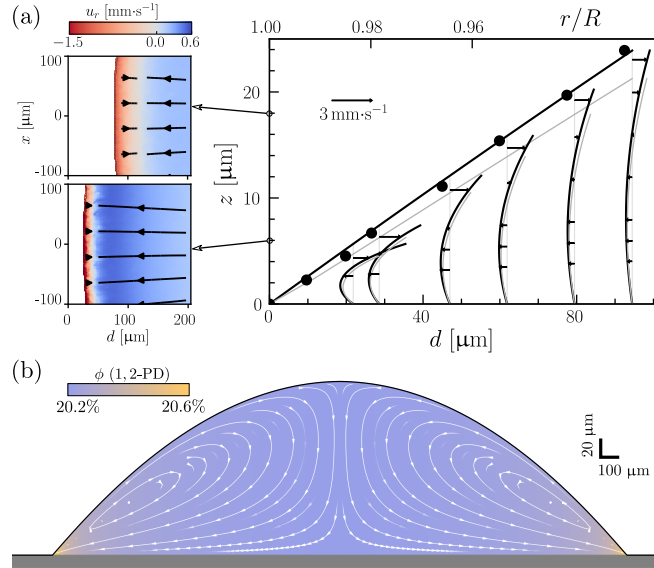


Figure 5.2: Flows in a Marangoni-contracted droplet ( $\phi = 0.20$  1,2-PD, RH = 33%). (a) Cross-sectional view: free surface (black discs & linear fit), horizontal velocity (black arrows) and parabolic fits (black lines) from experiments, compared to simulation results including shear dispersion (gray). Inset: experimental velocities and stream lines in two horizontal planes ( $z = 18 \mu\text{m}$  and  $6 \mu\text{m}$ ). (b) Simulation snapshot ( $t = 8.0$  s) with stream lines (white) and composition (color code).

performed with a telecentric lens (Figure 5.1(c)).

Figure 5.1(d) shows the evolution of the apparent contact angle  $\theta_{app}$  of spreading drops of pure water (diol mass fraction  $\phi = 0$ ), pure 1,2-Propanediol (PD,  $\phi = 1$ ) and of their mixtures. Pure liquids spread into complete wetting. In contrast, the binary mixtures reach a stationary non-equilibrium apparent contact angle  $\theta_{app} > 0$  shortly after deposition. The drops stay in this contracted state for several minutes. This wetting behavior has been described previously (Cira et al., 2015; Benusiglio et al., 2018; Karpitschka et al., 2017), showing that  $\theta_{eq}$  depends on  $\phi$  and the ambient relative humidity RH.

Figure 5.2(a) shows the velocity field inside the droplet, as determined by  $\mu$ PIV. The arrows indicate the velocities that have been measured in different  $z$ -planes. The insets show dense velocity fields for two exemplary  $z$ -planes. Close to the free surface, the flow is directed inward, precisely balanced by

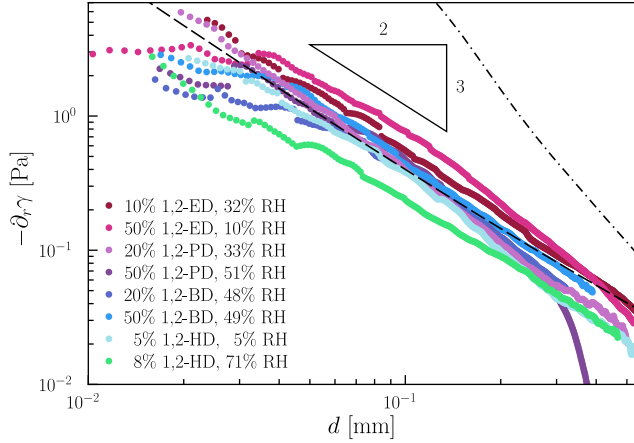


Figure 5.3: Surface tension gradient vs. distance to the contact line. Experimental data for various compositions and humidities (dots) follows a  $\sim d^{-3/2}$  power law. Simulations ( $\phi = 0.20$  1,2-PD, RH = 33%,  $t = 8.0$  s) with Taylor-Aris dispersion (dashed line) are in quantitative agreement with experiments, in contrast to the results obtained without Taylor-Aris dispersion (dash-dotted line).

an outward flow close to the substrate, leading to a quasi-stationary shape.

The surface tension gradient can be derived from the tangential stress boundary condition, using the measured shear rate and the viscosity  $\eta(\phi)$  from literature (Moosavi et al., 2017; George et al., 2003; Jarosiewicz et al., 2004). Figure 5.3 shows the experimentally derived surface tension gradient as a function of the distance  $d$  to the contact line, for various diols, compositions, and relative humidities. All curves follow a power law  $\partial_r \gamma \sim d^{-3/2}$ . Despite significant differences in composition, surface activity, and ambient humidities, the curves nearly collapse in physical units.

## 5.4 Lubrication theory

We consider the general case of a thin liquid film of a mixture on a flat solid surface. The film covers the entire substrate, with a continuous transition between the macroscopic droplet and a microscopically thin precursor surrounding it. The latter reflects the adsorption equilibrium of vapor molecules in the atmosphere around the droplet (Eggers et al., 2010). For water above

the dew point, adsorption layers on hydrophilic surfaces are typically on the order of a few nm (Verdaguer et al., 2007; Barnette et al., 2008). The free surface is described by  $h(\vec{r})$ , where  $\vec{r}$  is the location in the substrate plane (see Figure 5.1(a)). Incompressible Stokes flow without body forces is governed by

$$\eta \vec{\nabla}^2 \vec{u} = \vec{\nabla} p, \quad (5.1)$$

$$\vec{\nabla} \cdot \vec{u} = 0 \quad (5.2)$$

where  $\vec{u}$  is the fluid velocity,  $\eta$  is the dynamic viscosity of the fluid, and  $p$  is the fluid pressure. The evolution of the solute field  $\phi$  is given by

$$\partial_t \phi = \vec{\nabla} \cdot (D \vec{\nabla} \phi - \vec{u} \phi), \quad (5.3)$$

with  $t$  as time and  $D$  as diffusion coefficient of the solute. For simplicity we limit the following analysis to isothermal, isochoric, and isoviscous cases. We consider a no-slip and no-flux boundary condition at  $z = 0$ , kinematic and stress boundary conditions at  $z = h$ , and a Stefan-type boundary condition that links composition and evaporation (see supplemental material 5.8 for details).

To derive evolution equations in terms of vertically averaged quantities, we take the limit of long waves, where the characteristic horizontal scale,  $r_0$ , shall be much larger than the characteristic vertical scale,  $h_0$ :  $\epsilon_h = h_0/r_0 \ll 1$ . For sessile droplets,  $r_0$  and  $h_0$  are conveniently chosen as the footprint radius and the apical height of the droplet, respectively. We define the vertically averaged velocity  $\bar{\vec{u}}$ , the total hydrodynamic flux  $\vec{\Phi}$ , the vertically averaged composition  $\bar{\phi}$ , and the effective solute height  $\Psi$  through

$$\vec{\Phi} = \int_0^h dz \vec{u}, = \bar{\vec{u}} h, \quad \Psi = \int_0^h dz \phi, = \bar{\phi} h, \quad (5.4)$$

and the deviations from the average by

$$\vec{u} = \bar{\vec{u}} + \delta \vec{u}, \quad \phi = \bar{\phi} + \delta \phi. \quad (5.5)$$

We scale all horizontal coordinates as  $\vec{r} = r_0 \vec{r}'$ , and all vertical coordinates as  $z = \epsilon_h r_0 z'$ . Velocities and time are scaled with  $u_0$  and  $t_0$ , the characteristic velocity and time scales of the problem, respectively. Below,  $u_0$  and  $t_0$  will be identified with the natural scales that arise in the evolution equations.

## 5.4. LUBRICATION THEORY

---

Surface tension is scaled as  $\gamma = \gamma_0 \gamma'$ , where  $\gamma_0 = \gamma(\phi = 0)$ , the surface tension of the pure solvent. Diffusivity is treated similarly,  $D = D_0 D'$  with  $D_0 = D(\phi = 0)$ . We scale  $j = j_0 j'$  for the evaporation rate, where  $j$  and  $j_0$  are determined according to Eggers et al. (2010) for the diffusion limited regime.

Whether  $\bar{\phi}$ , the vertically averaged composition, is sufficient to describe the compositional evolution of the film, depends on the magnitude of the residual field  $\delta\phi$ . Thus we scale  $\delta\phi = \epsilon_\phi \delta\phi'$ , deriving  $\epsilon_\phi$  from the governing equation for  $\delta\phi$ . In the following we will omit the primes for readability and work exclusively with scaled quantities.

The derivation of the evolution equation for the film height follows the standard procedure described in the reviews Oron et al. (1997) and Craster et al. (2009). One obtains

$$\partial_t h = -\vec{\nabla} \cdot \vec{\Phi} - \mathcal{E} j, \quad (5.6)$$

from integrating 5.14 along  $z$ , where  $\mathcal{E} = j_0 \eta / (\epsilon_h^4 \gamma_0)$ . Note that 5.22 does not involve any approximation. The long wave expansion is used only in the expressions for the evaporation rate  $j$  (see Eggers et al., 2010) and the horizontal hydrodynamic flux (Matar, 2002)

$$\vec{\Phi} = \vec{\Phi}_C + \vec{\Phi}_M = \frac{h^3}{3} \vec{\nabla} p + \frac{1}{\epsilon_h^2} \frac{h^2}{2} \vec{\nabla} \gamma + \mathcal{O}(\epsilon_h^2). \quad (5.7)$$

Here we identified the natural velocity scale  $u_0 = \epsilon_h^3 \gamma_0 / \eta$ , the capillary velocity for thin films, to cancel the material properties from Eq. 5.26. For a typical 1,2-Propanediol/water droplet with  $\phi \sim 0.2$  (i.e.,  $\gamma \sim 56$  mN/m and  $\eta \sim 2$  mPas (Karpitschka et al., 2010)),  $r_0 \sim 1.5$  mm, and  $h_0 \sim 0.15$  mm one obtains  $u_0 \sim 28$  mm/s, much larger than the maximum experimentally observed velocities  $\sim 2$  mm/s. This is a common observation in wetting problems, where the capillary number typically remains small. The natural pressure- and time scales are  $p_0 = \epsilon_h \gamma_0 / r_0$  and  $t_0 = r_0 \eta / (\epsilon_h^3 \gamma_0)$ , respectively. The pressure  $p = \gamma \vec{\nabla}^2 h - \Pi(h)$  contains capillary and surface (disjoining) forces that stabilize the precursor film.

The capillary- ( $\vec{\Phi}_C$ ) and Marangoni ( $\vec{\Phi}_M$ ) fluxes are associated with Poiseuille- and Couette-type velocity profiles, respectively (Supplementary Materials 5.8). These will shear any horizontal compositional gradient, such that a vertical gradient arises naturally. Combined with molecular diffusion from Eq. 5.15, this leads to Taylor-Aris dispersion (Taylor, 1953; Aris, 1956). In addition,

the Stefan boundary condition for evaporation at the free surface requires a vertical compositional gradient (Karpitschka et al., 2015; Hennessy et al., 2017). It is commonly accepted that vertical compositional gradients are beyond the limit of the lubrication expansion (Matar, 2002; Oron et al., 2004; Shklyaev et al., 2007; Shklyaev et al., 2011; Thiele, 2011; Thiele et al., 2013; Xu et al., 2015; Thiele et al., 2016). We challenge this paradigm, identifying three regimes, depending on aspect ratio and Péclet number: i. A regime of faint vertical compositional gradients where previous long-wave models hold (Matar, 2002); ii. An intermediate regime of small but not negligible vertical gradients for which we derive a previously unknown evolution equation for  $\bar{\phi}$  including Taylor-Aris dispersion; iii. A regime of large vertical gradients where the full advection-diffusion problem has to be solved (Matar, 2002).

Inserting 5.20 into 5.15 and integrating over the film height gives

$$\begin{aligned} h \partial_t \bar{\phi} = & \text{Pe}^{-1} \vec{\nabla} \cdot \left( \bar{D} h \vec{\nabla} \bar{\phi} + \epsilon_\phi \int_0^h dz D \vec{\nabla} \delta \phi \right) \\ & - \vec{\Phi} \cdot \vec{\nabla} \bar{\phi} - \epsilon_\phi \vec{\nabla} \cdot \int_0^h dz \delta \phi \vec{u} + \mathcal{E} \phi(h) j, \end{aligned} \quad (5.8)$$

where  $\text{Pe} = u_0 r_0 / D_0$  is the Péclet number and  $\bar{D}$  is the vertically averaged diffusion coefficient (see supplement 5.8 for a detailed derivation). In contrast to Eq. 5.22, terms with non-averaged quantities remain. These terms scale as  $\sim \epsilon_\phi$ , while the next-order terms in 5.22 with 5.26 scale as  $\sim \epsilon_h^2$ . Thus, the magnitude of  $\epsilon_\phi$  relative to  $\epsilon_h$  determines which terms in 5.33 should be kept.

Limit i:  $\epsilon_\phi \delta \phi \lesssim \epsilon_h^2$ . We may ignore all terms  $\sim \epsilon_\phi$  and recover the previously known evolution equation (Matar, 2002; Jensen et al., 1993; Jensen et al., 1994):

$$h \partial_t \bar{\phi} = \text{Pe}^{-1} \vec{\nabla} \cdot \bar{D} h \vec{\nabla} \bar{\phi} - \vec{\Phi} \cdot \vec{\nabla} \bar{\phi} + \mathcal{E} \bar{\phi} j + \mathcal{O}(\epsilon_h^2). \quad (5.9)$$

Limit iii:  $\epsilon_\phi \delta \phi \sim 1$ . No simplified evolution equation for vertically averaged quantities can be derived, and the full problem has to be solved (Matar, 2002; Jensen et al., 1994).

Limit ii:  $\epsilon_\phi \delta \phi \sim \epsilon_h$ . In this case, terms up to  $\sim \epsilon_\phi$  have to be retained. We consider a convection dominated problem i.e.,  $\text{Pe} \gg 1$  and  $\mathcal{E} \ll 1$ . Far below the boiling point, and with typical  $D_0 \sim 10 \times 10^{-9} \text{ m}^2 \cdot \text{s}^{-1}$  and

## 5.4. LUBRICATION THEORY

---

$u_0 \sim 10 \times 10^{-3} \text{ m} \cdot \text{s}^{-1}$ , this holds for most sessile nano- to microliter droplets with small contact angles. Eq. 5.33 simplifies further (supplement 5.8):

$$h \partial_t \bar{\phi} = \text{Pe}^{-1} \bar{\nabla} \cdot \bar{D} h \bar{\nabla} \bar{\phi} - \bar{\Phi} \cdot \bar{\nabla} \bar{\phi} - \epsilon_\phi \bar{\nabla} \cdot \int_0^h dz \delta\phi \bar{u} + \mathcal{E} \bar{\phi} j + \mathcal{O}(\epsilon_\phi^2). \quad (5.10)$$

The remaining term with  $\delta\phi$  scales as  $\epsilon_\phi$ . Thus a governing equation for  $\delta\phi$  can be truncated to  $\mathcal{O}(1)$ . Inserting 5.20 into 5.15, multiplying with  $h$ , and subtracting 5.34 gives the leading order governing equation for  $\delta\phi$  (supplement 5.8):

$$\bar{D} \partial_z^2 \delta\phi = \mathcal{E} \bar{\phi} j/h + \delta\bar{u} \cdot \bar{\nabla} \bar{\phi} + \mathcal{O}(\epsilon_\phi), \quad (5.11)$$

where we recover the natural scale of the residual field,  $\epsilon_\phi = \epsilon_h^2 \text{Pe}$  (Jensen et al., 1993; Jensen et al., 1994).  $\epsilon_\phi$  is equivalent to a Péclet number for the characteristic vertical length- and velocity scales,  $\epsilon_h r_0$  and  $\epsilon_h u_0$ , respectively. Eq. 5.38 defines the advection-diffusion problem of the residual field in the co-moving frame of the mean flow: Diffusion along  $z$  balances the shearing due to the horizontal flow, and the residual field is stationary at leading order.

The requirements for limit ii became apparent now: The problem must be convection dominated in horizontal direction ( $\text{Pe} \gg 1$ ), but diffusion dominated in vertical direction, i.e., the residual field must remain small:  $\epsilon_h^2 \text{Pe} \delta\phi \ll 1$ . This is similar to the classical treatment of pipe flow by Taylor and Aris (Taylor, 1953; Aris, 1956), but here the velocity field and the film height, and thus  $\delta\phi$  vary in space. By scaling  $z$  in Eq. 5.38 with the local film height  $h$ , it becomes apparent that  $\delta\phi \sim h^2 \delta\bar{u} \bar{\nabla} \bar{\phi}$  if shear ( $\delta\bar{u}$ ) dominates. For Marangoni-contracted droplets, we find  $\delta\phi \ll 1$  everywhere:  $\bar{\nabla} \bar{\phi}$  and  $\delta\bar{u}$ , which are caused by evaporative enrichment and Marangoni convection, are strong only near the edge of the droplet where the height is small (see below for a quantitative estimate).

Eq. 5.38 can be integrated, and the resulting expressions for  $\delta\phi$  and the integral in 5.34 can be found in the supplement 5.8. In cases of axial or translational symmetry and slow evaporation ( $\mathcal{E} j/h \ll \delta\bar{u}$ ), which holds for our experiments, Eq. 5.34 reduces to Eq. 5.35 with  $\bar{D}$  replaced by  $\bar{D}_{\text{eff}}$  to account for Taylor-Aris dispersion:

$$\bar{D}_{\text{eff}} = \bar{D} + \frac{\epsilon_h^2 \text{Pe}^2}{\bar{D}} \left( \frac{2\bar{\Phi}_C^2}{105} + \frac{\bar{\Phi}_C \cdot \bar{\Phi}_M}{20} + \frac{\bar{\Phi}_M^2}{30} \right). \quad (5.12)$$

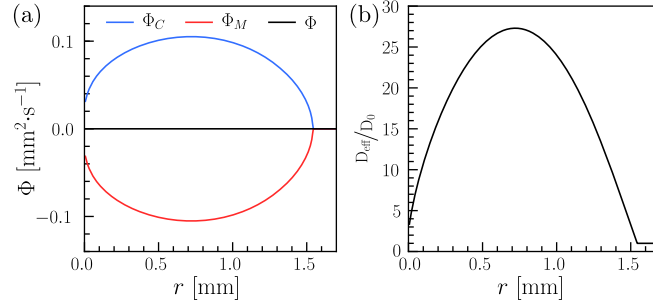


Figure 5.4: Simulated fluxes (a) and effective diffusivity (b) as a function of  $r$  ( $\phi = 0.20$  1,2-PD, RH = 33 %,  $t = 8.0$  s). (a) Capillary (blue) and Marangoni (red) fluxes balance each other, resulting in a total flux  $\Phi \sim 0$  (black). Although the net hydrodynamic transport vanishes, the different flow profiles of the two fluxes lead to strong shear dispersion. (b) Effective diffusivity (Eq. 5.12) scaled by the molecular diffusivity. Shear dispersion increases the effective diffusivity  $\sim 27$ -fold as compared to molecular diffusion alone.

## 5.5 Numerical simulations

We implemented the evolution equations 5.22 and 5.35 with the flux 5.26 and the effective diffusivity 5.12 in an axisymmetric finite volumes scheme with convergent numerical mobilities after Diez et al. (2000) and Lenz et al. (2002), and diffusion limited evaporation according to Eggers et al. (2010) and Karpitschka et al. (2017). We used accurate material properties  $\gamma(\phi)$ ,  $\eta(\phi)$ , found in literature (Moosavi et al., 2017; George et al., 2003; Jarosiewicz et al., 2004; Karpitschka et al., 2010), and assumed  $D \sim \eta(\phi)^{-1}$  in accordance with the Stokes-Einstein relation. Simulations were initiated with a droplet of  $\sim 0.7$   $\mu\text{L}$  volume and  $\sim 30^\circ$  apparent contact angle, on top of a precursor in equilibrium with the vapor field of the droplet. See supplement 5.8 for details.

Figure 5.1(d) compares the apparent contact angle observed in simulations with (dashed) and without (dash-dotted) Taylor-Aris dispersion. A near-quantitative agreement is observed for stationary contraction only if dispersion is taken into account. The remaining quantitative deviation is much smaller than the mismatch for simulations without dispersion and can be attributed to uncertainties in the material parameters, most importantly, the molecular diffusivity. We deliberately refrain from any parameter fit-

## 5.6. CONCLUSION

---

tings. Figure 5.2(b) shows stream lines and composition for a contracted droplet. The observed difference in composition between center and edge is merely 0.4%. The most striking feature of the simulations is a quantitative reproduction of the experimentally observed velocities (Figure 5.2(a), gray, simulation, vs. black, experiments) and surface tension gradients (Figure 5.3) for the case with Taylor-Aris dispersion.

Origin and importance of Taylor-Aris dispersion are highlighted in Figure 5.4. Panel (a) shows the strong but compensating capillary and Marangoni fluxes in the droplet. Although the net hydrodynamic flux vanishes, the different velocity profiles of capillary and Marangoni fluxes lead to a convection roll inside the droplet, and thus strong shear dispersion. This leads to an effective diffusivity (including shear dispersion and molecular diffusion, Figure 5.4(b)) which scales quadratically with the individual flux components (Eq. 5.12), meaning strong dispersion in regions where the fluxes are large. Here, the effective diffusivity reaches  $\overline{D}_{\text{eff}} \sim 27\overline{D}$  around  $r \sim R/2$ . Thus, Taylor-Aris dispersion becomes the governing phenomenon for the solute distribution in Marangoni-contracted droplets.

Inserting again our characteristic quantities ( $r_0 \sim 1.5$  mm,  $h_0 \sim 0.15$  mm,  $\phi \sim 0.2$ ,  $\gamma \sim 56$  mN/m, and  $\eta \sim 2$  mPas), we obtain  $\text{Pe} \sim 4 \cdot 10^4$  and  $\epsilon_h^2 \text{Pe} \sim 4 \cdot 10^2$ . Thus the applicability of Taylor dispersion for our droplets depends on the magnitude of the scaled  $\delta\phi \sim h^2 \delta u \partial_r \overline{\phi}$ . The largest measured velocities were  $\sim 2$  mm/s  $\sim 0.1u_0$ , close to the contact line where the scaled height  $h \sim 0.1$  (see Figure 5.2). The gradient of the mean composition in that region can be estimated from Figure 5.3 as  $\partial_r \overline{\phi} \sim \left(\frac{\partial\gamma}{\partial\phi}\right)^{-1} \partial_r \gamma \sim 0.05$ . Thus, the deviation from the mean composition is only  $\epsilon_h^2 \text{Pe} \delta\phi \sim 2 \cdot 10^{-2}$ , which justifies the approximations.

## 5.6 Conclusion

We measured the internal flow fields of Marangoni-contracted drops and derived the surface tension gradient, which follows a power law  $\sim d^{-3/2}$ . Through a systematic long wave expansion for free-surface films of mixtures, we could extend the widely used thin-film evolution equations to the case of bulk mixtures subject to Taylor-Aris dispersion. For Marangoni-contracted drops, Taylor-Aris dispersion governs the composition, and our model is in quantitative agreement with the experimental findings. The theoretical

analysis enables lubrication theory to be used for the very general case of advection-dominated thin free-surface films with advected bulk fields like temperature or composition.

## 5.7 Acknowledgements

We acknowledge financial support from the Max Planck – University of Twente Center for Complex Fluid Dynamics. S.K. acknowledges the hospitality of the Isaac Newton Institute, Cambridge, UK, during the workshop “Complex Fluids in Evolving Domains”, and helpful discussions with Uwe Thiele. We would like to thank Debmalya Roy for assistance with the experiments.

## 5.8 Supplementary materials

### 5.8.1 Experimental method

The microscope coverslips (VWR cover glass class 1, 24 mm  $\times$  24 mm size, 170  $\mu$ m thick) were cleaned with piranha solution (hydrogen peroxide 30%, VWR Chemicals, and sulfuric acid 95%, VWR Chemicals, mixture, volume fraction 1 : 3, respectively) for 20 min in a soda-lime glass staining jar (DWK Life Sciences). Afterwards, the substrates were rinsed five times with fresh water (“Milli-Q” water, resistivity 18 M $\Omega$   $\cdot$  cm) and were sonicated for 10 min in hot water at  $\sim$  80  $^{\circ}$ C, to ensure complete removal of residues from the piranha solution. The substrates were stored in fresh water and used on the day of preparation. The substrates were dried with a nitrogen drying gun immediately before the experiment under a laminar flow hood. The nitrogen was blown parallel to the substrate from the corner opposite of the tweezers that were used to hold the slide. The substrate was kept protected from dust with a glass petri dish during its transfer from the laminar flow hood to the humidity control chamber where the experiment was done.

The binary mixtures for the droplets were composed of water (“Milli-Q”) and one of the following carbon diols: Ethylene Glycol (Sigma Aldrich, purity  $\geq$  99.5%), 1,2-Propanediol (Sigma Aldrich, purity  $\geq$  99.5%), 1,2-Butanediol (Sigma Aldrich, purity  $\geq$  98%), and 1,2-Hexanediol (Sigma Aldrich, purity 98%). The chemicals were used as received. An analytical balance was used to prepare mixtures of desired mass fraction  $0 < \phi < 1$ .

## 5.8. SUPPLEMENTARY MATERIALS

---

The mixtures were prepared and stored in piranha cleaned borosilicate glass vials. Polystyrene microspheres (Thermo Fisher Scientific F8809, 0.2  $\mu\text{m}$  diameter, stock solution concentration 2% w/v, excitation/emission maxima = 540/560 nm) were added as tracers, with a mass fraction of  $7.8 \times 10^{-5}$  of the particle stock solution in the mixture. The mixtures were sonicated in an ultrasonic bath for  $\sim 2$  min. The mixtures were stored in a low temperature environment ( $\sim 5^\circ\text{C}$ ) to avoid changes in concentration due to evaporation and were protected from light with aluminum foil. The mixtures were used within the first two days after preparation and were replaced by fresh ones afterwards. Before experiments, the mixtures were sonicated for  $\sim 2$  min to ensure good dispersal of the particles. The syringes (Hamilton Gastight Series 1700, volume 10  $\mu\text{L}$ ) and the needles (Hamilton Removable Needle, small hub, gauge 22s, tip type 3) were cleaned with a series of solvents (ethanol, Carl Roth, purity  $\geq 99.5$ , and acetone, Sigma Aldrich, purity  $\geq 99.5$ , ethanol, and water).

During the experiments, a gas mixture of controlled humidity was continuously injected to membrane-separated antechambers in the atmospheric control chamber (aluminum walls, size  $\sim 10\text{ cm} \times 10\text{ cm} \times 10\text{ cm}$ , Figure 5.5). To achieve arbitrary humidities, fluxes of dry nitrogen and nitrogen saturated with water were regulated with mass flow controllers (MKS Instruments Type MF1) to the desired proportion, with a constant total flux of 500 sccm. The membranes connecting the antechambers to the main chamber were made of interwoven fabric (Wilox Hosiery GmbH tight VITAL 40, 88% polyamide, 12% elastane). They spanned almost the entire area of two opposing side walls, minimizing convection in the main chamber while ensuring quick diffusive exchange with the feed gas. Several humidity sensors (Honeywell HIH-4000 Series) provided a measurement of the humidity distribution in the chamber. Whenever changing the humidity conditions, we waited 1 to 5 minutes for equilibration, before injecting a droplet and starting an experiment.

The chamber was mounted on top of an inverted epi-fluorescence microscope (Nikon Eclipse Ti2E) with large field of view (diameter 25 mm in the image plane). A high power white light source (Lumencor SOLA Light Engine) was used for illumination. With a custom fluorescence filter cube (AHF Analysentechnik, transition wavelength 542 nm), the excitation/emission wavelength range of the fluorescent particles was selected. The microscope was equipped with a water immersion objective (Nikon CFI APO LWD 20X WI) with a numerical aperture of 0.95. By matching the

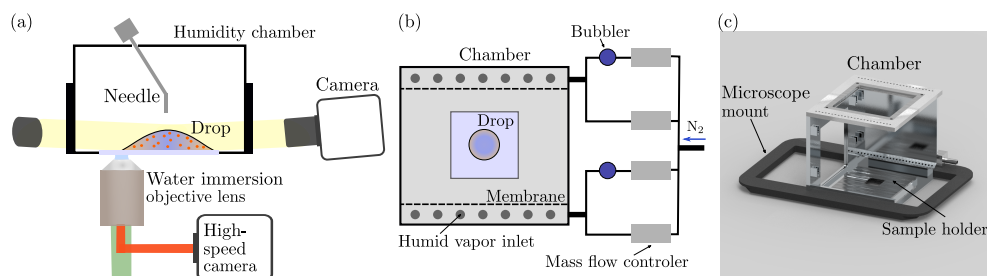


Figure 5.5: Experimental setup. (a) Sketch of the experimental setup from side view. (b) Sketch of the humidity chamber and the humidity control system from top view. (c) Inside view of humidity chamber together with microscope mounting system.

immersion medium of the objective with that of the drop, diffraction-limited imaging is achieved even in the bulk of the working medium. This is utterly important for a good  $z$ -plane selectivity. The focal plane, parallel to the substrate, was moved with the microscope focusing stage in vertical direction to scan the drop at different  $z$ -planes in an automated procedure. The time for switching between focal planes was  $\sim 100$  ms. The full  $z$ -scan was on the order of 10 s, shorter than the time scale on which the flow velocities change for a quasi-stationary drop. Successive upward and downward scans were done to check this. A sequence of  $\sim 300$  frames was recorded for each plane with a high-speed camera (Phantom VEO 4K-L, imaging speed at 600 to 1000 FPS).

Side-view shadowgraph imaging was performed with a second camera (Point Grey Grasshopper2, imaging speed at 27 FPS), equipped with a macro lens (Thorlabs Bi-Telecentric lens, 1.0X, W.D. 62.2 mm) and a collimated-light source on the opposite side, both attached to the sample stage of the microscope. The droplets were observed from an angle of  $6^\circ$  with respect to the substrate. The advantage of this arrangement is the possibility of observing the entire three phase contact line around the droplet. This allows for a precise measurement of the footprint diameter of the droplet. The top surface of the drop reflects light directly from the light source to the camera, which allows a precise detection of the drop height, and thereby the apparent contact angle.

### 5.8.2 Contact angle measurements

For each frame from the side-view camera, the droplet's radius  $R$  and maximum height  $h_0$  were extracted from the images. By assuming that the drop shape is close to a spherical cap, the apparent contact angle was calculated as  $\theta_{app} = 2h_0/R$ . The images were analyzed with an in-house-developed MATLAB code. The centroid location and the minor and major axes length of the drop are obtained with the `regionprops` function. The maximum intensity on the short axis corresponds to the top of the drop. For finding the apex position with subpixel resolution, a second order polynomial is fitted to the intensity peak. To calculate  $h_0$ , the distance from the major axis is measured. The finite observation angle is corrected according to  $h_o = h'/\cos(\alpha)$ , where  $\alpha$  is the tilting angle of the side view camera.  $R$  is defined as half of the major axis length.

### 5.8.3 Micro particle image velocimetry analysis

For the flow quantification, the images from the PIV measurements were analyzed with an in-house developed code. The data is evaluated through cross-correlation with correlation-averaging over  $\sim 100$  frames. The algorithm includes an adaptive interrogation window size method. First, single-pixel correlations are calculated for the entire image and all displacements within a pre-defined search range. Instead of correlating intensity values directly, we used the dot product of the gradient (first order differences). Then, correlations are integrated over interrogation windows of various sizes by convolution with a square kernel of the desired size. We used five different interrogation window sizes of 4, 8, 16, 32, and 64 px side-length. The final correlation maps are then evaluated by a weighted average between the different window sizes, using the mean square of the intensity gradient values in the interrogation window and a size-dependent bias as weight. This method allows for a high resolution in regions of strong velocity gradients, while preventing artifacts from false correlations where particle densities are low. The method was implemented through the Python API of Tensor Flow, to enable fast computation on graphics processing units. Figure 2(a) of the main text shows velocity measurements. The insets show velocity fields in two horizontal planes. The velocities shown in the cross section plot were obtained by azimuthally averaging over  $\sim 100 \mu\text{m}$ . Velocities from different focal planes are shown in Figure 5.6 as a function of  $d$ . The uncertainties

of the velocities (colored bands) are estimated using the standard deviation over the weighted interrogation windows.

Whenever the focal plane comes close to the free surface, correlations are picked up preferentially from below the focal plane because there are no particles outside the drop. This leads to a shift in the correlation plane relative to the focal plane. Accordingly, we applied a correction to the  $z$  location of the velocity signal relative to the distance from the free surface. To obtain this correction, we estimated the point spread function and the correlation sensitivity as a function of distance to the focal plane, and convolved this sensitivity with a unit-step function in  $z$  for the particle density. For the results shown here, we modeled the depth of correlation as a Gaussian with  $1.5\ \mu\text{m}$  standard deviation.

The substrate level was determined at the contact line of the droplet, by focusing onto particles at the substrate. To account for possible substrate tilt and non-planarity, we extracted the expected substrate location from parabolic fits to the velocity profile with a no-slip condition at an offset  $z_0$  in the  $z$ -coordinate. Then we obtained  $0 > z_0 \gtrsim 3\ \mu\text{m}$  for  $0 < d < 500\ \mu\text{m}$ , approximated  $z_0(d)$  over the full range of  $d$  by a third order polynomial with  $z_0(d = 0) = 0$ , and used it to correct the vertical substrate location as a function of  $d$ .

#### 5.8.4 Velocities and surface tension gradients

The velocity measurements for a set of experiments with different conditions are presented below. Figure 5.7 shows a table with plots for each case. Each row is for one liquid composition and the columns are for different ambient humidity conditions. The title of the plots contain the liquid composition,  $\phi$ , the relative humidity, RH, the drop radius,  $R$ , and the apparent contact angle  $\theta$ .

The surface tension gradient was obtained from the first derivative of the velocity profiles in the cross section, evaluated at the interface, and multiplied by the viscosity. The viscosities were interpolated from the data in Moosavi et al. (2017), George et al. (2003), and Jarosiewicz et al. (2004). Figure 5.6 shows the surface tension gradient vs. the distance to the contact line for a set of experiments with different conditions. Each plot presents the experimental data (circles), and the power law  $\partial_r \gamma \sim d^{-3/2}$  (solid lines).

## 5.8. SUPPLEMENTARY MATERIALS

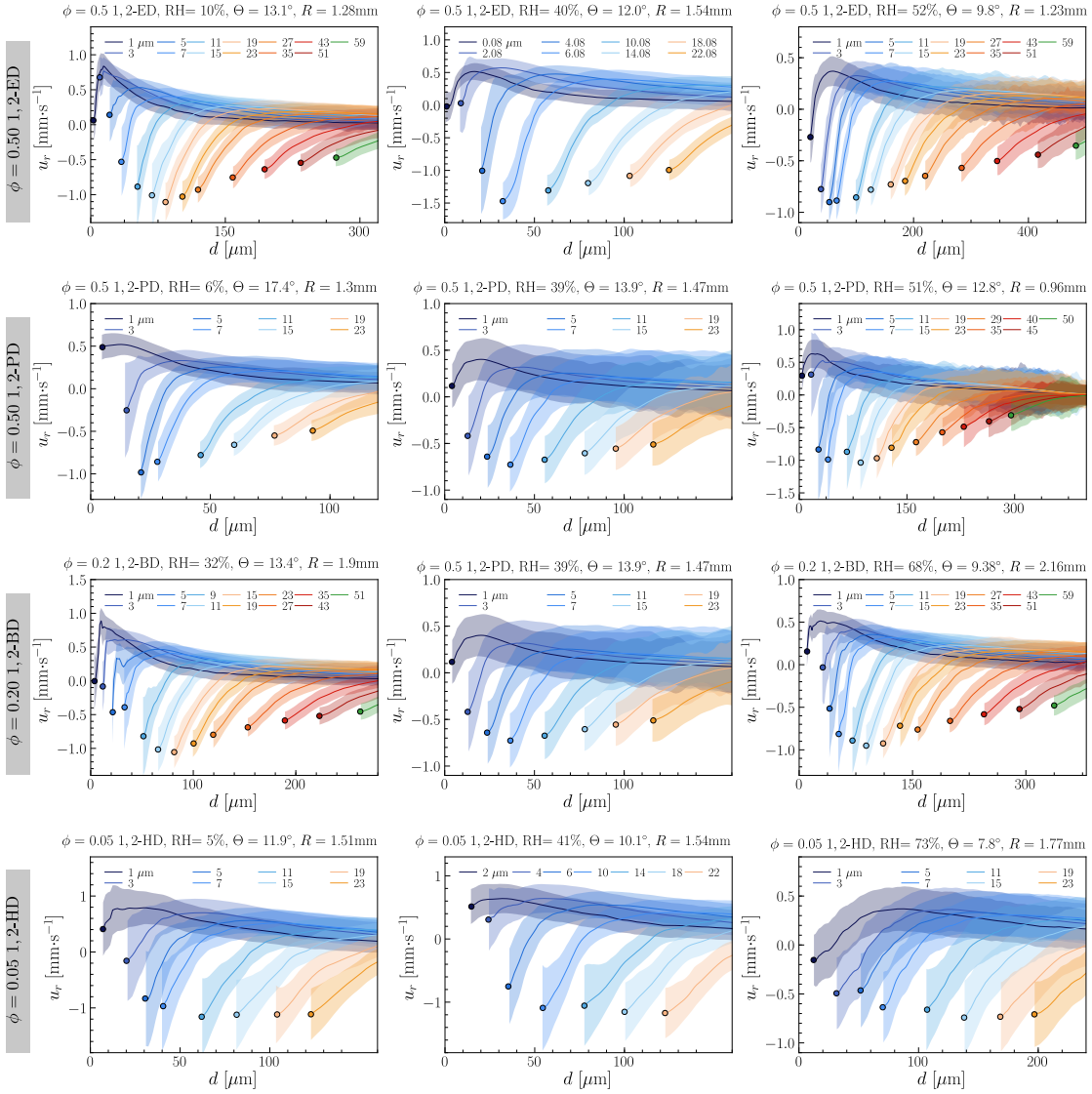


Figure 5.6: Radial velocity vs. distance to the contact line for different experimental conditions. Each plot contains the velocities for different  $z$  planes above the substrate (solid lines), the associated errors (shaded bands), and the velocities at the interface (circles).

### 5.8.5 Lubrication theory with bulk solutes

In absence of bulk solutes, deriving the film height evolution equation in lubrication approximation is a standard procedure that has been done for many situations (Oron et al., 1997), also including evaporation (Eggers et al., 2010). Here we introduce our notation, briefly repeat the derivation for the height evolution, and systematically extend this formalism for the compositional evolution of bulk solutes.

**Problem formulation.** We start from incompressible Stokes flow without body forces:

$$\eta \vec{\nabla}^2 \vec{u} = \vec{\nabla} p, \quad (5.13)$$

$$\vec{\nabla} \cdot \vec{u} = 0 \quad (5.14)$$

where  $\vec{u}$  is the (three-dimensional) fluid velocity field,  $\eta$  is the dynamic viscosity of the fluid, and  $p$  is the fluid pressure. The evolution of an advected, diffusive solute field  $\phi$  (defined as a mass fraction,  $\phi \in [0, 1]$ ) is given by

$$\partial_t \phi = \vec{\nabla} \cdot (D \vec{\nabla} \phi - \vec{u} \phi), \quad (5.15)$$

with  $t$  as time and  $D$  as diffusion coefficient. For simplicity we limit ourselves to the case where the fluid density is independent of  $\phi$ . We shall also assume that the solute is non-volatile, in contrast to the solvent, which evaporates and has a local mass fraction of  $1 - \phi$ .

The liquid film shall be limited to  $z \in [0, h]$ , with a no-slip and no-flux boundary condition at  $z = 0$  and a free surface with evaporation and stress boundary conditions at  $z = h$ :

$$\vec{u}|_{z=0} = 0 \quad (5.16a)$$

$$\vec{u}|_{z=h} \cdot \vec{n} + \vec{j}|_{z=h} \cdot \vec{n} = \vec{n} \cdot \vec{e}_z \partial_t h \quad (5.16b)$$

$$\vec{n} \cdot \sigma|_{z=h} = (\gamma \kappa + \Pi) \vec{n} + \vec{\nabla}_s \gamma \quad (5.16c)$$

$$\partial_z \phi|_{z=0} = 0 \quad (5.16d)$$

$$D \vec{\nabla} \phi \Big|_{z=h} \cdot \vec{n} = \phi \vec{j}|_{z=h} \cdot \vec{n} \quad (5.16e)$$

where  $\vec{n}$  shall be the outward normal vector at  $z = h$ ,  $\vec{j}$  the evaporative flux, expressed in units of volume in the liquid state,  $\sigma$  is the fluid stress,

$\gamma$  is the surface tension,  $\kappa$  is the curvature of the free surface (positive for a convex film surface),  $\Pi$  is the disjoining pressure and  $\vec{\nabla}_s$  is the surface gradient operator.

The gradient ( $\vec{\nabla}$ ) and divergence ( $\vec{\nabla}\cdot$ ) operators split into vertical and horizontal components, in both cylinder and Cartesian coordinates. In the following we use  $\vec{\nabla}\cdot$  and  $\vec{\nabla}$  to denote the horizontal components (parallel to the substrate plane) of divergence and gradient, respectively, to avoid explicit coordinates. The vertical components will be treated explicitly, using  $\partial_z$  for derivatives in vertical direction. Similarly, vector fields with the index refer to the the horizontal vector components only, which may, however, still depend on the vertical coordinate  $z$ .

As usual in the long-wave expansion, we assume that the film height  $h(\vec{r})$  is a function of the coordinate  $\vec{r}$  in the substrate plane and has small slopes. We define the vertically averaged velocity  $\bar{u}$ , the total hydrodynamic flux  $\bar{\Phi}$ , the vertically averaged composition  $\bar{\phi}$ , and the effective solute height  $\Psi$  through

$$\bar{\Phi} = \int_0^h dz \vec{u}, = \bar{u} h, \quad (5.17)$$

$$\Psi = \int_0^h dz \phi, = \bar{\phi} h, \quad (5.18)$$

and the deviations from the average velocity as

$$\vec{u} = \bar{u} + \delta\vec{u}, \quad (5.19)$$

$$\phi = \bar{\phi} + \delta\phi. \quad (5.20)$$

Note already that  $\delta\vec{u}$  is of the same order as  $\bar{u}$  while, at some later point, we will require  $\delta\phi$  to be small in order to allow for a long-wave description of the composition.

The task is now to derive evolution equations in terms of the vertically averaged quantities alone, taking the limit of long waves i.e., that the characteristic horizontal scale,  $r_0$  shall be much larger than the characteristic vertical scale,  $h_0$ . The aspect ratio,

$$\epsilon_h = \frac{h_0}{r_0} \ll 1, \quad (5.21)$$

will serve as a small parameter. We also define  $\delta\phi = \epsilon_\phi \delta\phi'$ , requiring  $\delta\phi'$  of  $\mathcal{O}(1)$  (or  $\mathcal{O}(\phi)$  if  $\bar{\phi} \ll 1$ ), to use  $\epsilon_\phi$  for the magnitude of vertical compositional gradients. In the following, we scale all horizontal coordinates as

$r = r_0 r'$ , and all vertical coordinates as  $h = \epsilon_h r_0 h'$ . Analogously, horizontal and vertical velocity components are scaled as  $\vec{u} = u_0 \vec{u}'$  and  $u_z = \epsilon_h u_0 u'_z$ , respectively. Time will be scaled as  $t = t_0 t'$  and surface tension as  $\gamma = \gamma_0 \gamma'$ , where  $\gamma_0 = \gamma(\phi = 0)$  is the surface tension of the pure solvent. The diffusivity  $D$  may depend on the local composition  $\phi$ , so we rescale  $D = D_0 D'$  and define  $D' = (1 + \delta D'(\phi))$ . Assuming  $\partial_\phi \delta D' = \mathcal{O}(1)$ , the differences in diffusivity in vertical direction will be small. We also assume that viscosity differences in  $z$ -direction are negligible. Finally, we scale  $j = j_0 j'$  for the evaporation rate.

$r_0$  and  $h_0$  reflect the morphology of the liquid film, while  $t_0$  and  $u_0$  will be associated with the natural scales that arise from the material properties and the evolution equations.  $\gamma_0$ ,  $D_0$ , and  $j_0$  are material properties. In the following we will omit the primes for readability and work exclusively with scaled quantities, unless stated explicitly.

**Hydrodynamic fluxes and height evolution** The vertical integral of Eq. 5.14, together with the kinematic boundary condition 5.16b and the flux 5.17, yields the evolution equation for thin films:

$$\partial_t h = \vec{\nabla} \cdot \vec{\Phi} - \mathcal{E} j, \quad (5.22)$$

where we have set  $t_0 = r_0/u_0 = r_0 \eta / (\epsilon_h^3 \gamma_0)$ , the natural time scale of the hydrodynamic film height evolution, and defined a dimensionless evaporation (Shearwood) number

$$\mathcal{E} = \frac{j_0 \eta}{\epsilon_h^4 \gamma_0}. \quad (5.23)$$

Note that Eq. 5.22 does not contain approximations, it fully accounts for volume conservation. All approximations are within the expression that will be used for  $\vec{\Phi}$ .

Applying the limit  $\epsilon_h \ll 1$  to Eq. 5.13, and making use of boundary condition 5.16c, the horizontal components of velocity are governed by

$$\partial_z^2 \vec{u} = \vec{\nabla} \left( -\gamma \vec{\nabla} \cdot \vec{\nabla} h + \frac{r_0}{\epsilon_h \gamma_0} \Pi \right) + \mathcal{O}(\epsilon_h^2), \quad (5.24)$$

where we have defined  $u_0 = \epsilon_h^3 \gamma_0 / \eta$  from the natural scale for the horizontal velocity components i.e., the capillary velocity for horizontal flow in a thin film.

Eq. 5.24 can be integrated to give an explicit expression for  $\vec{u}$ . The integration constants are determined by the boundary conditions 5.16a and 5.16c:

$$\vec{u} = \underbrace{\left(\frac{z^2}{2} - h z\right) \vec{\nabla} \left(-\gamma \vec{\nabla} \cdot \vec{\nabla} h + \frac{r_0}{\epsilon_h \gamma_0} \Pi\right)}_{=\vec{u}_C} + \underbrace{\frac{z}{\epsilon_h^2} \vec{\nabla} \gamma}_{=\vec{u}_M} + \mathcal{O}(\epsilon_h^2), \quad (5.25)$$

The vertical velocity component follows from Eq. 5.14. The characteristic velocity of vertical flows is therefore  $\epsilon_h u_0$ , much smaller than the horizontal components. The total hydrodynamic flux is given by the integral of Eq. 5.25 over the entire depth of the film:

$$\vec{\Phi} = \underbrace{\frac{h^3}{3} \vec{\nabla} \left(\gamma \vec{\nabla} \cdot \vec{\nabla} h - \frac{r_0}{\epsilon_h \gamma_0} \Pi\right)}_{=\vec{\Phi}_C} + \underbrace{\frac{1}{\epsilon_h^2} \frac{h^2}{2} \vec{\nabla} \gamma}_{=\vec{\Phi}_M} + \mathcal{O}(\epsilon_h^2). \quad (5.26)$$

The horizontal velocity and the total hydrodynamic flux both split up into a pressure-driven (capillary) component  $\vec{\Phi}_C$  with a Poiseuille-type velocity profile, and a Marangoni component  $\vec{\Phi}_M$  with a Couette-type velocity profile. The velocities can be expressed in terms of the fluxes:

$$\vec{u}_C = 3 \left(\frac{z}{h} - \frac{1}{2} \left(\frac{z}{h}\right)^2\right) \frac{\vec{\Phi}_C}{h} + \mathcal{O}(\epsilon_h^2), \quad (5.27)$$

$$\vec{u}_M = 2 \frac{z}{h} \frac{\vec{\Phi}_M}{h} + \mathcal{O}(\epsilon_h^2). \quad (5.28)$$

Therefore, the height evolution equation 5.22 with the horizontal flux from Eq. 5.26 is purely two-dimensional and does not require any  $z$ -resolved quantities. The profiles of the horizontal velocity components follow from Eqs. 5.27 & 5.28, the vertical velocity from the  $z$ -integral of Eq. 5.14.

**Compositional evolution** Inserting Eqs. 5.19, 5.20 into the evolution equation 5.15, applying our scalings, and explicitly writing horizontal and vertical components gives

$$\partial_t (\bar{\phi} + \epsilon_\phi \delta\phi) = \text{Pe}^{-1} \vec{\nabla} \cdot D \vec{\nabla} (\bar{\phi} + \epsilon_\phi \delta\phi) + \frac{\epsilon_\phi}{\epsilon_h^2 \text{Pe}} \partial_z D \partial_z \delta\phi - \vec{u} \cdot \vec{\nabla} (\bar{\phi} + \epsilon_\phi \delta\phi) - \epsilon_\phi u_z \partial_z \delta\phi. \quad (5.29)$$

Here we found  $\text{Pe} = \frac{r_0^2}{t_0 D_0} = \frac{u_0 r_0}{D_0} = \frac{\epsilon_h^3 r_0 \gamma_0}{D_0 \eta}$ , the Péclet number for characteristic scales in horizontal direction.

In order to obtain an evolution equation in terms of  $\bar{\phi}$  alone, we would like to find an expression without terms containing  $\delta\phi$ . Thus we integrate Eq. 5.29 in  $z$  direction, minding the dependence of  $h$  on space and time when changing the order of differentiation and integration:

$$\begin{aligned} \partial_t \int_0^h dz (\bar{\phi} + \epsilon_\phi \delta\phi) - (\bar{\phi} + \epsilon_\phi \delta\phi(h)) \partial_t h = & \text{Pe}^{-1} \vec{\nabla} \cdot \int_0^h dz D \vec{\nabla} (\bar{\phi} + \epsilon_\phi \delta\phi) \\ & + \text{Pe}^{-1} \left( \frac{\epsilon_\phi}{\epsilon_h^2} [D \partial_z \delta\phi]_0^h - D \vec{\nabla} (\bar{\phi} + \epsilon_\phi \delta\phi) \Big|_h \cdot \vec{\nabla} h \right) \\ & - \int_0^h dz (\vec{u} \cdot \vec{\nabla} \bar{\phi}) - \epsilon_\phi \int_0^h dz (\vec{u} \cdot \vec{\nabla} \delta\phi + u_z \partial_z \delta\phi). \end{aligned} \quad (5.30)$$

The integral on the left-hand side and the integral of the advection of the mean composition can readily be evaluated, using the properties of the  $z$ -dependence of  $\bar{\phi}$ ,  $\delta\phi$  and  $\vec{u}_h$ . We split the diffusion integral into  $\bar{\phi}$ - and  $\delta\phi$  terms and use the definition  $\bar{D} = 1 + \frac{1}{h} \int_0^h dz \delta D$  to simplify the former term. The boundary term from diffusion represents the total diffusive fluxes across the film boundaries at  $z = 0$  and  $z = h$ , per horizontal area element. These terms are determined by the boundary conditions 5.16d and 5.16e, where we use the shorthand  $j = \frac{\vec{j}(h) \cdot \vec{n}}{\vec{n} \cdot \vec{e}_z}$ . On the  $z$ -component of the advection of  $\delta\phi$  we perform integration by parts, and apply continuity equation 5.14 to the resulting term. Then, the integrand can be combined to a single divergence. The evolution equation reduces to

$$\begin{aligned} h \partial_t \bar{\phi} - \epsilon_\phi \delta\phi(h) \partial_t h = & \text{Pe}^{-1} \vec{\nabla} \cdot \left( \bar{D} h \vec{\nabla} \bar{\phi} + \epsilon_\phi \int_0^h dz D \vec{\nabla} \delta\phi \right) + \mathcal{E} (\bar{\phi} + \epsilon_\phi \delta\phi(h)) j \\ & - \vec{\Phi} \cdot \vec{\nabla} \bar{\phi} - \epsilon_\phi [u_z \delta\phi]_0^h + \epsilon_\phi \int_0^h dz (\vec{\nabla} \cdot \delta\phi \vec{u}). \end{aligned} \quad (5.31)$$

On the last term, we change the order of differentiation and integration once more:

$$\begin{aligned} h \partial_t \bar{\phi} - \underline{\epsilon_\phi \delta\phi(h) \partial_t h} = & \text{Pe}^{-1} \vec{\nabla} \cdot \left( \bar{D} h \vec{\nabla} \bar{\phi} + \epsilon_\phi \int_0^h dz D \vec{\nabla} \delta\phi \right) + \mathcal{E} (\bar{\phi} + \epsilon_\phi \delta\phi(h)) j \\ & - \vec{\Phi} \cdot \vec{\nabla} \bar{\phi} - \underline{\epsilon_\phi \left( [u_z \delta\phi]_0^h - \delta\phi \vec{u} \Big|_h \cdot \vec{\nabla} h \right)} - \epsilon_\phi \vec{\nabla} \cdot \int_0^h dz \delta\phi \vec{u}, \end{aligned} \quad (5.32)$$

## 5.8. SUPPLEMENTARY MATERIALS

---

As in the evolution equation for  $h$ , we make use of the boundary conditions 5.16a and 5.16b, to show that the underlined terms in the equation above cancel. This leads to

$$h \partial_t \bar{\phi} = \text{Pe}^{-1} \vec{\nabla} \cdot \left( \bar{D} h \vec{\nabla} \bar{\phi} + \epsilon_\phi \int_0^h dz D \vec{\nabla} \delta\phi \right) + \mathcal{E} (\bar{\phi} + \epsilon_\phi \delta\phi(h)) j - \vec{\Phi} \cdot \vec{\nabla} \bar{\phi} - \epsilon_\phi \vec{\nabla} \cdot \int_0^h dz \delta\phi \vec{u}. \quad (5.33)$$

Note that in deriving Eq. 5.33 from Eq. 5.15, no approximations have been made.

The integral of the continuity equation for velocity, Eq. 5.22, which is also exact apart from the expression used for  $\vec{\Phi}$ , can be formulated solely in terms of the vertical integral of velocity,  $\vec{\Phi}$ . This is not the case for Eq. 5.33, which still contains terms with  $\delta\phi$ . In order to derive an evolution equation in terms of  $\bar{\phi}$  alone, approximations must be made. Importantly, the expression that we intend to use for  $\vec{\Phi}$  (Eq. 5.26) in Eq. 5.22 is precise up to terms of  $\mathcal{O}(\epsilon_h^2)$ . Thus an analog equation for the evolution of  $\bar{\phi}$  should retain any terms of  $\mathcal{O}(\epsilon_h)$  in order to be consistent with Eqs. 5.22 and 5.26.

The approximate evolution equation for  $\bar{\phi}$  depends on the magnitude of  $\epsilon_\phi$ , which will be determined later. In the case that  $\epsilon_\phi$  is not small, typically a simple evolution equation in terms of  $\bar{\phi}$  cannot be derived. Then the full advection-diffusion problem has to be solved. Thus we now implement a first (mild) approximation that requires  $\epsilon_\phi \ll 1$  and  $\partial_\phi \delta D = \mathcal{O}(1)$  or smaller, in order to remove the  $z$ -dependence of the diffusivity. Then,  $\bar{D} = 1 + \delta D(\bar{\phi}) + \mathcal{O}(\epsilon_\phi)$  and  $D = \bar{D} + \mathcal{O}(\epsilon_\phi)$ . Further we assume  $\mathcal{E} \ll 1$ , which is the case for our droplets and eliminates  $\delta\phi$  from the evaporation term. This simplifies Eq. 5.33 to

$$h \partial_t \bar{\phi} = \text{Pe}^{-1} \vec{\nabla} \cdot \left( \bar{D} h \vec{\nabla} \bar{\phi} - \epsilon_\phi \bar{D} \delta\phi(h) \vec{\nabla} h \right) + \mathcal{E} \bar{\phi} j - \vec{\Phi} \cdot \vec{\nabla} \bar{\phi} - \epsilon_\phi \vec{\nabla} \cdot \int_0^h dz \delta\phi \vec{u} + \mathcal{O}(\epsilon_\phi^2). \quad (5.34)$$

In the following we will examine various limits and the resulting evolution equations for the composition.

**Limit I** —  $\epsilon_\phi \ll \epsilon_h$  If  $\epsilon_\phi$  turns out to be exceedingly small i.e.,  $\epsilon_\phi \ll \epsilon_h$ , vertical gradients in the composition are fully suppressed, and the governing equation simply becomes an advection-diffusion equation in terms of the vertically averaged quantities alone:

$$\underline{\epsilon_\phi \ll \epsilon_h}: \quad h \partial_t \bar{\phi} = \text{Pe}^{-1} \vec{\nabla} \cdot \bar{D} h \vec{\nabla} \bar{\phi} - \vec{\Phi} \cdot \vec{\nabla} \bar{\phi} + \mathcal{E} \bar{\phi} j. \quad (5.35)$$

This equation has been used in the existing literature and properly accounts for mass conservation and evaporation in a diffusion dominated problem. Dispersion terms are missing.

**Limit II** —  $\epsilon_\phi \sim \epsilon_h$  If we assume  $\epsilon_\phi \sim \epsilon_h \ll 1 \ll \text{Pe}$ , which is the case for an advection dominated problem, the leading order problem reduces to advection and evaporation alone. To be consistent with the order of Eq. 5.22 with Eq. 5.26, we should keep terms of  $\mathcal{O}(\epsilon_\phi)$  and  $\mathcal{O}(\text{Pe}^{-1})$  that account for diffusion and dispersion, but drop terms of  $\mathcal{O}(\epsilon_\phi \text{Pe}^{-1})$  or higher:

$$h \partial_t \bar{\phi} = \text{Pe}^{-1} \vec{\nabla} \cdot \bar{D} h \vec{\nabla} \bar{\phi} + \mathcal{E} \bar{\phi} j - \vec{\Phi} \cdot \vec{\nabla} \bar{\phi} - \epsilon_\phi \vec{\nabla} \cdot \int_0^h dz \delta \phi \vec{u}. \quad (5.36)$$

Next we will show that, consistent with the order-of-magnitude assumptions of limit II,  $\delta \phi$  is determined by a governing equation in terms of the averaged composition alone. Thus a closed evolution equation of  $\bar{\phi}$  can be derived, with additional terms that describe Taylor dispersion for the general case of a thin free surface film with capillary and Marangoni flows.

The difference between the original advection-diffusion equation and its vertical integral will provide a governing equation for  $\delta \phi$ . Thus we apply the same approximations to Eq. 5.29, multiply it with  $h$ , and subtract Eq. 5.36:

$$\begin{aligned} \epsilon_\phi h \partial_t \delta \phi = & \text{Pe}^{-1} \vec{\nabla} \cdot \bar{D} \vec{\nabla} \bar{\phi} \cdot \vec{\nabla} h - h \delta \vec{u} \cdot \vec{\nabla} \bar{\phi} - \mathcal{E} \bar{\phi} j + \frac{\epsilon_\phi}{\epsilon_h^2 \text{Pe}} \bar{D} h \partial_z^2 \delta \phi \\ & - \epsilon_\phi \left( h \vec{u} \cdot \vec{\nabla} \delta \phi - h u_z \partial_z \delta \phi + \vec{\nabla} \cdot \int_0^h dz \delta \phi \vec{u} \right), \end{aligned} \quad (5.37)$$

Since the remaining term with  $\delta \phi$  in Eq. 5.36 scales as  $\epsilon_\phi$ , it is sufficient to determine  $\delta \phi$  at  $\mathcal{O}(1)$ . Higher order terms in  $\delta \phi$  would be of  $\mathcal{O}(\epsilon^2)$  when inserted into 5.36. Thus, the governing equation for  $\delta \phi$  simplifies to

$$\frac{\epsilon_\phi}{\epsilon_h^2 \text{Pe}} \bar{D} \partial_z^2 \delta \phi = \mathcal{E} \frac{\bar{\phi} j}{h} + \delta \vec{u} \cdot \vec{\nabla} \bar{\phi} + \mathcal{O}(\epsilon_\phi). \quad (5.38)$$

No explicit time derivative of  $\delta \phi$  appears anymore. Rather,  $\delta \phi$  appears only in terms of its second vertical derivative. The advection term contains only  $\delta \vec{u}$ , the difference from the depth-averaged velocity. Therefore, Eq. 5.38 represents a stationary advection-diffusion problem in the co-moving frame of the mean flow and can be integrated. This yields an expression for  $\delta \phi$

## 5.8. SUPPLEMENTARY MATERIALS

---

that depends only on the averaged composition and the local evaporation rate. The appropriate choice for  $\epsilon_\phi$  now becomes obvious and depends on the relative dominance of the right hand side terms of Eq. 5.37. In our case,  $\mathcal{E} \ll 1$  while  $\delta\vec{u} = \mathcal{O}(1)$ , so we define  $\epsilon_\phi$  from the advection term:

$$\epsilon_\phi = \epsilon_h^2 \text{Pe} = \frac{h_0^2 u_0}{D_0 r_0} = \text{Pe}_z, \quad (5.39)$$

which is the Péclet number for the characteristic vertical scales. The important feature that allows for above simplifications is identical to that for pipe flow: the aspect ratio  $\epsilon_h$  must be small, such that  $\epsilon_h^2 \text{Pe} = \text{Pe}_z \ll 1$ , while  $\text{Pe} \gg 1$ . With this definition, Eq. 5.37 becomes (dropping the  $\mathcal{O}(\epsilon_\phi)$  from now on):

$$\bar{D} \partial_z^2 \delta\phi = \mathcal{E} \frac{\bar{\phi} j}{h} + \delta\vec{u} \cdot \vec{\nabla}\bar{\phi}. \quad (5.40)$$

Integrating Eq. 5.40 twice from 0 to  $z$  gives

$$\bar{D} [\delta\phi]_0^z = \mathcal{E} \frac{\bar{\phi} j}{h} \frac{z^2}{2} + \vec{\nabla}\bar{\phi} \cdot \int_0^z dz' \int_0^{z'} dz'' \delta\vec{u}(z''). \quad (5.41)$$

The integration constant  $\delta\phi|_{z=0}$  can be determined by integrating above expression over the entire film height and the vanishing mean of  $\delta\phi$ :

$$-\bar{D} \delta\phi|_{z=0} = \mathcal{E} \frac{h \bar{\phi} j}{6} + \frac{1}{h} \vec{\nabla}\bar{\phi} \cdot \int_0^h dz \int_0^z dz' \int_0^{z'} dz'' \delta\vec{u}(z''). \quad (5.42)$$

$\delta\vec{u}$  and its integrals can be expressed in terms of capillary and Marangoni fluxes as derived in the previous section, so the integrals can be evaluated:

$$\bar{D} \delta\phi = \mathcal{E} \frac{\bar{\phi} j}{h} \left( \frac{z^2}{2} - \frac{h^2}{6} \right) + \vec{\nabla}\bar{\phi} \cdot \left( \left( \frac{z^3}{2h} - \frac{z^4}{8h^2} - \frac{z^2}{2} + \frac{h^2}{15} \right) \frac{\vec{\Phi}_C}{h} + \left( \frac{z^3}{3h} - \frac{z^2}{2} + \frac{h^2}{12} \right) \frac{\vec{\Phi}_M}{h} \right). \quad (5.43)$$

With this, the (Taylor) dispersive flux in evolution equation 5.36 becomes

$$\vec{\Phi}_T = \epsilon_\phi \int_0^h dz \delta\phi \vec{u} = -\text{Pe}_z \frac{h}{\bar{D}} \left( \left( \frac{2}{105} \vec{\nabla}\bar{\phi} \cdot \vec{\Phi}_C + \frac{1}{40} \vec{\nabla}\bar{\phi} \cdot \vec{\Phi}_M - \frac{7}{120} \mathcal{E} \bar{\phi} j \right) \vec{\Phi}_C + \left( \frac{1}{40} \vec{\nabla}\bar{\phi} \cdot \vec{\Phi}_C + \frac{1}{30} \vec{\nabla}\bar{\phi} \cdot \vec{\Phi}_M - \frac{1}{12} \mathcal{E} \bar{\phi} j \right) \vec{\Phi}_M \right). \quad (5.44)$$

The evolution equation for  $\bar{\phi}$  finally reads

$$\underline{\epsilon_\phi \sim \epsilon_h \ll 1 \ll \text{Pe}}: \quad h \partial_t \bar{\phi} = \text{Pe}^{-1} \vec{\nabla} \cdot \bar{D} h \vec{\nabla} \bar{\phi} - \vec{\Phi} \cdot \vec{\nabla} \bar{\phi} + \mathcal{E} \bar{\phi} j - \vec{\nabla} \cdot \vec{\Phi}_T. \quad (5.45)$$

With radial or translational symmetry, the compositional gradient and the hydrodynamic fluxes are necessarily parallel. This, together with the assumption of a small evaporation rate allows for the following simplifications on  $\vec{\Phi}_T$ :

$$\vec{\Phi}_T = -\text{Pe}_z \frac{h}{\bar{D}} \left( \frac{2\vec{\Phi}_C^2}{105} + \frac{\vec{\Phi}_C \cdot \vec{\Phi}_M}{20} + \frac{\vec{\Phi}_M^2}{30} \right) \vec{\nabla} \bar{\phi}. \quad (5.46)$$

By defining an effective diffusivity

$$\bar{D}_{\text{eff}} = \bar{D} + \frac{\epsilon_h^2 \text{Pe}^2}{\bar{D}} \left( \frac{2\vec{\Phi}_C^2}{105} + \frac{\vec{\Phi}_C \cdot \vec{\Phi}_M}{20} + \frac{\vec{\Phi}_M^2}{30} \right), \quad (5.47)$$

the Taylor-dispersive flux can then be included in the diffusion term, which leads to the evolution equation

$$\underline{\epsilon_\phi \sim \epsilon_h \ll 1 \ll \text{Pe}, \quad 2\text{D or axisymmetric}}: \quad h \partial_t \bar{\phi} = \text{Pe}^{-1} \vec{\nabla} \cdot \bar{D}_{\text{eff}} h \vec{\nabla} \bar{\phi} - \vec{\Phi} \cdot \vec{\nabla} \bar{\phi} + \mathcal{E} \bar{\phi} j. \quad (5.48)$$

**Limit III** —  $\epsilon_\phi \gg \epsilon_h$  In this case, an evolution equation in terms of the averaged quantities alone cannot be derived.

## Simulations

We include quasi-stationary diffusion limited evaporation into our simulations by closely following the approach from Eggers et al. (2010): We assume that the macroscopic drop body is surrounded by a wetting precursor that is subject to a disjoining pressure and in equilibrium with the vapor above the substrate. Therefore, the local evaporation rate  $j$  is calculated by an integral transform of the local vapor pressure  $p_v$  of the liquid, which is subject to Raoult's law and Kelvin's law (in physical units):

$$p_v = p_v^{(0)} x \exp\left(\frac{M p}{\rho R_g T}\right), \quad (5.49)$$

where  $p_v^{(0)}$  is the saturation vapor pressure of the pure solvent at atmospheric pressure,  $x$  is the mole fraction of the solvent in the mixture,  $M$  is the molar

## 5.8. SUPPLEMENTARY MATERIALS

---

mass of the solvent molecule,  $\rho$  is the liquid density,  $R_g$  is the gas constant and  $T$  is the temperature. In contrast to Eggers et al. (2010), we do not linearize around  $p = 0$  to preserve the non-negativity property of Eq. 5.49. While the overall evolution does not seem to be influenced significantly by this, it gives physical vapor pressures also in regions with large negative pressures (i.e., the transition from the drop to the precursor).

As disjoining pressure, we use the standard long-range van-der-Waals form  $\Pi = \gamma_0 a^2 / h^3$  (in physical units), where  $a^2 = A / \gamma_0$  is a molecular length scale and  $A$  is the Hamaker constant (Eggers et al., 2010). For simplicity we assume that the disjoining pressure is independent of composition. The effect of composition-dependent surface forces in wetting scenarios has been analyzed in the literature (Thiele et al., 2013), but is beyond scope here. In scaled units, the pressure reads

$$p = -\gamma(\phi) \partial_r^2 h - \frac{a^2 r_0^2}{h_0^4} \frac{1}{h^3}, \quad (5.50)$$

where we have set  $p_0 = \frac{\gamma_0 h_0}{r_0^2}$  from the capillary term. To find a set of dimensionless scales for our simulations, we require the pressure term to be parameter-free, which defines

$$r_0 = \frac{h_0^2}{a}. \quad (5.51)$$

We define the characteristic vertical scale  $h_0$  from the liquid-vapor equilibrium of the precursor according to the Kelvin law (Eggers et al., 2010):

$$\ln \frac{p_v}{p_v^{(0)}} = \frac{M}{\rho R_g T} p_0 \Pi = \frac{M}{\rho R_g T} \frac{\gamma_0 a^2}{h_0^3} \frac{1}{h^3}, \quad (5.52)$$

finding

$$h_0 = \left( \frac{\rho R_g T}{\gamma_0 a^2 M} \right)^{1/3}. \quad (5.53)$$

With typical values of the material parameters,  $h_0 \sim 0.7$  nm and  $r_0 \sim 1.2$  nm. In contrast, typical initial droplet heights are  $\sim 0.1$  mm, radii  $\sim 1$  mm. This strong separation of scales leads to exceedingly small time steps and long run times of the simulations. We accelerate the simulations by choosing  $h_0$  five times larger than its natural value. According to 5.51, this increases  $r_0$  by a

factor of 25. We tested a factor of 10 or 20 in  $h_0$  as well, and no significant differences were noticeable.

The physical conservation law in the problem is the conservation of mass for either chemical species, rather than the total volume or the local mass fraction. Thus we cast the evolution equations into the conserved variables  $\Psi_i$ , the amount of material  $i$  per unit substrate area:

$$\Psi_1 = (1 - \bar{\phi}) h, \quad (5.54)$$

$$\Psi_2 = \bar{\phi} h. \quad (5.55)$$

Multiplying Eq. 5.22 with  $\bar{\phi}$  and adding Eq. 5.48, we obtain

$$\partial_t \Psi_1 = \text{Pe}^{-1} \vec{\nabla} \cdot \bar{D}_{\text{eff}} h \vec{\nabla} (1 - \bar{\phi}) - \vec{\nabla} \cdot (1 - \bar{\phi}) \vec{\Phi} - \mathcal{E} j, \quad (5.56a)$$

$$\partial_t \Psi_2 = \text{Pe}^{-1} \vec{\nabla} \cdot \bar{D}_{\text{eff}} h \vec{\nabla} \bar{\phi} - \vec{\nabla} \cdot \bar{\phi} \vec{\Phi}. \quad (5.56b)$$

Here,  $\Psi_1$  is the effective height of the solvent (water), and  $\Psi_2$  is the effective height of the solute (1,2-Propanediol). Although  $h = \Psi_1 + \Psi_2$  and  $\phi = \Psi_2/h$  still have to be calculated in order to evaluate the terms in the evolution equations, it is advantageous to use the conserved quantities in the finite volumes discretization.

Equations 5.56 are discretized in an axisymmetric finite volumes scheme according to Diez et al. (2000) and Lenz et al. (2002) (non-negativity preserving numerical mobilities for hydrodynamic fluxes). Compositions on the cell edges were extrapolated by an essentially non-oscillatory third-order upwind scheme according to Leonard et al. (1990). Here, the third order correction to the first order upwind composition is flux limited. This suppresses non-physical oscillations while minimizing numerical diffusion. We also tested a first-order upwind scheme and a central differences scheme, observing strong numerical (non-physical) diffusion and spurious oscillations, respectively.

We used a strongly graded grid where the grid spacing varies from 0.25 (in scaled units) close to the contact line to  $\sim 8000$  far away from the drop. Inside the drop, the grid spacing increases to  $\sim 400$ .

Time integration is performed with a splitting scheme, implemented with the sundials CVode package (Cohen et al., 1996), version 4.1.0. In the first substep, evaporation is applied explicitly. In the second step, the advection terms are integrated with a second order fully implicit backward differentiation (BDF) method. Importantly, capillary and Marangoni fluxes cannot be split into separate substeps as in Lenz et al. (2002), because this would lead

## 5.8. SUPPLEMENTARY MATERIALS

---

to strong numerical dispersion. In the third substep, solute diffusion and dispersion is integrated with an implicit second order BDF method, using explicit values for the hydrodynamic fluxes from the previous substep.

With this scheme, volume conservation of the nonvolatile component was observed to be better than  $V/V_0 - 1 \lesssim 10^{-6}$  over the simulated time. In terms of individual grid cells and time steps, this accuracy is around machine precision.

## 5.8. SUPPLEMENTARY MATERIALS

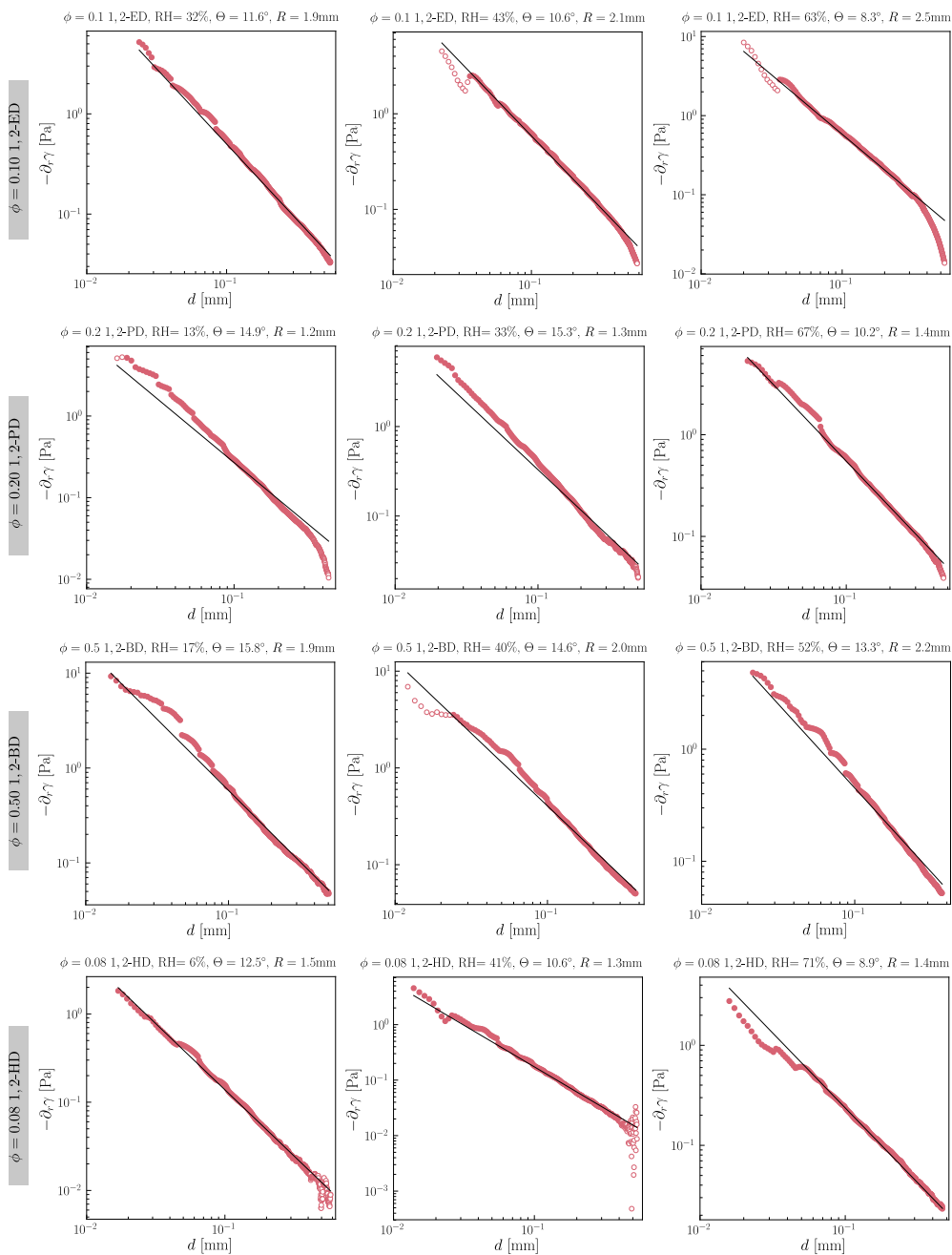


Figure 5.7: Surface tension gradient vs. the distance to the contact line. Each plot shows the experimental data (close circles) with the corresponding power law  $\partial_r \gamma \sim d^{-3/2}$  (solid lines). The open circles are the data that has not been considered in the fitting.

# Chapter 6

## Liquid-Liquid phase separation

**Citation and credit:** Submitted.

**Title:** *“How liquid-liquid phase separation induces active spreading”*

**Authors:** Youchuang Chao<sup>1</sup>, Olinka Ramírez-Soto<sup>1</sup>, Christian Bahr<sup>1</sup>, and Stefan Karpitschka<sup>1</sup>.

<sup>1</sup>Max Planck Institute for Dynamics and Self-Organization, 37077 Göttingen, Germany

**Contribution:** I designed and built the experimental setup for the side-view imaging and the control chamber, and edited the manuscript.

---

### 6.1 Abstract

The interplay between phase separation and wetting of multicomponent mixtures is ubiquitous in nature and technology and recently gained significant attention across scientific disciplines, due to the discovery of biomolecular condensates. It is well understood that sessile droplets, undergoing phase separation in a static wetting configuration, exhibit microdroplet nucleation at their contact line, forming an oil ring during later stages. However, very little is known about the dynamic counterpart, when phase separation occurs in a non-equilibrium wetting configuration i.e., spreading droplets. Here we report that liquid-liquid phase separation strongly couples to the spreading motion of three-phase contact lines. Thus, the classical Cox-Voinov law is

not applicable anymore, because phase separation adds an active spreading force beyond capillary driving. Intriguingly, we observe that spreading starts well before any visible nucleation of microdroplets in the main drop. Using high-speed ellipsometry, we further demonstrate that surface forces cause an even earlier nucleation in the wetting precursor film around the droplet, initiating the observed wetting transition. We expect our findings to enrich the fundamental understanding of phase separation processes that involve dynamical contact lines and/or surface forces, with implications in a wide range of applications, from oil recovery or inkjet printing to material synthesis and biomolecular condensates.

## 6.2 Introduction

Phase separation or demixing of homogeneous liquid mixtures into two or more distinct phases frequently occurs in nature and everyday life, and critically impacts a variety of engineering applications (Lohse et al., 2020), such as oil recovery (Muggeridge et al., 2014), inkjet printing (Xia et al., 2005), and materials synthesis (Chao et al., 2020). In most practical situations, phase separation processes occur in heterogeneous environments, i.e., in contact with surfaces, because the interaction with surfaces facilitates nucleation (Turnbull, 1950). Thus the interplay of phase separation and wetting is often nontrivial and can not be ignored (Gelb et al., 1999; Tanaka, 2001). For instance, the wettability of rock surfaces can strongly affect separation efficiency of the crude oil-water mixture for recovering oil from underground reservoirs (Muggeridge et al., 2014). Even for a single-component liquid, the kinetics of phase transition between different liquid states can be altered by the presence of solid surfaces (Murata et al., 2010). In addition to technical applications, coexistence of phase separation and wetting is found in biological settings. A typical example is the protein condensation, a key process for living cells to form membraneless organelles (Banani et al., 2017; Shin et al., 2017), which happens not only in bulk cytoplasm, but frequently on surfaces like the nucleus, microtubuli, and lipid bilayers (Brangwynne et al., 2015; Ditlev, 2021). In the latter case, the wetting properties of biological membranes plays an essential role, for instance, in regulating autophagy of the phase-separated compartments (Agudo-Canalejo et al., 2021).

Earlier studies have revealed the physical mechanisms of heterogeneous nucleation, such as the effect of particle sizes and surface properties on the nu-

creation efficiency (Fletcher, 1958; Kim et al., 2008), or the impact of preferential wetting on spinodal decomposition in binary liquid mixtures (Wiltzius et al., 1991; Genzer et al., 1997; Tanaka, 2001; Puri, 2005). Recent work has demonstrated how selective evaporation of sessile droplets in various static wetting configurations modulates nucleation and coarsening processes, e.g., in evaporating ternary Ouzo drops (Tan et al., 2016; Tan et al., 2017). Most of those studies focus on the aspect of static wetting, i.e., pinned three-phase contact line conditions (Fletcher, 1958; Genzer et al., 1997; Kim et al., 2008; Wiltzius et al., 1991; Puri, 2005; Li et al., 2011; Tan et al., 2016; Tan et al., 2017; Jensen et al., 2015). Therefore, it remains unclear how the dynamic counterpart, e.g., moving contact lines (Gennes, 1985; Bonn et al., 2009; Snoeijer et al., 2013) interact with phase separation, despite its abundance in many natural and industrial scenarios.

Here we explore the interplay between phase separation and wetting dynamics, using droplets of an evaporating, non-ideal, binary liquid mixture with a well-defined miscibility gap on complete wetting substrates. We adopt droplets of water and glycol ethers as a model system that exhibits a lower critical solution temperature (LCST) close to room temperature (see Supplementary Information 6.11, Figure 6.5 and Table 6.1). In the one-phase region, due to solutal Marangoni flows, the droplet maintains a quasi-stationary, contracted state with a nonzero apparent contact angle  $\theta_{app}$  and a high mobility, i.e., an unpinned contact line (Cira et al., 2015; Karpitschka et al., 2017; Malinowski et al., 2020; Molina et al., 2021; Parimalanathan et al., 2021; Williams et al., 2021) (Figure 6.1(a)). We then trigger phase separation by driving the droplet into the miscibility gap, by heating and/or selective evaporation (Figure 6.1(b,c)). Surprisingly, upon liquid-liquid phase separation (temperature  $T > T_C$ ), we see actively driven droplet spreading. Notably, spreading occurs before any visible nucleation of microdroplets in the main drop. High-speed ellipsometry reveals an even earlier phase separation in the precursor film around the droplet, evidencing the strong coupling of phase separation and surface forces, which leads to the observed wetting transition.

### 6.3 Experimental setup and system

To heat droplets in a precise manner, we built a computer-controlled heating system, which was mounted on top of an inverted microscope (Nikon Eclipse Ti2E). As substrates, we used precision microscopy coverslips (VWR, thick-

### 6.3. EXPERIMENTAL SETUP AND SYSTEM

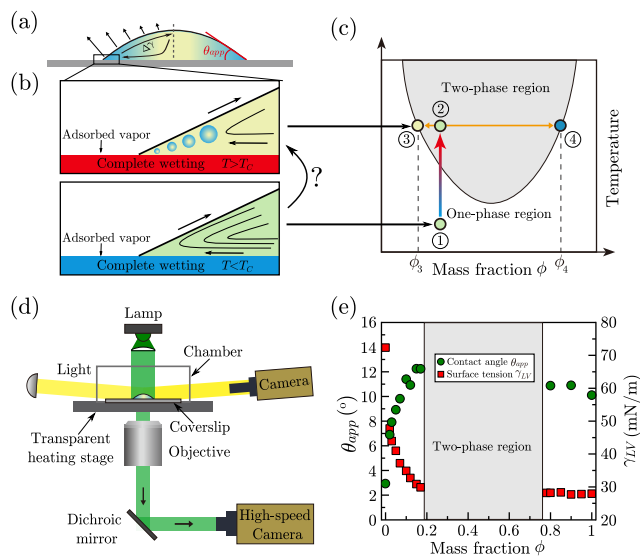


Figure 6.1: Experimental system and setup. (a) Schematic cross-section of an evaporating binary droplet on complete wetting surfaces, with a non-zero apparent contact angle due to solutal Marangoni flows. (b) Zoom to the contact line region before and during phase separation, triggered by heating the substrate. (c) Schematic phase diagram of a binary-liquid system with a lower critical solution temperature (LCST). Upon heating from the one-phase region ① to two-phase region ②, the mixture separates into two phases ③ and ④. (d) Schematic of the experimental setup, with simultaneous observation from the side and below. (e) Apparent contact angle  $\theta_{app}$  (green) and surface tension  $\gamma_{LV}$  (red) of the DPnP-water mixture versus DPnP mass fraction  $\phi$  on complete wetting surfaces at  $T \sim 20^\circ\text{C}$ .

ness 0.17 mm) and one-side frosted microscopy slides (Corning, thickness 0.96 ~ 1.06 mm), cleaned by piranha solution or plasma treatment to generate complete wetting surfaces, or by ethanol for partially wetted surfaces. Droplets of initial volumes  $\Omega = 0.5\text{--}2\ \mu\text{L}$  were deposited onto the substrates and then heated at a controlled rate. Bottom-view and side-view images were simultaneously recorded by a high-speed camera (Phantom VEO 4K-L, 50 – 500 fps) with the microscope and a CMOS camera (Point Grey Grasshopper2, 27 fps) attached to a telecentric lens from the side (Figure 6.1(d)). We used binary mixtures of water (“Milli-Q”, resistivity 18 M $\Omega$  cm) and di(propylene glycol) propyl ether (DPnP, Sigma-Aldrich,  $\geq 98.5\%$ , mass fraction  $\phi$ ), unless stated otherwise (see Materials and Methods for more experimental details). Figure 6.1(e) shows apparent contact angle  $\theta_{app}$  (green) and surface tension  $\gamma_{LV}$  (red) versus  $\phi$  of our DPnP-water mixture in the one-phase region on completely wetted substrates. However, the apparent contact angles are quasi-statically non-zero: the single-phase water-rich binary mixture exhibits strong Marangoni-contraction, whereas the glycol ether-rich mixture shows autophobing (Hack et al., 2021). What happens when the droplet is now forced into the two-phase region (Figure 6.1(b,c))?

## 6.4 Abrupt spreading

We begin with investigating the macroscopic dynamics by heating droplets in pinned and unpinned situations, i.e., partially and completely wetted, respectively. Figure 6.2(a) illustrates a typical image sequence of a 1  $\mu\text{L}$  DPnP-water binary droplet with  $\phi = 0.1$  heated on a completely wetted substrate. During heating the substrate, we first observe enhanced contraction (see Figure 6.2(a) 0–6.5 s, Figure 6.2(b)), owing to the increased selective evaporation and thus intensified Marangoni flows. However, surprisingly, above a certain temperature ( $T_C \sim 37^\circ\text{C}$ ), a sharp transition into an abrupt spreading motion is observed (Figure 6.2(a) 6.5–9.2 s, Figure 6.2(b)). Shortly thereafter, droplet spreading is accompanied by nucleation and growth of DPnP-rich microdroplets (Figure 6.2(a) 9.2 s, Supplementary Video S1). In contrast, droplets on the partially wetted surfaces phase-separate in their bulk as temperature increases, without any apparent change of droplet radius (Supplementary Video S2). This latter scenario is consistent with previous reports on evaporation-driven phase separation (segregation) of binary (Li et al., 2018; Kim et al., 2018) or ternary droplets (Tan et al., 2016; Tan et al., 2017) that

are subject to contact line pinning.

As a control experiment without phase separation, for instance to clarify the impact of thermal (Marangoni) convection (Ristenpart et al., 2007; Diddens et al., 2017; Gurralla et al., 2019; Williams et al., 2021), we replace DPnP with a glycol of similar surface activity, propylene glycol ( $\phi = 0.1$ , Sigma-Aldrich,  $\geq 99.5\%$ ). Note that water and propylene glycol are well miscible, meaning that their mixture does not exhibit liquid-liquid phase separation throughout our experimental conditions. In this case, we only see an enhanced contraction and no spreading motion, during the heating process.

## 6.5 Impact of phase separation on spreading

For pure liquids, the dynamics of advancing contact lines follows the classical Cox-Voinov law (Cox, 1986; Voinov, 1976)

$$\theta_{app}^3 - \theta_{eq}^3 = 9 \text{Ca} \ln \left( \alpha \frac{l_o}{l_i} \right), \quad (6.1)$$

where  $\theta_{app}$  and  $\theta_{eq}$  denote the dynamical apparent contact angle and the equilibrium contact angle, respectively.  $\text{Ca} = \mu U_{CL} / \gamma_{LV}$  is the capillary number,  $\mu$  the dynamic viscosity, and  $U_{CL}$  the speed of the moving contact line.  $\alpha$  is a nonuniversal numerical constant, and  $l_o$  and  $l_i$  indicate an outer (macroscopic) and an inner (microscopic) length (Eggers et al., 2004; Snoeijer et al., 2013). Figure 6.2(c) shows the dependence of  $\theta_{app}^3 - \theta_{eq}^3$  on  $\text{Ca}$  and, on the inset, on  $U_{CL}$ , for phase-separating DPnP-water ( $\phi = 0.1$ , light green and  $\phi = 0.15$ , dark green), toluene (dark gray) and water (light gray) droplets, respectively. Here, for the DPnP-water mixtures, toluene and water,  $\theta_{eq}$  are  $\sim 6.1^\circ$  ( $\phi = 0.1$ ),  $\sim 6.3^\circ$  ( $\phi = 0.15$ ),  $\sim 5.5^\circ$  and  $\sim 2.7^\circ$ , respectively. As expected, experimental data of toluene and water collapse onto a master curve (black straight line), following the Cox-Voinov law (Eq. 6.1). Surprisingly, we observe a deviation from the Cox-Voinov law for the phase-separating binary droplets, evidencing a direct coupling of phase separation to the spreading process. We find larger capillary numbers during phase separation, and a power law with an exponent greater than 1 that increases as the glycol-ether mass fraction is increased. Thus, phase separation accelerates spreading (Figure 6.2(c)).

## 6.5. IMPACT OF PHASE SEPARATION ON SPREADING

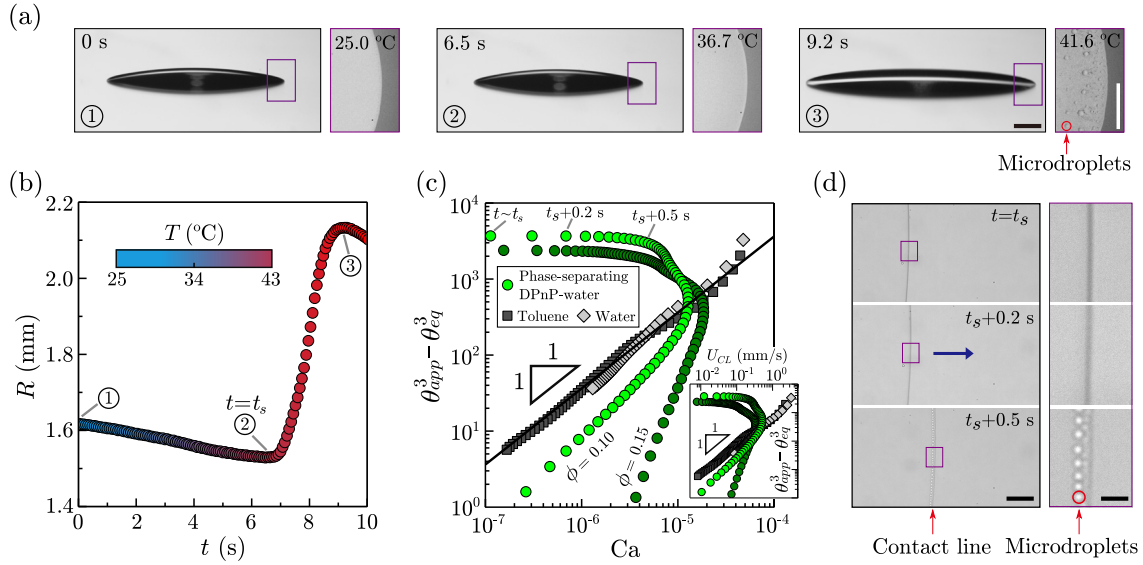


Figure 6.2: Active spreading of a 1  $\mu\text{L}$  phase-separating DPnP-water droplet on a substrate heated at  $\sim 1.8^\circ\text{C}/\text{s}$ . (a) Image sequence of the side aspect of the droplet ( $\phi = 0.1$ ) (left) together with the bottom view of the contact line region (right). Scale bars are 0.25 mm. (b) Droplet radius  $R$  versus time  $t$  and temperature as color code.  $t_s$  marks the onset of spreading. (c)  $\theta_{app}^3 - \theta_{eq}^3$  versus the capillary number  $\text{Ca}$  for phase-separating DPnP-water ( $\phi = 0.1$  &  $0.15$ , light & dark green, respectively), compared to simple fluids toluene and water (dark and light grey, respectively). Simple fluids follow the Cox-Voinov law Eq. (6.1), collapsing onto a single line of slope 1 (black line). Inset: same data, as function of the physical  $U_{CL}$  (also see Supplementary Information 6.11, Figure 6.7). (d) High-resolution images of the contact line region. Spreading (direction indicated by the arrow) starts first, followed by nucleation and growth of microdroplets. Scale bars are 50 and 10  $\mu\text{m}$  for main and zoom panels, respectively.

Of course, there is no single well-defined capillary velocity,  $U_{cap} = \gamma_{LV}/\mu$  for a droplet with ongoing phase separation, since in general, the two phases exhibit different viscosities, and an emulsion may, on top, show non-Newtonian behavior (Derkach, 2009). Nonetheless, it is instructive to non-dimensionalize the contact line velocity  $U_{CL}$  with a characteristic value that is representative for the given situation. We measure surface tensions and viscosities in water-rich ( $\phi = 0.1$  and  $0.15$ ) and the corresponding DPnP-rich one-phase regions at the temperature that droplet starts spreading, obtaining for  $\phi = 0.1$  capillary velocities  $\sim 40$  m/s and  $\sim 6.5$  m/s, respectively, and for  $\phi = 0.15$  capillary velocities  $\sim 18$  m/s and  $\sim 4.2$  m/s, respectively. In Figure 6.2(c), we use the value for the water-rich phase, which corresponds to the initial condition for the abrupt spreading and the volumetrically dominating phase throughout this process. The presence of glycol ether-rich microdroplets would increase the apparent viscosity (Supplementary Information 6.11, Figure 6.6). Thus the curves are a lower bound for the actual capillary number. In the Supplementary Information 6.11, we also depict the range of possible capillary numbers (Figure 6.7).

To identify phase separation near the contact line, we further record bright-field images at higher spatial resolution at  $\times 40$  magnification (NA 0.60). As previously observed for pinned droplets (Tan et al., 2016), microdroplets nucleate and grow at the contact line region (Figure 6.2(d) and Supplementary Video S3). However, microdroplets appear only around 0.44 s after the onset of contact line motion (Supplementary Information 6.11, Figure 6.8). We confirm the generality of this phenomenon in our experimental system, using a wide range of heating rates (0.9, 0.3 °C/s), different mass fractions of DPnP ( $\phi = 0.05, 0.15$ ), as well as binary mixtures made up of water and different glycol ethers (TPnP, DPnB). Nucleation is quantified in the images by the average pixel-wise absolute deviation of the intensity in the contact line region from a reference image, a signal that grows rapidly at the point of nucleation (Supplementary Information 6.11, Figure 6.9). This suggests physicochemical changes at the contact line or outside the main droplet, i.e., in the adsorbed precursor film, before the visible (macroscopic) phase separation occurs in the main droplet (Figure 6.3(a,b)).

## 6.6 Impact of surface forces on phase separation

Based on above observations (Figure 6.2(d)), we hypothesize that surface forces drive an earlier change within the precursor film by promoting liquid-liquid phase separation. In our system, surface forces are mainly due to van der Waals interactions across the three phases, air/liquid/substrate, which can be quantified in the form of a disjoining pressure (Israelachvili, 2011)

$$\Pi(h) = \frac{A}{6\pi h^3}, \quad (6.2)$$

where  $A \sim -10^{-20}\text{J}$ , the Hamaker constant (Israelachvili, 2011). Thus, for Eq. (6.2) to attain values significant to chemical equilibrium,  $h \sim \mathcal{O}(1\text{ nm})$  is required, a typical thickness of a precursor film (Bonn et al., 2009). For complete wetting conditions, surface forces are repulsive, i.e.,  $\Pi(h) < 0$ , giving rise to a reduced pressure in the precursor film,  $p_f = p_\infty + \Pi(h)$  where  $p_\infty$  is the ambient pressure. Pressure is a key factor in chemical equilibrium and well-known to modify the location of phase boundaries (Gibbs, 1876). To this end, we conjecture that inside the precursor film, the reduced pressure  $p_f$  lowers the thermodynamical demixing boundary of the binary mixture, and therefore promotes phase separation. Literature data for mixtures of water and 2-butoxyethanol shows that the LCST decreases with decreasing pressure (Wenzel et al., 1980; Compostizo et al., 1992).

To demonstrate the impact of the disjoining pressure on phase separation, we use high-speed *in situ* ellipsometry, which allows for detecting subtle variations of thickness or refractive index in molecularly thin films (Bahr, 2007; Popescu et al., 2012) (Supplementary Information 6.11, Figure 6.10). Figs. 6.3(c-f) show the ellipsometric angle  $\Delta$  (symbols) as a function of time relative to the onset of spreading,  $t - t_s$ , at three different heating rates (0.5, 0.25, and 0 °C/min, panels (c-e), respectively). Note that phase separation also occurs at constant temperatures above the LCST, due to selective evaporation (panels (e) & (f)). For panels (c-e), the measurement spot is located at a distance  $d \approx 0.5\text{ mm}$  away from the macroscopic contact line (see Figure 6.3(a), and Supplementary Information 6.11, Figure 6.10). For panel (f), the distance is around 5 mm.

Long before the onset of spreading ( $t - t_s \lesssim -20\text{ s}$ ), we find a fluctuating  $\Delta$ . We attribute this to the fluctuations in the evaporation/condensation

## 6.6. IMPACT OF SURFACE FORCES ON PHASE SEPARATION

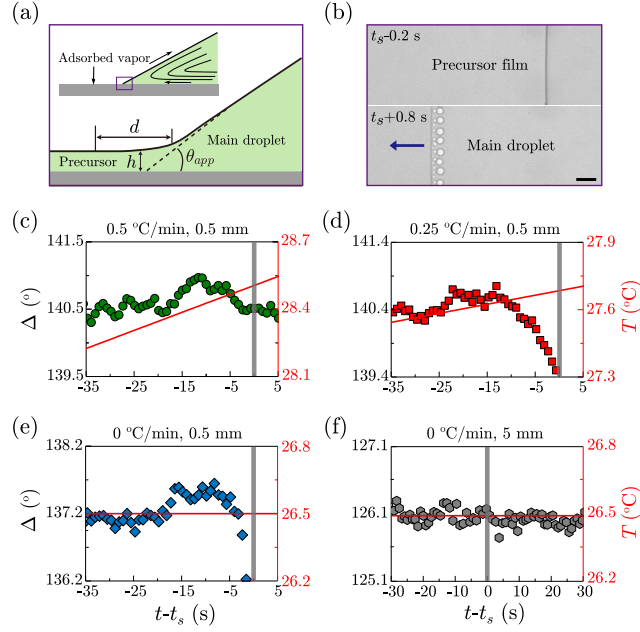


Figure 6.3: Analysis of the precursor film around the main droplet. (a) Schematic cross-section of the micro/nano-scopic contact line region.  $h$  and  $d$  denote film thickness and distance to the contact line, respectively. (b) High-resolution images of the contact line region 0.2 s before and 0.8 s after the onset of spreading at  $t_s$  (scale bar 20  $\mu\text{m}$ ). (c-f) Ellipsometric angle  $\Delta$  (symbols) measured at distance  $d$  to the contact line, and temperature  $T$  (red lines), vs.  $t - t_s$ : three different heating rates of 0.5, 0.25, and 0 °C/min at  $d \sim 0.5$  mm (c-e, respectively), and 0 °C/min at  $d \sim 5$  mm (f). For constant  $T \sim 26.5$  °C (panels (e) & (f)), phase separation is triggered by selective evaporation.

equilibrium between the vapor and the hydrophilic surface (Hack et al., 2021), which is also observed when placing a pendant droplet above a fully wetted substrate (Supplementary Information 6.11, Figure 6.11). Around  $t - t_s \sim -20$  s, we observe an abrupt increase of  $\Delta$ , which is small but distinguishable from noise and reproduced in all repetitions of these experiments. Another  $\sim 5 - 10$  s later, we see a rapid decrease of  $\Delta$ . On the contrary, at a large distance to the droplet (comparable to its radius), we do not observe any measurable change in the ellipsometric signal (panel (f)).

Our results clearly evidence the existence of a composition or morphology variation in the precursor close to the droplet, ahead of any macroscopically visible effect, most probably caused by earlier nucleation in the precursor film. This variation is sensitive to the distance  $d$  from the macroscopic contact line, since the precursor film is, due to its microscopic thickness, always very close to equilibrium with the vapor above it, and the vapor density around an evaporating droplet decays  $\sim 1/d$  (Deegan et al., 2000; Eggers et al., 2010). Far from the contact line, the less volatile DPnP molecules are outnumbered by the more volatile water molecules, which are abundant in the atmosphere due to the natural humidity. As such, the phase boundary is hardly ever reached far from the droplet, even though the precursor film becomes much thinner (Novotny et al., 1991). We note here that no visible increase of  $\Delta$  could be observed for large heating rates  $\gtrsim 1.2^\circ\text{C}/\text{min}$  (Supplementary Information 6.11, Figure 6.12), for which the effect is probably beyond the sampling period ( $\sim 0.8$  s) of our ellipsometer.

## 6.7 Preferential wetting in the two-phase region

Finally, to rationalize on which surface (solid-liquid or liquid-vapor) nucleation first emerges, we test the wetting preference of water-rich and glycol ether-rich droplets on either surface. Here, mutually saturated water-rich and DPnP-rich phases are extracted from bottom and top phases of a well equilibrated DPnP-water mixture at 1:1 mass ratio, respectively (Materials and Methods). A water-rich droplet in a DPnP-rich outer phase (green, Figure 6.4(a)) preferentially wets clean glass, spreading to small contact angles. Exchanging droplet and outer phase (red, Figure 6.4(b)), the contact angle remains large, close to 180 degrees. In both cases, buoyancy is used

## 6.7. PREFERENTIAL WETTING IN THE TWO-PHASE REGION

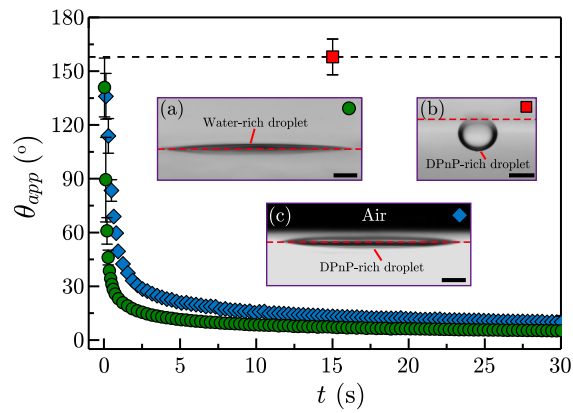


Figure 6.4: Preferential wetting of the two mutually saturated liquid phases at the interface with glass and air: contact angle vs. time (main panel) and side aspects of the immersed droplets (insets). (a) Water-rich droplet spreading on hydrophilic glass in a DPnP-rich ambient phase (green circles). (b) DPnP-rich droplet dewetted from hydrophilic glass (located above the droplet to have buoyancy pushing the drop against the glass) in a water-rich ambient phase (red square). (c) DPnP-rich droplet spreading at the free surface of a water-rich ambient phase (blue diamonds). Red dashed lines represent the surface location, and scale bars are 0.5 mm.

to push the droplet against the substrate, which is thus located above the droplet in the latter case. The opposite behavior is observed at the liquid-air interface, where the DPnP-rich phase spreads along the free surface (blue, Figure 6.4(c), see also Supplementary Information 6.11, Figure 6.13 for additional cases on fully and partially wetted substrates). These observations suggest that the glycol ether-rich phase nucleates initially at the liquid-air interface, before microdroplets appear in the bulk of the main droplet or at the substrate surface.

Although these observations can not readily be transferred to the precursor region, where the presence of three phases in close proximity leads to strong surface forces may alter wetting preferences, it renders a “leaking-out” (Brochard-Wyart et al., 2000) of DPnP rather unlikely. Rather, an increased water fraction in the precursor film would be expected. Yet, there the phase change appears well before the spreading or visible microdroplet nucleation.

## 6.8 Discussion and conclusions

In contrast to binary or ternary droplets on partially wetted surfaces with pinned contact lines (Tan et al., 2016; Tan et al., 2017; Li et al., 2018; Kim et al., 2018; Christy et al., 2011; Kim et al., 2016; Edwards et al., 2018; Li et al., 2019; Moon et al., 2020; Guo et al., 2021), here we report unexpected spreading of phase-separating binary-mixture droplets on fully wetted surfaces with free contact lines. Interestingly, we find that Cox-Voinov law is not applicable anymore for such droplets, because phase separation accelerates the speed of moving contact line. A closer inspection of the contact line region reveals that the nucleation in the main droplet occurs later than the advancing motion of contact line. We argue that surface forces inside the wetting precursor shift the thermodynamic phase boundary considerably, promoting phase separation well in advance to the observed spreading or bulk droplet behavior, which we verify by ellipsometric measurements. We demonstrate that the nucleating (glycol ether-rich) phase has a strong wetting preference for the liquid-air interface. We therefore conclude that, when the binary mixture is pushed into the two-phase region, surface forces facilitate phase separation at the free surface, in nanoscopic proximity to the contact line. It is this earlier phase separation that drives the contracted droplet away from stationary state and changes the force balance at the three-phase

contact line (Cira et al., 2015; Karpitschka et al., 2017), thus causing the active spreading. It is worth noting that no apparent spreading motion can be seen for droplets made up of single-phase glycol ether-rich binary mixtures, such as DPnP with  $\phi = 0.8$  (see Supplementary Video S4). This might be because molecular autophobicity dominates over Marangoni contraction: the droplet is unable to spread on its own adsorbed film, causing contact line pinning on the surface (Novotny et al., 1991; Hack et al., 2021).

To summarize, we have demonstrated that the strong coupling between phase separation, moving contact lines, and surface forces results in forced spreading on complete wetting surfaces, well beyond the capillarity-dissipation balance of Cox-Voinov spreading. Our work shows experimentally the crucial roles of phase separation and surface forces in dynamic multi-phase systems, motivating future studies to reveal the molecular processes and a theoretical understanding of these observations (Thiele et al., 2013). We expect these findings to enrich also the fundamental understanding of active wetting transition in tissue morphogenesis (Pérez-González et al., 2019), phase separation nano-engineering applications (Wasan et al., 2003; Sadafi et al., 2020; Pahlavan et al., 2021b), or liquid-liquid phase separation dynamics in cell biology (Banani et al., 2017; Shin et al., 2017).

## 6.9 Acknowledgements

We acknowledge financial support from the Max Planck – University of Twente Center for Complex Fluid Dynamics. Y.C. acknowledges support through an Alexander von Humboldt Fellowship. We also would like to thank L. D. Rodriguez, A. Barthel, W. Keiderling, K. Hantke, J. Chateau and H. Jeon for assistance with the experiments.

## 6.10 Materials and Methods

### 6.10.1 Preparation of the substrate

Microscope coverslips (VWR,  $24 \times 24$  mm, thickness 0.17 mm) or one-side frosted microscope slides (Corning,  $75 \times 25$  mm, thickness 0.96–1.06 mm) were treated with either ethanol, plasma, or piranha solutions, and then used as substrates. For ethanol cleaning, the substrates were sonicated in ethanol for 20 min, and then stored in fresh water (“Milli-Q”, resistivity 18 M $\Omega$  cm).

For plasma cleaning, the substrate was cleaned in an acetone solution in the ultrasonic bath for 15 min, sonicated in ethanol solution for 15 min, and then rinsed with deionized water, dried in the oven, and finally treated with oxygen plasma (Harrick Plasma) for  $\sim 3$  min. For piranha solution cleaning, the substrates were treated in piranha solutions (hydrogen peroxide 30% and sulfuric acid 95%, VWR, mixture 1:3 by volume) for 20 min. Then, the substrates were rinsed with fresh water for five times, sonicated in hot water ( $\sim 80^\circ\text{C}$ ) for 10 min, and stored in fresh water. The ethanol and piranha cleaned substrates were used on the day of preparation, and dried with a nitrogen drying gun in a laminar flow hood before each measurement. The plasma-cleaned substrate was used immediately after preparation.

### 6.10.2 Preparation of the binary mixture

For binary solutions, we prepared a mixture consisting of water (“Milli-Q” water, resistivity 18 M $\Omega$  cm) and one of the following glycol ethers: Di(propylene glycol) propyl ether (DPnP,  $\geq 98.5\%$ ), tri(propylene glycol) propyl ether (TPnP, 97%), and di(propylene glycol) butyl ether (DPnB,  $\geq 98.5\%$ ) or a typical glycol: Propylene glycol ( $\geq 99.5\%$ ). For spreading of pure liquids, we use “Milli-Q” water and toluene ( $\geq 99.9\%$ ). All chemicals were purchased from Sigma-Aldrich. The corresponding experimental phase diagrams of water and glycol ether mixture adapted from Bauduin et al. (2004) are shown in Figure 6.5 (Supplementary Information 6.11), and the basic physicochemical parameters of glycol ethers at room temperature ( $\sim 25^\circ\text{C}$ ) from existing literature (Staples et al., 2002; Bauduin et al., 2004; Frank et al., 2007) are summarized in Table 6.1 (Supplementary Information 6.11).

### 6.10.3 Preparation of two mutually saturated phases

The immiscible DPnP-water solution were prepared by first mixing DPnP and water with a weight ratio of 1:1. The well-mixed solution was then centrifuged in a laboratory centrifuge (Centrifuge 5804R, Eppendorf) at 4000 r.p.m for 2 hours and allowed to phase-separate for more than 48 hours. Finally, the two mutually saturated phases, i.e., water-rich and DPnP-rich solutions, were collected from the bottom and top layers of the well equilibrated mixture, respectively.

#### 6.10.4 Measurements of liquid viscosity, surface tension and contact angle

The viscosity  $\mu$  of liquid mixture was measured by a temperature-controlled rheometer (Anton Paar MCR 502). The surface tension  $\gamma_{LV}$  was measured with a goniometer (DataPhysics OCA 20) using the pendant drop method. For each mixture, at least ten droplets were measured and analyzed to obtain the surface tension, with an average error of 0.16 mN/m. The static apparent contact angle  $\theta_{app}$  (Figure 6.1(e)) was measured with this goniometer using the sessile drop method.

#### 6.10.5 Observation of the main droplet

The recording of main droplet was performed in a custom-built chamber ( $\sim 10 \times 10 \times 5$  cm), mounted on the top of an inverted (epi-fluorescence) microscope (Nikon Eclipse Ti2E). A computer-controlled heating system was further built into the chamber, allowing the substrate to be set at defined temperature and heating rate. The heating system composed of a transparent ITO glass ( $28 \times 28$  mm, thickness 0.7 mm, CEC020B, Praezisions Glas & Optik GmbH), a home-assembled PID controller, and a Python-based controlling interface, which was also calibrated by an IR thermal imaging camera (Laserliner). Droplets composed of mixtures of water (“Milli-Q”) and a glycol ether or propylene glycol, with initial volumes  $\Omega = 0.5\text{--}2$   $\mu\text{L}$ , were gently deposited onto the cleaned microscope coverslip with a glass syringe (Hamilton GasTight). Afterward, droplet behavior was observed simultaneously by two cameras: one high-speed camera (Phantom VEO 4K-L, 50–500 fps) for the bottom-view recording, and another cmos camera (Point Grey Grasshopper2, 27 fps) attached to a macro lens (Thorlabs Bi-Telecentric lens, 1.0X, W.D. 62.2 mm) with a collimated-light source for the side-view recording (also see Figure 6.1(d)). The bright-field microscopy was performed with either a  $\times 2$  Plan Apo objective for observing the whole droplet or a  $\times 40$  (numerical aperture 0.60) Plan Fluor objective for detecting the region of contact line. The relative humidity RH and ambient temperature were stable,  $30 \pm 5\%$  and  $21 \pm 1$   $^{\circ}\text{C}$ , respectively. All images were analyzed by custom-made MATLAB codes and/or the open-source IMAGEJ software. The dynamical apparent contact angle  $\theta_{app}$  (Figure 6.2(c)) was obtained from the side-view images as  $\theta_{app} \simeq 2h_0/R$ , where  $h_0$  and  $R$  are the maximal height and the foot radius of the droplet, respectively.

### 6.10.6 On-site ellipsometric measurements of the precursor film

The variation of precursor film was detected in separate experiments using a high-speed phase-modulated ellipsometer (NeHe laser beam, diameter 0.63 mm, wavelength  $\lambda = 633$  nm, sampling period  $\sim 0.8$  s) (Bahr, 2007). To regulate the substrate temperature, the ellipsometer was equipped with a temperature controller (Eurotherm), which was sampled by a thermal sensor. Furthermore, to minimize the light reflection from the bottom side of glass substrates, one-side frosted microscope slides, instead of coverslips, were applied, and additionally a half part of the substrate were untreated so as to fix the droplet during measurements. The angle of incidence  $\alpha_i$  was adjusted so that the value of ellipsometric angle  $\Delta$  was near  $135^\circ$ . Typically, low heating rates ( $\leq 1^\circ\text{C}/\text{min}$ ) were applied in order to efficiently capture the fast dynamics of precursor film, and additionally, droplets with large size  $\Omega = 5\text{--}10$   $\mu\text{L}$  were adopted to reduce the evaporation-induced volume shrinkage. During ellipsometric measurements, the main droplet was simultaneously recorded by a camera (Point Grey Grasshopper2, 10 fps) from the top-view, accompanying with a green light ( $\lambda = 550$  nm, KL 1500 LCD) as illumination from the side (Supplementary Information 6.11, Figure 6.10). Here, the green light was applied to avoid its interference with the HeNe laser light ( $\lambda = 633$  nm). Under this condition, the value of  $\Delta$  was assumed to be most sensitive to the variation inside the precursor film. Measurements were also performed in an atmospheric control chamber to minimize external disturbances in the vapor field due to ambient air currents. For all experiments, each measurement begun when the deposited droplet reached a steady state ( $\sim 1\text{--}3$  min). During this period, droplets were assumed to form an effective  $\theta_{app}$  as well as to develop a stable precursor film.

## 6.11 Supplementary Information

### 6.11.1 Supplementary Videos

**Video S1:** A  $1\ \mu\text{L}$  droplet of DPnP-water mixture ( $\phi = 0.1$ ) heated on a complete wetting substrate. The heating starts from  $25^\circ\text{C}$  at a rate of  $\sim 1.8^\circ\text{C}/\text{s}$ . The video plays at real time.

**Video S2:** Similar to Video S1, but on a partial wetting substrate.

**Video S3:** A high-resolution video showing the abrupt motion of contact line, followed by nucleation and growth of emulsion microdroplets ( $\phi = 0.1$ ). The video starts at 0.2 s before droplet spreading, and plays at  $0.2 \times$  real time.

**Video S4:** A  $1.5 \mu\text{L}$  droplet of DPnP-water mixture ( $\phi = 0.8$ ) heated on a complete wetting substrate. The heating is triggered from  $25^\circ\text{C}$  with a rate of  $\sim 1.8^\circ\text{C}/\text{s}$ . The video plays at real time.

### 6.11.2 Supplementary Figures and Table

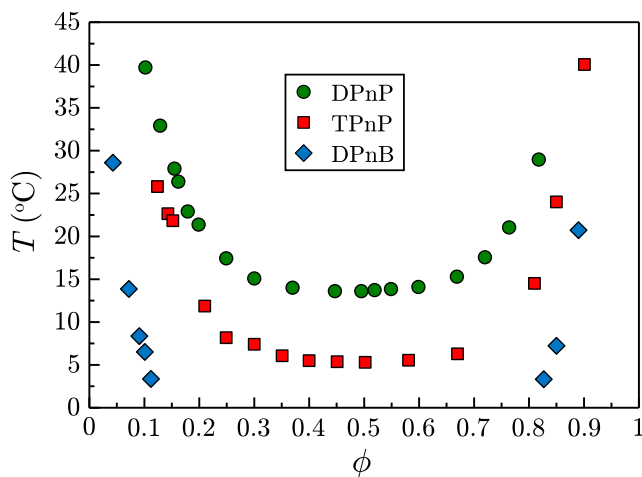


Figure 6.5: Experimental phase diagrams, temperature  $T$ -mass fraction  $\phi$  of mixture of water and three different glycol ethers: DPnP (green circles), TPnP (red squares), and DPnP (blue diamonds), which are adapted from Bauduin et al. (2004).

## 6.11. SUPPLEMENTARY INFORMATION

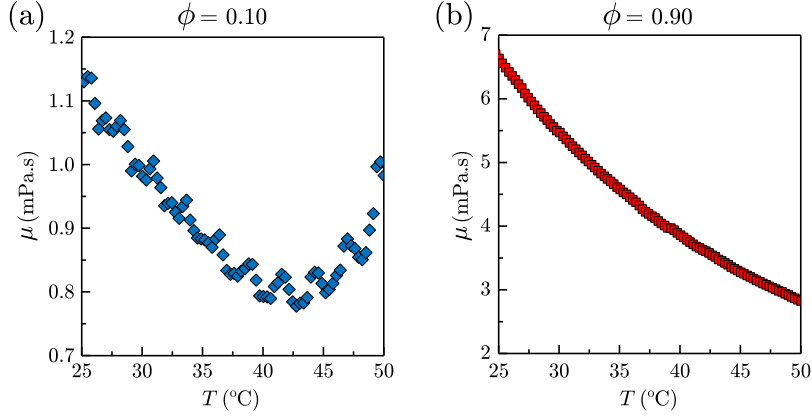


Figure 6.6: The viscosity  $\mu$  of water-rich ( $\phi = 0.1$ , a) and DPnP-rich ( $\phi = 0.9$ , b) binary mixture as a function of temperature  $T$ . The apparent viscosity of water-rich mixture reaches a minimum at around  $T \sim 40$  °C due to the phase-separated microdroplets. No apparent increase of viscosity of DPnP-rich mixture is seen, which is probably due to the minor effect of emulsion droplets compared to that of temperature.

Table 6.1: The adopted glycol ethers and associated basic physicochemical parameters at 25 °C (Staples et al., 2002; Bauduin et al., 2004; Frank et al., 2007).

GE <sup>a,b</sup>	Mw	$\rho$ (g/cm <sup>3</sup> )	$p_v$ (mmHg)	$\gamma$ (mN/m)	Molecular structure
DPnP <sup>c</sup>	176.25	0.916	0.12	27.8	
TPnP	234.33	0.935	0.0002	27.6	
DPnB	190.28	0.913	0.068	28.4	

<sup>a</sup>GE: glycol ether; Mw: molecular weight;  $\rho$ : density;  $p_v$ : vapor pressure;  $\gamma_{LV}$ : surface tension.

<sup>b</sup>For another component of binary droplets, H<sub>2</sub>O,  $p_v = 23.756$  mmHg and  $\gamma_{LV} \sim 72.4$  mN/m at 25 °C.

<sup>c</sup>LCST of the DPnP-water mixture is 13.8 °C at the DPnP mass fraction  $\phi \approx 0.4$  (Bauduin et al., 2004).

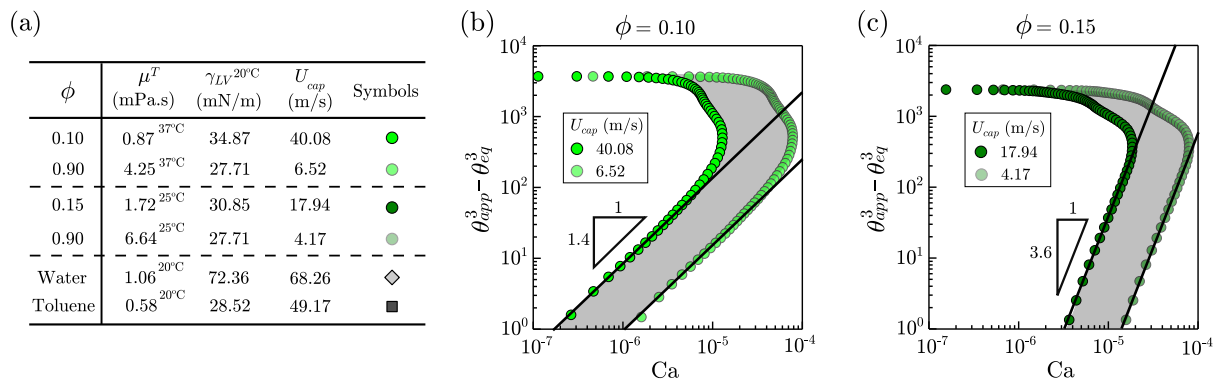


Figure 6.7: (a) The estimated capillary velocity  $U_{cap} = \gamma_{LV}/\mu$  of DPnP-water mixtures, water and toluene at the temperature of spreading. We assume that the effect of temperature on surface tension is insignificant, and adapt surface-tension values at room temperature  $T \sim 20^\circ\text{C}$ . (b,c) The range of possible capillary numbers  $Ca$  (gray shadows) based on capillary velocities  $U_{cap}$  obtained from water-rich ( $\phi = 0.1, 0.15$ , light & dark green circles, respectively) and DPnP-rich ( $\phi = 0.9$ , transparent light & dark green circles, respectively) mixtures at the temperature of spreading. In (b), droplet spreads at  $T \sim 37^\circ\text{C}$ , and in (c), droplet spreads at  $T \sim 25^\circ\text{C}$ . Here we point out that in our case, the capillarity-viscous dissipation balance of Cox-Voinov spreading is still applicable for low-viscosity pure liquids because the drops are thin ( $\theta_{app} < 20^\circ$ ): when the Reynolds number is much smaller than the aspect ratio, namely,  $\rho U_{CL} h^2 / (\mu R) \ll 1$  ( $\rho$  is the liquid density and  $h$  the droplet height), the lubrication approximation is still valid and thus the inertia can be neglected (Bonn et al., 2009; Jambon-Puillet et al., 2018). For all our droplets,  $\rho U_{CL} h^2 / (\mu R) \lesssim 0.1$ .

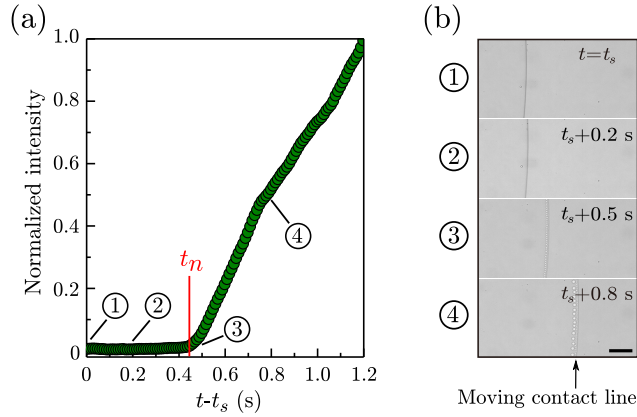


Figure 6.8: (a) The normalized maximal intensity of contact line region used to identify the nucleation event. The intensity signal grows rapidly upon nucleation  $t_n \approx t_s + 0.44$  s, where  $t_s$  represents the onset of spreading. (b) The corresponding high-resolution images showing the motion of advancing contact line, followed by nucleation and growth of microdroplets. The scale bar is  $50 \mu\text{m}$ .

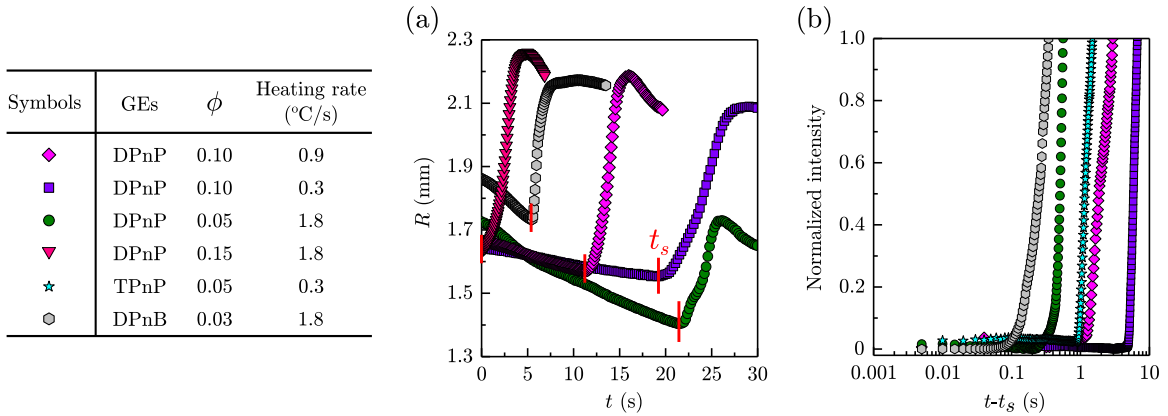


Figure 6.9: Abrupt spreading of phase-separating binary droplets with different heating rates, mass concentrations, and glycol ethers. (a) The droplet radius  $R$  versus  $t$ , where red vertical lines indicate the onset of each spreading  $t = t_s$ . (b) The normalized intensity signals to identify the nucleation event. In all experiments, the heating is triggered from  $25^{\circ}\text{C}$  at  $t = 0$  s, and the droplet size is  $1 \mu\text{L}$ . It should be noted that the horizontal axis in (b) is defined as  $t - t_s$  for clarity.

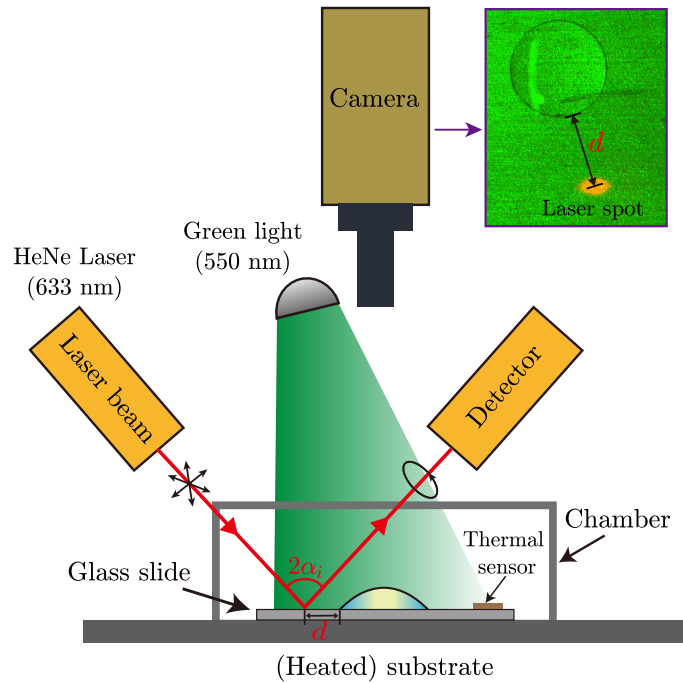


Figure 6.10: Schematic showing the on-site ellipsometric measurement of the precursor-film dynamics and simultaneous top-view monitoring of the main drop (not to scale). Here,  $\alpha_i$  and  $d$  refer to the angle of incidence and the distance between the center of laser spot and macroscopic contact line, respectively. The inset shows a typical experimental image captured from the top-view camera.

## 6.11. SUPPLEMENTARY INFORMATION

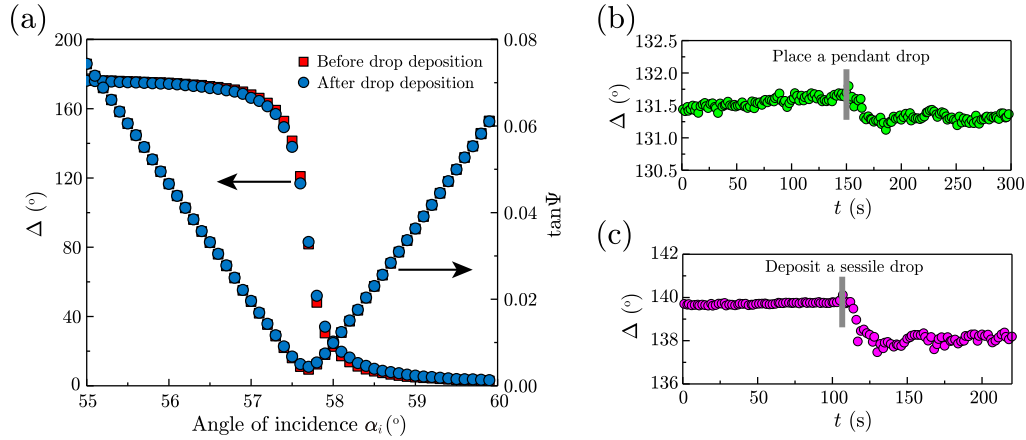


Figure 6.11: (a) Dependence of  $\Delta$  and  $\tan\Psi$  on the angle of incidence  $\alpha_i$  before (red squares) and after (blue circles) droplet deposition on a full wetting substrate. Note that when the chosen  $\alpha_i$  is near  $57.5^\circ$  where the ellipsometric angle  $\Delta$  is around  $135^\circ$ ,  $\Delta$  is most sensitive to the droplet deposition. (b,c) Change of  $\Delta$  when a droplet is suspended above (b) and deposited on (c) the substrate, where  $\alpha_i = 57.5^\circ$ . Here, Droplets are made up of water and DPnP ( $\phi = 0.1$ ) with  $\Omega = 5 \mu\text{L}$ , and the detection distance  $d$  to droplet edge is around 5 mm. A decrease of  $\Delta$  can be observed in both cases, followed by slight fluctuations, indicating that the development of precursor film is given by the evaporation-condensation mechanism (Novotny et al., 1991; Hack et al., 2021).

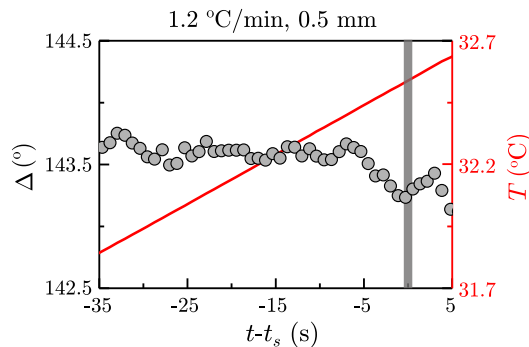


Figure 6.12: The profile of  $\Delta$  (circles) and  $T$  (red line) as a function of  $(t - t_s)$  for a high heating rate:  $1.2^\circ\text{C}/\text{s}$ . No obvious increase of  $\Delta$  can be observed before droplet spreading.

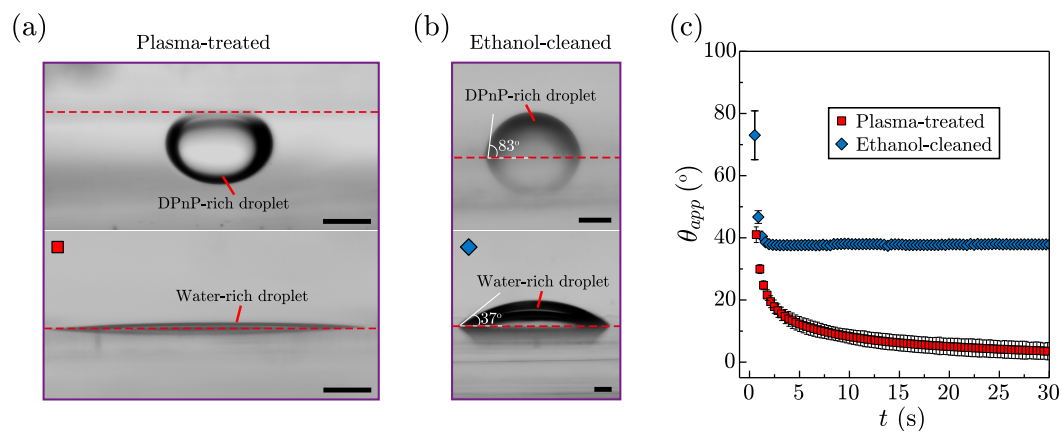


Figure 6.13: (a,b) Additional wettability test of DPnP-rich and water-rich droplets under/on plasma-treated (a) and ethanol-cleaned (b) cover glasses. All scale bars are 0.5 mm. (c)  $\theta_{app}$  versus  $t$  showing water-rich droplets spread on the plasma-treated (red squares) and the ethanol-cleaned (blue diamonds) substrates, respectively. Note that the hydrophilic surfaces applied in Figure 6.4 of the main text were cleaned by piranha solution.

# Chapter 7

## Dynamics of spreading and imbibition of Marangoni-contracted drops on porous substrates

**Citation and credit:** The manuscript is under preparation.

**Title:** *“Dynamics of spreading and imbibition of Marangoni-contracted drops on porous substrates”*

**Authors:** Olinka Ramírez-Soto<sup>1</sup> and Stefan Karpitschka<sup>1</sup>.

<sup>1</sup>Max Planck Institute for Dynamics and Self-Organization, 37077 Göttingen, Germany

**Contribution:** I designed and built the experimental setup, performed the experiments, analyzed the experimental data, made all figures, and wrote the manuscript together with Stefan Karpitschka.

---

### 7.1 Introduction

Wetting and transport of multicomponent liquids over solid surfaces are important processes in fields such as medicine (Horwath et al., 2001), arts

(Baglioni et al., 2013; Abdulsalam et al., 2015), biology (Gao et al., 2004; Bohn et al., 2004), and in engineering applications like coating (Overdiep, 1986). Mostly, the solid surfaces are not ideally smooth or pure, but present physical and chemical patterns. These inhomogeneities affect the motion of the liquid front where the solid, liquid and vapor phases meet, ie. the three phase contact line, either by preventing, enhancing, or redirecting its motion. These effects are widely used to control the wetting behavior by fabricating surfaces with specific chemical composition, topography, or by controlling the surface temperature. Moreover, the liquid complexity gives rise to a variety of wetting phenomena, frequently induced by surface tension gradients, originated by composition (Darhuber et al., 2003) or temperature (Venerus et al., 2015; Shiri et al., 2021) gradients near the contact line. Examples of these are enhanced spreading (Stoebe et al., 1996), fingering (Hamraoui et al., 2004), or dewetting (Takenaka et al., 2014), among others. Simultaneously, liquids induce or prevent modifications of the solid surface topography and composition, for instance pattern collapse (Tanaka et al., 1993), contamination (Fatima et al., 2016) or inhomogeneous coatings (Kim et al., 2016). Therefore, the fundamental understanding of the interplay between surface tension gradients and contact line dynamics over patterned surfaces is of great interest.

Marangoni drying is a technique used for removing liquid films from hydrophilic solid surfaces (Leenaars et al., 1990). This technique is used for example in the semiconductor fabrication for cleaning silicon wafers (Marra, 1993). While pulling a hydrophilic substrate out of a water bath or spinning the wetted substrate, vapor of a water-soluble organic solvent is blown onto the contact line region, thereby enhancing its receding motion to dewet the solid surface. The origin of the effect is an inward Marangoni flow resulting from vapor absorption at the water interface. Since the surface tension of the organic solvent is lower than that of water, an inward surface tension gradient appears due to the preferential absorption near the contact line, similarly to what is observed in selective evaporation of binary mixtures drops (Karpitschka et al., 2017; Benusiglio et al., 2018). In the contracted state, induced by Marangoni flows, contact lines show high mobilities (Huethorst et al., 1991; Cira et al., 2015) while almost no deposition of contaminants from the liquid onto the surface is observed (Leenaars et al., 1990). While the majority of existing studies focused on Marangoni contraction on homogeneous surfaces, little is known about this effect on heterogeneous surfaces (Marra et al., 1991). Here we investigate the wetting

## 7.1. INTRODUCTION

---

dynamics of Marangoni contracted drops on a porous surface in a controlled atmosphere.

Porous materials are common in every day life situations. Examples of these are paper (Sarah et al., 2018), fabrics (Zhao et al., 2017), biological materials like wood (Zhou et al., 2018), and geological formations like rocks and soil (Bakhshian et al., 2020). When a drop is placed on the surface of a hydrophilic porous solid, the drop spreads and is simultaneously absorbed into the pores of the solid, forming an imbibition zone underneath the surface, which expands from the drop edge into the solid. On a thin porous coating on an inert support, the main (slow) transport is directed in radial direction, while full imbibition is quickly achieved along the vertical direction (Figure 7.1(a)). The imbibition, which is the sorption of liquid into porous media, is relevant for technological applications such as medical diagnostics (Martinez et al., 2010), irrigation, and water injection into geothermal reservoirs (March et al., 2016). Both drop spreading and imbibition are affected by different aspects like porosity, permeability, gravity, surface tension and wettability (Kumar et al., 2006; van Gaalen et al., 2021). In particular, when a drop is placed on a porous surface, the spreading dynamics follow distinct stages (Kumar et al., 2006; Arjmandi-Tash et al., 2017; Léang et al., 2019), and one has to distinguish between partial and complete wetting of the external surface of the porous medium. For partial wetting, first the drop radius increases until reaching a maximum while the apparent contact angle decreases. Second, the radius remains constant and the contact angle continues to decrease, due a volume loss by imbibition into the pores. In the final stage, a simultaneous decrease of the drop radius and volume happens, as the wicking procedes. For complete wetting, the dynamics are similar but without the second stage. The case where the vapor of a second, miscible, liquid is present in the atmosphere around the drop and the porous material, has not been studied. However, combining the strong impact of organic vapors on dynamic wetting with the huge internal surface area of porous media, one may expect a significant impact of the vapor also on the wicking dynamics.

In this work we show that the dynamics of water drops over a thin hydrophilic porous media are affected by the presence of IPA vapor in the surrounding atmosphere.

## 7.2 Experimental methods

Experiments were done inside an atmospheric control chamber (size  $\sim 10\text{ cm} \times 10\text{ cm} \times 10\text{ cm}$ ), at room temperature. The atmosphere was composed of a mixture of dry nitrogen and 2-Propanol (IPA, Carl Roth, purity  $\geq 99.9\%$ ) vapor. Nitrogen and IPA vapor were continuously injected to membrane-separated antechambers, behind gas-permeable membranes at opposite side-walls of the main chamber (see Chapter 3 and Ramírez-Soto and Karpitschka 2021 for detailed description on the setup). To achieve arbitrary vapor conditions, the mixing ratio of dry and IPA-saturated gas fluxes was regulated with mass flow controllers (MKS Instruments Type MF1) to the desired proportion, mixing the two fluxes prior to injection, keeping total flux constant at 500 sccm. When forming homogeneous atmospheres, both sides of the chamber had the same mixing ratio. For atmospheres with vapor gradients, different conditions were set, 0% IPA vapor in one side of the chamber and 100% water vapor in the other.

The substrates used were made of a porous silicon oxide layer, templated by candle soot, on top of quartz microscope cover slides. Candle soot consists of a porous network of  $\sim 50\text{ nm}$  size carbon nanobeads (Deng et al., 2012), ideally suited as a low-cost bulk porous material with a hierarchical multi-scale porosity down to a few nanometers. The preparation protocol was inspired by the technique reported previously for preparing superamphiphobic surfaces (Paven et al., 2013; Paven et al., 2014; Ramírez-Soto et al., 2020).

The quartz cover slips (Thermo Fisher Scientific,  $25.4\text{ mm} \times 25.4\text{ mm}$  size,  $0.15\text{--}0.25\text{ mm}$  thick) were first cleaned by sonication in a series of solvents (ethanol, Carl Roth, purity  $\geq 99.5$ , acetone, Sigma Aldrich, purity  $\geq 99.5$ , and toluene, Sigma Aldrich, purity  $\geq 99.9\%$ , and water, “Milli-Q”, resistivity  $18\text{ M}\Omega \cdot \text{cm}$ ) for  $\sim 3\text{ min}$  in each chemical. Afterward, the slides were dried in an oven at  $70^\circ\text{C}$ . The slides were then coated on one side with a layer of candle soot. To coat the slides, the glass slides were held above the candle flame, with constant oscillatory motion in the horizontal plane, perpendicular to the flame, to form a uniform layer of soot particles. The coated slides were placed in a desiccator and stored for 24 h with an open borosilicate glass vial containing 3 ml of ammonium and a second vial with 3 ml of tetraethoxysilane. By this, a chemical vapor deposition and cross-linking of tetraethyl orthosilicate, catalyzed by ammonia, takes place. A  $30\text{--}40\text{ nm}$  thick silica layer is deposited over the porous nanostructures (Paven et al.,

## 7.2. EXPERIMENTAL METHODS

---

2013). The substrates were annealed in an oven (Carbolite Gero 30-3000 °C) at 990 °C for 3 h, contained in ceramic boxes for dust protection. At this annealing temperature, the rigidity of the silica layer increases, coming closer to that of fused silica (Zhang et al., 2010), while the soot burns, resulting in a transparent (nano-)porous silica medium. The substrates were kept dry and protected from dust until use. The main difference with Paven et al. (2013) and Paven et al. (2014) is that we skipped the application of oxygen plasma and the silanization step, to keep the substrates hydrophilic instead of making them superamphiphobic.

Pure water drops (“Milli-Q”) with initial volumes of 1-2  $\mu\text{l}$ , were deposited with a needle (Hamilton Removable Needle, small hub, gauge 22s, tip type 3, Hamilton syringe Gastight Series 1700, volume 10  $\mu\text{l}$ ) onto the substrate, at atmospheres with different IPA vapor content. Experiments with pure water or pure IPA drops were done in atmospheres saturated with the vapor of the same liquid as the drop as reference experiments.

Side-view imaging at an oblique angle ( $\sim 6^\circ$ ) of the drop and the imbibition film was performed with a monochromatic camera at 27 FPS, equipped with a telecentric lens (Thorlabs Bi-Telecentric lens, 1.0X, W.D. 62.2 mm), illuminating the scene with collimated light from the opposite side, at the same angle of incidence, leading to bright specular reflections on horizontal liquid surfaces. Figure 7.1(a) shows a typical snapshot of a droplet surrounded by an imbibition layer. The drop (black lens) is surrounded by an imbibition zone (bright inner and dark outer zone) and the gray (scattering) porous substrate. The radius and the baseline of the drop is determined by the transition from the dark lens and the bright (inner) imbibition zone. The height of the drop is determined by the bright (specular) reflection of the illuminating light on its top part. By measuring the radius  $R$  of the drop and the apical height of the drop  $h$  (above the porous layer), the apparent contact angle is calculated by  $\theta_{\text{app}} = 2h/R$ , assuming a spherical cap shape approximation, with small contact angle. Precise measurements were possible down to  $\theta_{\text{app}} \sim 2^\circ$ , limited by imaging artifacts due to reflection and scattering on the imbibition film, such that the edge of the drop base and the apex of the drop can no longer be distinguished from the porous layer. Frequently, the drop pins after spreading and its shape is no longer close to a spherical cap. In these cases, the measurements were obtained just before the drop deforms significantly. The inner, bright part of the imbibition zone corresponds to a (almost) complete imbibition, leading to a flat, horizontal liquid surface and specular reflection of the light source. The outer, dark

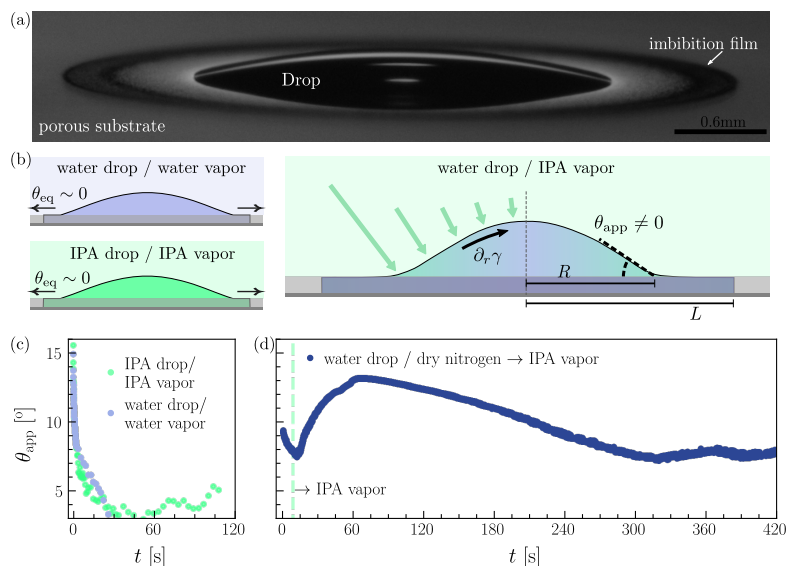


Figure 7.1: (a) Side view of a drop spreading over a substrate made of a porous silicon oxide layer. The drop lies above the porous substrate. The liquid from the drop imbibes into the porous layer and forms a film ahead of the main drop. (b) Drops of pure water or pure IPA in atmospheres saturated with vapor of the same liquid as the drop spread and fully imbibe into the porous medium. In contrast, water drops in atmospheres with IPA content remain contracted: absorption of the IPA vapor on the water drop interface creates a surface tension gradient, inducing a Marangoni flow that prevents the liquid to fully imbibe. (c) Evolution of the apparent contact angle of a pure water drop on a water vapor saturated atmosphere and a pure IPA drop on a IPA vapor saturated atmosphere. (d) Apparent contact angle vs. time for a water drop on an atmosphere that is initially dry, then it is saturated with IPA vapor.

part of the imbibition zone corresponds to partial imbibition. Here, incident light is strongly scattered due to the contrast in refractive indices between the dry and the wet regions. The dry substrate is visible as the outermost, gray zone, indicating a less pronounced scattering of the incident light by the porous structure. The radius of the imbibition front  $L$  was determined from the side-view images by the transition from the black to the gray zone.

Bottom view imaging was performed with an inverted fluorescence microscope (Nikon Eclipse Ti2E). For optical imaging of the drop edge and imbi-

tion front, a plan APO dry immersion objective lens (4x, NA 0.20) was used. For flow visualization experiments, a high-aperture water-immersion objective (20x, NA 0.95) was used. Fluorescent polystyrene microspheres (Thermo Fisher Scientific F8809, diameter 200 nm) were used as flow tracers, with a mass fraction of  $7.8 \times 10^{-5}$  of the particle stock solution. Images of the particles were captured with a high-speed camera at 900 FPS, quickly switching between  $z$ -planes by automating the focus system of the microscope. Flow traces of the particles were obtained by projecting the pixel-wise maximum intensity along a stack of 100 subsequent frames.

### 7.3 Results and Discussion

When a liquid drop is deposited on the porous substrate, it spreads over the top outer surface of the porous layer, while simultaneously wicking into the medium, forming an imbibition zone ahead of the spreading drop. This is generally the case, independent of the chemical composition of the drop and the atmosphere. Panel (a) of Figure 7.1 shows a representative side-view image of a drop on a substrate with a porous layer. The main drop is visible as a dark lens, with a specular reflection of the light source at the apex. The imbibition zone appears bright near the edge of the drop, and becomes dark towards its periphery. This gradient in gray scale results from the difference between specular reflection on a fully imbibed layer versus the strong scattering properties of partially imbibed porous silica.

Panel (b) shows cross-sectional sketches of the drop and the imbibition zone in the substrate, for three cases: a water drop in water vapor (small sketch, blue), an IPA drop in IPA vapor (small sketch, green), and a water drop in IPA vapor (main sketch). In both of the chemically homogeneous cases (pure water and pure IPA), there are no compositional gradients and the drop spreads and imbibes into the porous medium, as has been observed in many previous studies (Kumar et al., 2006; Arjmandi-Tash et al., 2017; Léang et al., 2019; van Gaalen et al., 2021). In contrast, a water drops in an IPA vapor saturated atmosphere is expected to develop strong compositional gradients and internal flows, as indicated by the arrows.

Panel (c) shows the evolution of  $\theta_{\text{app}}$  for chemically homogeneous systems. A pure water drop in a water vapor saturated atmosphere spreads until it pins while wicking continues, reaching  $\theta_{\text{app}} = 0$  simultaneous to complete imbibition at ( $t_{\text{D,f}} = 61.3\text{s}$ ). A pure IPA drop on a IPA vapor saturated

atmosphere spreads, reaching a non-zero minimum  $\theta_{\text{app}} \sim 4^\circ$  which remains nearly constant until complete imbibition at ( $t_{\text{D},f} = 125.2 \text{ s}$ ).

Panel (d) contrasts this simple behavior with the evolution of  $\theta_{\text{app}}$  for a water drop in an atmosphere that is initially dry but then quickly switched to saturated IPA vapor. Initially, the drop spreads with  $\theta_{\text{app}}$  decreasing continuously, similar to water in high ambient humidity. When the IPA vapor is introduced,  $\sim 10 \text{ s}$  after drop deposition, the trend of  $\theta_{\text{app}}$  reverses, increasing up to a maximum of  $\sim 13^\circ$ , ie. the drop contracts on top of a porous layer. This behavior can be explained with inward Marangoni flows induced by the absorption of IPA vapor on the interface of the water drop, similar to what is known on smooth, inert substrates.

In the following we study how the presence of IPA vapor affects the spreading of a water drop and the progress of imbibition front in the porous layer. Additionally we show preliminary results on the internal flow of a Marangoni contracted drop and preliminary results on drop motion induced by atmospheric vapor gradients.

### 7.3.1 Dynamics of the drop

To quantify the impact of the IPA vapor on the spreading dynamics of water drops, the evolution of the drop shape was measured in atmospheres with different IPA content.

Figure 7.2 shows the evolution of  $\theta_{\text{app}}$  (top row) and  $R$  (bottom row) for the first 40 s after drop deposition, except for the case presented in the last column where the experiment happens in a shorter time. Column (a) shows the measurements of the chemically homogeneous systems. A pure water drop on a water vapor saturated atmosphere completely spreads and imbibes into the substrate. During the entire process  $\theta_{\text{app}}$  decreases to zero. Simultaneously,  $R$  shows two stages. In the first stage it increases and reaches a maximum, in the second stage it decreases to zero. For a pure IPA drop on an IPA vapor saturated atmosphere  $R$  also shows the same two stages as the water drop. But different than the water case, the IPA drop reaches a minimum  $\theta_{\text{app}} \sim 4^\circ$  in the first stage, and it increases few degrees during the second stage, remaining nearly constant until the drop completely imbibes. The behavior of both liquids is characteristic of complete wetting in porous media, where the drop lying over the porous surface shows these two distinct stages (Kumar et al., 2006; Arjmandi-Tash et al., 2017; Léang et al., 2019). The main difference between the water drop and the IPA drop is the receding

### 7.3. RESULTS AND DISCUSSION

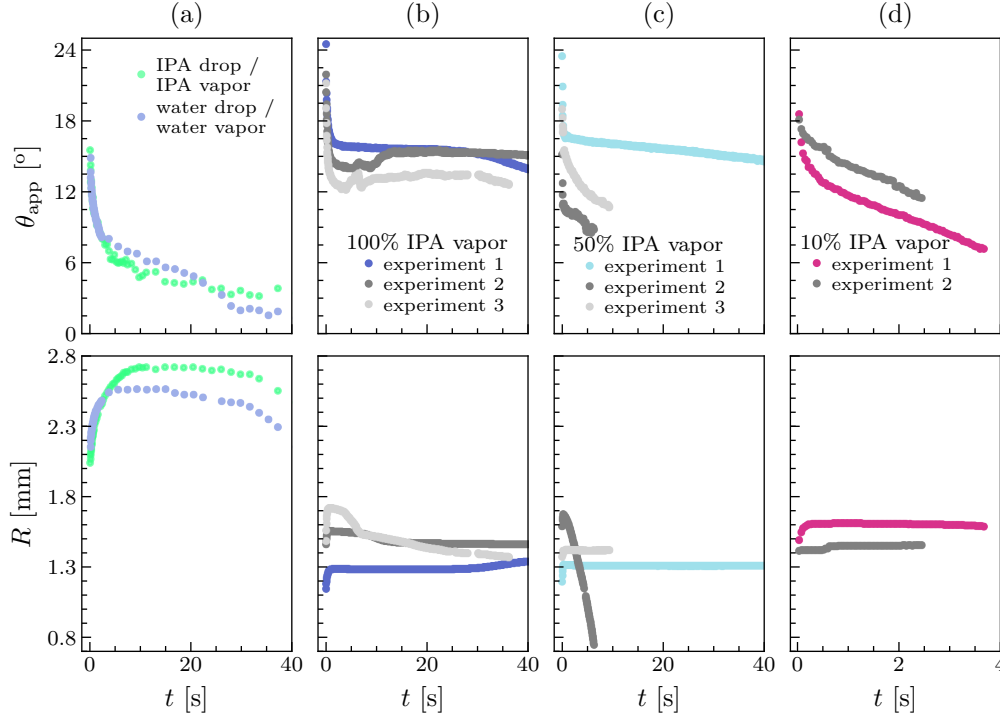


Figure 7.2: Apparent contact angle (top row) and radius (bottom row) vs. time. Column (a): A pure water drop and a pure IPA drop in atmospheres saturated with the vapor of the same liquid. Columns (b-d) Pure water drops in atmospheres with an IPA content of 100% (column b), 50% (column c), and 10% (column d; note the different time scale on this panel).

apparent contact angle during the shrinkage of the drop base,  $\sim 0^\circ$  and  $\sim 4^\circ$ , respectively.

Columns (b-d) show  $\theta_{\text{app}}$  (top row) and  $R$  (bottom row) vs.  $t$  for heterogeneous systems. Three measurements for water drops in an atmosphere with 100% IPA content are shown in column (b), with 50% in column (c), and with 10% in column (d). It was observed for 100% IPA content that  $\theta_{\text{app}} \geq 6^\circ$  for several minutes after deposition. Moreover, the evolution of  $R$  goes through three stages, characteristic of partial wetting on porous substrates (Kumar et al., 2006; Arjmandi-Tash et al., 2017; Léang et al., 2019). In the first stage, as in complete wetting, the drop spreads until  $R$  reaches a maximum. In the second stage, different than in complete wetting,  $R$  remains

constant. In the last stage, as in complete wetting, the drop base shrinks to  $R = 0$ . Although the behavior is similar for the three repeated experiments, the measurements are not reproducible. A similar result is obtained for the cases with atmospheres with 50% IPA content. With 10% IPA content,  $R$  also shows the three stages but the intermediate stage is shorter than with 100 and 50% IPA content, and  $\theta_{\text{app}}$  decreases faster to lower values than on those cases.

The high variability between measurements with same experimental parameters is caused by the stochastic pinning of the contact line. During the spreading process, when  $R$  increases, material of the porous network is collected at the perimeter of the main drop and due to the growing of the imbibition film, forming rings of accumulated material where the edge of the main drop tends to pin. When  $R$  decreases, the pinning sites prevent the edge of the main drop to uniformly recede. This is also one reason why in some cases  $\theta_{\text{app}}$  and  $R$  in the receding stage are not measured, since the drop shape deforms due to pinning the spherical cap shape assumption no longer holds. Another reason for the non-reproducibility is the varying thickness of the porous layer, which is not fixed due to the fabrication process. By volumetric arguments, in a thin porous layer the liquid is expected to expand more in the horizontal direction than in a thick porous layer. The difference in thickness is not expected to be orders of magnitude since the relevant aspects in the fabrication process (time and the distance of the exposure to the candle flame (Paven et al., 2013)) are kept similar, but variations by a factor 2 or more are expected.

A related aspect to consider for the evolution of the drop shape is the initial drop volume  $V_{\text{D},i}$ . It affects the maximum radius of the drop base, the final radius of the imbibition film and the total imbibition time (Starov et al., 2003; Kumar et al., 2006). The drop volume is calculated using the formula for the volume of a spherical cap

$$V_{\text{D}} = \frac{\pi}{6} h (3R^2 + h^2). \quad (7.1)$$

Figure 7.3 shows the evolution of the drop volume for the chemically homogeneous and heterogeneous systems (crosses and dots, respectively). The left panel shows the evolution in physical units on linear axes. The drop volumes decrease continuously to zero, at different rates for the different cases, in a non-linear way. The right panel shows the same data but non-dimensionalized and on logarithmic axes.  $V_{\text{D}}$  is scaled with the initial drop

### 7.3. RESULTS AND DISCUSSION

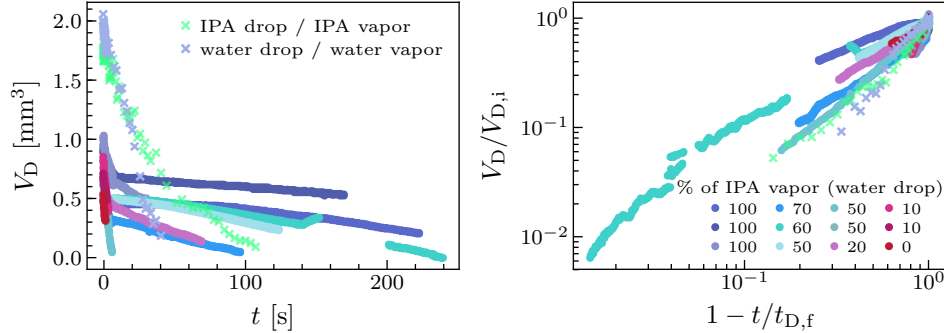


Figure 7.3: Left panel: Volume of the drop above the outer surface of the porous substrate vs. time, for a pure water drop and a pure IPA drop in atmospheres saturated with the vapor of the same liquid (crosses), and for water drops in atmospheres with different IPA content (dots). Missing data is caused by imaging artifacts that are especially problematic at very small apparent contact angles. Right panel: Same data, drop volume scaled with the initial volume and time scaled as  $1 - t/t_{D,f}$ , where  $t_{D,f}$  is the time at which the drop imbibed completely.

volume  $V_{D,i}$ , and time is scaled as  $1 - t/t_{D,f}$ , where  $t_{D,f}$  is the time at which the droplet completely imbibed into the porous layer. Although the data expands over only about a decade, it is compatible with power laws of different exponents, ranging from  $\sim 0.5$  to  $\sim 1$  for the different cases. In particular, for water drops in atmospheres with IPA content no trend is observed with respect to the percentage of IPA.

Two simultaneous processes are involved in the volume decrease of the droplets: evaporation and imbibition. For the chemically homogeneous cases, where the droplets sit in an atmosphere that is (almost) saturated with the vapor of the droplet, the imbibition process clearly dominates, i.e. most of the liquid flows into the porous layer. In Figure 7.3, right panel, these two cases appear very similar. Contrarily, water drops in dry atmospheres or atmospheres with some IPA vapor content decrease in volume not just due to imbibition but also because water evaporates. Additionally, in atmospheres with IPA vapor, Marangoni flows cause a recirculation within the drop, caused by absorption of IPA on the drop interface. This leads to an inhomogeneous pressure in the droplet which is different from the rather constant capillary pressure in pure droplets. With these different processes

taking place, it is expected that  $V_D$  for water drops evolve differently specially for the extreme cases, ie. in dry atmospheres, in atmospheres with saturated water vapor, or with saturated IPA vapor.

### 7.3.2 Dynamics of the imbibition front.

The evolution of the imbibition was observed from the side view (Figure 7.1(a)). For pure liquid drops in atmospheres saturated with the vapor of the same liquid, the liquid fully imbibed into the porous substrate, reaching a maximum wet area that did not change considerably during the remaining observation time. In contrast, for water drops in dry atmospheres and atmospheres with IPA vapor, imbibed liquid evaporates, and the wet area decreases again after some time, until disappearing completely.

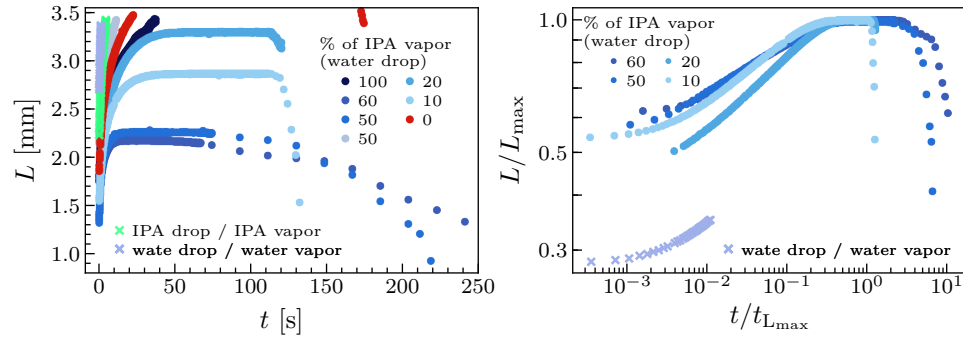


Figure 7.4: Left panel: Length of the imbibition film vs. time, for a pure water drop and a pure IPA drop in atmospheres saturated with the vapor of the same liquid as the drop (crosses), and for water drops in atmospheres with different percentages in IPA content (dots). Right panel: Same data but with  $L$  scaled with the maximum length of the imbibition film and  $t$  scaled with the time taken to reach the maximum length. For the experiments were the entire evolution of the imbibition film could be observed within the field of view.

Figure 7.4 shows the evolution of the imbibition film radius  $L$  (Figure 7.1(b)). The left panel shows the data in physical units on linear axes. For the homogeneous cases,  $L$  increases continuously. For water drops in dry atmospheres or atmospheres with IPA content, the evolution of  $L$  vs.  $t$  exhibits three stages. In the first stage,  $L$  increases up to a maximum value,

### 7.3. RESULTS AND DISCUSSION

---

followed by the second stage where  $L$  remains constant. In the last stage,  $L$  decreases to 0 where the wet area disappears completely. The last two stages are observed only in the cases where evaporation is present. The right panel shows the same data but in dimensionless units on logarithmic axes, for the experiments where the maximum expansion was still in the field of view of the side view image. For the water drop on water vapor, the maximum expansion was obtained separately from the bottom view images.  $L$  was scaled with the maximum radius  $L_{\max}$ , and  $t$  with  $t_{\max}$ , the time at which  $L_{\max}$  was reached. By this scaling, the data is forced to collapse in the second stage, and different trends in the first and last stage are visible. The data follows a similar trend in the first stage, and differs significantly in the last stage. In the first stage, the presence of IPA vapor seems to reduce the speed of the imbibition front. In the last stage, there is a pronounced dependence of on the IPA content in the atmosphere. The rate at which the extent of the imbibition zone shrinks decreases with increasing IPA content.

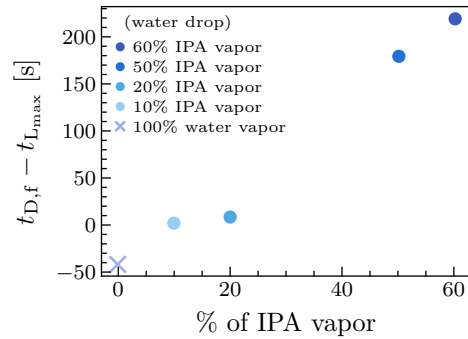


Figure 7.5: Time taken by the drop to imbibe minus the time taken by the imbibition film to reach its maximum radius, as a function of the IPA content in the atmosphere.

Next we plot the delay between the time when the maximum imbibition zone radius is reached,  $t_{L_{\max}}$ , and the complete imbibition of the droplet,  $t_{D,f}$ , as a function of the IPA vapor content (Figure 7.5). Here, a dependence is observed: This delay increases significantly with the IPA content of the atmosphere. For a water drop in a water vapor saturated atmosphere, the drop completely imbibes well before the maximum imbibition film radius is reached. For water drops in atmospheres that are undersaturated with water vapor, but contain IPA vapor, the opposite is observed: The maximum

imbibition film radius is reached before complete imbibition. Moreover,  $t_{D,f} - t_{L_{\max}}$  increases with IPA content. For low IPA content,  $t_{D,f}$  and  $t_{L_{\max}}$  are nearly the same, ie. the maximum imbibed area is given by the initial volume of the liquid. For higher IPA content,  $L$  starts decreasing even there is still liquid above the surface. Two main effects could be responsible for this observation. On the one hand, the liquid in the main drop recirculates within the drop, and the pressure at the substrate is different from the capillary pressure in homogeneous situations. On the other hand, absorption of IPA vapor in the imbibed liquid would alter the wicking force directly. Thus, the presence of IPA vapor changes the pressure gradient between the imbibition front and the reservoir, and essentially prevents imbibition at some point.

Figure 7.6 shows snapshots of the imbibition film of water drops during the imbibition process from bottom view. Each row corresponds to the process for different atmospheric conditions. The first column corresponds to the drop deposition. The second column corresponds to an intermediate time when the drop spreads and wicks, and the imbibition film advances ahead of the contact line of the drop (blue dots). The third column shows when  $L_{\max}$  is reached. The last column corresponds to an intermediate time when the imbibition film recedes. The region covered by the drop has been colored (yellow) for illustration. The droplet is surrounded by the imbibition film, showing up as a gray zone with varying brightness, depending on the filling degree of the porous medium. In all the images after drop deposition, we can observe sharp transition zones in the imbibition film and at the edge of the droplet. Here, the topography of the substrate changes, due to capillary forces breaking the the porous network apart and accumulating the material in concentric rings which remain after the region has dried.

The presence of water vapor (bottom row) leads to a more homogeneous filling, whereas for dry and IPA vapor atmospheres, a large dark zone is visible, corresponding to the strong scattering or partial imbibition. In the third column, the imbibition film appears bright near the main drop and becomes darker at the periphery, this is due to the difference in transmission properties of dry, fully and partially imbibed porous layer. This gradient increases with increasing IPA content in the atmosphere. When reaching the maximum imbibition length, regions that were previously fully imbibed become partially imbibed or dry. This is observed when dark spots appear in the brighter zones and the dark region becomes larger (third and fourth columns). For dry ambient conditions, there is no dark region during spreading which appears only when the imbibition front recedes. And in atmospheres saturated

### 7.3. RESULTS AND DISCUSSION

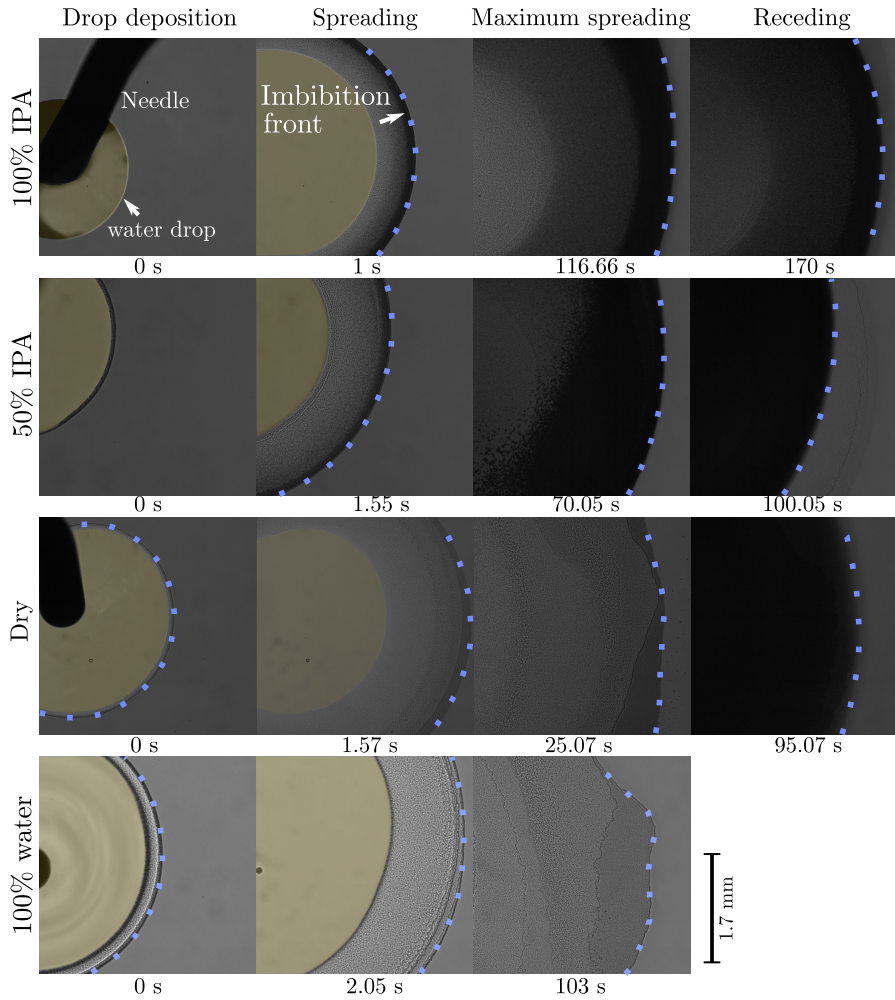


Figure 7.6: Time-lapse images of the imbibition film of water drops in different atmospheric conditions (rows), from bottom view. The field of view moves with the imbibition front (blue dotted line). The water drop (yellow region) is deposited on the porous substrate (first column), it spreads and the imbibition film forms (second column). The imbibition film spreads until reaching a maximum length (third column), and then recedes (fourth column) until it disappears completely. The imbibition film appears bright near the main drop and becomes darker at the periphery due to the difference in transmission of dry, partially and fully imbibed porous medium.

with water vapor, wicked pores remain imbibed.

These observations show that, without IPA, the liquid imbibes almost homogeneously into the porous medium. In the atmosphere with near-saturated water vapor content, the pores remain fully imbibed. In a dry atmosphere, evaporation is responsible of drying of the pores. IPA vapor in the atmosphere, changes this behavior drastically. A strong gradient from dry, over partially imbibed, to complete imbibition is observed from the periphery of the substrate to the contact line of the droplet. The evolution of this gradient depends on the IPA content in the atmosphere. Another consequence of IPA vapor is to keep the front of the imbibition film regularly shaped, in the form of a circle that is nearly concentric to the droplet, as opposed to an irregular front in dry and water vapor atmospheres.

The details of the mechanisms behind these observations remain to be explored. In the next section we present some preliminary qualitative observations on the flows within droplets above the porous medium.

### 7.3.3 Internal flow.

In order to visualize the flows in the drops, fluorescent particles were seeded into the liquids prior to deposition and observed in epifluorescence from the bottom view. Figure 7.7 shows the trajectories of the particles by streak visualization, inside a drop on a porous substrate, in an atmosphere saturated with IPA vapor. Each column corresponds to a different  $z$ -plane parallel to the substrate. Bottom images are a closeup of the top ones, they show the zone where the in-plane velocity of the particles change sign, i.e., where they move predominantly in the vertical direction. The dark zone with no particle trajectories corresponds to the space outside the drop. The free surface of the drop can be identified by the transition between the dark and bright zones. In the plane below the substrate surface (first column), the particles do not reach the edge of the imbibition film, indicating an interaction with the pores.

In all planes inside the droplet, it is observed that the particles move radially outwards in the central region of the drop, and inwards in the regions near the edge of the droplet. This is characteristic of contractile Marangoni flows, with a surface tension gradient pointing toward the drop apex. The trajectories are straight for  $z$ -planes above the substrate surface. Close to the surface, trajectories become irregular because of the irregular top surface of the porous network. This effect becomes more pronounced for the plane

### 7.3. RESULTS AND DISCUSSION

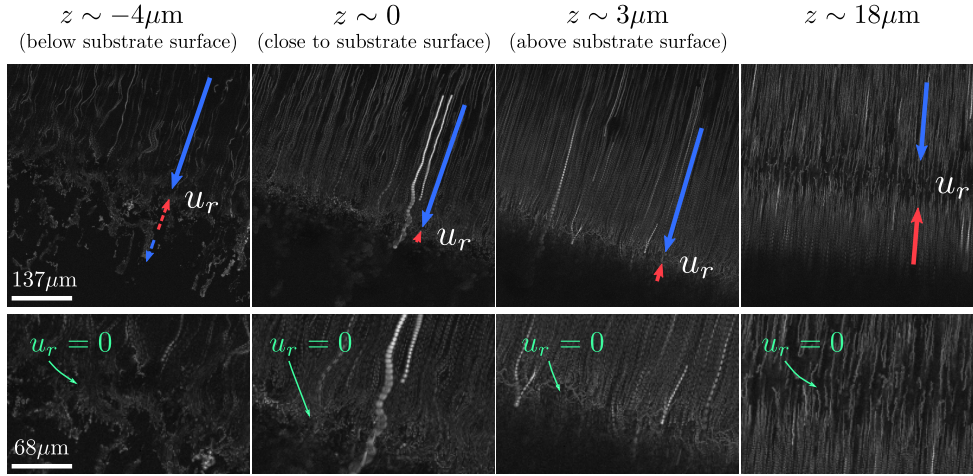


Figure 7.7: Top row: Streak images of fluorescent particles (200 nm diameter) inside a Marangoni contracted drop, from bottom view, at different focal planes below and above the substrate surface. Focal planes above the top substrate of the porous medium ( $z > 0$ ), cross the liquid-vapor interface at some point, and the latter is thus visualized by the transition to a dark zone with no particle trajectories. In the plane below the substrate surface, particles are found in the imbibition film, but not at the advancing front of the film. Bottom row: Zooms of the images above, near the in-plane stagnation zone, where the particles move vertically.

below the substrate surface. Some particles remain trapped in front of the reversal zone, moving back and forth in small and shallow convective rolls perpendicular to the substrate plane. Some particles move from the center of the imbibition film toward the free interface, reverse there, and continue in the upward direction. Close to the surface of the porous layer, particles coming from lower planes are observed along the free interface. This shows that liquid from the film may flow back into the drop above the surface, driven by Marangoni convection at the droplet surface.

Quantification of these velocity fields, with large velocity gradients and irregular trajectories would require additional modifications to the PIV technique presented in the first chapters of this thesis. Also, for the construction of cross-sectional velocity profiles in the droplet, modifications to the data post-processing and analysis will be required. These would be valuable for modeling flows in/on rough surfaces. An important experimental difficulty

is to precisely locate a referential z-plane. On smooth surfaces, this could be achieved by focusing to particles at the contact line of the droplet with the substrate. This is not possible on porous substrates since the transition from the drop to the imbibition film is smooth and particles are not trapped at the contact line but randomly propagate into the pore network.

### 7.3.4 Drop motion in inhomogeneous atmospheres.

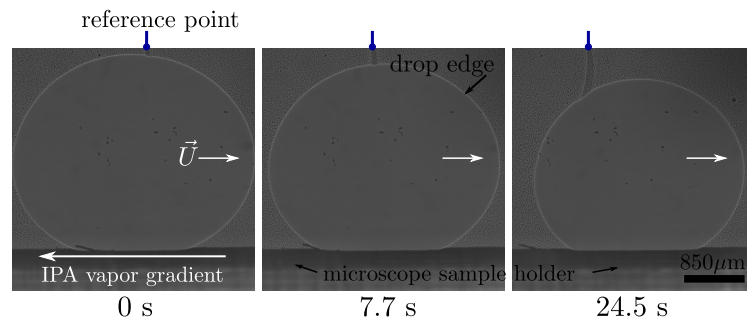


Figure 7.8: Time-lapse images of a water drop moving over a porous substrate due to a controlled IPA vapor gradient in the atmosphere (bottom view). The contact line is visible as a bright ring. The field of view moves with the droplet. Drop motion relative to the substrate is visualized by the indicated reference point, a defect in the porous layer.

Two main questions can be formulated from the previous sections: Is Marangoni contraction sufficiently strong to depin droplets from the irregular outer surface of a porous network, such that they can move freely on top of an imbibed zone? And what is the mechanism by which the IPA vapor modifies the imbibition pattern? To address these questions, droplet on porous layers have been subjected to vapor gradients. It is known from experiments on smooth surfaces [Cira et al., 2015](#); [Benusiglio et al., 2018](#) that Marangoni contracted droplet move in vapor gradients unless their contact line becomes pinned ([Hack et al., 2021](#); Chapter 4). Figure 7.8 shows snapshots of a water drop that moves on a porous substrate, observed from the bottom view. The atmosphere was set with 60% relative humidity to reduce the evaporation rate of water. An IPA vapor gradient was set in the atmosphere by injecting continuously nitrogen mixed with IPA vapor in one side of the chamber. The IPA vapor started being inject into the chamber  $\sim 20$  s before depositing the

drop. Under this atmosphere, the drop moves parallel to the direction of the IPA vapor gradient, toward decreasing IPA concentration. The field of view on the images is kept centered around the droplet, and the net motion of the droplet can be identified by the surface structure moving through the field of view, best identified by the trajectory of a defect that has been labelled in the images. Responsible for this motion is, presumably, a surface tension gradient on the free surface of the drop: The side closer to the IPA source should exhibit a lower surface tension than the other side, originating from the difference in the absorption rate of IPA vapor on the drop interface. Consequentially, the induced Marangoni flows point toward the side with the higher surface tension, leading to a net fluid transport to the side of lower IPA vapor concentration. The fact that the droplet moves demonstrates that its contact line is not pinned on the asperities of the rough porous surface. We can see in Figure 7.8 that the drop is shrinking while it moves, but the motion of the contact lines due to the vapor gradient dominates, causing an advancing motion on the front and a somewhat faster motion on the receding side. The droplet provides an imbibition film to the porous medium that also serves as a lubricant, similar to lubricant impregnated surfaces although here the lubricant and the droplet are perfectly miscible, and the lubricant is supplied by the drop, making it a self-lubricated droplet.

It is important to note that droplet motion is not always observed or sustained throughout an experiment. In many experiments with similar conditions (identical up to the random nature of the substrate surface), motion was not induced, and the drop remained pinned. Surprisingly, when reusing a substrate, though dried before re-use, the drop moved freely, and we could even observe how the imbibition film moved with it. This indicates the importance of the microscopic boundary condition on the inner and top outer surface of the porous layer, which may be influenced by adsorption of water or IPA molecules from the previous experiment. More controlled experiments will be needed to find and control the parameters that affect the unpinning transition.

## 7.4 Conclusion.

We observed the evolution of the shape of water drops and the imbibition film on porous substrates in atmospheres with different composition, dry, wet, and with varying IPA vapor content. We compare these to the chemically

homogeneous cases of pure water and pure IPA droplets in atmosphere that were close to saturation with the vapor of the respective liquid. Pure liquid drops in atmospheres with vapor of the same liquid exhibit two stages in the evolution of their radius, characteristic of complete wetting conditions on the internal and external surfaces of porous substrates: 1) increasing radius to a maximum and 2) decreasing radius to zero. Water drops in atmospheres with IPA vapor show three stages: 1) increasing radius, 2) constant radius and 3) decreasing radius, characteristic of partial wetting. It was found that the volume of the liquid after spreading above the surface follows power laws, but no significant dependency between the exponent of the power laws with the percentage of IPA content was observed. A reason for the absence of such a trend could be the variable thickness of the porous layer, which affects the spreading and imbibition processes.

It was observed that the evolution of the imbibition film radius of water drops in atmospheres with IPA vapor follows three stages: 1) increasing length to a maximum, 2) constant length, and 3) decreasing length to zero. The evolution follows a similar trend for the first two stages and differ mainly in the last one. The difference depends on the amount of IPA vapor in the atmosphere. The life time of the imbibition film after reaching the maximum expansion increases with IPA vapor content. Further, the filling degree of the pores depends on the IPA vapor content: higher IPA concentrations promote partial imbibition, while dry or wet atmospheres promote complete (homogeneous) filling conditions. At the same time, the imbibition front appears more regular with increasing IPA vapor concentration.

Images of tracer particles inside a water drop in an atmosphere saturated with IPA vapor show the presence of Marangoni flows in the droplet, and also regions in which liquid flows from the porous medium back into the droplet. The latter may prevent a complete wicking of the droplet into the porous medium, maintaining a contracted drop above the porous layer. Motion of Marangoni contracted drops on top of porous substrates could be induced by a gradient of IPA vapor in the atmosphere, showing high mobilities on a substrate where pure liquids tend to pin.

These experimental observations will help building an understanding of the behavior of liquid mixtures on and in porous media, both in the fluid phase above the solid i.e., Marangoni contracted drops on porous surfaces, and for imbibition dynamics in presence of compositional gradients.

# Chapter 8

## Conclusion and perspectives

This chapter summarizes the main research results presented over the entire thesis, and gives the general conclusions and perspectives for further investigations.

### 8.1 Main results

The main results correspond to Chapters 4, 5, 6, and 7.

#### 8.1.1 Marangoni contraction and autophobic wetting regimes

In Chapter 4, the mechanisms responsible of the apparent contact angle observed in two wetting regimes in a single systems were investigated. The system used were drops of water and 1,2-Hexanediol mixtures, with different concentrations, over high energy surfaces, at different ambient humidities. Measurements of the apparent contact angles, the internal flows, and the adsorption properties at the solid-vapor interface were done. The results from this investigation are:

- The apparent contact angle continuously increases with the diol concentration despite the diol shows a surfactant-like behavior, which is expected to induce spreading.
- Two wetting mechanism describe the increase of the apparent contact angle: Below the critical micelle concentration (cmc), the apparent

contact angle is determined by Marangoni contraction, whereas above the cmc, it is determined by autophobing. Observation of the internal flows show strong Marangoni flows for concentrations below the cmc and weak flows for larger concentrations. Ellipsometric measurements show an increase of adsorbed molecules ahead of the main drop for larger concentrations.

- Similar experiments with different diols show that the autophobing effect increases with the molecular chain length. Autophobing dominates at large concentrations for molecules with a long aliphatic chain. Marangoni contraction can dominate over the entire concentration range for small molecular chain length.

### 8.1.2 Taylor dispersion in thin liquid films

In Chapter 5, the effect of compositional gradients is studied. The system used were water-diol drops of different concentrations over high energy surfaces at different ambient humidities. Surface tension gradients were derived from measurements of the internal flows. The results from this investigation are:

- The surface tension gradients nearly collapse in physical units, following a power law  $\sim d^{-3/2}$ .
- The lubrication approximation was extended to liquid mixtures where Taylor-Aris dispersion is important. The regime where Taylor dispersion should be considered was identified. This regime is when convection dominates in the horizontal direction, and diffusion dominates in the vertical direction.
- A quantitative agreement between the proposed model, where Taylor-Aris dispersion is included through a long-wave expansion, coupled to diffusion limited evaporation, and the measured velocity fields and surface tensions is obtained.
- From simulations it was observed that capillary and Marangoni flows, opposing to each other, create convective rolls inside the drop that induce a strong shear dispersion that at the same time increase the

effective diffusivity. Thus, the governing mechanism of the evolution of the compositional field is Taylor-Aris dispersion.

### 8.1.3 Liquid-liquid phase separation and wetting dynamics

In Chapter 6, the effect of liquid-liquid phase separation over dynamic contact lines is studied. The model system were Marangoni contracted drops of water-diol mixtures over high energy surfaces. Phase separation is induced by heating the substrate to a critical temperature. Measurements of the drop shape and variations of the thickness of the precursor film were done. The results from this investigation are:

- Marangoni contracted drops loose the contracted state and spread when phase separation happens. Cox-Voinov law no longer describes the dynamics of these moving contact lines.
- The spreading starts before microdroplets nucleate in the main drop. The responsible of the early spreading are surface forces which induce an earlier phase separation.

### 8.1.4 Marangoni contraction over porous substrates

In Chapter 7, the effect of compositional gradients on the spreading and imbibition of drops into porous substrates is studied. The studied model were water drops on atmospheres with different IPA vapor content. Measurements of the apparent contact angle and the imbibition length were done. The results from this investigation are:

- For pure liquid drops (of water or IPA) in atmospheres saturated with the vapor of the same liquid as the drop, the drop radius shows two stages, characteristic of complete wetting on porous media, while water drops on atmospheres with IPA vapor content show three stages, characteristic of partial wetting over porous media.
- For the chemically homogeneous cases (pure water and pure IPA), the liquid imbibes completely reaching a maximum wetted area that did

not change during the remaining observation time. In contrast, the chemically inhomogeneous cases (water drop on atmospheres with IPA vapor) reach a maximum wetted area which then decreases due to the liquid evaporation until complete disappearance. In the first stage, the presence of IPA vapor seems to decrease the rate at which the imbibition front expands. In the last stage, the presence of IPA vapor decreases the rate at which the imbibition front shrinks. For the chemically homogeneous case, the drop completely imbibes before the maximum imbibition film radius is reached, opposite for the chemically inhomogeneous cases.

- Preliminary observations of seeded particles inside the drop show the presence of Marangoni flows. Moreover, it was observed that liquid flows from the porous medium to the drop lying above the surface.
- Motion of Marangoni contracted drops over the porous substrate was induced by introducing atmospheric vapor gradients.

## 8.2 General conclusions and perspectives

The general conclusion from chapters 4, 5, 6, and 7 are presented below.

In Chapter 4, it was observed an unexpected increase of the apparent contact angle for water-diol drops with respect to the diol concentration. The mechanism governing the wetting behavior was distinguished from measurements of the internal flows and the adsorption properties at the solid-vapor interface. Two distinct mechanisms are responsible of the wetting behavior: Marangoni contraction which dominates at low diol concentrations, and autophobing, which dominates at high diol concentrations. The effect of autophobing increases with molecular chain length and may not dominate in the entire concentration range for small molecular chain length. The requirement for Marangoni contraction to dominate the wetting behavior is that the contact angle induced by Marangoni contraction should be larger than the microscopic contact angle.

In Chapter 5, it was observed that surface tension gradients of Marangoni contracted drops follow a power law with respect to the distance to the contact line. A general expression that accounts for Taylor-Aris dispersion, coupled to diffusion limited evaporation, in thin liquid films was given. The pro-

## 8.2. GENERAL CONCLUSIONS AND PERSPECTIVES

---

posed model qualitatively describes the measured surface tension gradients and gives insights of the system. From this, it is observed that Taylor-Aris dispersion is the dominant mechanism for the evolution of the compositional field.

In Chapter 6, it was observed that the Marangoni contracted state can be disturbed by liquid-liquid phase separation, which induces spreading. Surface forces are responsible of the phase separation at the free interface, close to the contact line. This phase separation happens at earlier times than the one observed in the bulk drop. Thus, showing the strong coupling between moving contact lines, phase separation, and surface forces.

In Chapter 7, it was observed that the spreading and imbibition of water drops on porous substrates is affected by the presence of IPA vapor in the atmosphere. The study of the mechanisms responsible of the spreading and imbibition are left for future research. Preliminary observations show that the spreading of the drop above the porous layer is affected simultaneously by the liquid evaporation, which reduces the total liquid volume, by the imbibition, which reduces the liquid volume above the porous layer, and by Marangoni flows, that recirculate the flow within the drop and from the porous medium to the drop. At the same time, the imbibition is affected by the the recirculation of the liquid within the drop, and the capillary wicking could be affected by the presence of IPA. This could change the pressure gradient between the main drop and the imbibition film, preventing imbibition. Experiments that allow for the quantification of the internal flow, of the impact of evaporation, of the impact of the porous layer thickness and mechanical properties will be required for a better understanding of the mechanisms affecting the spreading and imbibition dynamics of liquid mixtures on porous substrates.

# Bibliography

- Aarts, Dirk G. A. L., Henk N. W. Lekkerkerker, Hua Guo, Gerard H. Wegdam, and Daniel Bonn (2005). “Hydrodynamics of Droplet Coalescence”. In: *Phys. Rev. Lett.* 95 (16), p. 164503. DOI: 10.1103/PhysRevLett.95.164503. URL: <https://link.aps.org/doi/10.1103/PhysRevLett.95.164503>.
- Abdulsalam, Surajudeen and Zebulu Dauma Maiwada (2015). “Production of Emulsion House Paint Using Polyvinyl Acetate and Gum Arabic as Binder”. In: *International Journal of Materials Science and Applications* 4.5, pp. 350–353. DOI: 10.11648/j.ijmsa.20150405.20.
- Adachi, Eiki, Antony S. Dimitrov, and Kuniaki Nagayama (1995). “Stripe Patterns Formed on a Glass Surface during Droplet Evaporation”. In: *Langmuir* 11.4, pp. 1057–1060. DOI: 10.1021/1a00004a003.
- Afsar-Siddiqui, A. B., P. F. Luckham, and O. K. Matar (2004). “Dewetting Behavior of Aqueous Cationic Surfactant Solutions on Liquid Films”. In: *Langmuir* 20, pp. 7575–7582. DOI: 10.1021/1a040041z.
- Afsar-Siddiqui, Abia B., Paul F. Luckham, and Omar K. Matar (2003). “The spreading of surfactant solutions on thin liquid films”. In: *Advances in Colloid and Interface Science* 106.1, pp. 183–236. ISSN: 0001-8686. DOI: [https://doi.org/10.1016/S0001-8686\(03\)00111-8](https://doi.org/10.1016/S0001-8686(03)00111-8). URL: <https://www.sciencedirect.com/science/article/pii/S0001868603001118>.
- Agard, D A (1984). “Optical Sectioning Microscopy: Cellular Architecture in Three Dimensions”. In: *Annual Review of Biophysics and Bioengineering* 13.1. PMID: 6742801, pp. 191–219. DOI: 10.1146/annurev.bb.13.060184.001203.
- Agudo-Canalejo, Jaime, Sebastian W Schultz, Haruka Chino, Simona M Migliano, Chieko Saito, Ikuko Koyama-Honda, Harald Stenmark, Andreas Brech, Alexander I May, Noboru Mizushima, et al. (2021). “Wetting reg-

## BIBLIOGRAPHY

---

- ulates autophagy of phase-separated compartments and the cytosol”. In: *Nature* 591.7848, pp. 142–146.
- Ajaev, Vladimir S. (2005). “Spreading of thin volatile liquid droplets on uniformly heated surfaces”. In: *Journal of Fluid Mechanics* 528, 279–296. DOI: 10.1017/S0022112005003320.
- Ajdari, Armand, Nathalie Bontoux, and Howard A. Stone (2006). “Hydrodynamic Dispersion in Shallow Microchannels: the Effect of Cross-Sectional Shape”. In: *Analytical Chemistry* 78.2, pp. 387–392. DOI: 10.1021/ac0508651.
- Alany, R.G, T Rades, S Agatonovic-Kustrin, N.M Davies, and I.G Tucker (2000). “Effects of alcohols and diols on the phase behaviour of quaternary systems”. In: *International Journal of Pharmaceutics* 196.2, pp. 141–145. ISSN: 0378-5173. DOI: [https://doi.org/10.1016/S0378-5173\(99\)00408-1](https://doi.org/10.1016/S0378-5173(99)00408-1). URL: <https://www.sciencedirect.com/science/article/pii/S0378517399004081>.
- Anderson, D. M. and S. H. Davis (1995). “The spreading of volatile liquid droplets on heated surfaces”. In: *Physics of Fluids* 7.2, pp. 248–265. DOI: 10.1063/1.868623.
- Aris, R. (1956). “On the dispersion of a solute in a fluid flowing through a tube”. In: *Proceedings of the Royal Society of London. Series A. Mathematical and Physical Sciences* 235.1200, pp. 67–77. DOI: 10.1098/rspa.1956.0065.
- Arjmandi-Tash, Omid, Nina M. Kovalchuk, Anna Trybala, Igor V. Kuchin, and Victor Starov (2017). “Kinetics of Wetting and Spreading of Droplets over Various Substrates”. In: *Langmuir* 33.18, pp. 4367–4385. DOI: 10.1021/acs.langmuir.6b04094.
- Askounis, Alexandros, Khellil Sefiane, Vasileios Koutsos, and Martin E.R. Shanahan (2014). “The effect of evaporation kinetics on nanoparticle structuring within contact line deposits of volatile drops”. In: *Colloids and Surfaces A: Physicochemical and Engineering Aspects* 441, pp. 855–866. ISSN: 0927-7757. DOI: <https://doi.org/10.1016/j.colsurfa.2012.10.017>. URL: <https://www.sciencedirect.com/science/article/pii/S0927775712006930>.
- Ausserré, D., A. M. Picard, and L. Léger (1986). “Existence and Role of the Precursor Film in the Spreading of Polymer Liquids”. In: *Phys. Rev. Lett.* 57 (21), pp. 2671–2674. DOI: 10.1103/PhysRevLett.57.2671. URL: <https://link.aps.org/doi/10.1103/PhysRevLett.57.2671>.

- Baglioni, Piero, David Chelazzi, Rodorico Giorgi, and Giovanna Poggi (2013). “Colloid and Materials Science for the Conservation of Cultural Heritage: Cleaning, Consolidation, and Deacidification”. In: *Langmuir* 29.17, pp. 5110–5122. DOI: 10.1021/1a304456n.
- Bahr, Ch (2007). “Surface triple points and multiple-layer transitions observed by tuning the surface field at smectic liquid-crystal–water interfaces”. In: *Physical Review Letters* 99.5, p. 057801.
- Bakhshian, Sahar, Margaret Murakami, Seyyed Abolfazl Hosseini, and Qunjun Kang (2020). “Scaling of Imbibition Front Dynamics in Heterogeneous Porous Media”. In: *Geophysical Research Letters* 47.14, e2020GL087914. DOI: <https://doi.org/10.1029/2020GL087914>.
- Banani, Salman F, Hyun O Lee, Anthony A Hyman, and Michael K Rosen (2017). “Biomolecular condensates: organizers of cellular biochemistry”. In: *Nature Reviews Molecular Cell Biology* 18.5, pp. 285–298.
- Bangham, D. H. and Z. Saweris (1938). “The behaviour of liquid drops and adsorbed films at cleavage surfaces of mica”. In: *Trans. Faraday Soc.* 34 (0), pp. 554–570. DOI: 10.1039/TF9383400554.
- Barnes, Geoffrey and Ian Gentle (2011). *Capillarity and the mechanics of surfaces*. Oxford University Press. Chap. 2.
- Barnette, Anna L., David B. Asay, and Seong H. Kim (2008). “Average molecular orientations in the adsorbed water layers on silicon oxide in ambient conditions”. In: *Phys. Chem. Chem. Phys.* 10, pp. 4981–4986. DOI: [doi.org/10.1039/B810309G](https://doi.org/10.1039/B810309G).
- Bascom, Willard D., Robert L. Cottington, and Curtis R. Singleterry (1964). *Dynamic Surface Phenomena in the Spontaneous Spreading of Oils on Solids*. Ed. by Frederick M. Fowkes. Vol. 43. American Chemical Society. Chap. 26, pp. 355–379.
- Bauduin, Pierre, L Wattebled, S Schrödle, Didier Touraud, and Werner Kunz (2004). “Temperature dependence of industrial propylene glycol alkyl ether/water mixtures”. In: *Journal of Molecular Liquids* 115.1, pp. 23–28.
- Beaglehole, D. (1989). “Profiles of the precursor of spreading drops of siloxane oil on glass, fused silica, and mica”. In: *The Journal of Physical Chemistry* 93.2, pp. 893–899. DOI: 10.1021/j100339a067.
- Benusiglio, Adrien, Nate J. Cira, and Manu Prakash (2018). “Two-component marangoni-contracted droplets: friction and shape”. In: *Soft Matter* 14 (37), pp. 7724–7730. DOI: 10.1039/C7SM02361H. URL: <http://dx.doi.org/10.1039/C7SM02361H>.

## BIBLIOGRAPHY

---

- Bera, B., O. Carrier, E. H. G. Backus, M. Bonn, N. Shahidzadeh, and D. Bonn (2018). “Counteracting interfacial energetics for wetting of hydrophobic surfaces in the presence of surfactants”. In: *Langmuir* 34, pp. 12344–12349. DOI: 10.1021/acs.langmuir.8b02874.
- Bera, B., M. H. G. Duits, M. A. Cohen Stuart, D. van den Ende, and F. Mugele (2016). “Surfactant induced autophobing”. In: *Soft Matter* 12, pp. 4562–4571. DOI: 10.1039/C6SM00128A.
- Birch, W. R., M. A. Knewtson, S. Garoff, R. M. Suter, and S. Satija (1995). “Structure of precursing thin films of an anionic surfactant on a silicon oxide/silicon surface”. In: *Langmuir* 11, pp. 48–56. DOI: 10.1021/1a00001a012.
- Birch, W.R., M.A. Knewtson, S. Garoff, R.M. Suter, and S. Satija (1994). “The molecular structure of autophobed monolayers and precursing films of a cationic surfactant on the silicon oxide/silicon surface”. In: *Colloids and Surfaces A: Physicochemical and Engineering Aspects* 89.2, pp. 145–155. ISSN: 0927-7757. DOI: [https://doi.org/10.1016/0927-7757\(94\)80114-2](https://doi.org/10.1016/0927-7757(94)80114-2). URL: <https://www.sciencedirect.com/science/article/pii/0927775794801142>.
- Blake, T.D and J.M Haynes (1969). “Kinetics of liquidliquid displacement”. In: *Journal of Colloid and Interface Science* 30.3, pp. 421–423. ISSN: 0021-9797. DOI: [https://doi.org/10.1016/0021-9797\(69\)90411-1](https://doi.org/10.1016/0021-9797(69)90411-1). URL: <https://www.sciencedirect.com/science/article/pii/0021979769904111>.
- Blake, Terence D. (2006). “The physics of moving wetting lines”. In: *Journal of Colloid and Interface Science* 299.1, pp. 1–13. ISSN: 0021-9797. DOI: <https://doi.org/10.1016/j.jcis.2006.03.051>.
- Bohn, Holger F. and Walter Federle (2004). “Insect aquaplaning: Nepenthes pitcher plants capture prey with the peristome, a fully wettable water-lubricated anisotropic surface”. In: *Proceedings of the National Academy of Sciences* 101.39, pp. 14138–14143. DOI: 10.1073/pnas.0405885101. eprint: <https://www.pnas.org/content/101/39/14138.full.pdf>.
- Bonn, Daniel, Jens Eggers, Joseph Indekeu, Jacques Meunier, and Etienne Rolley (2009). “Wetting and spreading”. In: *Rev. Mod. Phys.* 81.2, pp. 739–805. DOI: 10.1103/revmodphys.81.739.
- Botcherby, Edward J., Christopher W. Smith, Michael M. Kohl, Delphine Débarre, Martin J. Booth, Rimantas Juškaitis, Ole Paulsen, and Tony Wilson (2012). “Aberration-free three-dimensional multiphoton imaging of neuronal activity at kHz rates”. In: DOI: 10.1073/pnas.1111662109.

- Bourgès-Monnier, C. and M. E. R. Shanahan (1995). “Influence of Evaporation on Contact Angle”. In: *Langmuir* 11.7, pp. 2820–2829. DOI: 10.1021/1a00007a076.
- Brangwynne, Clifford P, Peter Tompa, and Rohit V Pappu (2015). “Polymer physics of intracellular phase transitions”. In: *Nature Physics* 11.11, pp. 899–904.
- Brochard-Wyart, F, R Fondecave, and M Boudoussier (2000). “Wetting of antagonist mixtures: the ‘leak out’ transition”. In: *International Journal of Engineering Science* 38.9-10, pp. 1033–1047.
- Bruning, M. A., M. Costalonga, S. Karpitschka, and J. H. Snoeijer (2018). “Delayed coalescence of surfactant containing sessile droplets”. In: *Phys. Rev. Fluids* 3, p. 073605. DOI: 10.1103/PhysRevFluids.3.073605.
- Brutin, D., B. Sobac, B. Loquet, and J. Sampol (2010). “Pattern formation in drying drops of blood”. In: *Journal of Fluid Mechanics* 667, pp. 85–95. DOI: 10.1017/s0022112010005070.
- Brutin, D. and V. Starov (2018). “Recent advances in droplet wetting and evaporation”. In: *Chemical Society Reviews* 47.2, pp. 558–585. DOI: 10.1039/C6CS00902F.
- Cachile, M., O. Bénichou, and A. M. Cazabat (2002). “Evaporating Droplets of Completely Wetting Liquids”. In: *Langmuir* 18.21, pp. 7985–7990. DOI: 10.1021/1a020231e.
- Carle, F., B. Sobac, and D. Brutin (2013). “Experimental evidence of the atmospheric convective transport contribution to sessile droplet evaporation”. In: *Applied Physics Letters* 102.6, p. 061603. DOI: 10.1063/1.4792058.
- Cassie, A. B. D. (1948). “Contact angles”. In: *Discuss. Faraday Soc.* 3 (0), pp. 11–16. DOI: 10.1039/DF9480300011. URL: <http://dx.doi.org/10.1039/DF9480300011>.
- Cassie, A. B. D. and S. Baxter (1944). “Wettability of porous surfaces”. In: *Trans. Faraday Soc.* 40 (0), pp. 546–551. DOI: 10.1039/TF94444000546. URL: <http://dx.doi.org/10.1039/TF94444000546>.
- Cates, Michael E. and Elsen Tjhung (2018). “Theories of binary fluid mixtures: from phase-separation kinetics to active emulsions”. In: *Journal of Fluid Mechanics* 836. DOI: 10.1017/jfm.2017.832.
- Cazabat, A. M. and M. A. Cohen Stuart (1986). “Dynamics of wetting: effects of surface roughness”. In: *The Journal of Physical Chemistry* 90.22, pp. 5845–5849. DOI: 10.1021/j100280a075.

## BIBLIOGRAPHY

---

- Cazabat, A.M., S. Gerdes, M.P. Valignat, and M.P. Valignat (1997). “Dynamics of Wetting: From Theory to Experiment”. In: *Interface Science* 5, pp. 129–139. DOI: 10.1023/A:1008657225779.
- Cazabat, Anne-Marie and Geoffroy Guéna (2010). “Evaporation of macroscopic sessile droplets”. In: *Soft Matter* 6 (12), pp. 2591–2612. DOI: 10.1039/B924477H. URL: <http://dx.doi.org/10.1039/B924477H>.
- Chakrabarti, Brato and David Saintillan (2020). “Shear-induced dispersion in peristaltic flow”. In: *Physics of Fluids* 32.11, p. 113102. DOI: 10.1063/5.0030569.
- Chao, Youchuang and Ho Cheung Shum (2020). “Emerging aqueous two-phase systems: from fundamentals of interfaces to biomedical applications”. In: *Chemical Society Reviews* 49.1, pp. 114–142.
- Chen, Jing-Den and N. Wada (1989). “Wetting dynamics of the edge of a spreading drop”. In: *Phys. Rev. Lett.* 62 (26), pp. 3050–3053. DOI: 10.1103/PhysRevLett.62.3050. URL: <https://link.aps.org/doi/10.1103/PhysRevLett.62.3050>.
- Cheng, Alan K. H., Dinah M. Soolaman, and Hua-Zhong Yu (2006). “Evaporation of Microdroplets of Ethanol-Water Mixtures on Gold Surfaces Modified with Self-Assembled Monolayers”. In: *The Journal of Physical Chemistry B* 110.23, pp. 11267–11271. DOI: 10.1021/jp0572885.
- Choi, Yongjoon, Jeongin Han, and Chongyoun Kim (2011). “Pattern formation in drying of particle-laden sessile drops of polymer solutions on solid substrates”. In: *Korean Journal of Chemical Engineering* 28.11, pp. 2130–2136. DOI: 10.1007/s11814-011-0084-7.
- Christy, John R. E., Yoshinori Hamamoto, and Khellil Sefiane (2011). “Flow Transition within an Evaporating Binary Mixture Sessile Drop”. In: *Phys. Rev. Lett.* 106 (20), p. 205701. DOI: 10.1103/PhysRevLett.106.205701.
- Churaev, N.V. (1995). “Contact angles and surface forces”. In: *Advances in Colloid and Interface Science* 58.2, pp. 87–118. ISSN: 0001-8686. DOI: [https://doi.org/10.1016/0001-8686\(95\)00245-L](https://doi.org/10.1016/0001-8686(95)00245-L). URL: <https://www.sciencedirect.com/science/article/pii/000186869500245L>.
- Cira, N. J., A. Benusiglio, and M. Prakash (2015). “Vapour-mediated sensing and motility in two-component droplets”. In: *Nature* 519.7544, pp. 446–450. DOI: 10.1038/nature14272. URL: <https://doi.org/10.1038/nature14272>.
- Cohen, Scott D., Alan C. Hindmarsh, and Paul F. Dubois (1996). “CVODE, A Stiff/Nonstiff ODE Solver in C”. In: *Computers in Physics* 10.2, p. 138. DOI: 10.1063/1.4822377.

- Compostizo, A, A Crespo Colin, MR Vigil, RG Rubio, and M Diaz Pena (1992). “Thermal expansion and pressure dependence of the critical temperature near the lower-critical solution point of 2-butoxyethanol+ water”. In: *Chemical Physics* 164.3, pp. 465–471.
- Conway, James, Heather Kornis, and Michael R. Fisch (1997). “Evaporation Kinematics of Polystyrene Bead Suspensions”. In: *Langmuir* 13.3, pp. 426–431. DOI: 10.1021/1a960833w.
- Cox, R. G. (1986). “The dynamics of the spreading of liquids on a solid surface. Part 1. Viscous flow”. In: *Journal of Fluid Mechanics* 168, 169–194. DOI: 10.1017/S0022112086000332.
- Craster, R. V. and O. K. Matar (2009). “Dynamics and stability of thin liquid films”. In: *Rev. Mod. Phys.* 81 (3), pp. 1131–1198. DOI: 10.1103/RevModPhys.81.1131. URL: <https://link.aps.org/doi/10.1103/RevModPhys.81.1131>.
- Dabiri, Dana (2007). “Cross-Correlation Digital Particle Image Velocimetry – A Review”. In: (Seattle, WA). University of Washington.
- Darhuber, Anton A. and Sandra M. Troian (2003). “Marangoni Driven Structures in Thin Film Flows”. In: *Physics of Fluids* 15.9, S9–S9. DOI: 10.1063/1.4739213. URL: <https://doi.org/10.1063/1.4739213>.
- Decker, E. L., B. Frank, Y. Suo, and S. Garoff (1999). “Physics of contact angle measurements”. In: *Colloids Surf. A* 156, pp. 177–189. DOI: 10.1016/S0927-7757(99)00069-2.
- Deegan, Robert D. (2000). “Pattern formation in drying drops”. In: *Phys. Rev. E* 61 (1), pp. 475–485. DOI: 10.1103/PhysRevE.61.475. URL: <https://link.aps.org/doi/10.1103/PhysRevE.61.475>.
- Deegan, Robert D., Olgica Bakajin, Todd F. Dupont, Greg Huber, Sidney R. Nagel, and Thomas A. Witten (1997). “Capillary flow as the cause of ring stains from dried liquid drops”. In: *Nature* 389.6653, pp. 827–829. DOI: 10.1038/39827.
- Deegan, Robert D., Olgica Bakajin, Todd F. Dupont, Greg Huber, Sidney R. Nagel, and Thomas A. Witten (2000). “Contact line deposits in an evaporating drop”. In: *Phys. Rev. E* 62 (1), pp. 756–765. DOI: 10.1103/PhysRevE.62.756. URL: <https://link.aps.org/doi/10.1103/PhysRevE.62.756>.
- Degiorgio, Vittorio (1985). “Physics of Amphiphiles, Micelles and Microemulsions”. In: *Europhysics News* 16, pp. 9–12.
- Deng, Xu, Lena Mammen, Hans-Jürgen Butt, and Doris Vollmer (2012). “Candle Soot as a Template for a Transparent Robust Superamphipho-

## BIBLIOGRAPHY

---

- bic Coating”. In: *Science* 335.6064, pp. 67–70. DOI: 10.1126/science.1207115.
- Derjaguin, B.V and N.V Churaev (1978). “On the question of determining the concept of disjoining pressure and its role in the equilibrium and flow of thin films”. In: *Journal of Colloid and Interface Science* 66.3, pp. 389–398. ISSN: 0021-9797. DOI: [https://doi.org/10.1016/0021-9797\(78\)90056-5](https://doi.org/10.1016/0021-9797(78)90056-5). URL: <https://www.sciencedirect.com/science/article/pii/0021979778900565>.
- Derkach, Svetlana R (2009). “Rheology of emulsions”. In: *Advances in colloid and interface science* 151.1-2, pp. 1–23.
- Diddens, Christian (2017). “Detailed finite element method modeling of evaporating multi-component droplets”. In: *Journal of Computational Physics* 340, pp. 670–687. DOI: 10.1016/j.jcp.2017.03.049.
- Diddens, Christian, Huanshu Tan, Pengyu Lv, Michel Versluis, J. G. M. Kuerten, Xuehua Zhang, and Detlef Lohse (2017). “Evaporating pure, binary and ternary droplets: thermal effects and axial symmetry breaking”. In: *Journal of Fluid Mechanics* 823, 470–497. DOI: 10.1017/jfm.2017.312.
- Dietrich, Erik, Maaïke Rump, Pengyu Lv, E. Stefan Kooij, Harold J. W. Zandvliet, and Detlef Lohse (2017). “Segregation in dissolving binary-component sessile droplets”. In: *Journal of Fluid Mechanics* 812, 349–369. DOI: 10.1017/jfm.2016.802.
- Diez, Javier A., L. Kondic, and Andrea Bertozzi (2000). “Global models for moving contact lines”. In: *Physical Review E* 63.1, p. 011208. DOI: 10.1103/physreve.63.011208.
- Ditlev, Jonathon A (2021). “Membrane-associated phase separation: organization and function emerge from a two-dimensional milieu”. In: *Journal of Molecular Cell Biology* 3, mjab010.
- Doumenc, F. and B. Guerrier (2010). “Drying of a Solution in a Meniscus: A Model Coupling the Liquid and the Gas Phases”. In: *Langmuir* 26.17, pp. 13959–13967. DOI: 10.1021/1a1018373.
- Drelich, J. W., L. Boinovich, E. Chibowski, C. D. Volpe, L. Hołysz, A. Marmur, and S. Siboni (2020). “Contact angles: history of over 200 years of open questions”. In: *Surface Innovations* 8, pp. 3–27. DOI: 10.1680/jsuin.19.00007.
- Dussan V., E. B. (1979). “On the Spreading of Liquids on Solid Surfaces: Static and Dynamic Contact Lines”. In: *Annual Review of Fluid Mechanics* 11.1, pp. 371–400. DOI: 10.1146/annurev.fl.11.010179.002103.

- Dussan V., E. B., E. Ramé, and S. Garrof (1991). “On identifying the appropriate boundary conditions at a moving contact line: an experimental investigation”. In: *Journal of Fluid Mechanics* 230, pp. 97–116.
- Dussan V., Elizabeth B. (1976). “The moving contact line: the slip boundary condition”. In: *J. Fluid Mech.* 77, pp. 665–684.
- Dussan V., Elizabeth B. and Stephen H. Davis (1974). “On the motion of a fluid-fluid interface along a solid surface”. In: *Journal of Fluid Mechanics* 65.1, 71–95. DOI: 10.1017/S0022112074001261.
- Edwards, A. M. J., P. S. Atkinson, C. S. Cheung, H. Liang, D. J. Fairhurst, and F. F. Ouali (2018). “Density-Driven Flows in Evaporating Binary Liquid Droplets”. In: *Phys. Rev. Lett.* 121 (18), p. 184501. DOI: 10.1103/PhysRevLett.121.184501. URL: <https://link.aps.org/doi/10.1103/PhysRevLett.121.184501>.
- Eggers, J. and L. M. Pismen (2010). “Nonlocal description of evaporating drops”. In: *Physics of Fluids* 22.11, p. 112101. DOI: 10.1063/1.3491133.
- Eggers, Jens and Howard A Stone (2004). “Characteristic lengths at moving contact lines for a perfectly wetting fluid: the influence of speed on the dynamic contact angle”. In: *Journal of Fluid Mechanics* 505, pp. 309–321.
- Elbaum, M. and S. G. Lipson (1994). “How does a thin wetted film dry up?” In: *Phys. Rev. Lett.* 72 (22), pp. 3562–3565. DOI: 10.1103/PhysRevLett.72.3562. URL: <https://link.aps.org/doi/10.1103/PhysRevLett.72.3562>.
- Fatima, Nowshir, Ichiro Minami, Allan Holmgren, Pär Marklund, and Roland Larsson (2016). “Surface chemistry of wet clutch influenced by water contamination in automatic transmission fluids”. In: *Tribology International* 96, pp. 395–401. ISSN: 0301-679X. DOI: <https://doi.org/10.1016/j.triboint.2015.04.010>. URL: <https://www.sciencedirect.com/science/article/pii/S0301679X15001516>.
- Feslot, F, A M Cazabat, and N Fraysse (1989). “Diffusion-controlled wetting films”. In: *Journal of Physics: Condensed Matter* 1.33, pp. 5793–5798. DOI: 10.1088/0953-8984/1/33/024. URL: <https://doi.org/10.1088/0953-8984/1/33/024>.
- Fletcher, Neville H (1958). “Size effect in heterogeneous nucleation”. In: *The Journal of Chemical Physics* 29.3, pp. 572–576.
- Frank, B. and S. Garoff (1995a). “Origins of the Complex Motion of Advancing Surfactant Solutions”. In: *Langmuir* 11.1, pp. 87–93. DOI: 10.1021/la00001a018.

## BIBLIOGRAPHY

---

- (1995b). “Temporal and spatial development of surfactant self-assemblies controlling spreading of surfactant solutions”. In: *Langmuir* 11, pp. 4333–4340. DOI: 10.1021/1a00011a027.
- (1996). “Surfactant self-assembly near contact lines: control of advancing surfactant solutions”. In: *Colloids Surf. A* 116, pp. 31–42. DOI: 10.1016/0927-7757(96)03622-9.
- Frank, Timothy C, Felipe A Donate, Andrei S Merenov, Grant A Von Wald, Barbara J Alstad, Christian W Green, and Thomas C Thyne (2007). “Separation of Glycol Ethers and Similar LCST-Type Hydrogen-Bonding Organics from Aqueous Solution Using Distillation or Liquid-Liquid Extraction”. In: *Industrial & Engineering Chemistry Research* 46.11, pp. 3774–3786.
- Frindi, M., B. Michels, and R. Zana (1991). “Ultrasonic absorption studies of surfactant exchange between micelles and bulk phase in aqueous micellar solutions of nonionic surfactants with short alkyl chains 1. 1,2-hexanediol and 1,2,3-octanetriol”. In: *J. Phys. Chem.* 95, pp. 4832–4837. DOI: 10.1021/j100165a044.
- Fujiwara, H. (2007). *Spectroscopic Ellipsometry: Principles and Applications*. John Wiley & Sons, pp. 158–177.
- Gaalen, R.T. van, C. Diddens, H.M.A. Wijshoff, and J.G.M. Kuerten (2021). “Marangoni circulation in evaporating droplets in the presence of soluble surfactants”. In: *Journal of Colloid and Interface Science* 584, pp. 622–633. DOI: 10.1016/j.jcis.2020.10.057.
- Gans, B. J. De and U. S. Schubert (2004). “Inkjet Printing of Well-Defined Polymer Dots and Arrays”. In: *Langmuir* 20.18, pp. 7789–7793. DOI: 10.1021/1a049469o.
- Gao, Xuefeng and Lei Jiang (2004). “Water-repellent legs of water striders”. In: *Nature* 432.7013, p. 36. DOI: 10.1038/432036a.
- Gelb, Lev D, KE Gubbins, R Radhakrishnan, and M Sliwinska-Bartkowiak (1999). “Phase separation in confined systems”. In: *Reports on Progress in Physics* 62.12, p. 1573.
- Genes, P.-G. de, F. Brochard-Wyart, and D. Quéré (2004). Springer, New York, pp. 35–38. DOI: 10.1007/978-0-387-21656-0.
- Genes, P.G. de (1985). “Wetting: statics and dynamics”. In: *Rev. Mod. Phys.* 57 (3), pp. 827–863. DOI: 10.1103/RevModPhys.57.827. URL: <https://link.aps.org/doi/10.1103/RevModPhys.57.827>.

- Genzer, Jan and Edward J Kramer (1997). “Wetting of substrates with phase-separated binary polymer mixtures”. In: *Physical review letters* 78.26, p. 4946.
- George, J. and N. V. Sastry (2003). “Density, dynamic viscosities, speeds of sound, and relative permittivities for Water + Alkanediols (Propane-1,2- and -1,3-diol and Butane-1,2-, -1,3-, -1,4-, and -2,3-Diol) at Different Temperatures”. In: *Journal of Chemical and Engineering Data* 48.1, pp. 1529–1539. DOI: 10.1021/je0340755.
- Ghiradella, Helen, William Radigan, and H.L Frisch (1975). “Electrical resistivity changes in spreading liquid films”. In: *Journal of Colloid and Interface Science* 51.3, pp. 522–526. ISSN: 0021-9797. DOI: [https://doi.org/10.1016/0021-9797\(75\)90149-6](https://doi.org/10.1016/0021-9797(75)90149-6). URL: <https://www.sciencedirect.com/science/article/pii/0021979775901496>.
- Gibbs, Josiah Willard (1876). “On the equilibrium of heterogeneous substances”. In: *Transactions of the Connecticut Academy of Arts and Sciences* 3, p. 108.
- Giorgiutti-Dauphiné, F. and L. Pauchard (2016). “Painting cracks: A way to investigate the pictorial matter”. In: *Journal of Applied Physics* 120.6, p. 065107. DOI: 10.1063/1.4960438.
- Gotkis, Y., I. Ivanov, N. Murisic, and L. Kondic (2006). “Dynamic Structure Formation at the Fronts of Volatile Liquid Drops”. In: *Phys. Rev. Lett.* 97 (18), p. 186101. DOI: 10.1103/PhysRevLett.97.186101.
- Guo, Wei, Andrew B Kinghorn, Yage Zhang, Qingchuan Li, Aditi Dey Poonam, Julian A Tanner, and Ho Cheung Shum (2021). “Non-associative phase separation in an evaporating droplet as a model for prebiotic compartmentalization”. In: *Nature Communications* 12.1, pp. 1–13.
- Gurrula, Pradeep, Pallavi Katre, Saravanan Balusamy, Sayak Banerjee, and Kirti Chandra Sahu (2019). “Evaporation of ethanol-water sessile droplet of different compositions at an elevated substrate temperature”. In: *International Journal of Heat and Mass Transfer* 145, p. 118770.
- Haagh, M. E. J., N. Schilderink, F. Mugele, and M. H. G. Duits (2019). “Wetting of mineral surfaces by fatty-acid-laden oil and brine: carbonate effect at elevated temperature”. In: *Energy Fuels* 33, pp. 9446–9456. DOI: 10.1021/acs.energyfuels.9b01351.
- Hack, Michiel A., Wojciech Kwieciński, Olinka Ramírez-Soto, Tim Segers, Stefan Karpitschka, E. Stefan Kooij, and Jacco H. Snoeijer (2021). “Wetting of Two-Component Drops: Marangoni Contraction Versus Auto-

## BIBLIOGRAPHY

---

- phobing”. In: *Langmuir* 37.12, pp. 3605–3611. DOI: 10.1021/acs.langmuir.0c03571.
- Hajji, Said M., Mohamed Brahim Errahmani, Robert Coudert, Rene R. Durand, An Cao, and Eliane Taillandier (1989). “A comparative study of 1,2-hexanediol and 1,2,3-octanetriol in aqueous solutions by different physical techniques”. In: *The Journal of Physical Chemistry* 93.12, pp. 4819–4824. DOI: 10.1021/j100349a028.
- Hamraoui, A., M. Cachile, C. Poulard, and A.M. Cazabat (2004). “Fingering phenomena during spreading of surfactant solutions”. In: *Colloids and Surfaces A: Physicochemical and Engineering Aspects* 250.1. In honour of the 250th volume of Colloid and Surfaces A and the 25th Anniversary of the International Association of Colloid and Interface Scientists (IACIS), pp. 215–221. ISSN: 0927-7757. DOI: <https://doi.org/10.1016/j.colsurfa.2003.12.035>. URL: <https://www.sciencedirect.com/science/article/pii/S0927775704004984>.
- Hänggi, Peter, Peter Talkner, and Michal Borkovec (1990). “Reaction-rate theory: fifty years after Kramers”. In: *Rev. Mod. Phys.* 62 (2), pp. 251–341. DOI: 10.1103/RevModPhys.62.251. URL: <https://link.aps.org/doi/10.1103/RevModPhys.62.251>.
- Hansen, F. K. and G. Rødsrud (1991). “Surface Tension by Pendant Drop”. In: *J. Colloid Interface Sci* 140, pp. 1–8. DOI: 10.1016/0021-9797(91)90296-K.
- Hao, Chonglei, Yahua Liu, Xuemei Chen, Jing Li, Mei Zhang, Yanhua Zhao, and Zuankai Wang (2016). “Bioinspired Interfacial Materials with Enhanced Drop Mobility: From Fundamentals to Multifunctional Applications”. In: *Small* 12.14, pp. 1825–1839. DOI: <https://doi.org/10.1002/smll.201503060>.
- Hardy, W.B. (1919). “III. The spreading of fluids on glass”. In: *The London, Edinburgh, and Dublin Philosophical Magazine and Journal of Science* 38.223, pp. 49–55. DOI: 10.1080/14786440708635928.
- Hardy, W.B. and Flight Lieutenant J.K. Hardy R.A.F. (1919). “II. Note on static friction and on the lubricating properties of certain chemical substances”. In: *The London, Edinburgh, and Dublin Philosophical Magazine and Journal of Science* 38.223, pp. 32–48. DOI: 10.1080/14786440708635927.
- Hashimoto, Shota, Chungpyo Hong, and Ichiro Ueno (2012). “Transient Growth Process of Precursor Film at Early Stage of Droplet Spreading”. In: *Jour-*

- nal of Thermal Science and Technology* 7.3, pp. 487–496. DOI: 10.1299/jtst.7.487.
- He, Yunfei, Pavel Yazhgur, Anniina Salonen, and Dominique Langevin (2015). “Adsorption–desorption kinetics of surfactants at liquid surfaces”. In: *Advances in Colloid and Interface Science* 222. Reinhard Miller, Honorary Issue, pp. 377–384. ISSN: 0001-8686. DOI: <https://doi.org/10.1016/j.cis.2014.09.002>. URL: <https://www.sciencedirect.com/science/article/pii/S0001868614002498>.
- Hennessy, Matthew G., Giulia L. Ferretti, João T. Cabral, and Omar K. Matar (2017). “A minimal model for solvent evaporation and absorption in thin films”. In: *Journal of Colloid and Interface Science* 488, pp. 61–71. DOI: 10.1016/j.jcis.2016.10.074.
- Hertz, H. (1882). “Ueber die Verdunstung der Flüssigkeiten, insbesondere des Quecksilbers, im luftleeren Raume”. In: *Annalen der Physik* 253.10, pp. 177–193. DOI: <https://doi.org/10.1002/andp.18822531002>.
- Hoang, A. and H. P. Kavehpour (2011). “Dynamics of Nanoscale Precursor Film near a Moving Contact Line of Spreading Drops”. In: *Phys. Rev. Lett.* 106 (25), p. 254501. DOI: 10.1103/PhysRevLett.106.254501. URL: <https://link.aps.org/doi/10.1103/PhysRevLett.106.254501>.
- Hocking, L. M. (1976). “A moving fluid interface on a rough surface”. In: *Journal of Fluid Mechanics* 76.4, 801–817. DOI: 10.1017/S0022112076000906.
- Horwath, J., K. Ettinger, M. Bachernegg, E. Bodner, and O. Schmut (2001). “Ocular Ferning Test - Effect of Temperature and Humidity on Tear Ferning Patterns”. In: *Ophthalmologica* 215.2, pp. 102–107. DOI: 10.1159/000050838.
- Hu, Hua and Ronald G. Larson (2002). “Evaporation of a Sessile Droplet on a Substrate”. In: *The Journal of Physical Chemistry B* 106.6, pp. 1334–1344. DOI: 10.1021/jp0118322.
- Hu, J., X.-D. Xiao, D. F. Ogletree, and M. Salmeron (1995). “Imaging the condensation and evaporation of molecularly thin films of water with nanometer resolution”. In: *Science* 268, pp. 267–269. DOI: 10.1126/science.268.5208.267.
- Huethorst, J. A. M. and J. Marra (1991). “Motion of Marangoni-contracted water drops across inclined hydrophilic surfaces”. In: *Langmuir* 7, pp. 2756–2763.
- Huh, Chun and L.E Scriven (1971). “Hydrodynamic model of steady movement of a solid/liquid/fluid contact line”. In: *Journal of Colloid and Interface Science* 35.1, pp. 85–101. ISSN: 0021-9797. DOI: <https://doi.org/>

## BIBLIOGRAPHY

---

- 10.1016/0021-9797(71)90188-3. URL: <https://www.sciencedirect.com/science/article/pii/0021979771901883>.
- Israelachvili, Jacob N (2011). *Intermolecular and Surface Forces*. Academic press.
- Jambon-Puillet, Etienne, Odile Carrier, Noushine Shahidzadeh, David Brutin, Jens Eggers, and Daniel Bonn (2018). “Spreading dynamics and contact angle of completely wetting volatile drops”. In: *Journal of Fluid Mechanics* 844, 817–830. DOI: 10.1017/jfm.2018.142.
- Jarosiewicz, P., G. Czechowski, and J. Jadzyn (2004). “The viscous properties of diols. V. 1,2-Hexanediol in water and Butanol solutions”. In: *Verlag der Zeitschrift für Naturforschung A* 59.9, pp. 559–562. DOI: 10.1515/zna-2004-0905.
- Jensen, Katharine E, Raphael Sarfati, Robert W Style, Rostislav Boltyanskiy, Aditi Chakrabarti, Manoj K Chaudhury, and Eric R Dufresne (2015). “Wetting and phase separation in soft adhesion”. In: *Proceedings of the National Academy of Sciences* 112.47, pp. 14490–14494.
- Jensen, O. E. and J. B. Grotberg (1993). “The spreading of heat or soluble surfactant along a thin liquid film”. In: *Physics of Fluids A: Fluid Dynamics* 5.1, pp. 58–68. DOI: 10.1063/1.858789.
- Jensen, O.E., D. Halpern, and J.B. Grotberg (1994). “Transport of a passive solute by surfactant-driven flows”. In: *Chemical Engineering Science* 49.8, pp. 1107–1117. ISSN: 0009-2509. DOI: [https://doi.org/10.1016/0009-2509\(94\)85083-6](https://doi.org/10.1016/0009-2509(94)85083-6).
- Kahlweit, Manfred and Reinhard Strey (1985). “Phase Behavior of Ternary Systems of the Type H<sub>2</sub>O-Oil-Nonionic Amphiphile (Microemulsions)”. In: *Angewandte Chemie International Edition in English* 24.8, pp. 654–668. DOI: <https://doi.org/10.1002/anie.198506541>. URL: <https://onlinelibrary.wiley.com/doi/abs/10.1002/anie.198506541>.
- Kajiya, Tadashi, Daisaku Kaneko, and Masao Doi (2008). “Dynamical Visualization of “Coffee Stain Phenomenon” in Droplets of Polymer Solution via Fluorescent Microscopy”. In: *Langmuir* 24.21, pp. 12369–12374. DOI: 10.1021/la8017858.
- Karapetsas, George, Richard V. Craster, and Omar K. Matar (2011). “On surfactant-enhanced spreading and superspreading of liquid drops on solid surfaces”. In: *Journal of Fluid Mechanics* 670, 5–37. DOI: 10.1017/S0022112010005495.
- Karapetsas, George, Kirti Chandra Sahu, and Omar K. Matar (2016). “Evaporation of Sessile Droplets Laden with Particles and Insoluble Surfac-

- tants”. In: *Langmuir* 32.27, pp. 6871–6881. DOI: 10.1021/acs.langmuir.6b01042.
- Karpitschka, S. (2018). “The value of a fading tracer”. In: *Journal of Fluid Mechanics* 856, 1–4. DOI: 10.1017/jfm.2018.673.
- Karpitschka, S., C. Weber, and H. Riegler (2015). “Spin Casting of Dilute Solutions: Vertical Composition Profile During Hydrodynamic-Evaporative Film Thinning”. In: *Chem. Eng. Sci.* 129, pp. 243–248. DOI: 10.1016/j.ces.2015.01.028.
- Karpitschka, Stefan, Ferenc Liebig, and Hans Riegler (2017). “Marangoni Contraction of Evaporating Sessile Droplets of Binary Mixtures”. In: *Langmuir* 33.19, pp. 4682–4687. DOI: 10.1021/acs.langmuir.7b00740.
- Karpitschka, Stefan and Hans Riegler (2010). “Quantitative Experimental Study on the Transition between Fast and Delayed Coalescence of Sessile Droplets with Different but Completely Miscible Liquids”. In: *Langmuir* 26.14, pp. 11823–11829. DOI: 10.1021/1a1007457.
- Kavehpour, H. Pirouz, Ben Ovryn, and Gareth H. McKinley (2003). “Microscopic and Macroscopic Structure of the Precursor Layer in Spreading Viscous Drops”. In: *Phys. Rev. Lett.* 91 (19), p. 196104. DOI: 10.1103/PhysRevLett.91.196104. URL: <https://link.aps.org/doi/10.1103/PhysRevLett.91.196104>.
- Keiser, L., H. Bense, P. Colinet, J. Bico, and E. Reyssat (2017). “Marangoni Bursting: Evaporation-Induced Emulsification of Binary Mixtures on a Liquid Layer”. In: *Phys. Rev. Lett.* 118 (7), p. 074504. DOI: 10.1103/PhysRevLett.118.074504. URL: <https://link.aps.org/doi/10.1103/PhysRevLett.118.074504>.
- Kelly-Zion, P.L., J. Batra, and C.J. Pursell (2013). “Correlation for the convective and diffusive evaporation of a sessile drop”. In: *International Journal of Heat and Mass Transfer* 64, pp. 278–285. ISSN: 0017-9310. DOI: <https://doi.org/10.1016/j.ijheatmasstransfer.2013.04.051>. URL: <https://www.sciencedirect.com/science/article/pii/S0017931013003645>.
- Kim, BJ, J Tersoff, S Kodambaka, MC Reuter, EA Stach, and FM Ross (2008). “Kinetics of individual nucleation events observed in nanoscale vapor-liquid-solid growth”. In: *Science* 322.5904, pp. 1070–1073.
- Kim, Hyungsoo, Fran çois Boulogne, Eujin Um, Ian Jacobi, Ernie Button, and Howard A. Stone (2016). “Controlled Uniform Coating from the Interplay of Marangoni Flows and Surface-Adsorbed Macromolecules”. In: *Phys. Rev. Lett.* 116 (12), p. 124501. DOI: 10.1103/PhysRevLett.116.

## BIBLIOGRAPHY

---

124501. URL: <https://link.aps.org/doi/10.1103/PhysRevLett.116.124501>.
- Kim, Hyoungsoo and Howard A Stone (2018). “Direct measurement of selective evaporation of binary mixture droplets by dissolving materials”. In: *Journal of Fluid Mechanics* 850, pp. 769–783.
- Kim, Ihl Yong and Peter C. Wayner (1996). “Shape of an evaporating completely wetting extended meniscus”. In: *Journal of Thermophysics and Heat Transfer* 10.2, pp. 320–325. DOI: 10.2514/3.790.
- Kirkwood, J. G. and J. Riseman (1948). “The intrinsic viscosities and diffusion constants of flexible macromolecules in solution”. In: *J. Chem. Phys.* 16, pp. 565–573. DOI: 10.1063/1.1746947.
- Knudsen, Martin (1915). “Die maximale Verdampfungsgeschwindigkeit des Quecksilbers”. In: *Annalen der Physik* 352.13, pp. 697–708. DOI: <https://doi.org/10.1002/andp.19153521306>.
- Kumar, Sathish M. and Abhijit P. Deshpande (2006). “Dynamics of drop spreading on fibrous porous media”. In: *Colloids and Surfaces A: Physicochemical and Engineering Aspects* 277.1, pp. 157–163. ISSN: 0927-7757. DOI: <https://doi.org/10.1016/j.colsurfa.2005.11.056>. URL: <https://www.sciencedirect.com/science/article/pii/S0927775705009003>.
- Kundu, P. K., I. M. Cohen, and D. R. Dowling (2012). *Fluid Mechanics*. Elsevier.
- Lai, Hsuan-Hong and Li-Jen Chen (1999). “Liquid-Liquid Equilibrium Phase Diagram and Density of Three Water + Nonionic Surfactant CiEj Binary Systems”. In: *Journal of Chemical & Engineering Data* 44.2, pp. 251–253. DOI: 10.1021/je980138l.
- Langmuir, Irving (1918). “The Evaporation of Small Spheres”. In: *Phys. Rev.* 12 (5), pp. 368–370. DOI: 10.1103/PhysRev.12.368. URL: <https://link.aps.org/doi/10.1103/PhysRev.12.368>.
- Larson, Ronald G. (2014). “Transport and deposition patterns in drying sessile droplets”. In: *AIChE Journal* 60.5, pp. 1538–1571. DOI: <https://doi.org/10.1002/aic.14338>.
- Lauga, E., M. P. Brenner, and H. A. Stone (2008). *Microfluidics: The no-slip boundary condition*. New York: Springer-Verlag. Chap. 19.
- Lebedev, N. N. (1965). *The Dirichlet Problem for a Domain Bounded by Two Intersecting Spheres*. Ed. by Richard A. Silverman. Prentice-Hall. Chap. 8, pp. 227–229.

- Leenaars, A. F. M., J. A. M. Huethorst, and J. J. Van Oekel (1990). “Marangoni drying: A new extremely clean drying process”. In: *Langmuir* 6.11, pp. 1701–1703. DOI: 10.1021/la00101a014.
- Lelah, Michael D. and Abraham Marmur (1981). “Spreading kinetics of drops on glass”. In: *Journal of Colloid and Interface Science* 82.2, pp. 518–525. ISSN: 0021-9797. DOI: [https://doi.org/10.1016/0021-9797\(81\)90393-3](https://doi.org/10.1016/0021-9797(81)90393-3). URL: <https://www.sciencedirect.com/science/article/pii/0021979781903933>.
- Lenz, M., M. Rumpf, and G. Grün (2002). “A finite volume scheme for surfactant driven thin film flow”. In: *Proceedings of the Third International Symposium on Finite Volumes for Complex Applications*. Ed. by R. Herbin and D. Kröner, 567–574.
- Leonard, B. P. and Simin Mokhtari (1990). “Beyond first-order upwinding: The ultra-sharp alternative for non-oscillatory steady-state simulation of convection”. In: *International Journal for Numerical Methods in Engineering* 30.4, pp. 729–766. DOI: 10.1002/nme.1620300412.
- Lessel, M., O. Bäumchen, M. Klos, H. Hähl, R. Fetzer, M. Paulus, R. Seemann, and K. Jacobs (2015). “Self-assembled silane monolayers: an efficient step-by-step recipe for high-quality, low energy surfaces”. In: *Surface and Interface Analysis* 47.5, pp. 557–564. DOI: <https://doi.org/10.1002/sia.5729>.
- Levinson, P., A.M. Cazabat, M. A. Cohen Stuart, F. Heslot, and S. Nicolet (1988). “The spreading of macroscopic droplets”. In: *Rev. Phys. Appl.* 23 (6), pp. 1009–1016. DOI: 10.1051/rphysap:019880023060100900. URL: <https://doi.org/10.1051/rphysap:019880023060100900>.
- Li, Yanhong, Reinhard Lipowsky, and Rumiana Dimova (2011). “Membrane nanotubes induced by aqueous phase separation and stabilized by spontaneous curvature”. In: *Proceedings of the National Academy of Sciences* 108.12, pp. 4731–4736.
- Li, Yaxing, Christian Diddens, Pengyu Lv, Herman Wijshoff, Michel Versluis, and Detlef Lohse (2019). “Gravitational Effect in Evaporating Binary Microdroplets”. In: *Phys. Rev. Lett.* 122 (11), p. 114501. DOI: 10.1103/PhysRevLett.122.114501. URL: <https://link.aps.org/doi/10.1103/PhysRevLett.122.114501>.
- Li, Yaxing, Christian Diddens, Tim Segers, Herman Wijshoff, Michel Versluis, and Detlef Lohse (2020). “Rayleigh–Taylor instability by segregation in an evaporating multicomponent microdroplet”. In: *Journal of Fluid Mechanics* 899, A22. DOI: 10.1017/jfm.2020.449.

## BIBLIOGRAPHY

---

- Li, Yaxing, Pengyu Lv, Christian Diddens, Huanshu Tan, Herman Wijshoff, Michel Versluis, and Detlef Lohse (2018). “Evaporation-Triggered Segregation of Sessile Binary Droplets”. In: *Phys. Rev. Lett.* 120 (22), p. 224501. DOI: 10.1103/PhysRevLett.120.224501. URL: <https://link.aps.org/doi/10.1103/PhysRevLett.120.224501>.
- Lindken, Ralph, Massimiliano Rossi, Sebastian Große, and Jerry Westerweel (2009). “Micro-Particle Image Velocimetry ( $\mu$ PIV): Recent developments, applications, and guidelines”. In: *Lab Chip* 9 (17), pp. 2551–2567. DOI: 10.1039/B906558J.
- Lohse, Detlef and Xuehua Zhang (2020). “Physicochemical hydrodynamics of droplets out of equilibrium”. In: *Nature Reviews Physics* 2.8, pp. 426–443. DOI: 10.1038/s42254-020-0199-z.
- Lu, Zhengmao, Ikuya Kinefuchi, Kyle L. Wilke, Geoffrey Vaartstra, and Evelyn N. Wang (2019). “A unified relationship for evaporation kinetics at low Mach numbers”. In: *Nature Communications* 10.2368. DOI: 10.1038/s41467-019-10209-w.
- Lu, Zhengmao, Kyle L. Wilke, Daniel J. Preston, Ikuya Kinefuchi, Elizabeth Chang-Davidson, and Evelyn N. Wang (2017). “An Ultrathin Nanoporous Membrane Evaporator”. In: *Nano Letters* 17.10, pp. 6217–6220. DOI: 10.1021/acs.nanolett.7b02889.
- Lv, Pengyu, Yahui Xue, Yipeng Shi, Hao Lin, and Huiling Duan (2014). “Metastable States and Wetting Transition of Submerged Superhydrophobic Structures”. In: *Phys. Rev. Lett.* 112 (19), p. 196101. DOI: 10.1103/PhysRevLett.112.196101. URL: <https://link.aps.org/doi/10.1103/PhysRevLett.112.196101>.
- Léang, Marguerite, Ludovic Pauchard, Lay-Theng Lee, and Frédérique Giorgiutti-Dauphiné (2019). “Imbibition on a porous layer: dynamical and mechanical characterization”. In: *Soft Matter* 15 (10), pp. 2277–2283. DOI: 10.1039/C8SM02295J.
- Mak, Paul (2010). *Piranha Clean Procedure*. Boston University Photonics Center.
- Malinowski, Robert, Ivan P. Parkin, and Giorgio Volpe (2020). “Nonmonotonic contactless manipulation of binary droplets via sensing of localized vapor sources on pristine substrates”. In: *Science Advances* 6.40, eaba3636. DOI: 10.1126/sciadv.aba3636.
- Manikantan, Harishankar and Todd M. Squires (2020). “Surfactant dynamics: hidden variables controlling fluid flows”. In: *Journal of Fluid Mechanics* 892. DOI: 10.1017/jfm.2020.170.

- Marangoni, Carl (1871). "Ueber die Ausbreitung der Tropfen einer Flüssigkeit auf der Oberfläche einer anderen". In: *Annalen der Physik* 219.7, pp. 337–354. DOI: <https://doi.org/10.1002/andp.18712190702>. eprint: <https://onlinelibrary.wiley.com/doi/pdf/10.1002/andp.18712190702>. URL: <https://onlinelibrary.wiley.com/doi/abs/10.1002/andp.18712190702>.
- March, Rafael, Florian Doster, and Sebastian Geiger (2016). "Accurate early-time and late-time modeling of countercurrent spontaneous imbibition". In: *Water Resources Research* 52.8, pp. 6263–6276. DOI: <https://doi.org/10.1002/2015WR018456>.
- Marin, A., S. Karpitschka, D. Noguera-Marín, M.A. Cabrerizo-Vílchez, M. Rossi, C.J. Kähler, and M.A. Rodríguez Valverde (2019). "Solutal Marangoni flow as the cause of ring stains from drying salty colloidal drops". In: *Phys. Rev. Fluids* 4.4, 041601(R). DOI: [10.1103/physrevfluids.4.041601](https://doi.org/10.1103/physrevfluids.4.041601).
- Marmur, Abraham and Micheal D. Lelah (1981). "The Spreading of aqueous surfactant solutions on glass". In: *Chemical Engineering Communications* 13.1-3, pp. 133–143. DOI: [10.1080/00986448108910901](https://doi.org/10.1080/00986448108910901).
- Marra, J. (1993). "Ultraclean Marangoni Drying". In: *Particles in Gases and Liquids 3: Detection, Characterization, and Control*. Ed. by K. L. Mittal. Boston, MA: Springer US, pp. 269–282. ISBN: 978-1-4899-1187-2. DOI: [10.1007/978-1-4899-1187-2\\_18](https://doi.org/10.1007/978-1-4899-1187-2_18).
- Marra, J. and J. A. M. Huethorst (1991). "Physical principles of Marangoni drying". In: *Langmuir* 7.11, pp. 2748–2755. DOI: [10.1021/1a00059a057](https://doi.org/10.1021/1a00059a057).
- Martinez, Andres W., Scott T. Phillips, George M. Whitesides, and Emanuel Carrilho (2010). "Diagnostics for the Developing World: Microfluidic Paper-Based Analytical Devices". In: *Analytical Chemistry* 82.1, pp. 3–10. DOI: [10.1021/ac9013989](https://doi.org/10.1021/ac9013989).
- Matar, O. K. (2002). "Nonlinear evolution of thin free viscous films in the presence of soluble surfactant". In: *Physics of Fluids* 14.12, pp. 4216–4234. DOI: [10.1063/1.1516597](https://doi.org/10.1063/1.1516597).
- Matar, O. K. and R. V. Craster (2009). "Dynamics of surfactant-assisted spreading". In: *Soft Matter* 5 (20), pp. 3801–3809. DOI: [10.1039/B908719M](https://doi.org/10.1039/B908719M). URL: <http://dx.doi.org/10.1039/B908719M>.
- Maxwell, James Clerk (2011a). *Diffusion*. Ed. by W. D. Editor Niven. Vol. 2. Cambridge Library Collection - Physical Sciences. Cambridge University Press, 625–646. DOI: [10.1017/CB09780511710377.064](https://doi.org/10.1017/CB09780511710377.064).

## BIBLIOGRAPHY

---

- (2011b). *Molecules (A Lecture)*. Ed. by W. D. Editor Niven. Vol. 2. Cambridge Library Collection - Physical Sciences. Cambridge University Press, 361–378. DOI: 10.1017/CB09780511710377.037.
- McLaughlin, John B. (1991). “Inertial migration of a small sphere in linear shear flows”. In: *Journal of Fluid Mechanics* 224, 261–274. DOI: 10.1017/S0022112091001751.
- Meinhart, Carl D., Steve T. Wereley, and Juan G. Santiago (2000). “A PIV Algorithm for Estimating Time-Averaged Velocity Fields”. In: *Journal of Fluids Engineering* 122.2, pp. 285–289.
- Melling, A (1997). “Tracer particles and seeding for particle image velocimetry”. In: *Measurement Science and Technology* 8.12, pp. 1406–1416. DOI: 10.1088/0957-0233/8/12/005. URL: <https://doi.org/10.1088/0957-0233/8/12/005>.
- Molina, Anton, Shailabh Kumar, Stefan Karpitschka, and Manu Prakash (2021). “Droplet tilings for rapid exploration of spatially constrained many-body systems”. In: *Proceedings of the National Academy of Sciences* 118.34.
- Moon, Byeong-Ui, Lidija Malic, Keith Morton, Morteza Jeyhani, Abdelrahman Elmanzalawy, Scott SH Tsai, and Teodor Veres (2020). “Evaporation-Driven Water-in-Water Droplet Formation”. In: *Langmuir* 36.47, pp. 14333–14341.
- Moosavi, Mehrdad and Abbas Ali Rostami (2017). “Densities, Viscosities, Refractive Indices, and Excess Properties of Aqueous 1,2-Etanediol, 1,3-Propanediol, 1,4-Butanediol, and 1,5-Pentanediol Binary Mixtures”. In: *Journal of Chemical & Engineering Data* 62.1, pp. 156–168. DOI: 10.1021/acs.jced.6b00526.
- Morris, S. J. S. (2001). “Contact angles for evaporating liquids predicted and compared with existing experiments”. In: *Journal of Fluid Mechanics* 432, 1–30. DOI: 10.1017/S0022112000003074.
- (2014). “On the contact region of a diffusion-limited evaporating drop: a local analysis”. In: *Journal of Fluid Mechanics* 739, 308–337. DOI: 10.1017/jfm.2013.577.
- Moshinskii, A. I. (2004). “Equivalent Diffusion in a Thin Film Flow with a Non-One-Dimensional Velocity Field and Anisotropic Diffusion Tensor”. In: *Fluid Dynamics* 39.2, pp. 230–238. DOI: 10.1023/b:flui.0000030307.90317.f6.
- Mouat, A. P., C. E. Wood, J. E. Pye, and J. C. Burton (2020). “Tuning Contact Line Dynamics and Deposition Patterns in Volatile Liquid Mix-

- tures”. In: *Phys. Rev. Lett.* 124, p. 064502. DOI: 10.1103/PhysRevLett.124.064502.
- Muggeridge, Ann, Andrew Cockin, Kevin Webb, Harry Frampton, Ian Collins, Tim Moulds, and Peter Salino (2014). “Recovery rates, enhanced oil recovery and technological limits”. In: *Philosophical Transactions of the Royal Society A: Mathematical, Physical and Engineering Sciences* 372.2006, p. 20120320.
- Mukahal, F. H. H. Al, B. R. Duffy, and S. K. Wilson (2017). “Advection and Taylor–Aris dispersion in rivulet flow”. In: *Proceedings of the Royal Society A: Mathematical, Physical and Engineering Sciences* 473.2207, p. 20170524. DOI: 10.1098/rspa.2017.0524.
- Murata, Ken-ichiro and Hajime Tanaka (2010). “Surface-wetting effects on the liquid–liquid transition of a single-component molecular liquid”. In: *Nature Communications* 16.1, pp. 1–9.
- Novotny, V. J. and A. Marmur (1991). “Wetting autophobicity”. In: *J. Colloid Interface Sci.* 145, pp. 355–361. DOI: 10.1016/0021-9797(91)90367-H.
- Oron, A. and A. A. Nepomnyashchy (2004). “Long-wavelength thermocapillary instability with the Soret effect”. In: *Physical Review E* 69.1, p. 016313. DOI: 10.1103/physreve.69.016313.
- Oron, Alexander, Stephen H. Davis, and S. George Bankoff (1997). “Long-scale evolution of thin liquid films”. In: *Reviews of Modern Physics* 69.3, pp. 931–980. DOI: 10.1103/revmodphys.69.931.
- Ottino, J. M., S. R. Wiggins, A. A. Darhuber, J. Z. Chen, J. M. Davis, and S. M. Troian (2004). “A study of mixing in thermocapillary flows on micropatterned surfaces”. In: *Philosophical Transactions of the Royal Society of London. Series A: Mathematical, Physical and Engineering Sciences* 362.1818, pp. 1037–1058. DOI: 10.1098/rsta.2003.1361.
- Overdiep, W.S. (1986). “The levelling of paints”. In: *Progress in Organic Coatings* 14.2, pp. 159–175. ISSN: 0300-9440. DOI: [https://doi.org/10.1016/0033-0655\(86\)80010-3](https://doi.org/10.1016/0033-0655(86)80010-3). URL: <https://www.sciencedirect.com/science/article/pii/0033065586800103>.
- Pahlavan, Amir A., Lisong Yang, Colin D. Bain, and Howard A. Stone (2021a). “Evaporation of Binary-Mixture Liquid Droplets: The Formation of Picoliter Pancakelike Shapes”. In: *Phys. Rev. Lett.* 127 (2), p. 024501. DOI: 10.1103/PhysRevLett.127.024501.

## BIBLIOGRAPHY

---

- Pahlavan, Amir A, Lisong Yang, Colin D Bain, and Howard A Stone (2021b). “Evaporation of Binary-Mixture Liquid Droplets: The Formation of Picoliter Pancakelike Shapes”. In: *Physical Review Letters* 127.2, p. 024501.
- Paredes, Virginia, Emiliano Salvagni, Enrique Rodríguez-Castellón, and José María Manero (2017). “Comparative Study of Surface Chemical Composition and Oxide Layer Modification upon Oxygen Plasma Cleaning and Piranha Etching on a Novel Low Elastic Modulus Ti25Nb21Hf Alloy”. In: *Metallurgical and Materials Transactions A* 48 (8), pp. 3770–3776. DOI: 10.1007/s11661-017-4144-4.
- Parimalanathan, Senthil Kumar, Sam Dehaeck, Alexey Rednikov, and Pierre Colinet (2021). “Controlling the wetting and evaporation dynamics of non-ideal volatile binary solutions”. In: *Journal of Colloid and Interface Science* 592, pp. 319–328.
- Park, J. and J. Moon (2006). “Control of Colloidal Particle Deposit Patterns within Picoliter Droplets Ejected by Ink-Jet Printing”. In: *Langmuir* 22.8, pp. 3506–3513. DOI: 10.1021/la053450j.
- Paven, Maxime, Periklis Papadopoulos, Lena Mammen, Xu Deng, Hermann Sachdev, Doris Vollmer, and Hans-Jürgen Butt (2014). “Optimization of superamphiphobic layers based on candle soot”. In: *Pure and Applied Chemistry* 86.2, pp. 87–96. DOI: doi : 10.1515/pac-2014-5015. URL: <https://doi.org/10.1515/pac-2014-5015>.
- Paven, Maxime, Periklis Papadopoulos, Susanne Schöttler, Xu Deng, Volker Mailänder, Doris Vollmer, and Hans-Jürgen Butt (2013). “Super liquid-repellent gas membranes for carbon dioxide capture and heart–lung machines”. In: *Nature Communications* 4.1. DOI: 10.1038/ncomms3512.
- Pérez-González, Carlos, Ricard Alert, Carles Blanch-Mercader, Manuel Gómez-González, Tomasz Kolodziej, Elsa Bazellieres, Jaume Casademunt, and Xavier Trepát (2019). “Active wetting of epithelial tissues”. In: *Nature Physics* 15.1, pp. 79–88.
- Petrov, Jordan G., John Ralston, Matthew Schneemilch, and Robert A. Hayes (2003). “Dynamics of Partial Wetting and Dewetting in Well-Defined Systems”. In: *The Journal of Physical Chemistry B* 107.7, pp. 1634–1645. DOI: 10.1021/jp026723h.
- Picknett, R.G and R Bexon (1977). “The evaporation of sessile or pendant drops in still air”. In: *Journal of Colloid and Interface Science* 61.2, pp. 336–350. ISSN: 0021-9797. DOI: [https://doi.org/10.1016/0021-9797\(77\)90396-4](https://doi.org/10.1016/0021-9797(77)90396-4). URL: <https://www.sciencedirect.com/science/article/pii/0021979777903964>.

- Popescu, M. N., G. Oshanin, S. Dietrich, and A. Cazabat (2012). “Precursor films in wetting phenomena.” In: *Journal of physics. Condensed matter : an Institute of Physics journal* 24 24.
- Popov, Yuri O. (2005). “Evaporative deposition patterns: Spatial dimensions of the deposit”. In: *Phys. Rev. E* 71 (3), p. 036313. DOI: 10.1103/PhysRevE.71.036313. URL: <https://link.aps.org/doi/10.1103/PhysRevE.71.036313>.
- Popov, Yuri O. and Thomas A. Witten (2003). “Characteristic angles in the wetting of an angular region: Deposit growth”. In: *Phys. Rev. E* 68 (3), p. 036306. DOI: 10.1103/PhysRevE.68.036306. URL: <https://link.aps.org/doi/10.1103/PhysRevE.68.036306>.
- Poulard, C., O. Bénichou, and A. M. Cazabat (2003). “Freely Receding Evaporating Droplets”. In: *Langmuir* 19.21, pp. 8828–8834. DOI: 10.1021/1a030162j.
- Poulard, C., G. Guéna, A. M. Cazabat, A. Boudaoud, and M. Ben Amar (2005). “Rescaling the Dynamics of Evaporating Drops”. In: *Langmuir* 21.18, pp. 8226–8233. DOI: 10.1021/1a050406v.
- Puri, Sanjay (2005). “Surface-directed spinodal decomposition”. In: *Journal of Physics: Condensed Matter* 17.3, R101.
- Quéré, David (2008). “Wetting and Roughness”. In: *Annual Review of Materials Research* 38.1, pp. 71–99. DOI: 10.1146/annurev.matsci.38.060407.132434.
- Quéré, David (1999). “Fluid coating on a fiber”. In: *Annual Review of Fluid Mechanics* 31.1, pp. 347–384. DOI: 10.1146/annurev.fluid.31.1.347.
- Radigan, W, H Ghiradella, H.L Frisch, H Schonhorn, and T.K Kwei (1974). “Kinetics of spreading of glass on fernico metal”. In: *Journal of Colloid and Interface Science* 49.2, pp. 241–248. ISSN: 0021-9797. DOI: [https://doi.org/10.1016/0021-9797\(74\)90357-9](https://doi.org/10.1016/0021-9797(74)90357-9). URL: <https://www.sciencedirect.com/science/article/pii/0021979774903579>.
- Ramírez-Soto, Olinka and Stefan Karpitschka (2021). *Taylor Dispersion Governs the Compositional Evolution of Marangoni-Contracted Droplets*.
- Ramírez-Soto, Olinka, Vatsal Sanjay, Detlef Lohse, Jonathan T. Pham, and Doris Vollmer (2020). “Lifting a sessile oil drop from a superamphiphobic surface with an impacting one”. In: *Science Advances* 6.34, eaba4330. DOI: 10.1126/sciadv.aba4330.
- Reynolds, Osborne (1886). “On the theory of lubrication and its application to Mr. Beauchamp tower’s experiments, including an experimental determination of the viscosity of olive oil”. In: *Philosophical Transactions of*

## BIBLIOGRAPHY

---

- the Royal Society* 177, pp. 157–234. DOI: <http://doi.org/10.1098/rstl.1886.0005>.
- Rio, E., A. Daerr, F. Lequeux, and L. Limat (2006). “Moving Contact Lines of a Colloidal Suspension in the Presence of Drying”. In: *Langmuir* 22.7, pp. 3186–3191. DOI: [10.1021/la052989e](https://doi.org/10.1021/la052989e).
- Ristenpart, W. D., P. G. Kim, C. Domingues, J. Wan, and H. A. Stone (2007). “Influence of Substrate Conductivity on Circulation Reversal in Evaporating Drops”. In: *Phys. Rev. Lett.* 99 (23), p. 234502. DOI: [10.1103/PhysRevLett.99.234502](https://doi.org/10.1103/PhysRevLett.99.234502). URL: <https://link.aps.org/doi/10.1103/PhysRevLett.99.234502>.
- Rolley, E. and C. Guthmann (2007). “Dynamics and Hysteresis of the Contact Line between Liquid Hydrogen and Cesium Substrates”. In: *Phys. Rev. Lett.* 98 (16), p. 166105. DOI: [10.1103/PhysRevLett.98.166105](https://doi.org/10.1103/PhysRevLett.98.166105). URL: <https://link.aps.org/doi/10.1103/PhysRevLett.98.166105>.
- Romero, C. M., M. S. Páez, J. A. Miranda, D. J. Hernández, and L. E. Oviedo (2007). “Effect of temperature on the surface tension of diluted aqueous solutions of 1,2-hexanediol, 1,5-hexanediol, 1,6-hexanediol and 2,5-hexanediol”. In: *Fluid Ph. Equilibria* 258, pp. 67–72. DOI: [10.1016/j.fluid.2007.05.029](https://doi.org/10.1016/j.fluid.2007.05.029).
- Rossi, Massimiliano, Alvaro Marin, and Christian J. Kähler (2019). “Interfacial flows in sessile evaporating droplets of mineral water”. In: *Physical Review E* 100.3, p. 033103. DOI: [10.1103/physreve.100.033103](https://doi.org/10.1103/physreve.100.033103).
- Rowan, S. M., M. I. Newton, F. W. Driewer, and G. McHale (2000). “Evaporation of Microdroplets of Azeotropic Liquids”. In: *The Journal of Physical Chemistry B* 104.34, pp. 8217–8220. DOI: [10.1021/jp000938e](https://doi.org/10.1021/jp000938e).
- Ruckenstein, E and C.S Dunn (1977). “Slip velocity during wetting of solids”. In: *Journal of Colloid and Interface Science* 59.1, pp. 135–138. ISSN: 0021-9797. DOI: [https://doi.org/10.1016/0021-9797\(77\)90347-2](https://doi.org/10.1016/0021-9797(77)90347-2). URL: <https://www.sciencedirect.com/science/article/pii/0021979777903472>.
- Ruijter, M. J. de, T. D. Blake, and J. De Coninck (1999). “Dynamic Wetting Studied by Molecular Modeling Simulations of Droplet Spreading”. In: *Langmuir* 15.22, pp. 7836–7847. DOI: [10.1021/la990171l](https://doi.org/10.1021/la990171l). URL: <https://doi.org/10.1021/la990171l>.
- Rupprecht, H. and T. Gu (1991). “Structure of adsorption layers of ionic surfactants at the solid/liquid interface”. In: *Colloid and Polymer Science* 269.5, pp. 506–522. DOI: [10.1007/BF00655889](https://doi.org/10.1007/BF00655889).

- Sadafi, Hosein, Sam Dehaeck, Alexey Rednikov, and Pierre Colinet (2019). “Vapor-Mediated versus Substrate-Mediated Interactions between Volatile Droplets”. In: *Langmuir* 35.21, pp. 7060–7065. DOI: 10.1021/acs.langmuir.9b00522.
- Sadafi, Hosein, Ramin Rabani, Sam Dehaeck, Hatim Machrafi, Benoit Haut, Pierre Dauby, and Pierre Colinet (2020). “Evaporation induced demixing in binary sessile drops”. In: *Colloids and Surfaces A: Physicochemical and Engineering Aspects* 602, p. 125052.
- Saffman, P. G. (1965). “The lift on a small sphere in a slow shear flow”. In: *Journal of Fluid Mechanics* 22.2, 385–400. DOI: 10.1017/S0022112065000824.
- Sarah, Krainer and Hirn Ulrich (2018). “Short timescale wetting and penetration on porous sheets measured with ultrasound, direct absorption and contact angle”. In: *RSC Adv.* 8 (23), pp. 12861–12869. DOI: 10.1039/C8RA01434E.
- Scales, P. J., F. Grieser, D. N. Furlong, and T. W. Healy (1986). “Contact angle changes for hydrophobic and hydrophilic surfaces induced by non-ionic surfactants”. In: *Colloids Surf.* 21, pp. 55–68. DOI: 10.1016/0166-6622(86)80082-8.
- Schwartz, L. W., D. E. Weidner, and R. R. Eley (1995). “An Analysis of the Effect of Surfactant on the Leveling Behavior of a Thin Liquid Coating Layer”. In: *Langmuir* 11.10, pp. 3690–3693. DOI: 10.1021/1a00010a017.
- Sefiane, K., L. Tadrist, and M. Douglas (2003). “Experimental study of evaporating water–ethanol mixture sessile drop: influence of concentration”. In: *International Journal of Heat and Mass Transfer* 46.23, pp. 4527–4534. ISSN: 0017-9310. DOI: [https://doi.org/10.1016/S0017-9310\(03\)00267-9](https://doi.org/10.1016/S0017-9310(03)00267-9).
- Sefiane, Khellil (2014). “Patterns from drying drops”. In: *Advances in Colloid and Interface Science* 206. Manuel G. Velarde, pp. 372–381. ISSN: 0001-8686. DOI: <https://doi.org/10.1016/j.cis.2013.05.002>. URL: <https://www.sciencedirect.com/science/article/pii/S0001868613000523>.
- Sefiane, Khellil, Samuel David, and Martin E. R. Shanahan (2008). “Wetting and Evaporation of Binary Mixture Drops”. In: *The Journal of Physical Chemistry B* 112.36, pp. 11317–11323. DOI: 10.1021/jp8030418.
- Semenov, S., A. Trybala, R. G. Rubio, N. Kovalchuk, V. Starov, and M. G. Velarde (2014). “Simultaneous spreading and evaporation: recent developments”. In: *Adv. Colloid Interface Sci.* 206, pp. 382–398. DOI: 10.1016/j.cis.2013.08.006.

## BIBLIOGRAPHY

---

- Shahidzadeh-Bonn, Noushine, Salima Rarafaï, Aza Azouni, and Daniel Bonn (2006). “Evaporating droplets”. In: *Journal of Fluid Mechanics* 549, 307–313. DOI: 10.1017/S0022112005008190.
- Sharma, Ashutosh (1998). “Equilibrium and Dynamics of Evaporating or Condensing Thin Fluid Domains: Thin Film Stability and Heterogeneous Nucleation”. In: *Langmuir* 14.17, pp. 4915–4928. DOI: 10.1021/1a971389f.
- Shen, Chonghui and Douglas W. Ruth (1998). “Experimental and numerical investigations of the interface profile close to a moving contact line”. In: *Physics of Fluids* 10.4, pp. 789–799. DOI: 10.1063/1.869603.
- Sheth, Tanvi, Serena Seshadri, Tamás Prileszky, and Matthew E. Helgeson (2020). “Multiple nanoemulsions”. In: *Nature Reviews Materials* 5.3, pp. 214–228. DOI: 10.1038/s41578-019-0161-9.
- Shimizu, Ryotaro and Hajime Tanaka (2015). “A novel coarsening mechanism of droplets in immiscible fluid mixtures”. In: *Nature Communications* 6.1. DOI: 10.1038/ncomms8407.
- Shin, Yongdae and Clifford P Brangwynne (2017). “Liquid phase condensation in cell physiology and disease”. In: *Science* 357.6357.
- Shiri, Samira, Shayandev Sinha, Dieter A. Baumgartner, and Nate J. Cira (2021). “Thermal Marangoni Flow Impacts the Shape of Single Component Volatile Droplets on Thin, Completely Wetting Substrates”. In: *Phys. Rev. Lett.* 127 (2), p. 024502. DOI: 10.1103/PhysRevLett.127.024502. URL: <https://link.aps.org/doi/10.1103/PhysRevLett.127.024502>.
- Shklyaev, S., A. A. Nepomnyashchy, and A. Oron (2007). “Three-dimensional oscillatory long-wave Marangoni convection in a binary liquid layer with the Soret effect: Bifurcation analysis”. In: *Physics of Fluids* 19.7, p. 072105. DOI: 10.1063/1.2749305.
- (2011). “Oscillatory long-wave Marangoni convection in a layer of a binary liquid: Hexagonal patterns”. In: *Physical Review E* 84.5, p. 056327. DOI: 10.1103/physreve.84.056327.
- Shmuylovich, Leonid, Amy Q. Shen, and Howard A. Stone (2002). “Surface Morphology of Drying Latex Films: Multiple Ring Formation”. In: *Langmuir* 18.9, pp. 3441–3445. DOI: 10.1021/1a011484v.
- Smit, B., A. G. Schlijper, L. A. M. Rupert, and N. M. Van Os (1990). “Effects of chain length of surfactants on the interfacial tension: molecular dynamics simulations and experiments”. In: *The Journal of Physical Chemistry* 94.18, pp. 6933–6935. DOI: 10.1021/j100381a003.

- Smith, Edward R., Panagiotis E. Theodorakis, Richard V. Craster, and Omar K. Matar (2018). “Moving Contact Lines: Linking Molecular Dynamics and Continuum-Scale Modeling”. In: *Langmuir* 34.42, pp. 12501–12518. DOI: 10.1021/acs.langmuir.8b00466.
- Snoeijer, Jacco H. (2006). “Free-surface flows with large slopes: Beyond lubrication theory”. In: *Physics of Fluids* 18.2, p. 021701. DOI: 10.1063/1.2171190.
- Snoeijer, Jacco H. and Bruno Andreotti (2013). “Moving Contact Lines: Scales, Regimes, and Dynamical Transitions”. In: *Annual Review of Fluid Mechanics* 45.1, pp. 269–292. DOI: 10.1146/annurev-fluid-011212-140734.
- Snoeijer, Jacco H. and Ko van der Weele (2014). “Physics of the granite sphere fountain”. In: *American Journal of Physics* 82.11, pp. 1029–1039. DOI: 10.1119/1.4886365.
- Soulie, V., S. Karpitschka, F. Lequien, P. Prené, T. Zemb, H. Möhwald, and H. Riegler (2015). “The evaporation behavior of sessile droplets from aqueous saline solutions”. In: *Phys. Chem. Chem. Phys.* 17, pp. 22296–22303. DOI: 10.1039/C5CP02444G.
- Squires, Todd M. and Stephen R. Quake (2005). “Microfluidics: Fluid physics at the nanoliter scale”. In: *Rev. Mod. Phys.* 77 (3), pp. 977–1026. DOI: 10.1103/RevModPhys.77.977. URL: <https://link.aps.org/doi/10.1103/RevModPhys.77.977>.
- Staples, Charles A and John W Davis (2002). “An examination of the physical properties, fate, ecotoxicity and potential environmental risks for a series of propylene glycol ethers”. In: *Chemosphere* 49.1, pp. 61–73.
- Starov, V. M. and H.-J. Butt (2018). “Editorial overview: Worldwide increasing interest in wetting phenomena”. In: *Curr. Opin. Colloid Interface Sci.* 36, A1–A4. DOI: 10.1016/j.cocis.2018.06.005.
- Starov, V.M., S.A. Zhdanov, S.R. Kosvintsev, V.D. Sobolev, and M.G. Velarde (2003). “Spreading of liquid drops over porous substrates”. In: *Advances in Colloid and Interface Science* 104.1, pp. 123–158. ISSN: 0001-8686. DOI: [https://doi.org/10.1016/S0001-8686\(03\)00039-3](https://doi.org/10.1016/S0001-8686(03)00039-3).
- Stoebe, T., Zuxuan Lin, Randal M. Hill, Michael D. Ward, and H. Ted Davis (1996). “Surfactant-Enhanced Spreading”. In: *Langmuir* 12.2, pp. 337–344. DOI: 10.1021/la950513x.
- Sultan, Eric, Arezki Boudaoud, and Martine Ben Amar (2005). “Evaporation of a thin film: diffusion of the vapour and Marangoni instabil-

## BIBLIOGRAPHY

---

- ities". In: *Journal of Fluid Mechanics* 543, 183–202. DOI: 10.1017/S0022112005006348.
- Székely, N., L. Almásy, A. Rădulescu, and L. Rosta (2007). "Small-angle neutron scattering study of aqueous solutions of pentanediol and hexanediol". In: *J. Appl. Cryst.* 40, s307–s311. DOI: 10.1107/S0021889807001483.
- Tadmor, R., A. Baksi, S. Gulec, S. Jadhav, H. E. N'guessan, K. Sen, V. Somasi, M. Tadmor, P. Wasnik, and S. Yadav (2019). "Drops that change their mind: spontaneous reversal from spreading to retraction". In: *Langmuir* 35, pp. 15734–15738. DOI: 10.1021/acs.langmuir.9b02592.
- Takenaka, Y., Y. Sumino, and T. Ohzono (2014). "Dewetting of a droplet induced by the adsorption of surfactants on a glass substrate". In: *Soft Matter* 10 (30), pp. 5597–5602. DOI: 10.1039/C4SM00798K. URL: <http://dx.doi.org/10.1039/C4SM00798K>.
- Tam, Daniel, Volkmar von Arnim, G. H. McKinley, and A. E. Hosoi (2009). "Marangoni convection in droplets on superhydrophobic surfaces". In: *Journal of Fluid Mechanics* 624, pp. 101–123. DOI: 10.1017/S0022112008005053.
- Tan, Huanshu, Christian Diddens, Pengyu Lv, J. G. M. Kuerten, Xuehua Zhang, and Detlef Lohse (2016). "Evaporation-triggered microdroplet nucleation and the four life phases of an evaporating Ouzo drop". In: *Proceedings of the National Academy of Sciences* 113.31, pp. 8642–8647. ISSN: 0027-8424. DOI: 10.1073/pnas.1602260113.
- Tan, Huanshu, Christian Diddens, Michel Versluis, Hans-Jürgen Butt, Detlef Lohse, and Xuehua Zhang (2017). "Self-wrapping of an ouzo drop induced by evaporation on a superamphiphobic surface". In: *Soft Matter* 13.15, pp. 2749–2759.
- Tan, Y. H. and J. A. Finch (2018). "Frothers and gas dispersion: a review of the structure-property function relationship". In: *Physicochem. Probl. Miner. Process.* 54, pp. 40–53. DOI: 10.5277/ppmp1814.
- Tanaka, Hajime (2001). "Interplay between wetting and phase separation in binary fluid mixtures: roles of hydrodynamics". In: *Journal of Physics: Condensed Matter* 13.21, p. 4637.
- Tanaka, Toshihiko, Mitsuaki Morigami, and Nobufumi Atoda (1993). "Mechanism of Resist Pattern Collapse during Development Process". In: *Japanese Journal of Applied Physics* 32.Part 1, No. 12B, pp. 6059–6064. DOI: 10.1143/jjap.32.6059. URL: <https://doi.org/10.1143/jjap.32.6059>.
- Tanner, L H (1979). "The spreading of silicone oil drops on horizontal surfaces". In: *Journal of Physics D: Applied Physics* 12.9, pp. 1473–1484.

- DOI: 10.1088/0022-3727/12/9/009. URL: <https://doi.org/10.1088/0022-3727/12/9/009>.
- Tarafdar, Sujata, Yuri Yu. Tarasevich, Moutushi Dutta Choudhury, Tapati Dutta, and Duyang Zang (2018). “Droplet Drying Patterns on Solid Substrates: From Hydrophilic to Superhydrophobic Contact to Levitating Drops”. In: *Advances in Condensed Matter Physics* 2018. Ed. by Charles Rosenblatt. DOI: 10.1155/2018/5214924.
- Taylor, G. I. (1953). “Dispersion of soluble matter in solvent flowing slowly through a tube”. In: *Proceedings of the Royal Society of London. Series A. Mathematical and Physical Sciences* 219.1137, pp. 186–203. DOI: 10.1098/rspa.1953.0139.
- Thiele, U. (2011). “Note on thin film equations for solutions and suspensions”. In: *The European Physical Journal Special Topics* 197.1, pp. 213–220. DOI: 10.1140/epjst/e2011-01462-7.
- Thiele, U., J. H. Snoeijer, S. Trinschek, and K. John (2018). “Equilibrium contact angle and adsorption layer properties with surfactants”. In: *Langmuir* 34, pp. 7210–7221. DOI: 10.1021/acs.langmuir.8b00513.
- Thiele, Uwe, Andrew J. Archer, and Len M. Pismen (2016). “Gradient dynamics models for liquid films with soluble surfactant”. In: *Physical Review Fluids* 1.8, p. 083903. DOI: 10.1103/physrevfluids.1.083903.
- Thiele, Uwe, Andrew J. Archer, and Mathis Plapp (2012). “Thermodynamically consistent description of the hydrodynamics of free surfaces covered by insoluble surfactants of high concentration”. In: *Physics of Fluids* 24.10, p. 102107. DOI: 10.1063/1.4758476.
- Thiele, Uwe, Desislava V. Todorova, and Hender Lopez (2013). “Gradient Dynamics Description for Films of Mixtures and Suspensions: Dewetting Triggered by Coupled Film Height and Concentration Fluctuations”. In: *Physical Review Letters* 111.11, p. 117801. DOI: 10.1103/physrevlett.111.117801.
- Thomson, James (1855). “XLII. On certain curious motions observable at the surfaces of wine and other alcoholic liquors”. In: *The London, Edinburgh, and Dublin Philosophical Magazine and Journal of Science* 10.67, pp. 330–333. DOI: 10.1080/14786445508641982.
- Thomson, Sir William (1871). “LX. On the equilibrium of vapour at a curved surface of liquid”. In: *The London, Edinburgh, and Dublin Philosophical Magazine and Journal of Science* 42.282, pp. 448–452. DOI: 10.1080/14786447108640606.

## BIBLIOGRAPHY

---

- Traipe-Castro, L., D. Salinas-Toro, D. López, M. Zanolli, M. Srur, F. Valenzuela, A. Cáceres, H. Toledo-Araya, and R. López-Solís (2014). “Dynamics of tear fluid desiccation on a glass surface: a contribution to tear quality assessment”. In: *Biological Research* 47.25. DOI: 10.1186/0717-6287-47-25.
- Trybala, Anna, Adaora Okoye, Sergey Semenov, Hezekiah Agogo, Ramón G. Rubio, Francisco Ortega, and Víctor M. Starov (2013). “Evaporation kinetics of sessile droplets of aqueous suspensions of inorganic nanoparticles”. In: *Journal of Colloid and Interface Science* 403, pp. 49–57. ISSN: 0021-9797. DOI: <https://doi.org/10.1016/j.jcis.2013.04.017>. URL: <https://www.sciencedirect.com/science/article/pii/S0021979713003639>.
- Turnbull, David (1950). “Kinetics of heterogeneous nucleation”. In: *The Journal of Chemical Physics* 18.2, pp. 198–203.
- van Gaalen, R.T., C. Diddens, D.P. Siregar, H.M.A. Wijshoff, and J.G.M. Kuerten (2021). “Absorption of surfactant-laden droplets into porous media: A numerical study”. In: *Journal of Colloid and Interface Science* 597, pp. 149–159. ISSN: 0021-9797. DOI: <https://doi.org/10.1016/j.jcis.2021.03.119>.
- Venerus, David C. and David Nieto Simavilla (2015). “Tears of wine: new insights on an old phenomenon”. In: *Scientific Reports* 5 (1), p. 16162. DOI: 10.1038/srep16162.
- Verdaguer, Albert, Christoph Weis, Gerard Oncins, Guido Ketteler, Hendrik Bluhm, and Miquel Salmeron (2007). “Growth and Structure of Water on SiO<sub>2</sub> Films on Si Investigated by Kelvin Probe Microscopy and in Situ X-ray Spectroscopies”. In: *Langmuir* 23.19, pp. 9699–9703. DOI: 10.1021/1a700893w.
- Vilquin, Alexandre, Vincent Bertin, Pierre Soulard, Gabriel Guyard, Elie Raphael, Frederic Restagno, Thomas Salez, and Joshua D. McGraw (2020). “Time dependence of advection-diffusion coupling for nanoparticle ensembles”. In: *arXiv*, p. 2007.08261.
- Voinov, O. V. (1976). “Hydrodynamics of wetting”. In: *Fluid Dynamics* 11.5, pp. 714–721. DOI: 0.1007/BF01012963.
- Wasan, Darsh T and Alex D Nikolov (2003). “Spreading of nanofluids on solids”. In: *Nature* 423.6936, pp. 156–159.
- Wayner, Peter C. (1991). “The effect of interfacial mass transport on flow in thin liquid films”. In: *Colloids and Surfaces* 52. A Collection of Invited Papers Presented at an International Symposium on Thin Solid and Liq-

- uid Films, pp. 71–84. ISSN: 0166-6622. DOI: [https://doi.org/10.1016/0166-6622\(91\)80006-A](https://doi.org/10.1016/0166-6622(91)80006-A). URL: <https://www.sciencedirect.com/science/article/pii/016666229180006A>.
- Wenzel, J, U Limbach, G Bresonik, and GM Schneider (1980). “Kinetics of phase separation in binary liquid mixtures”. In: *The Journal of Physical Chemistry* 84.15, pp. 1991–1995.
- Wenzel, Robert N. (1936). “Resistance of solid surfaces to wetting by water”. In: *Industrial & Engineering Chemistry* 28.8, pp. 988–994. DOI: 10.1021/ie50320a024.
- Wereley, Steven T. and Carl D. Meinhart (2010). “Recent Advances in Micro-Particle Image Velocimetry”. In: *Annual Review of Fluid Mechanics* 42.1, pp. 557–576. DOI: 10.1146/annurev-fluid-121108-145427.
- Westerweel, J., P. F. Geelhoed, and R. Lindken (2004). “Single-pixel resolution ensemble correlation for micro-PIV applications”. In: *Experiments in Fluids* 37.3, pp. 375–384. DOI: 10.1007/s00348-004-0826-y.
- Wijshoff, H. (2010). “The dynamics of the piezo inkjet printhead operation”. In: *Phys. Rep.* 491, pp. 77–177. DOI: 10.1016/j.physrep.2010.03.003.
- (2018). “Drop dynamics in the inkjet printing process”. In: *Curr. Opin. Colloid Interface Sci.* 36, pp. 20–27. DOI: <https://doi.org/10.1016/j.cocis.2017.11.004>.
- Williams, A. G. L., G. Karapetsas, D. Mamalis, K. Sefiane, O. K. Matar, and P. Valluri (2021). “Spreading and retraction dynamics of sessile evaporating droplets comprising volatile binary mixtures”. In: *Journal of Fluid Mechanics* 907, A22. DOI: 10.1017/jfm.2020.840.
- Wiltzius, Pierre and Andrew Cumming (1991). “Domain growth and wetting in polymer mixtures”. In: *Physical Review Letters* 66.23, p. 3000.
- Winkels, K. G., I. R. Peters, F. Evangelista, M. Riepen, A. Daerr, L. Limat, and J. H. Snoeijer (2011). “Receding contact lines: from sliding drops to immersion lithography”. In: *Eur. Phys. J. Special Topics* 192, pp. 195–205. DOI: 10.1140/epjst/e2011-01374-6.
- Wodlei, F., J. Sebilliau, J. Sebilliau, J. Magnaudet, V. Pimienta, and V. Pimienta (2018). “Marangoni-driven flower-like patterning of an evaporating drop spreading on a liquid substrate”. In: *Nature Communications* 9 (1), p. 820. DOI: 10.1038/s41467-018-03201-3.
- Woodward, J. T. and D. K. Schwartz (1997). “Dewetting Modes of Surfactant Solution as a Function of the Spreading Coefficient”. In: *Langmuir* 13.26, pp. 6873–6876. DOI: 10.1021/1a9707991.

## BIBLIOGRAPHY

---

- Wynne-Jones, W. F. K. and Henry Eyring (1935). “The Absolute Rate of Reactions in Condensed Phases”. In: *J. Chem. Phys.* 3, pp. 492–502. DOI: 10.1063/1.1749713. URL: <https://doi.org/10.1063/1.1749713>.
- Xia, Yajun and Richard H Friend (2005). “Controlled phase separation of polyfluorene blends via inkjet printing”. In: *Macromolecules* 38.15, pp. 6466–6471.
- Xu, Hui, David Shirvanyants, Kathryn Beers, Krzysztof Matyjaszewski, Michael Rubinstein, and Sergei S. Sheiko (2004). “Molecular Motion in a Spreading Precursor Film”. In: *Phys. Rev. Lett.* 93 (20), p. 206103. DOI: 10.1103/PhysRevLett.93.206103. URL: <https://link.aps.org/doi/10.1103/PhysRevLett.93.206103>.
- Xu, Xinpeng, Uwe Thiele, and Tiezheng Qian (2015). “A Variational approach to thin film hydrodynamics of binary mixtures”. In: *Journal of Physics: Condensed Matter* 27.8, p. 085005. DOI: 10.1088/0953-8984/27/8/085005.
- Yaminsky, Vasili, Tommy Nylander, and Barry Ninham (1997). “Thermodynamics of Transfer of Amphiphiles between the Liquid-Air Interface and a Solid Surface-Wetting Tension Study of Langmuir-Blodgett Films”. In: *Langmuir* 13.6, pp. 1746–1757. DOI: 10.1021/1a9607161.
- Young, Thomas (1805). “III. An essay on the cohesion of fluids”. In: *Philosophical Transactions of the Royal Society of London* 95, pp. 65–87. DOI: 10.1098/rstl.1805.0005.
- Zenit, R. (2019). “Some fluid mechanical aspects of artistic painting”. In: *Physical Review Fluids* 4.11, p. 110507. DOI: 10.1103/PhysRevFluids.4.110507.
- Zhang, Jie, Alexander Oron, and Robert P. Behringer (2011). “Novel pattern forming states for Marangoni convection in volatile binary liquids”. In: *Physics of Fluids* 23.7, p. 072102. DOI: 10.1063/1.3609287.
- Zhang, Lijuan, Maria D’Acunzi, Michael Kappl, Arnout Imhof, Alfons van Blaaderen, Hans-Jürgen Butt, Robert Graf, and Doris Vollmer (2010). “Tuning the mechanical properties of silica microcapsules”. In: *Phys. Chem. Chem. Phys.* 12 (47), pp. 15392–15398. DOI: 10.1039/C0CP00871K.
- Zhao, Yan, Hongxia Wang, Hua Zhou, and Tong Lin (2017). “Directional Fluid Transport in Thin Porous Materials and its Functional Applications”. In: *Small* 13.4, p. 1601070. DOI: <https://doi.org/10.1002/smll.201601070>.

- Zhong, X. and F. Duan (2016). “Dewetting transition induced by surfactants in sessile droplets at the early evaporation stage”. In: *Soft Matter* 12, pp. 508–513. DOI: 10.1039/C5SM01976A.
- Zhou, M., S. Caré, D. Courtier-Murias, P. Faure, S. Rodts, and P. Coussot (2018). “Magnetic resonance imaging evidences of the impact of water sorption on hardwood capillary imbibition dynamics”. In: *Wood Science and Technology* 52 (4), pp. 929–955. DOI: 10.1007/s00226-018-1017-y.
- Zhu, B.-Y. and T. Gu (1991). “Surfactant adsorption at solid-liquid interfaces”. In: *Adv. Colloid Interface Sci* 37, pp. 1–32. DOI: 10.1016/0001-8686(91)80037-K.
- Zhu, S., W.G. Miller, L.E. Scriven, and H.T. Davis (1994). “Superspreading of water—silicone surfactant on hydrophobic surfaces”. In: *Colloids and Surfaces A: Physicochemical and Engineering Aspects* 90.1, pp. 63–78. ISSN: 0927-7757. DOI: [https://doi.org/10.1016/0927-7757\(94\)02904-0](https://doi.org/10.1016/0927-7757(94)02904-0). URL: <https://www.sciencedirect.com/science/article/pii/0927775794029040>.

# Acknowledgements

I acknowledge financial support from the Max Planck – University of Twente Center for Complex Fluid Dynamics.

I would like to thank my supervisor Dr.Stefan Karpitschka for the opportunity to work on this project, for the guidance and support I received, and for all the learnings during this process.

I would like to thank Prof.Dr.Doris Vollmer for her support.

I would like to thank the members of my thesis advisory committee and the members of the examination board.

I would like to thank my collaborators of the projects presented in this thesis.

Many thanks to Wolf Keiderling, Kristian Hantke, Markus Benderoth, Thomas Eggers, and Sarah Romanowski for their technical support in the lab.

Thanks to my office mates, my colleagues, the technicians in the workshops and the human resources staff, who made friendlier the working place.

Many thanks to my family and friends for sharing our ups and downs. Thanks to my parents and brother for the love and solidarity we have built, thanks for their affection and their support beyond my education.